# Mountain Glacier Change Across Regions and Timescales

Joshua M. Maurer

Submitted in partial fulfillment of the
requirements for the degree of
Doctor of Philosophy
under the Executive Committee
of the Graduate School of Arts and Sciences

COLUMBIA UNIVERSITY

2020

# Abstract

Mountain Glacier Change Across Regions and Timescales

Joshua M. Maurer

Mountain glaciers have influenced the surface of our planet throughout geologic time. These large reservoirs of water ice sculpt alpine landscapes, regulate downstream river flows, perturb climate-tectonic feedbacks, contribute to sea level change, and guide human migration and settlement patterns. Glaciers are especially relevant in modern times, acting as buffers which supply seasonal meltwater to densely populated downstream communities and support economies via hydropower generation. Anthropogenic warming is accelerating ice loss in most glacierized regions of the world. This has sparked concerns regarding water resources and natural hazards, and placed glaciers at the forefront of climate research. Here we provide new observations of glacier change in key mountain regions to quantify rates of ice loss, better understand climate drivers, and help establish a more unified framework for studying glacier change across timescales.

In **Chapter 1** we use seismic observations, numerical modeling, and geomorphic analysis to investigate a destructive glacial lake outburst flood (GLOF) which occurred in Bhutan. GLOFs are a substantial hazard for downstream communities in many vulnerable regions. Yet key aspects of GLOF dynamics remain difficult to quantify, as in situ measurements are scarce due to

the unpredictability and remote source locations of these events. Here we apply cross-correlation based seismic analyses to track the evolution of the GLOF remotely (~100 km from the source region), use the seismic observations along with eyewitness reports and a downstream gauge station to constrain a numerical flood model, then assess geomorphic change and current state of the unstable lakes via satellite imagery. Coherent seismic energy is evident from 1 to 5 Hz beginning approximately 5 hours before the flood impacted Punakha village, which originated at the source lake and advanced down the valley during the GLOF duration. Our analysis highlights potential benefits of using real-time seismic monitoring to improve early warning systems.

The next two chapters in this work focus on quantifying multi-decadal glacier ice loss in the Himalayas. Himalayan glaciers supply meltwater to densely populated catchments in South Asia, and regional observations of glacier change are needed to understand climate drivers and assess impacts on glacier-fed rivers. Here we utilize a set of digital elevation models derived from cold war–era spy satellite film and modern stereo satellite imagery to evaluate glacier responses to changing climate over the last four decades. In **Chapter 2** we focus on the eastern Himalayas, centered on the Bhutan–China border. The wide range of glacier types allows for the first mass balance comparison between clean, debris, and lake-terminating (calving) glaciers in the area. Measured glaciers show significant ice loss, with statistically similar mass balance values for both clean-ice and debris-covered glacier groups. **Chapter 3** extends the same methodology to quantify glacier change across the entire Himalayan range during 1975–2000 and 2000–2016. We observe consistent ice loss along the entire 2000-km transect for both intervals and find a doubling of the average loss rate during 2000–2016 compared to 1975–2000. The similar magnitude and acceleration of ice loss across the Himalayas suggests a regionally coherent

climate forcing, consistent with atmospheric warming and associated energy fluxes as the dominant drivers of glacier change.

**Chapter 4** investigates millennial-scale glacier changes during the Late Glacial period (15-11 ka). Here we present a high-precision beryllium-10 chronology and geomorphic map from a sequence of well-preserved moraines in the Nendaz valley of the western European Alps, with the goal to shed light on the timing and magnitude of glacier responses during an interval of dramatic natural climate variability. Our chronology brackets a coherent glacier recession through the Younger Dryas stadial into the early Holocene, similar to glacier records from the southern hemisphere and a new chronology from Arctic Norway. These results highlight a general agreement between mountain glacier changes and atmospheric greenhouse gas records during the Late Glacial.

In **Chapter 5** we use a numerical glacier model to simulate glacier change across a typical alpine region in the European Alps. Model results suggest that shorter observational timespans focused on modern periods (when glaciers are far from equilibrium and undergoing rapid change) exhibit greater spatial variability of mean annual ice thickness changes, compared to intervals which extend further back in time (to include decades when climate was more stable). The model agrees with multi-decadal satellite observations of glacier change, and clarifies the positive correlation between glacier disequilibrium and spatial variability of glacier mass balance. This relationship should be taken into account in regional glacier studies, particularly when analyzing recent spatial patterns of ice loss.

Advances made in this work are of practical value for societies vulnerable to glacier change. This includes potential improvements to GLOF early warning systems via seismic monitoring, better constraints on glacier-sourced water scenarios in South Asia, strengthened understanding

of long-term glacier responses to baseline natural climate variability, and a clarified relationship between glacier disequilibrium and spatial variability of ice loss. When placed within a global context, our observations highlight the correlation between regional mountain glacier change and greenhouse gas forcing through time.

# Table of Contents

# List of Figures

# List of Tables

# List of Supplementary Figures

# List of Supplementary Tables

# Acknowledgments

I would first like to sincerely thank my advisor Joerg Schaefer for giving me the opportunity to work with him in pursuing earth science at Columbia and LDEO. His drive, enthusiasm, and vision really inspired and catapulted this work to a level I never thought possible. Thanks also to my advisory committee members Sid Hemming and Chris Small, who provided valuable input for my research and assisted me in navigating through graduate school. I'm grateful to the LDEO Cosmogenic Nuclide Group including Jean Hanley, Jeremy Frisch, and Roseanne Schwarz, who patiently helped me in the lab and taught me beryllium extraction and cosmogenic nuclide techniques. A special thanks to Olivia Gardner, without whose love, encouragement, and support I never would have succeeded. Thank you for hauling a backpack full of metamorphic rocks up and down mountains (in the rain!) in the name of science. I'm grateful to Summer Rupper, who is largely responsible for getting me interested in glaciers and climate to begin with, and whose skillful guidance has been invaluable throughout my studies. Also Mike Kaplan who assisted with fieldwork, and from whom I was able to glean a bit of knowledge on the subject of glacial geomorphology. Thanks to Josh Russell, who shared his seismological and data processing expertise, as well as many fun and therapeutic birding excursions to Central Park. Finally, I would like to acknowledge and thank all my family, friends, teachers, and professors who guided, inspired, and supported my scientific endeavors through the years.

*To Mom and Dad, who instilled in me a love and curiosity for the natural world*

# Introduction

The state of any glacier is determined by its mass and energy balance through time, primarily via interaction with the atmosphere (e.g. precipitation and air temperature). Substantial glacier changes can occur over a range of different timescales, from glacial lake outburst floods which drastically alter landscapes and devastate downstream communities in a matter of minutes (Chapter 1), to 21$^{st}$ century acceleration of glacier ice loss across large mountain regions affecting availability of seasonal meltwater in densely populated environments (Chapters 2 and 3), to landscape-altering, millennial-scale glacier advances and retreats which occurred through the Quaternary (Chapter 4). Quantifying rates of ice loss and understanding climate drivers of glacier change are vital for accurate projections of hydrological impacts in the coming decades.

Within the scientific literature, some contrasting viewpoints exist regarding spatiotemporal patterns of glacier behavior in various regions. Annual to multi-decadal studies (based on in-situ field measurements and satellite observations) often highlight complex spatial patterns of ice loss and significant spatiotemporal variability, while centennial to millennial studies (based on techniques such as surface exposure dating of moraine boulders) suggest largely synchronous glacier changes across regions and hemispheres in response to long-term natural climate variability. This contrast is generally understood to be partially caused by the way in which glacier dynamics integrate and average climate signals through time; however, there is a clear disconnect regarding the topic in glaciological literature. This may be largely due to a deficiency of observational data in climatically and topographically complex mountain regions, as well as somewhat limited overlap between existing observations of glacier change and numerical modeling of glacier dynamics. Here we focus on specific aspects of mountain glacier change most relevant to society today, with the overall goal of bringing together different methodologies

in order to help establish a more unified framework of glacier change across regions and timescales. The chapters in this work are organized by duration of change, beginning with the analysis of a destructive event which took place over a few hours – a glacial lake outburst flood (GLOF).

# Chapter 1: Seismic observations, numerical modeling, and geomorphic analysis of a glacier lake outburst flood in the Himalayas

Note: a modified version of this chapter has been accepted for publication in *Science Advances*.
Authors: J.M. Maurer, J.M. Schaefer, J.B. Russell, S. Rupper, N. Wangdi, A. Putnam, N. Young.

Glacial lake outburst floods (GLOFs) are a substantial hazard for downstream communities in vulnerable regions. Many aspects of GLOF dynamics are difficult to quantify, as in situ measurements are scarce due to the unpredictability and remote source locations of these events. Here we revisit a destructive GLOF which occurred in Bhutan in 1994, and apply cross-correlation based seismic analyses to track the evolution of the GLOF remotely (~100 km from the source region). We use the seismic observations along with eyewitness reports and a downstream gauge station to constrain a numerical flood model, then assess geomorphic change and current state of the unstable lakes via satellite imagery. Coherent seismic energy is evident from 1 to 5 Hz beginning approximately 5 hours before the flood impacted Punakha village, which originated at the source lake and advanced down the valley during the GLOF duration. Our analysis highlights potential benefits of using real-time seismic monitoring to improve early warning systems.

## 1.1 Introduction

Glacial lakes in the Himalayas are rapidly growing due to climate change and acceleration of glacier melt in recent decades (Maurer et al., 2019; Schwanghart et al., 2016). Many of these lakes are dammed by unstable, often ice-cored moraines (Richardson and Reynolds, 2000), surrounded by steep topography prone to landslides, and frequently subjected to seismic events and intense monsoonal precipitation. Risks associated with glacial lake outburst floods (GLOFs) are substantial for downstream inhabitants in these regions, and thousands of fatalities have

already occurred as a direct result of sudden catastrophic releases of water (Carrivick and Tweed, 2016). Societies and economies of GLOF-prone regions are severely impacted, including destruction of infrastructure, disruption to communities, and loss of life (Carrivick and Tweed, 2016; Richardson and Reynolds, 2000; Schwanghart et al., 2016; Watanabe and Rothacher, 1996). The nation of Bhutan, in particular, has been classified as having some of the greatest national-level economic consequences of glacier flood impacts, as hydropower dominates the nations GDP and socio-economic development potential (Carrivick and Tweed, 2016; Uddin et al., 2007). The electric power demands of Himalayan nations are on a steep rise with rapid economic growth, and hydropower development continues to expand into higher sites closer to glaciers (Schwanghart et al., 2016).

Numerous GLOFs have been documented in the Himalayas by firsthand observation and satellite imagery after their occurrence (Iwata, 2002; Rounce et al., 2017; Veh et al., 2019). The most comprehensive analysis to-date of the Landsat imagery archive finds an average GLOF frequency in High Mountain Asia (HMA) of 1.3 GLOFs per year since the 1980's (Veh et al., 2019). Despite this steady rate, quantitative in situ observations of GLOFs are scarce (Richardson and Reynolds, 2000) and limited to rare situations where pre-installed instruments are coincidentally located in the same valley as the GLOF (Cook et al., 2018). Efficient strategies to mitigate outbursts, design reliable early-warning systems, and minimize destructive impacts would benefit from continuous observation of flood evolution through time. While satellite observations can help identify regions of high GLOF-risk and quantify geomorphic impacts after occurrence, they cannot capture GLOF events in real-time. Numerical flood models can be used to simulate dam outbursts and flood waves (Koike and Takenaka, 2012; Osti et al., 2013; Rounce et al., 2017; Watson et al., 2015) yet require numerous physical parameters as input, which are

often unknown or poorly constrained (Watson et al., 2015). For example, the shape of a breach hydrograph can strongly influence flood characteristics downstream (Westoby et al., 2014). Yet these essential upstream boundary conditions in flood routing models are usually unknown, and must be estimated using physical or parametric dam breach models with large uncertainties (Wahl, 2004). In this regard any physical measurements of river flow behavior can be highly useful. Seismic monitoring in particular can measure seismic energy released by GLOF mass movements through time, from initial trigger events such as landslides and glacial calving to subsequent flood-generated energy from water turbulence and bedload transport (Burtin et al., 2008; Burtin et al., 2016; Burtin et al., 2010; Gimbert et al., 2014; Lai et al., 2018; Schmandt et al., 2013). Such continuous measurements of the timing, location, and magnitude of high flow regimes can potentially improve constraints on model parameters which determine simulated flood magnitudes and arrival times downstream.

The Pho Chhu (river) flows from the pristine mountain region of Lunana (4500 m a.s.l.), southward through the Bhutan foothills where it eventually joins the Brahmaputra River in northern India (Figure 1.1). The valley has a typical step-like elevation profile, alternating between sections of very steep and relatively flat terrain separated by river knickpoints. Fed by seasonal snow melt, glacier melt, and summer monsoon rains, the river plays a vital role in the welfare and livelihood of the people of Bhutan. In the Pho Chhu valley, residents of small villages live and farm along the banks of the river, with rice paddies being a primary seasonal crop. In the river source region, several large proglacial lakes are continually expanding in size as a result of accelerated glacier melting in recent decades (Maurer et al., 2019; Schwanghart et al., 2016). Approximately 90 km downstream from the proglacial lakes is the village of Punakha (1200 masl), where a large 17$^{th}$ century Buddhist temple (the Punakha Dzong) is situated along

the riverbank at the confluence of the Mo Chhu and Pho Chhu. This temple and surrounding region are historically and culturally significant, and there is a great deal of concern about catastrophic outburst floods from the unstable lakes above.

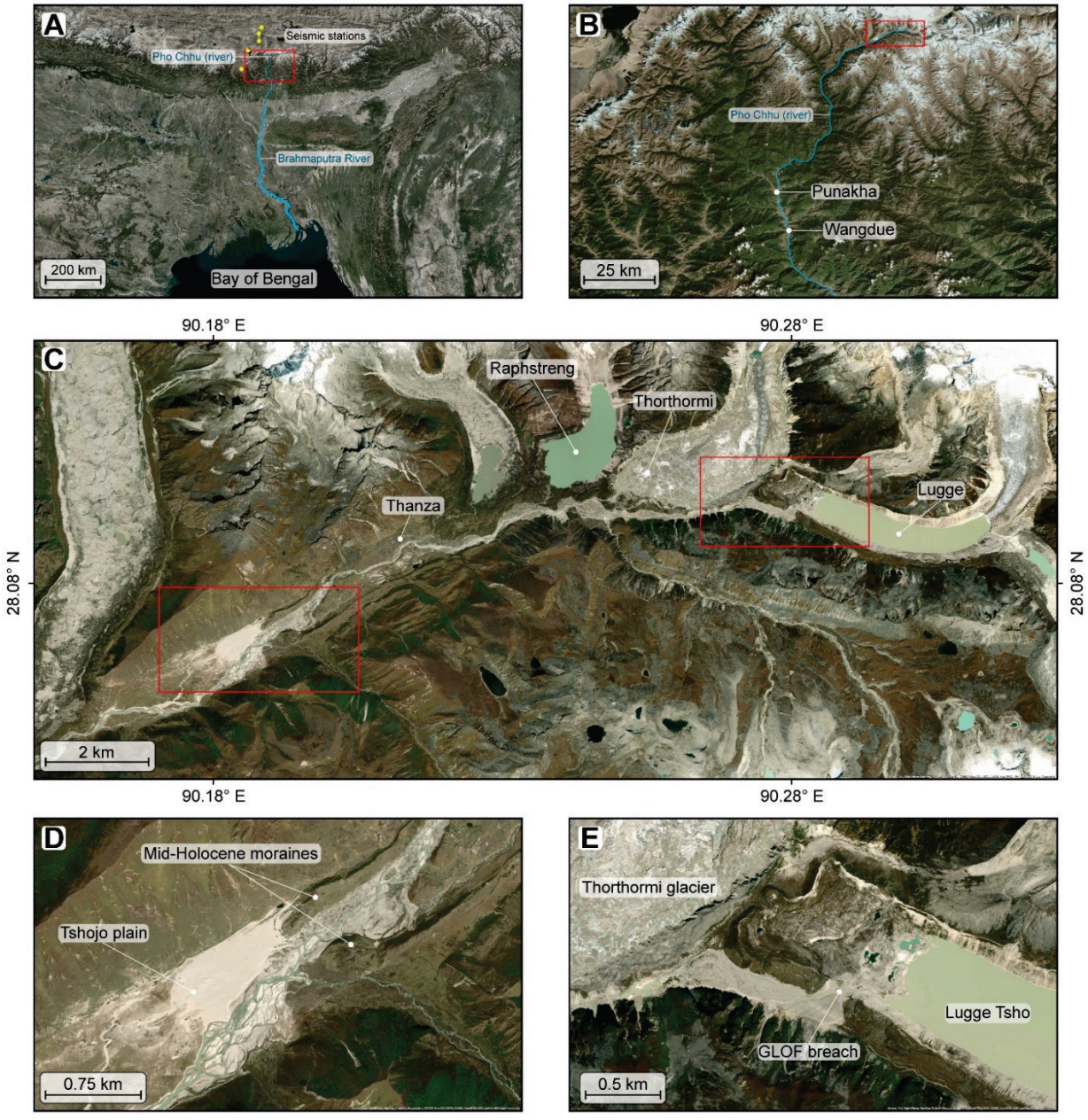


Figure 1.1. Region of study. Lugge Tsho was the source of the 1994 GLOF event, while Raphstreng Tsho and Thorthormi Tsho are also considered high-risk for future GLOFs. Locations of the 5 seismometers used in the study are denoted by the yellow circles in A.

Such an event occurred on the night of Oct 7$^{th}$, 1994, when the moraine dam of Lugge Tsho

breached and debris-laden flood waters surged down the Pho Chhu valley. Twenty-one lives were lost, and the flood destroyed an estimated 12 houses, 5 water mills, 816 acres of crops, 965 acres of pasture land, 16 yaks, 6 tons of stored food grains, 4 bridges, 2 stupas, and damaged part of the Punakha Dzong (Wangdi and Kusters, 2012). While the exact trigger of the Lugge Tsho breach is unknown, various causes of moraine failure have been hypothesized such as the melting of its ice core (Iwata, 2002), a gradual increase in hydrostatic pressure as the lake depth increased due to melting (Watanabe and Rothacher, 1996), or collapse of part of the right lateral hillside into the lake, causing a sudden increase in hydrostatic pressure (Fujita et al., 2008). After the tragic incident, much effort was put forth by the government of Bhutan to assess the risk of future GLOFs in the region, establish an emergency warning system, artificially lower lake water levels, and study Lugge Tsho in more detail. Post-GLOF field investigations found a mean lake depth of approximately 50 meters, a lake volume of 58.3 million $m^3$, and a typical discharge at the lake outlet varying from 2.5 to 5 $m^3$ $s^{-1}$ during September and October of 2002. The total volume of water released during the GLOF was estimated by Yamada et al. as 17.2 ± 5.3 million $m^3$ based on a differential GPS survey of the lowering of the lake level by 16.9 ± 3.2 m (Yamada, 2004), while an integration of the Wangdue station hydrograph (Figure S1.1) during the GLOF yields approximately 25 million $m^3$ (JICA, 2001). In addition, dam breach, flood propagation, and debris flow models (sediment-water mixtures) have also been used to simulate GLOF scenarios in this region, including sequential and simultaneous (as may happen during a large earthquake) breaches occurring below high-risk lakes in Bhutan. These models suggest that downstream villages including Punakha and the major portion of Wangdue Phodrang are at risk for severe inundation if another large GLOF occurs (JICA, 2001; Koike and Takenaka, 2012; Meyer et al., 2006; Osti et al., 2013; Watson et al., 2015).

Across the Himalayan region as a whole, the destructive potential of GLOFs is increasing. Yet the scarcity of observational measurements deters robust validation of numerical simulations, hinders quantification of GLOF dynamics, limits real-time warning, and increases uncertainties regarding societal impacts. Continuous observational coverage offered by seismic monitoring is one potential avenue for addressing this problem. Displacement of mass at Earth's surface generates elastic seismic waves which carry information about the source, and can be recorded by seismometers at high temporal resolution across large spatial scales (Burtin et al., 2016). Proof-of-concept studies have already shown the potential of seismic monitoring for diverse types of surface activities including river bedload transport and debris flows (Badoux et al., 2009; Burtin et al., 2008; Burtin et al., 2016; Schmandt et al., 2013), and further demonstrate the ability of seismic records to specifically provide insight into flood mechanics (Cook et al., 2018; Schmandt et al., 2013). Here we extend the application of seismic data to a Himalayan GLOF, using data from the International Deep Profiling of Tibet and the Himalaya (INDEPTH) II experiment (Nelson et al., 1996; Yuan et al., 1997). This data was collected by a passive broadband seismic array situated on the Tibetan Plateau, which was coincidentally recording when the GLOF occurred in Bhutan in 1994. Insofar as the authors are aware, INDEPTH II is the only seismic data available from 1994 in the region (within a 150 km radius). We perform a time-frequency analysis of the seismic signal produced by the GLOF, and use cross-correlation functions (CCFs) between seismic stations to locate and track the source of coherent seismic energy through time. With the seismic data, firsthand accounts, and gauge station measurements, we constrain the progression of the flood from initial outburst to arrival in populated villages using a numerical flood model. To further quantify geomorphic impacts of the GLOF, we apply historical spy satellite images, Landsat, and modern high-resolution imagery to analyze lake area

changes over time, the extent of flood-deposited sediments, the rate of vegetation regrowth post-GLOF, and pre- and post-flood morphology of the source area dated by $^{10}$Be.

## 1.2 Results

### 1.2.1 Analysis of seismic data

Seismic energy generated during the GLOF was recorded by five seismometers (with locations ranging from approximately 75 to 130 km distance from the breach point) as a clear high frequency (1–4 Hz) signal lasting several hours (Figure 1.2, Figure S1.2). Seismic energy at these frequencies was most likely excited by energy from turbulent flow and bedload transport processes, as observed in previous studies of seismic signals generated during high flow regimes (Burtin et al., 2008; Burtin et al., 2016; Cook et al., 2018; Goodling et al., 2018; Schmandt et al., 2013). The GLOF signal strength was 5–15 dB above typical background noise levels (Figure S1.10), and occurred during the night and early morning when local anthropogenic noise was at a minimum (i.e. anthropogenic noise). Spectrograms show a similar pattern on vertical and horizontal components across all five stations (Figure S1.2). Some interstation variability in peak frequency content is observed during the two GLOF phases, likely due to lateral heterogeneity in attenuation structure and differences in distance from the source. The first detectable high frequency signal arrived at approximately 1:45 am, beginning with relatively weak amplitude and limited primarily to frequencies between 1-3 Hz. Over the next several hours, the seismic energy varied somewhat through time, as the flood wave passed through sections of the valley with different slope and river channel characteristics. Around 25 minutes after this first arrival, an increase in spectral amplitude occurred across a wider range of frequencies (1–4 Hz) (Figure S1.2) then subsequently tapered off over the next 1.5 hours. At approximately 3:50 am the signal power began increasing again and reached a maximum at 6:00 am with frequency content

ranging from approximately 1–5 Hz. During this interval the flood wave passed through the main branch of the Pho Chhu and impacted Punakha at approximately 7:00 am based on eyewitness accounts.

We further examined the signal correlation across stations to constrain the origin of the seismic energy in space and time (Burtin et al., 2016; Burtin et al., 2010; Chao et al., 2015). Computing CCFs for every station pair across a series of frequencies ranging from 1 to 5 Hz, we find strong correlation of waveforms during two distinct intervals (see Materials and Methods, Figure S1.13). The first spans from approximately 1:45 to 3:15 am, during which a strong peak in CCF amplitude is apparent (Figure S1.3). Migrating the CCFs during this interval and subsequently summing them together, a region of high coherence emerges, focused directly on the GLOF breach location at Lugge Tsho (Figure 1.2), indicating that during this time the outburst event was the dominant source of seismic energy at these frequencies. Approximately four hours later, a second prominent interval of high coherence spans from around 5:45 to 7:15 am. Migration of the CCFs during this later interval indicates that the GLOF-induced seismic energy originated from a lower (downstream) section of river, indicating that the flood wave had reached this point in the valley (approximately 70 km from the breach, and 20 km above Punakha) by around 5:45 am.

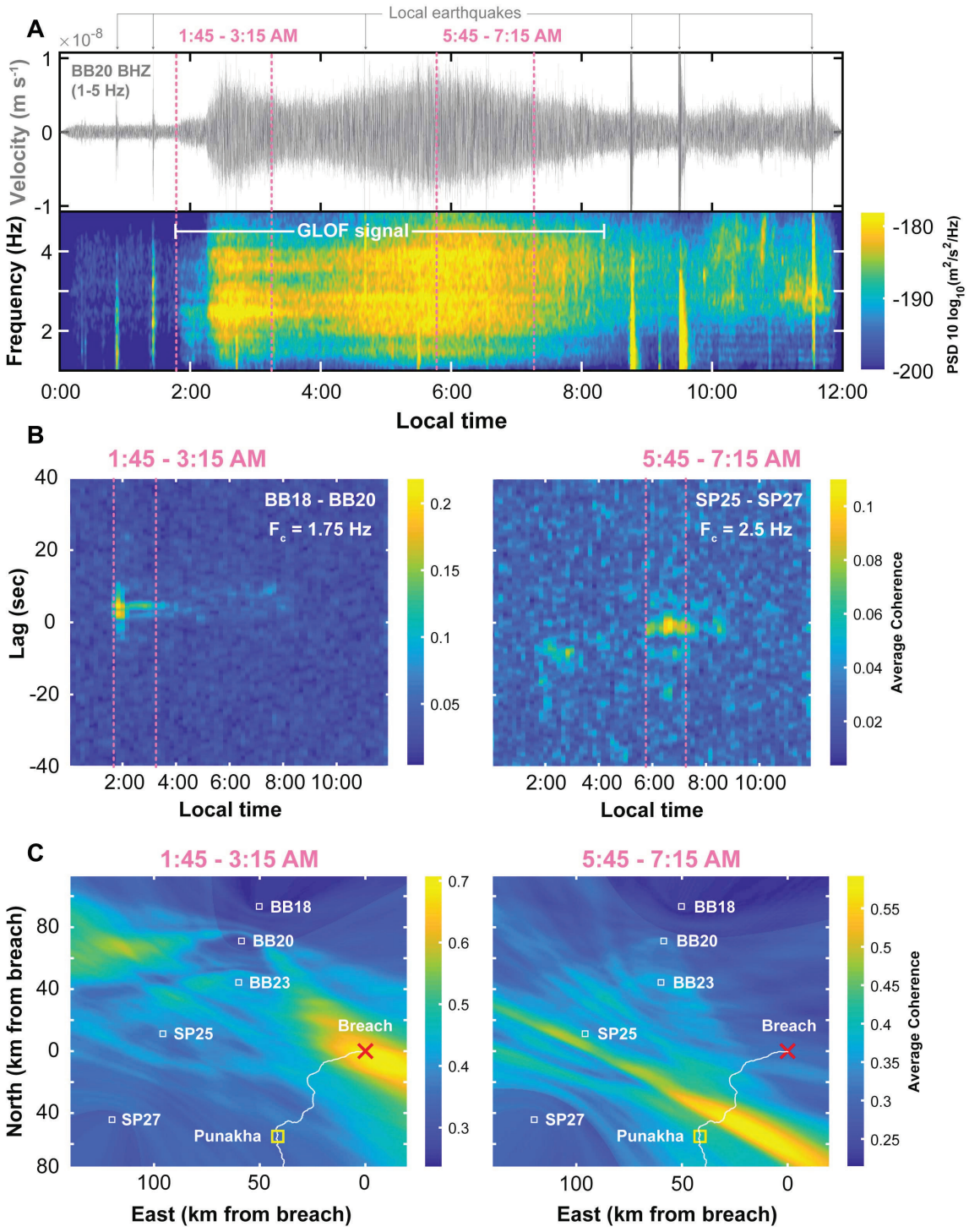


Figure 1.2. Key seismic observations on Oct. 7, 1994. (A) Example of a seismic trace (station BB20 BHZ) bandpass filtered between 1 to 5 Hz, and spectrogram from 1 to 5 Hz during the GLOF duration. (B) Two examples of CCFs between station pairs BB18-BB20 and SP25-SP27 averaged for the three components (BHZ-BHZ, BHE-BHE, BHN-BHN) for frequency ranges 1.5 to 2 Hz and 2.25 to 2.75 Hz, respectively. Peaks in coherent seismic energy are evident from approximately 1:45 to 3:15 am in the first station pair, and from 5:45 to 7:15 am in the second

pair at these frequencies. (C) Migration of the CCFs during the two intervals using a velocity of 3.0 km $s^{-1}$ (Figure S1.3; likely indicating regional short period Rayleigh waves) for several station pairs, then summed together to form these final coherence maps (see Methods and Figure S1.3). These two images illustrate the downstream progression of seismic energy generated by the GLOF. The coherence map on the left corresponds to seismic energy generated during the initial GLOF breach, while the map on the right corresponds to seismic energy generated approximately 4 hours later and ~70 km downstream. Times are Asia/Thimphu local time (UTC+6).

### 1.2.2 Seismic signal generation

Generation of seismic waves from fluvial processes is understood to occur by two main processes: 1) transport of sedimentary grains that stochastically impact the river bed and 2) turbulent fluid flow that interacts with the riverbed. Previous observations of seismic energy associated with turbulent flow and bedload transport processes made at much smaller distances from the seismic source (typically less than a few hundred meters away) show peak frequencies ranging from 1–100 Hz depending on distance from the source and local seismic attenuation structure (Burtin et al., 2008; Burtin et al., 2016; Cook et al., 2018; Goodling et al., 2018; Schmandt et al., 2013). Here, we demonstrate that coherent seismic energy from approximately 1–5 Hz is generated and can propagate to distances as far as ~100 km from the source region during large GLOF events. Numerical models that predict seismic energy excitation due to turbulent flow and bedload transport processes show that >1 Hz seismic energy is difficult to generate at such large distances (Gimbert et al., 2014; Lai et al., 2018; Tsai et al., 2012). However, the high river flow rates (~2500 $m^3$ $s^{-1}$) and thick water flow depths associated with the GLOF represent extreme conditions that have not been explored in detail in numerical models and may well violate their underlying physical assumptions. Additional work is needed to fully understand the physical processes responsible for the observed seismic signal generation during the GLOF event on Oct 7th, 1994 and how these observations compare with predictions from recent numerical models.

### 1.2.3 Constraining a flood model

Hydropower viability, disaster preparedness, and paleoseismic investigations have previously simulated flood events in this region using numerical models (JICA, 2001; Koike and Takenaka, 2012; Meyer et al., 2006; Osti et al., 2013; Watson et al., 2015). Here we build on results from these earlier studies by calibrating a flood model using the new set of independent observations: 1) an estimated start time and location based on the beginning of detectable seismic energy and migrated CCFs, 2) the second interval of correlated seismic energy which occurred several hours later and ~70 km downstream of the initial breach, 3) the approximate arrival time of the flood at Punakha from firsthand observations, and 4) the flood hydrograph from Wangdue station (around 110 km downstream from the breach). Together these provide key constraints on the location of the flood wave through the duration of the GLOF, and allow us to parameterize a model with a higher degree of confidence than previously possible. The start time of the GLOF in particular is a key aspect which was previously unknown. Due to the sensitivity of flood models to input parameters (Figure S1.1), these independent observations are especially useful for validating and selecting model runs which are most realistic (see Materials and Methods).We use the U.S. Army Corps of Engineers Hydrologic Engineering Center's River Analysis System (HEC-RAS) software to perform a series of 2D unsteady flow simulations, select model runs which agree with the independent observations within a ± 30 minute threshold (see Materials and Methods and Figure 1.3), and report ranges of simulated breach-to-arrival times for the main populated villages along the river valley for Thanza (0.4-0.6 hours), Thsojo (1.0-1.3 hours), Lhedi (1.4-1.8 hours), Samdingkha (3.9-4.6 hours), Punakha (4.4-5.2 hours), and Wangdue (5.7-6.5 hours) (Table 1.1). We note that around 6:30 am, the peak flows in the best-fit model runs precede (in time) the peak in seismic coherence, approximately 70 km downstream from the

breach. While this may reflect the actual order of events, the model may also be overestimating the flood wave velocity above this section of the valley. In all model runs, the duration between arrival and peak flow gradually decreases as the flood travels down the section of valley above Punakha. This consistent aspect of the flood illustrates the manner in which topography can shape a flood wave, in this case causing the wave to become steeper and more prominent while traveling down a steep valley gorge. Results from model runs with different breach hydrographs all converge to a similar shape before reaching the larger villages downstream. In the village of Samdingkha for example (~8 km above Punakha), the duration between first arrival and peak flow ranges from 10 to 30 minutes. Without an external early warning system, this sudden rise in water level permits only a short time for inhabitants to move to safe ground, particularly if the early stages of the rise go unnoticed for several minutes.

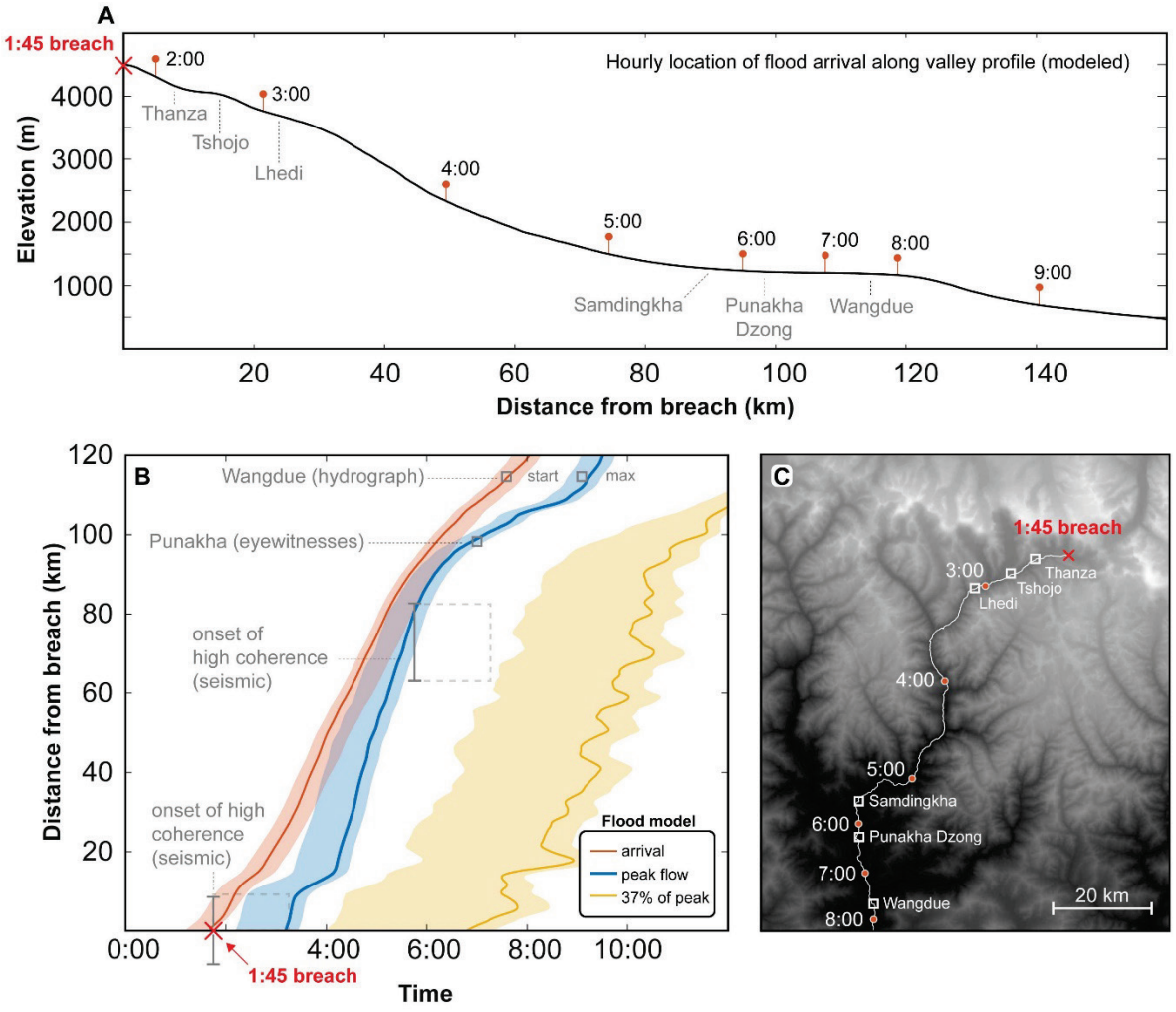


Figure 1.3. Results from the HEC-RAS 2D unsteady flood model. (A) Elevation profile of the river valley, with hourly locations of flood arrival time from the best-fit model run. (B) Distance from the moraine breach versus time. The grey square symbols and brackets are independent observations from seismic, eyewitness, and gauge station sources. The color-shaded regions represent the range of model outputs which match observations within ± 30 minutes, and the colored curves represent the single best-fit model run. The orange curve is the simulated arrival of the flood wave, the blue curve is the peak flow, and the yellow curve indicates when the flow has subsided and reached 1/e (~37%) of the peak. The horizontal separation of the orange and blue curves indicate the duration between flood arrival and peak flow for a given location. The grey (dashed) boxes indicate the intervals in Figure 2 during which the peaks in coherent seismic energy were detected. (C) Map view of region also with modeled flood arrival times. Times are Asia/Thimphu local time (UTC+6).

### 1.2.4 Geomorphic change caused by the GLOF

Satellite imagery reveals prominent changes in the Lunana region both before and after the GLOF. The most consistent change is a steady increase in the area of Lugge Tsho over the last

45 years, starting at approximately 0.42 $km^2$ in January of 1976. The lake area increased at a rate of 0.038 $km^2$ $yr^{-1}$ as the glacier receded and melted, reached 1.1 $km^2$ in September of 1994, then underwent a sudden decrease to 0.87 $km^2$ after the GLOF in October of 1994. Subsequently, the lake area continued increasing at a rate of 0.025 $km^2$ $yr^{-1}$, and has since reached a size of 1.42 $km^2$ as of September 2018 (Figure S1.4). We note that the lake expansion is primarily due to the receding glacier rather than rising lake level (see Discussion). The location of the 1994 breach is evident in both visible imagery and digital elevation model on the lower left lateral moraine, where a cross section along the moraine crest shows a channel approximately 180 m wide and 40 m deep. Declassified satellite imagery from 1976 clearly shows this location was a pre-existing outlet for Lugge Tsho (Figure S1.5). Below the breach, changes in spectral reflectance are visible in post-GLOF Landsat imagery where the flood deposited debris and sediment along large regions of the valley floor. Upon first breaching the lake-fringing moraine, the flood waters flowed into another small lake approximately 500 m downstream. This seasonal lake was full at the time the GLOF occurred due to accumulated snowmelt and monsoonal precipitation from the prior summer months. The flood washed out the natural dam of this small lake basin, thus now it no longer accumulates water as it did in years prior.

Around 10 km from the breach, a prominent set of glacier moraines is situated below Thanza (Figure 1.4, Table S1.2). Here we analyzed three boulders on the well-preserved outermost moraine ridge using $^{10}Be$ surface exposure dating, following procedures in Schaefer et al. (2009). Results yielded three consistent ages ranging from 4.4 to 4.7 kyr, indicating that the moraines were deposited during the mid-Holocene and left largely intact by the 1994 flood (Figure S1.5). After passing through the moraines, the flood wave spilled over the Tshojo plain, where it subsequently deposited a 2.2 $km^2$ swath of sediment. In total, we estimate approximately 4.8 $km^2$

of valley floor was covered by sediment as a result of the GLOF. This occurred primarily along the upper 25 km of the river (Figure S1.6), as below this upper region the channel is highly confined and sediment deposition was minimal. In the decades following, the impacted vegetation has slowly recovered (Figure S1.7). In 1994 the mean enhanced vegetation index (EVI) of the Tshojo plain dropped to around 25% of the pre-GLOF value as a result of the flood. From 1994-2005 the EVI steadily increased as the vegetation began reclaiming the area, attaining around 75% of the pre-GLOF value in 2005 and remaining steady for several years afterward. Another increase occurred from 2011-2013, during which time an EVI approaching that of the pre-GLOF conditions was attained.

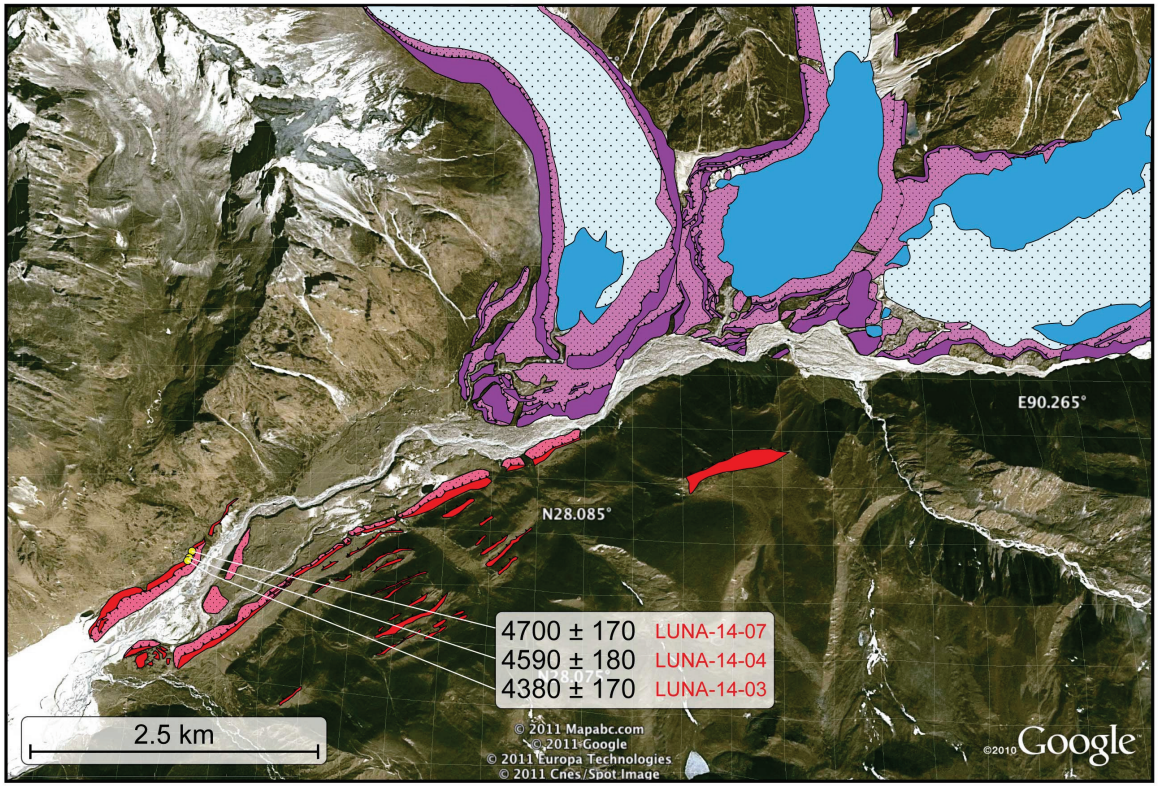


Figure 1.4. Geomorphic Map of the Lunana area. The lower (red) moraines were deposited by the glacier more than 4000 years ago during the mid-Holocene, as indicated by the $^{10}$Be ages of three sampled boulders given with 1-sigma analytical error. The younger lake-fringing (purple) moraines are late-Holocene in age.

Table 1.1 Range of modeled flood arrival and peak flow times at populated villages

| Location | Lat | Lon | Elev (m) | Dist from breach (km) | Flood arrival | | | | | | Peak flow | | | | | |
|---|---|---|---|---|---|---|---|---|---|---|---|---|---|---|---|---|
| | | | | | Time | | | Hrs from breach | | | Time | | | Hrs from breach | | |
| | | | | | Low | Best fit | Upp | Low | Best fit | Upp | Low | Best fit | Upp | Low | Best fit | Upp |
| Thanza | 28.089 | 90.213 | 4150 | 7 | 01:43 | 02:08 | 02:19 | 0.4 | 0.4 | 0.6 | 02:22 | 03:20 | 03:35 | 0.9 | 1.8 | 2.1 |
| Tshojo | 28.062 | 90.164 | 4060 | 14 | 02:19 | 02:41 | 03:00 | 1.0 | 1.0 | 1.3 | 03:20 | 04:10 | 04:25 | 1.8 | 2.7 | 3.0 |
| Lhedi | 28.034 | 90.092 | 3690 | 23 | 02:47 | 03:06 | 03:26 | 1.4 | 1.4 | 1.8 | 03:33 | 04:21 | 04:36 | 2.0 | 2.9 | 3.2 |
| Samdingkha | 27.641 | 89.865 | 1270 | 90 | 05:29 | 05:39 | 06:08 | 3.9 | 3.9 | 4.6 | 05:43 | 06:09 | 06:24 | 4.1 | 4.6 | 4.9 |
| Punakha Dzong | 27.582 | 89.863 | 1210 | 98 | 06:01 | 06:12 | 06:38 | 4.4 | 4.5 | 5.2 | 06:37 | 06:58 | 07:13 | 5.0 | 5.5 | 5.8 |
| Wangdue | 27.462 | 89.901 | 1190 | 114 | 07:19 | 07:35 | 07:54 | 5.7 | 5.9 | 6.5 | 08:47 | 09:12 | 09:27 | 7.1 | 7.7 | 8.1 |

## 1.3 Discussion

### 1.3.1 Arrival time of flood in Punakha

Well-constrained GLOF arrival times are vital for disaster preparedness, yet existing model estimates for Punakha include 4.75 hours (JICA, 2001), 5.75 hours (Meyer et al., 2006), and 7 hours or more (Watanabe and Rothacher, 1996). Given the onset of seismic energy at 1:45 am at Lugge Tsho and eyewitness accounts of rising waters around 7:00 am in the village, we estimate the flood took approximately 5 hours to reach Punakha. Assuming the delay between the initial breach and generation of detectable seismic energy was short (see Materials and Methods), our results suggest that some previously published simulations give reasonably accurate arrival times (within ± 30 minutes), and the shorter (4.75 to 5.75 hours, 17 km $hr^{-1}$ average) times are more accurate than the 7 hour (12 km $hr^{-1}$ average) estimate (Watanabe and Rothacher, 1996). These results show how a simple estimate of the GLOF start time based on the onset of seismic energy can be highly useful for validation of numerical models, by providing an estimate of the average velocity of the flood wave. However, a future breach may have different hydrograph characteristics depending on the trigger mechanism and nature of the moraine dam failure. The 1994 GLOF also cleared out a substantial amount of blocking debris, which would allow a future GLOF to travel more quickly down the valley. Further research toward constraining probable breach hydrograph characteristics and valley roughness parameters will be crucial for refinement of GLOF models. With the vast amount of existing seismic data (in databases such as the IRIS

DMC for example) and increasing number of seismic networks, it is likely that other GLOF events have been recorded by seismic instruments, but have yet to be investigated. A comprehensive search and deeper analysis of any available seismic records in GLOF-prone locations may reveal new insights toward quantifying and modeling GLOF trigger events and flood waves in these regions.

### 1.3.2 Sediment deposition and vegetation recovery

The area covered by new sediment from the GLOF (4.8 $km^2$) combined with existing sediment-covered areas (3.0 $km^2$) amount to 7.8 $km^2$. This approximately agrees with previous damage assessments, which estimated a total of 7.2 $km^2$ of crops and pastures affected by the flood. The 2.2 $km^2$ region of most prominent GLOF sediment deposition is located in a scrub alpine vegetation zone which receives around 1 m $yr^{-1}$ of precipitation primarily during the summer monsoon months (Suzuki et al., 2007). The flora in this area are composed of sedges, mosses, accessorial herbs, and some patches of woody vegetation (rhododendrons, junipers, spireas) (Meyer et al., 2009). The nonlinear vegetation recovery rates (Figure S1.7) are likely due to factors such as soil moisture, nutrient availability, competition between species, and seasonal precipitation in this high elevation ecosystem. The observed recovery patterns may inform future studies regarding resilience of aromatic medicinal plants to changing climate, as these flora play key roles in the lives of local inhabitants (Joshi et al., 2016).

### 1.3.3 Comparison with other GLOFs in the Himalayas

Compared to other GLOF occurrences in HMA during the last three decades, this 1994 event is a top contender for the largest volume of water released. Yet in terms of the percentage of lake volume released, it is on the lower end (Figure S1.8). Yamada (2004) surveyed the lake bathymetry and estimated the total volume of Lugge Tsho to be 58.3 million $m^3$ in September of

2002. Correcting for the lake growth between 1994 and 2002 (3 million $m^3$), and volume of water released during the GLOF (17 to 25 million $m^3$), we estimate that the lake volume was 73 to 80 million $m^3$ in 1994. Based on this approximation, around 24 to 30% of the volume of Lugge Tsho was released. Due to the large size of the lake, substantial rate of outflow during the breach, and considerable vertical relief, this smaller-than-average percentage of draining resulted in a major destructive GLOF downstream. This is consistent with the flood simulations which suggest very low dampening and low deceleration of the flood wave peak due to high-relief energy and the gorge character of the Pho river (Meyer et al., 2006) (Figure 1.2). Regarding the seismic signal, we note the large magnitude of this GLOF event was likely a primary factor which caused the high signal-to-noise ratio. Smaller GLOF events which produce less seismic energy would require seismometers to be located closer to the GLOF source in order to observe the weaker signal. This trade-off between geographical coverage of a seismic array versus the capability of detecting smaller events is an optimization problem which future studies could address. A search for smaller GLOF events which have occurred in other locations, along with any associated seismic signals (observed by nearby stations) may help further constrain signal strength versus distance from the source. Such observations could also be used to constrain numerical models which simulate seismic energy generated by various flood magnitudes.

### 1.3.4 Current state of high-risk lakes in Lunana

We find Lugge Tsho surpassed the pre-GLOF size of 1.1 $km^2$ in 2005, and reached an area of 1.4 $km^2$ in 2018 due to retreat of the glacier terminus (Figure S1.4). If a future event were to cause the same 16 to 23 meters of lake surface lowering as occurred during the 1994 GLOF, this would translate to 22 to 32 million $m^3$ of water released, or approximately 30% more than the 1994 flood volume. While satellite imagery indicates that the lake boundaries (excluding the retreating

glacier terminus) are nearly unchanged since the GLOF, the ongoing glacier retreat has also exposed unstable steep valley walls and lateral moraines above the lake (González-Vida et al., 2019; Kos et al., 2016). A large mass movement into the water could result in a sudden increase in hydrostatic pressure and subsequent overtopping or structural failure of the Lugge Tsho moraine dam. The adjacent Thorthormi and Raphstreng lakes are also vulnerable to the same problem. Thorthormi sits topographically above Raphstreng by approximately 80 meters, and a breach in its moraine could result in a cascading combined GLOF from both lakes (Richardson and Reynolds, 2000). Efforts to artificially lower the level of Raphstreng by enlarging the outlet channel were undertaken during 2009-2012 in an attempt to reduce the risk, but this dangerous manual work by the local people was extremely difficult with uncertain effectiveness. On June 20, 2019 a minor breach occurred below Thorthormi lake, during which residents of Lunana were evacuated and no deaths or serious injuries occurred. While the increased flow was relatively minimal (water level increased by approximately 1 meter during ~6:00 to 7:20 pm), it was large enough to wash away two bridges in Thanza and Tenchey. A field investigation after the event found that enhanced melting and basal sliding of the Thorthormi glacier had caused it to surge – this displaced water from Thorthormi lake, which overtopped the primary moraine, spilled into the subsidiary lakes, and breached the lower subsidiary lake which drained completely. Satellite imagery before and after the event confirmed the draining of the subsidiary lake, but the stability of the primary Thorthormi moraine dam is uncertain (Kuensel, 2019).

### 1.3.5 Potential for early warning systems

In Bhutan and elsewhere across the Himalayas, numerous glacial lakes pose immediate GLOF threats (Schwanghart et al., 2016). Existing warning systems usually consist of automatic water level (AWL) stations installed in priority locations to monitor lake levels and river flows, and

transmit data in real-time using GSM or Iridium satellite technologies. If lake levels are detected to suddenly drop and/or stream levels rise, emergency warnings are issued (via mobile text messages), and a network of warning sirens are sounded. However, AWL sensors are known to be somewhat unreliable and susceptible to false alarms (Hydrology-Division, 2013). Our results demonstrate the feasibility of seismic monitoring as another way to remotely detect GLOFs, which could potentially improve the next generation of early warning systems. The CCF methodology would need to be automated and tested more robustly to ensure reliable distinction between GLOF seismic signatures and other tectonic, meteorological, anthropogenic, or geomorphic sources (Burtin et al., 2016), but with further refinement a network of seismometers strategically deployed across a region could hypothetically monitor for sustained signals originating from probable GLOF source locations. During the CCF peak at the onset of the GLOF (around 1:45 am), we find that only a few minutes of seismic data are sufficient to detect the anomalous high frequency signal originating from the upper Lunana valley (Figure S1.9). Unlike AWL sensors, seismometers can be installed in safer and more accessible sites with the capability to monitor large regions across multiple valleys, although further research is needed to determine the optimal trade-off between array density and event detection. The use of seismometers and AWL sensors jointly could substantially improve existing early warning systems, with cross-validation of the two independent detection methods helping to minimize occurrence of false alarms and maximize warning time.

## 1.4 Conclusion

The risk of larger and potentially more destructive floods is rapidly increasing across the Himalayas, due to growing glacial lakes and ongoing construction of hydroelectric dams and other infrastructure in vulnerable regions (Schwanghart et al., 2016). We have demonstrated that

a GLOF can be detected remotely from seismometers located many kilometers away from the source, which has potential to improve efficiency and maximize warning time. Our robust spatiotemporal constraints indicate at least 5 hours between source and main impact areas in Punakha, which affords sufficient warning time for many downstream inhabitants if a GLOF is detected in its earliest phase. We find the 1994 flood event eroded, transported, and deposited large quantities of sediment in the Lunana valley, but left the local moraine ridges largely intact near the source region. We also estimate a post-GLOF recovery of 2-3 decades for the affected alpine scrub vegetation, which may help to quantify resilience of the local ecosystem in future studies. Given the current situation and ongoing GLOF risks in the Himalayas, future research could focus on: 1) deeper analysis and characterization of tectonic, meteorological, anthropogenic, and geomorphic seismic signatures to ensure clear distinction of natural hazard signals and prevention of false alarms, 2) continued development of efficient algorithms for automated real-time processing of environmental seismic data, and 3) deployment of optimized seismic arrays in vulnerable regions to detect GLOF events and provide efficient early warning systems.

## 1.5 Materials and Methods

### 1.5.1 Seismic data

Recent proliferation of high-quality broadband seismic data in addition to developments in the analysis of the ambient seismic wavefield and other seismic signals have forged new avenues in studying characteristics of seismic energy generated by environmental processes (Badoux et al., 2009; Burtin et al., 2008; Burtin et al., 2016; Cook et al., 2018; Goodling et al., 2018; Schmandt et al., 2013). For example, time-frequency analyses of passive broadband seismic data have been used to quantify increases in high frequency energy associated with high flow regimes in rivers,

and cross-correlation between multiple stations used to isolate coherent seismic phases and provide estimates of their origin (Brzak et al., 2009; Burtin et al., 2010). Here we utilize seismic data from the INDEPTH II experiment as a tool to investigate the 1994 GLOF in Bhutan, which coincidentally occurred while this temporary seismic network was actively recording. INDEPTH II was a collaborative geoscience project between the Chinese Academy of Geological Sciences, and investigators from U.S., German, and Canadian Geoscience institutions to investigate the deep structure and mechanics of the Himalaya-Tibet region (Nelson et al., 1996). In 1994 the second phase of the project acquired passive seismic data in southern Tibet and the Himalayas, continuously recording three-component broadband and short-period 24-bit data along a ~350 km linear array at a sample rate of 50 Hz (Sandvol et al., 1997). For our analysis, we used data from a total of five broadband and short-period INDEPTH stations ranging from 75 to 135 km in distance (99 km average) to the northwest of the GLOF source area (Lugge Tsho). We downloaded the data from the IRIS DMC (Incorporated Research Institutions for Seismology Data Management Center), using a window for the approximate time of the GLOF occurrence (October 7$^{th}$ 1994, from 00:00 to 12:00 hours, Asia/Thimphu time zone) for stations BB18, BB20, BB23, SP25, and SP27 (network code XR). The corresponding seismic traces were detrended, instrument responses removed to obtain units of velocity (m s$^{-1}$) using the open-source Python framework ObsPy (Beyreuther et al., 2010), and band-pass filtered between 1 and 5 Hz. This frequency range corresponded to the coherent high frequency signal observed across all five stations (Figure S1.2) during the GLOF duration, and also excluded lower frequency bands associated with noise sources such as ocean-generated microseisms (Berger et al., 2004; Webb, 1998) as well as higher frequency anthropogenic noise. Previous studies also observed a similar increase in seismic energy in these same frequency bands originating from turbulence

and sediment transport by rivers and flood events (Burtin et al., 2008; Cook et al., 2018; Goodling et al., 2018; Schmandt et al., 2013). For the purposes of this study, we assume that the beginning of detectable seismic energy marked the initiation of the GLOF event. We note that the actual outflow may have begun slightly earlier, but the seismic energy was below the threshold of detection at first due to a gradual increase in outflow through the moraine breach. This remains difficult to constrain as the exact shape of the breach hydrograph is unknown, thus our evaluation of the time between the breach and downstream arrival of the flood wave is a minimum estimate.

### 1.5.2 Time-frequency analysis and cross-correlation functions

To explore the spectral characteristics of the event and quantify the temporal variation of the seismic signal generated by the GLOF, we estimated the power spectral density (PSD) of the time series for each station using Welch's averaging method. We first divided each seismic trace into two-minute segments each with 50% overlap. Then for each two-minute segment, we used Welch's method to average modified periodograms computed using 10-second windows, also overlapping by 50%. To approximate source locations of the GLOF energy, we followed an approach similar to those outlined by previous studies for locating coherent seismic noise sources (Bensen et al., 2007; Brzak et al., 2009; Burtin et al., 2010). We first applied a 1-bit normalization to reduce the influence of punctual sources of seismic energy, such as earthquakes, anthropogenic noise, or instrument issues. This simply means keeping the sign of the time series (-1 if less than zero and +1 if greater than zero) and discarding the magnitude (Bensen et al., 2007). We then calculated the normalized cross-correlation of 20-minute segments (overlapping by 50%) in the time series and computed their envelopes (hereafter referred to as the CCFs) for every station pair along the seismic array for time lags ranging from -40 to +40 seconds for a

series of frequencies ranging from 1 to 5 Hz, using window size of 0.5 Hz. Time information from each CCF envelope was migrated to positions in space as follows: We defined a regular grid of potential source locations in the region, and for each station pair we calculated the theoretical time delays between the two stations for every grid point. The CCF amplitude at each corresponding lag time was then mapped to positions in space. The resulting coherence map $A_{ij}$ for stations *i* and *j* is given by:

$$A_{ij}(x,y) = CCF_{ij}\left(\frac{d_i - d_j}{v}\right) \quad (1.1)$$

where *d* is the distance between the hypothetical source and corresponding station and *v* is the assumed seismic velocity (see below). Thus, each CCF delay time (i.e. the delay is along the vertical axis in Figure 1.2B and Figure S1.3) maps to a hyperbola, where the amplitude of the hyperbola is simply the CCF amplitude. This was repeated for each 20-minute segment and station pair. The resulting maps for hand-selected station pairs and frequencies (those with distinct correlation peaks, see Figure S1.3 and Table S1.1) were summed together to form a final coherence map for a given interval, where high coherence values indicate the most probable source locations (Figure 1.2). Similar results are also obtained if all station pairs are included in the stack (Figure S1.11). In order to determine an appropriate velocity during migration, we calculated coherence maps for a range of velocities between 1 and 5 km $s^{-1}$. We found that a velocity of 3.0 km $s^{-1}$ resulted in the highest coherence (Figure S1.3) for these frequencies, similar to previous studies (Burtin et al., 2010) and likely indicates short period Rayleigh wave energy. We found two distinct peaks in coherence occurred at approximately 2:00 am and 6:30 am, and chose to focus on these peaks for further analysis. We defined time windows of 1.5 hour

duration centered on each respective peak, which we determined to be a reasonable length to span their duration (including initial rises preceding the peaks). We also note that quasi-linear placement of the seismometers parallel to the valley northwest of the GLOF means the source location was well constrained along the valley but poorly constrained perpendicular to the valley leading to blurring in that direction. This artifact may be remedied by invoking a probability density function centered on the river channel to better localize the signal, though the GLOF event studied here was large enough such that this was not necessary. While this and other sources of error such as lateral velocity heterogeneities and varying surface topography caused some blurring of the coherence maps, we found this basic methodology precise enough to clearly track the start and a subsequent down-valley shift in the location of seismic energy during the GLOF.

### 1.5.3 Flood model

We implemented the U.S. Army Corps of Engineers Hydrologic Engineering Center's River Analysis System (HEC-RAS) software to perform a 2D unsteady flow simulation using the diffusion wave equation (DWE) (Brunner, 2010). This equation is a simplified version of a full dynamic wave model (neglects inertial force and advective accelerations) and has been found to be a satisfactory approximation in many situations (Moussa and Bocquillon, 1996). Simulations were run at a nominal mesh resolution of 30 m using a timestep of 1 second, solved using an implicit finite volume approach (Brunner, 2010). We used the 30 m ALOS DEM as terrain input, preprocessed using standard carve and fill operations to remove any spurious elevation artifacts which may cause unrealistic damming and pooling in localized sections where the river channel may be narrower than the DEM resolution (Schwanghart and Scherler, 2014; Watson et al., 2015). To approximate the normal (pre-GLOF) river flow conditions, we specified inflows for 15

major tributaries between Lugge Tsho and Wangdue station and allowed the model to come to equilibrium. The (relative) contributions of each tributary were estimated by performing a flow accumulation analysis for the region based on upstream watershed areas (Schwanghart and Scherler, 2014). We then multiplied all the relative inflow values with a single scale factor to estimate (absolute) contributions, so that the river flow at Wangdue station (located downstream of all tributaries) matched the observed pre-GLOF conditions of approximately 290 $m^3 s^{-1}$ (Figure S1.1). In HEC-RAS we expressed the tributaries as inflow boundary conditions, and allowed the model to run for 24 hours to establish initial conditions before simulating the flood. We then performed multiple model runs using a range of Manning roughness coefficient values ($n$) and various breach hydrograph shapes (Figure S1.1). We tested values of $n$ spanning from 0.05 to 0.07 (in increments of 0.01), which is the typical range for mountain streams with cobbles and large boulders (Brunner, 2010). For the breach hydrographs, we used a simple triangular approximation scaled to have ramp-up times ($t_{ru}$) ranging from 15 to 120 minutes (in increments of 15 minutes). Based on previously published differential GPS survey of the lowering of the lake level (Yamada, 2004) and the Wangdue station GLOF hydrograph (JICA, 2001), we assumed 17 to 25 million $m^3$ as a probable range for the total volume of water released during the GLOF, and constrained the simulated breach hydrographs to 25 million $m^3$. As a conservative threshold, we discarded any model runs which did not agree with all independent constraints within ± 30 minutes, and report the corresponding range of input parameters and model outputs of the remaining ones. We note that the breach may have initiated before the seismic signal was detectable (see Seismic Data section), thus we also include simulated breach times of 1:15,1:30, and 1:45 am in our analysis. Out of a total of 72 model runs (3 values of $n$, 8 values of $t_{ru}$, and 3 breach times), 14 runs produced output which satisfied the specified ± 30

minute threshold. Lastly, we quantified the model sensitivity of arrival time estimates in Punakha (Figure S1.1). In general, a more gradual release of water and greater channel roughness both resulted in a slower-moving flood wave. Increasing $t_{ru}$ from 45 to 60 minutes delayed arrival in Punakha by 20 to 25 minutes (Figure S1.1E), and increasing $n$ from 0.05 to 0.06 delayed arrival time in Punakha by 25 to 35 minutes (Figure S1.1F). Generally, we found the HEC-RAS model performed well in satisfying the independent observations within the specified range of model parameters. However, we stress the overall sensitivity to breach hydrograph characteristics requires caution if external constraints are not available.

### 1.5.4 Satellite imagery

For analyzing GLOF-induced changes in land cover, we used the USGS Landsat 5 through 8 TM Collection 1 Tier 1 calibrated top-of-atmosphere (TOA) reflectance product in Google Earth Engine (Gorelick et al., 2017). We quantified Lugge Tsho area changes over time by manual delineation of the lake boundaries and glacier front between 1976 and 2018 using declassified spy satellite imagery (KH-9 Hexagon) and Landsat. The Hexagon images were downloaded from the USGS Earth Explorer website (https://earthexplorer.usgs.gov/) after digital scanning of the images by the USGS and have a ground resolution of approximately 15 meters. To measure the extent of sediments deposited by the GLOF, we selected two Landsat 5 scenes acquired in August of 1994 (pre-GLOF) and September of 1995 (post-GLOF) and used supervised classification with manually defined training samples of vegetation, sediment, water, ice, and clouds from the pre-GLOF scene. We classified both images using the maximum likelihood algorithm, and retained the pixels classified as sediment along the valley bottom before and after the GLOF. To analyze the post-GLOF vegetation recovery trend, we focused on the largest swath of sediment deposition over the Tshojo plain. For this region, we computed the enhanced

vegetation index (EVI) for all Landsat 5 and 7 scenes excluding those acquired during monsoon season months (May-Oct). We evaluated the topography of the Lunana region using the High Mountain Asia 8 m DEM data (version 1) distributed by the National Snow and Ice Data Center (NSIDC), and obtained the valley profile from the 30 m ALOS global digital surface model dataset distributed by the Japan Aerospace Exploration Agency (JAXA).

### 1.5.5 Cosmogenic $^{10}$Be surface exposure dating

We applied cosmogenic $^{10}$Be dating (Balco, 2011; Lal, 1991) to three boulders sampled in 2014 from the prominent and well-preserved lateral-terminal moraines near Thanza, about 10 km downstream from the GLOF breach location (Figure 1.4). Geochemical processing was performed at the Cosmogenic Nuclide Laboratory at LDEO following standard protocols given in Schaefer et al. (2009), and $^{10}$Be/$^{9}$Be measurements were completed at the Center for Accelerator Mass Spectrometry at the Lawrence Livermore National Laboratory. The background correction for these measurements was below 1%. We used version 3 of the online cosmogenic nuclide calculator (Balco et al., 2008) with the default production rate and time-dependent Stone/Lal scaling scheme for exposure age calculations (Borchers et al., 2016; Lal, 1991). Geographic and analytical data are given in Table S1.2 and the geomorphic map with the $^{10}$Be ages is shown in Figure 1.4. This glacier chronology will be discussed in detail in forthcoming papers.

## 1.6 Acknowledgements

We thank Victor Tsai and two anonymous reviewers for helping improve this manuscript. We would also like to acknowledge the National Center for Hydrology and Meteorology, Royal Government of Bhutan for providing field logistics and support for this study. **Funding:** J.M.M. and J.M.S. acknowledge support by a NASA Earth and Space Science Fellowship

(#NNX16AO59H). S.R. and J.M.S. acknowledge support by NSF Geography and Spatial Sciences award 17-566. J.M.S. also acknowledges support by Global Change award EAR 10-574. S.B. acknowledges support by NASA #NNX16AQ61G and NSF #1853881.

## 1.7 Supplementary Materials

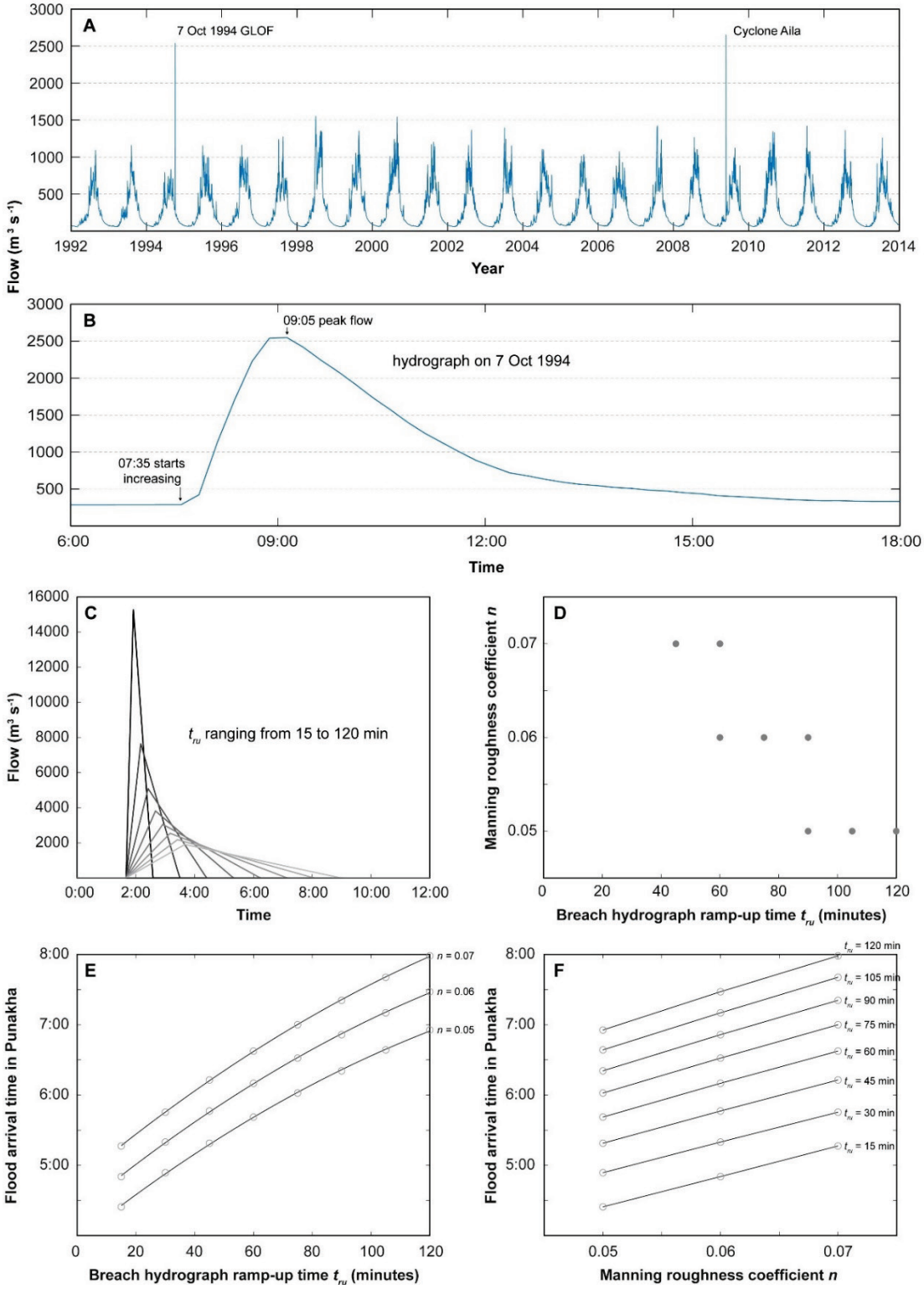


Figure S1.1. River flow ($m^3 s^{-1}$) measured at Wangdue station (~110 km downstream from the breach), flood model input parameters, and model sensitivity. (A) Daily flow from 1992 to 2014.

The extreme flows during the 1994 GLOF and 2009 Cyclone Aila are highlighted. (B) Flow measured every 15 minutes on 7 October 1994 (JICA, 2001). (C) Simulated breach hydrographs used as inflow for the flood model runs, with ramp-up times ranging from 15 to 120 minutes. Each hydrograph has an integrated volume of 25 million $m^3$. (D) Here the data points represent combinations of model parameters ($t_{ru}$ and $n$) which produce output satisfying all independent observations within ± 30 minutes. (E) Flood arrival time in Punakha as function of $t_{ru}$. (F) Flood arrival time in Punakha as a function of $n$.

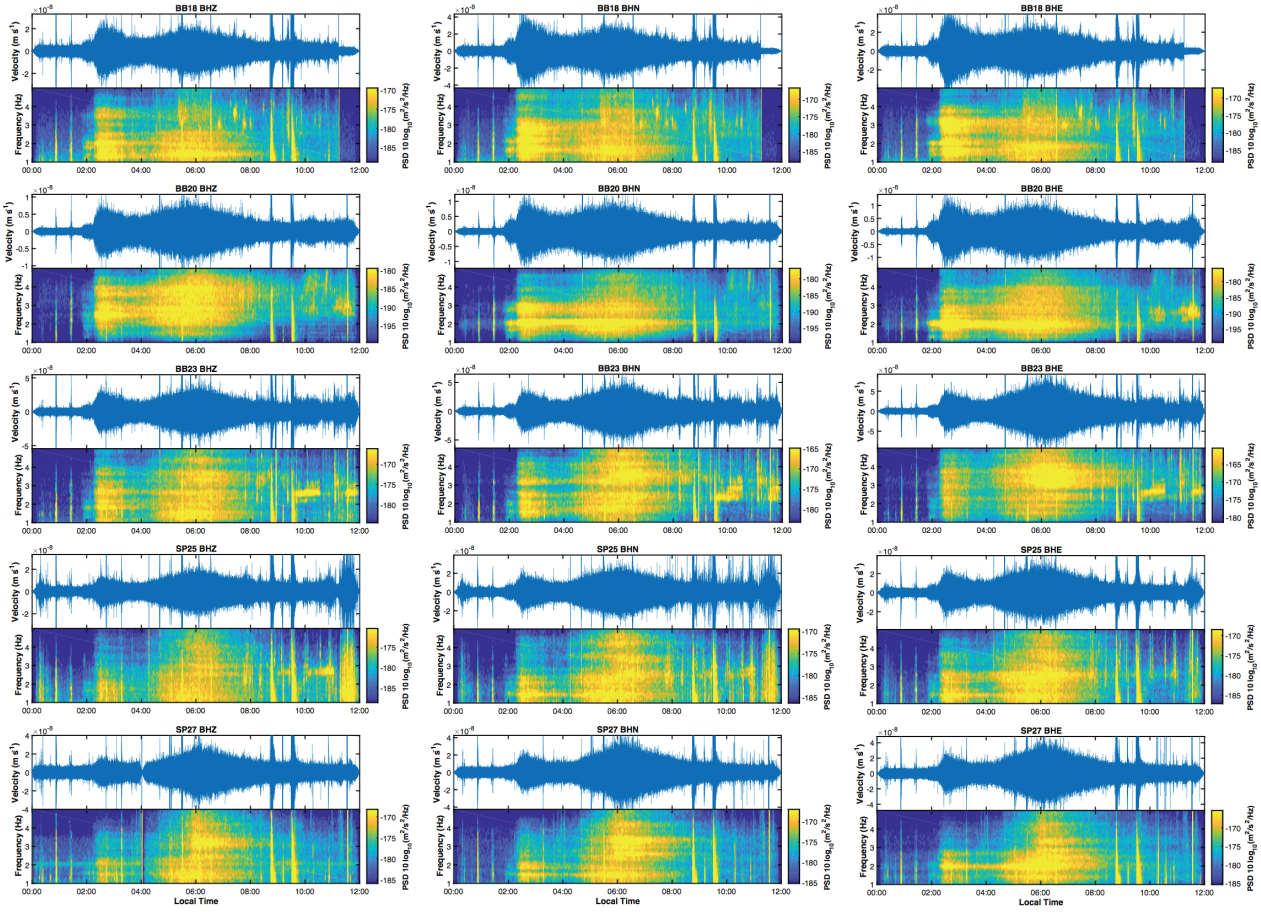


Figure S1.2. Seismic traces and spectrograms for each component of the five stations during the GLOF on Oct. 7, 1994. Seismic traces are filtered from 1–5 Hz and clearly demonstrate the GLOF signal across all five seismometers and on all components. Some interstation variability in peak frequency content of the GLOF signal is likely due to lateral variations in seismic attenuation as well as distance from the source.

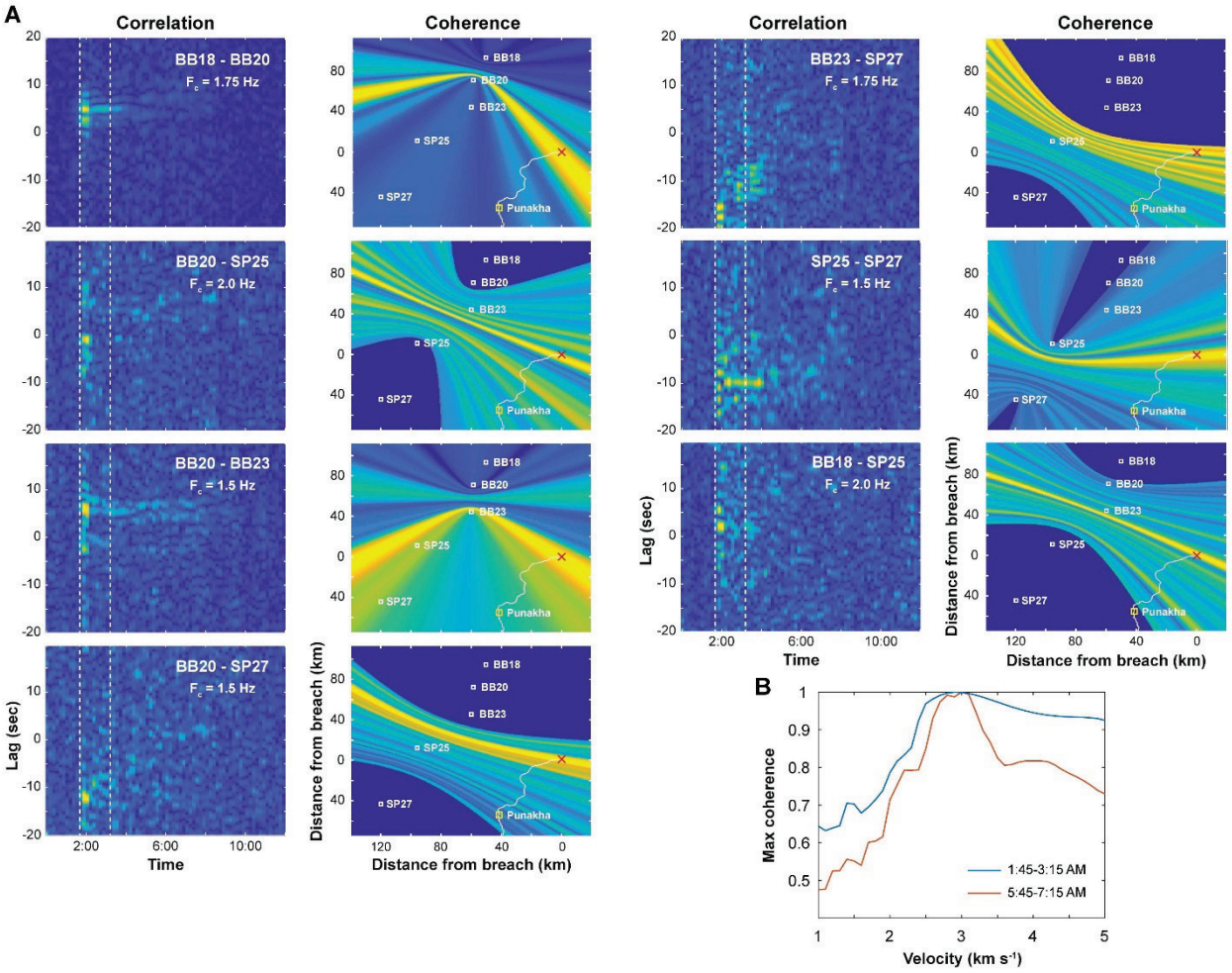


Figure S1.3. Example of CCFs migrated to coherence maps for selected station pairs. (A) Data from the interval 1:45 to 3:15 am (as indicated by the dashed vertical lines) were used during the migration process to create these coherence maps. The CCF amplitudes map to hyperbolae during the migration, and the highest values for each station intersect with the GLOF breach location (red 'x' symbol) using the optimal velocity of 3.0 km $s^{-1}$. All coherence maps from these station pairs were summed together to create the final coherence map for this interval in Figure 1.2C. (B) For the selected station and frequency pairs (Table S1.1), migrating the CCF amplitudes using velocities ranging from 1 to 5 km $s^{-1}$ for the two intervals results in the blue and orange curves here. Note the peaks at 3.0 km $s^{-1}$.

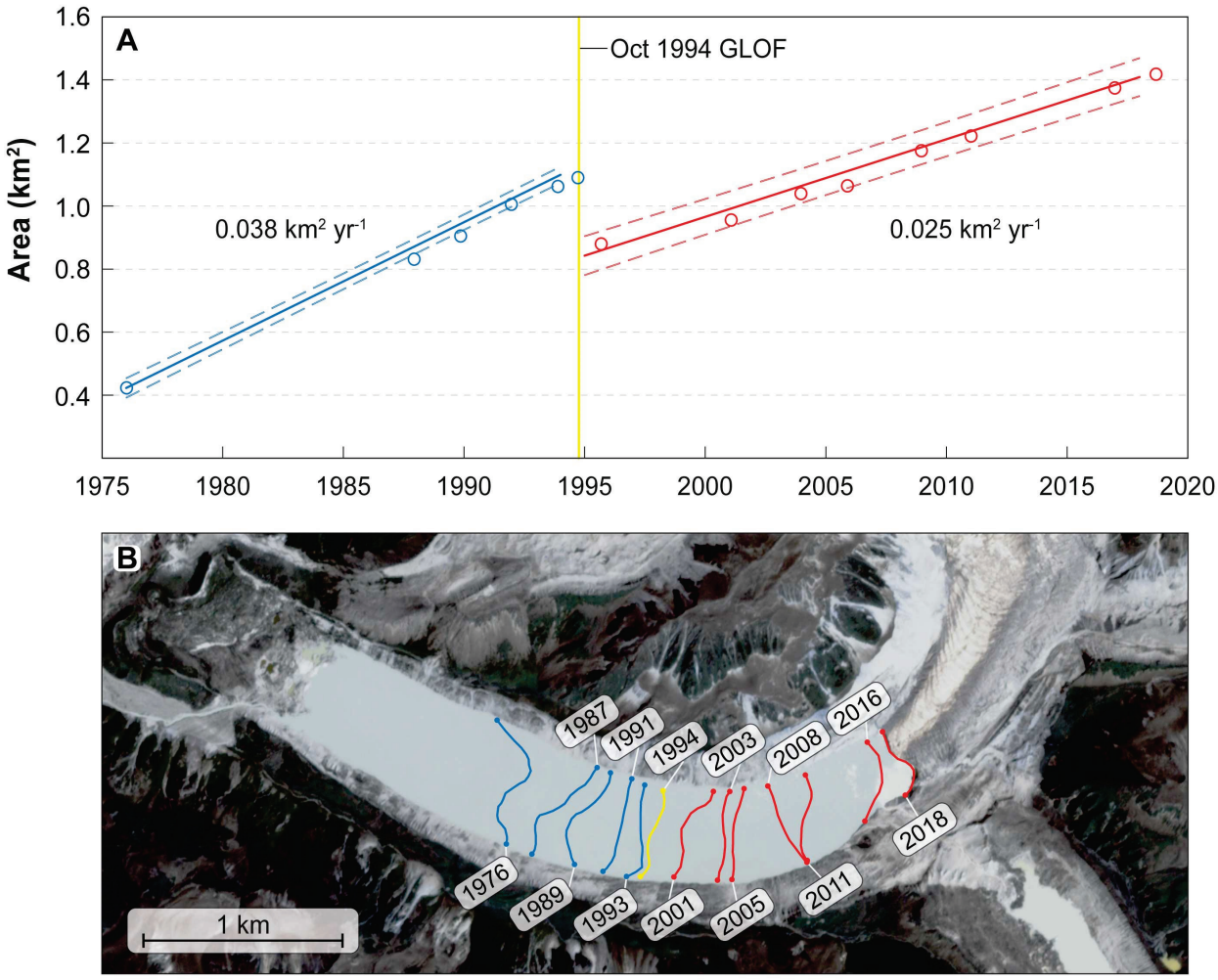


Figure S1.4. Lake area (Lugge Tsho) through time. (A) Trend in lake area over the past 43 years. (B) The progression of the Lugge glacier front through time. Pre-GLOF trend and glacier front in blue, Post-GLOF trend and glacier front in red.

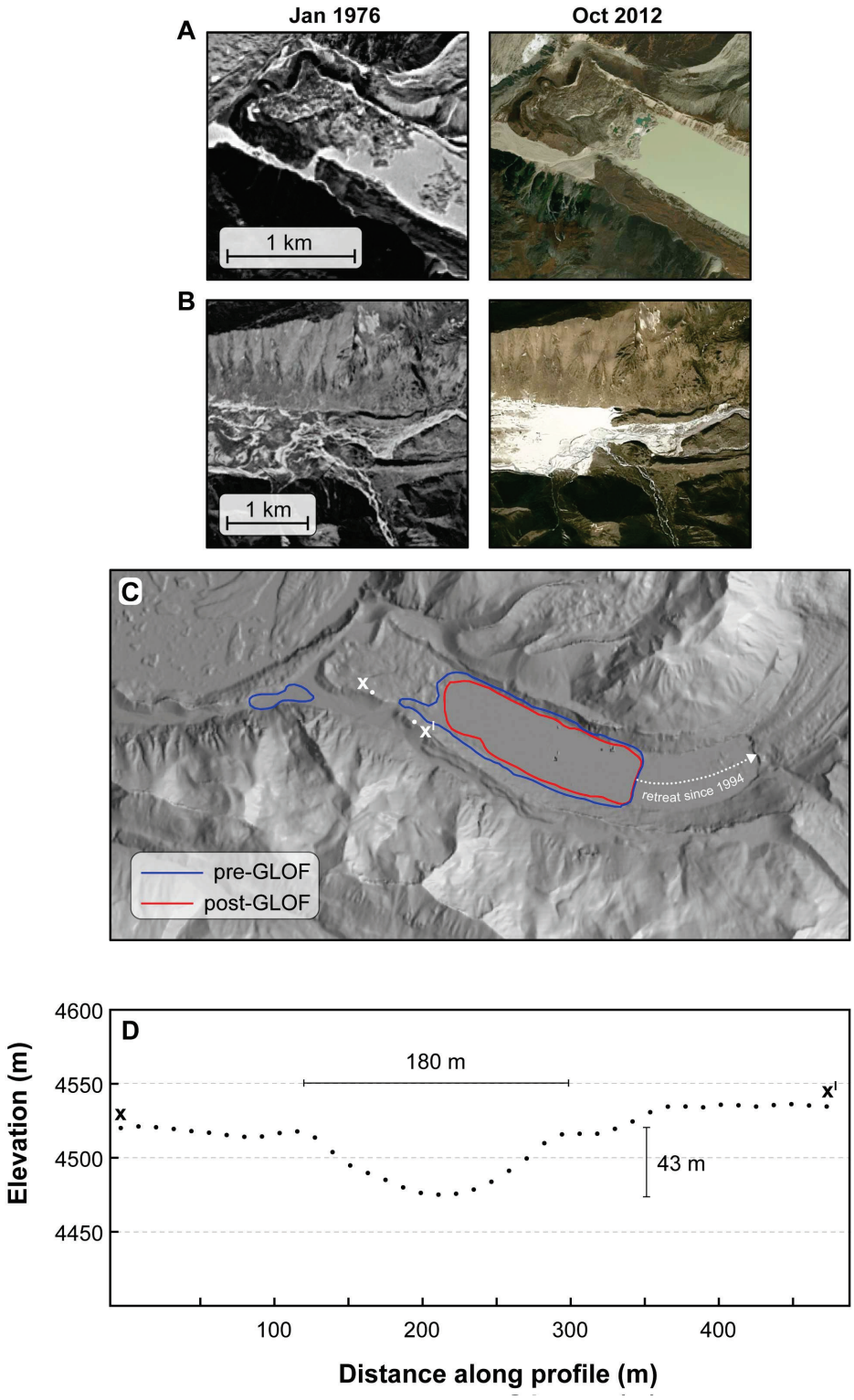


Figure S1.5. Closeup view of glacier moraines in 1976 and 2012, along with hillshade of region around Lugge Tsho and elevation profile across the outlet channel where the breach occurred. (A) Lake-fringing moraines where the GLOF breach occurred. The natural outlet of Lugge Tsho is evident in 1976, and was widened during the 1994 GLOF. (B) Mid-Holocene moraine ridges and

Tshojo plain. The GLOF left these moraines largely intact. (C) blue outline indicates the lake extent before the 1994 GLOF event, red outline is after the event. The lake area decreased by approximately 25%, and the small seasonal lake below Lugge Tsho was completely drained during the GLOF. (D) Elevation profile across the moraine breach, from point x to point x[1].

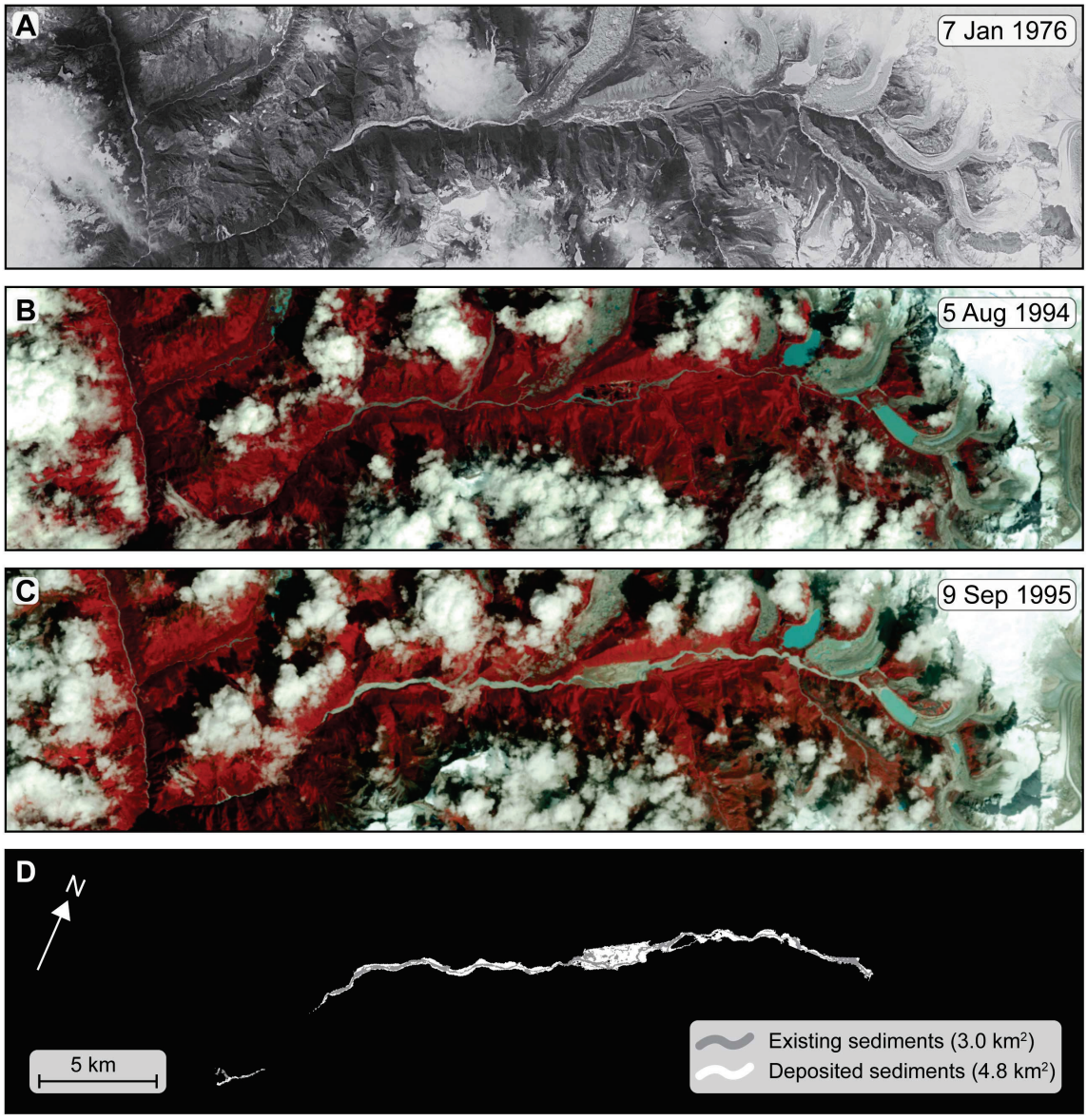


Figure S1.6. Landsat images showing extent of sediments deposited by the GLOF. (A) Declassified spy satellite image from 1976. At that time Lugge Tsho was only beginning to form. (B) False-color (near-infrared, red, green bands mapped to RGB) Landsat image before the GLOF, where vegetation appears red. (C) Same as (B) except after the GLOF. (D) Results from the supervised classification, where existing (pre-GLOF) sediments are in grey, and GLOF-deposited sediments are in white.

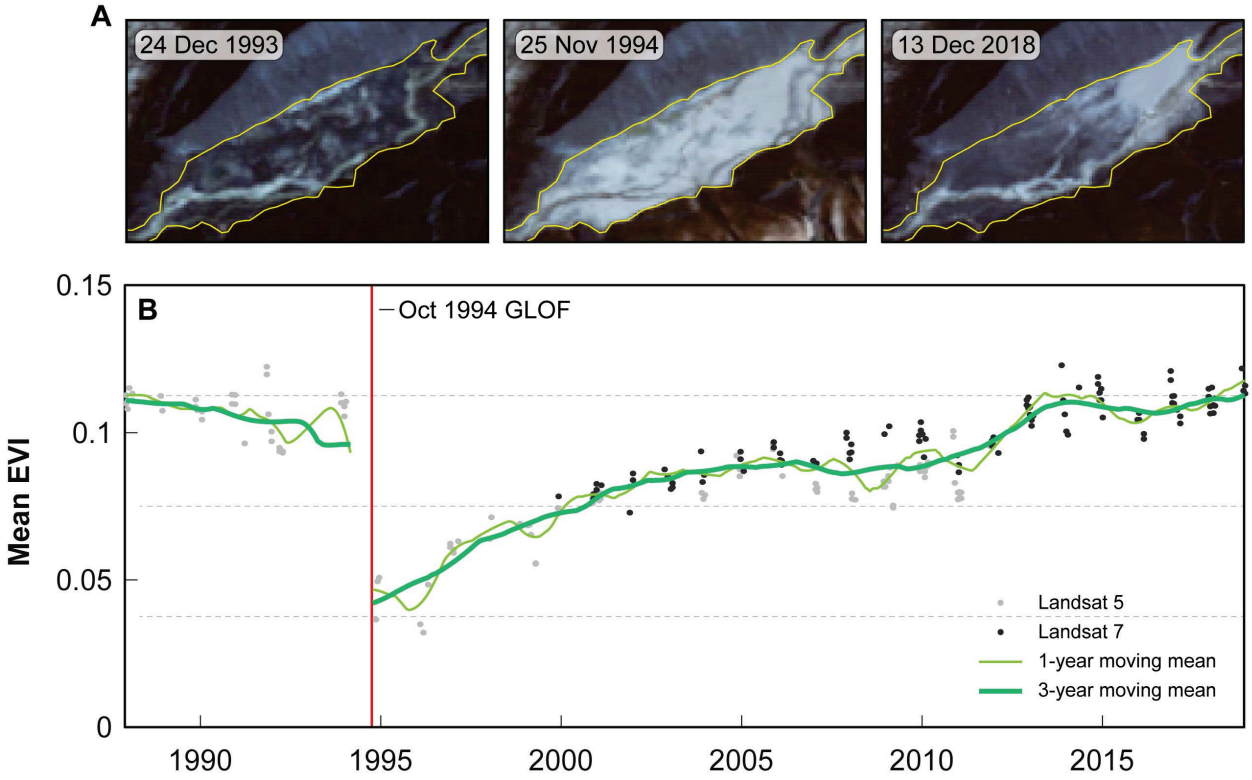


Figure S1.7. Mean enhanced vegetation index (EVI) of the 2.2 km$^2$ region on the Tshojo plain. (A) Landsat images showing state of alpine scrub vegetation in the GLOF-affected region on the Tshojo plain. Dark colors are vegetation, light colors are sediments. The region of analysis is outlined in yellow. (B) Trend in mean EVI of the region of analysis over the past 30 years, showing the sudden decrease in vegetation from the GLOF and subsequent recovery. Landsat 5 and Landsat 7 data points, along with one-year and three-year moving means are shown.

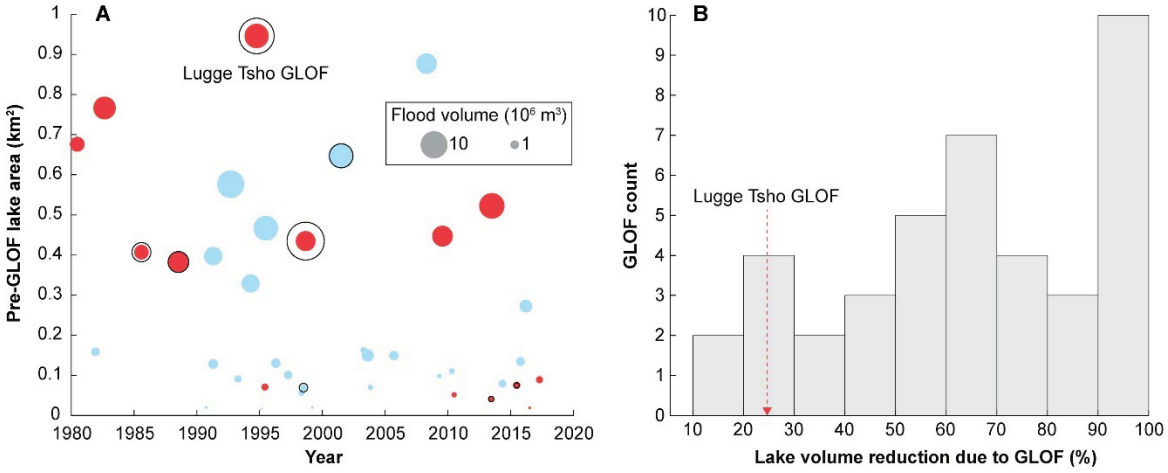


Figure S1.8. Comparison of the Lugge Tsho GLOF with other known GLOFs in high mountain Asia. Data from comprehensive analysis of the Landsat archive by Veh et al. (2019) (A) Pre-GLOF lake areas versus year of occurrence. Circle size is proportional to the estimated flood volumes using an empirical relationship between lake area and volume (Veh et al., 2019). Black

unfilled circles are estimated flood volumes from the literature. Red circles are GLOFs in which damage was reported, blue circles are GLOFs in which no damage was reported. (B) Histogram of the estimated percent lake volume reduction due to GLOFs, from the same Veh 2019 dataset. The value for the Lugge Tsho GLOF is indicated by the red dotted line.

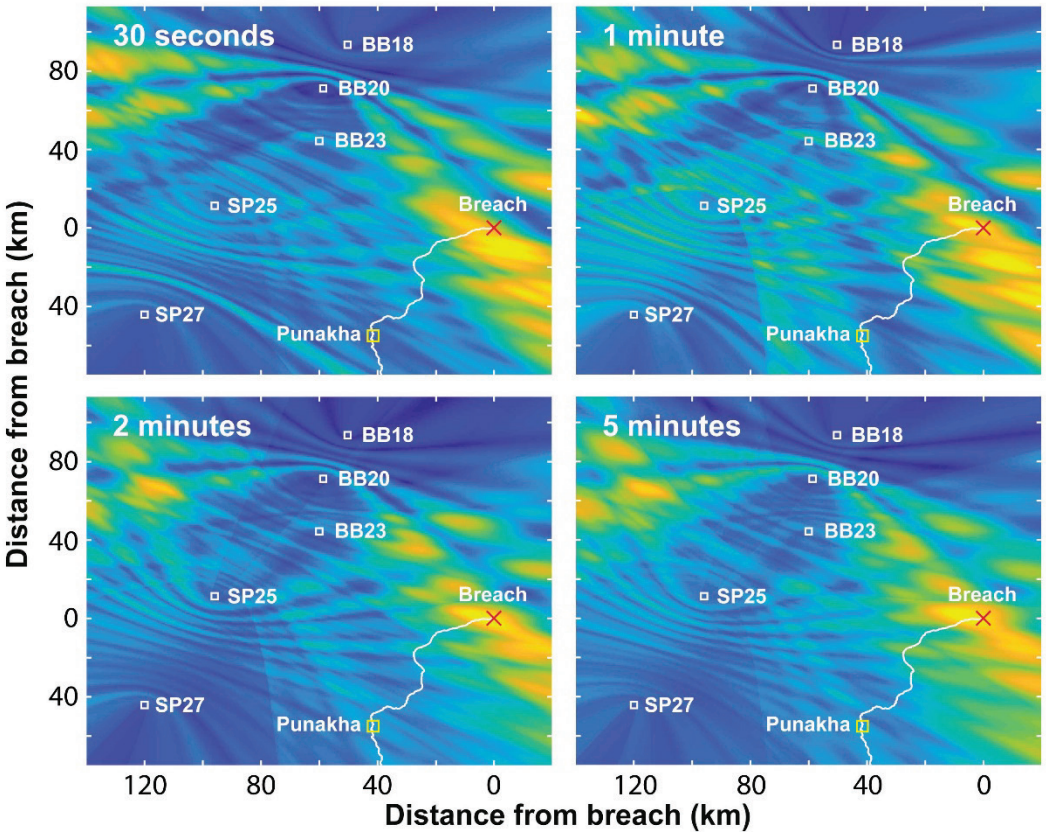


Figure S1.9. Coherence maps created from short durations of seismic data. These were produced the same way as the coherence maps described in the Methods section, but for much shorter intervals (30 sec, 1 min, 2 min, and 5 min) of seismic data centered on the CCF peak around 1:55 am (~10 minutes after start of the GLOF signal). The coherence maximum centered on the breach location is evident, although comparatively less distinct for these shorter intervals.

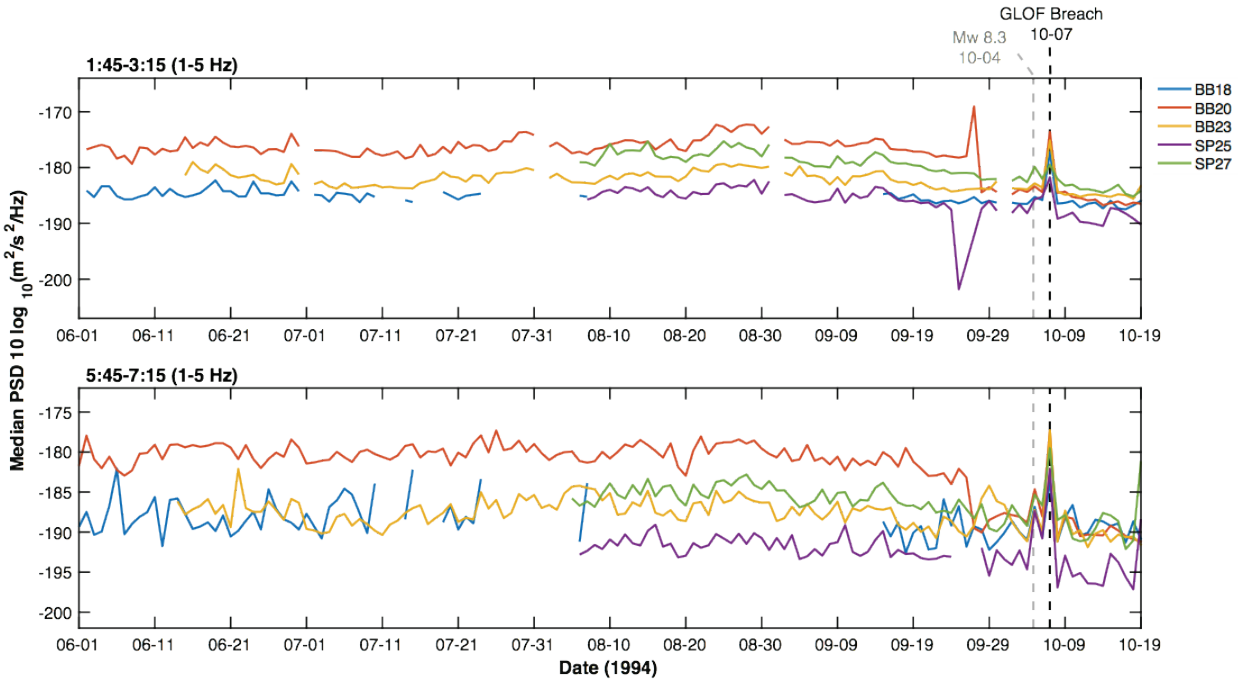


Figure S1.10. Strength of GLOF signal relative to background noise levels. Median vertical component (BHZ) PSD values from 1–5 Hz are calculated for the two key time windows identified in Figure 1.2c for each day of the deployment: (top) 1:45–3:15 local time (bottom) 5:45–7:15 local time. Both time windows show a clear power increase of 5–15 dB beyond background levels on 10-07, the day of the GLOF breach (black dashed line). Also denoted is a Mw 8.3 earthquake (gray dashed line) that occurred in the Kuril Islands (1994-10-04 13:22:55 UTC) ~5300 km away and was followed by several Mw ~6.0 aftershocks over the next 24-hour period. Although visible at all five seismic stations, the earthquake signals were significantly weaker (<7 dB increase relative to background) than the recorded GLOF breach at these frequencies. Although systematic fluctuations in power occur throughout the deployment, the GLOF signal is the most distinct and occurs contemporaneously across all stations.

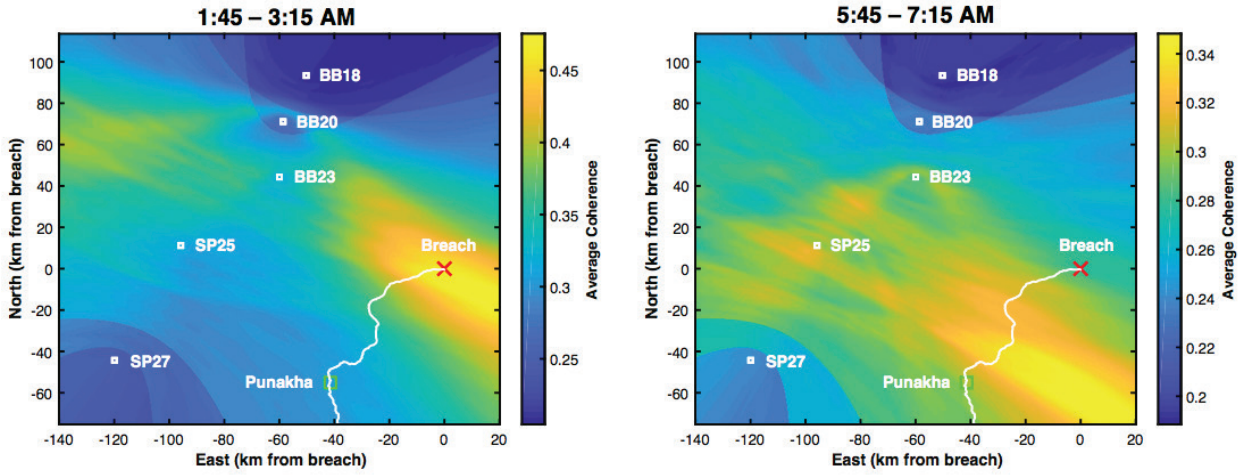


Figure S1.11. Coherence maps containing all station pairs. Coherence maps are calculated using all station pairs and all components (BHZ-BHZ, BHE-BHE, BHN-BHN) for frequencies ranging

from 1.5–4.25 Hz (total of 300 CCFs included in final stacks). The resulting maps are comparable to those shown in Figure 1.2c that include only the data from Table S1.1.

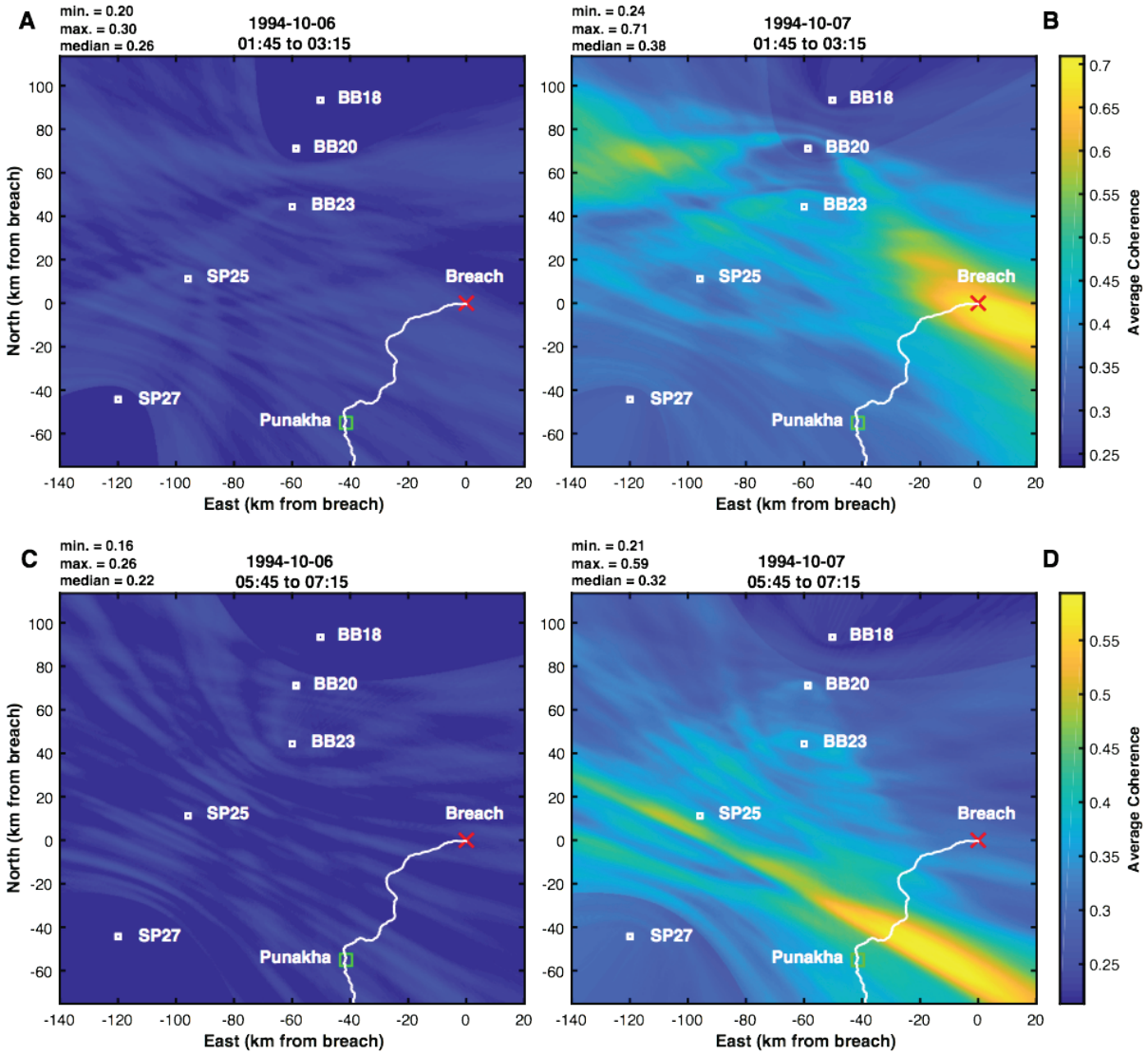


Figure S1.12. Coherence maps showing background noise levels from the day prior to GLOF breach for two time windows. (A) Coherence map for the day prior to the GLOF breach (1994-10-06) for the time window from 1:45–3:15 local time and for station pairs in Table S1. (B) Same as (A) but for the day of the GLOF breach (1994-10-07) as in Figure 1.2c in the main text. (C) and (D) same as (A) and (B) but for the time window from 5:45–7:15 local time.

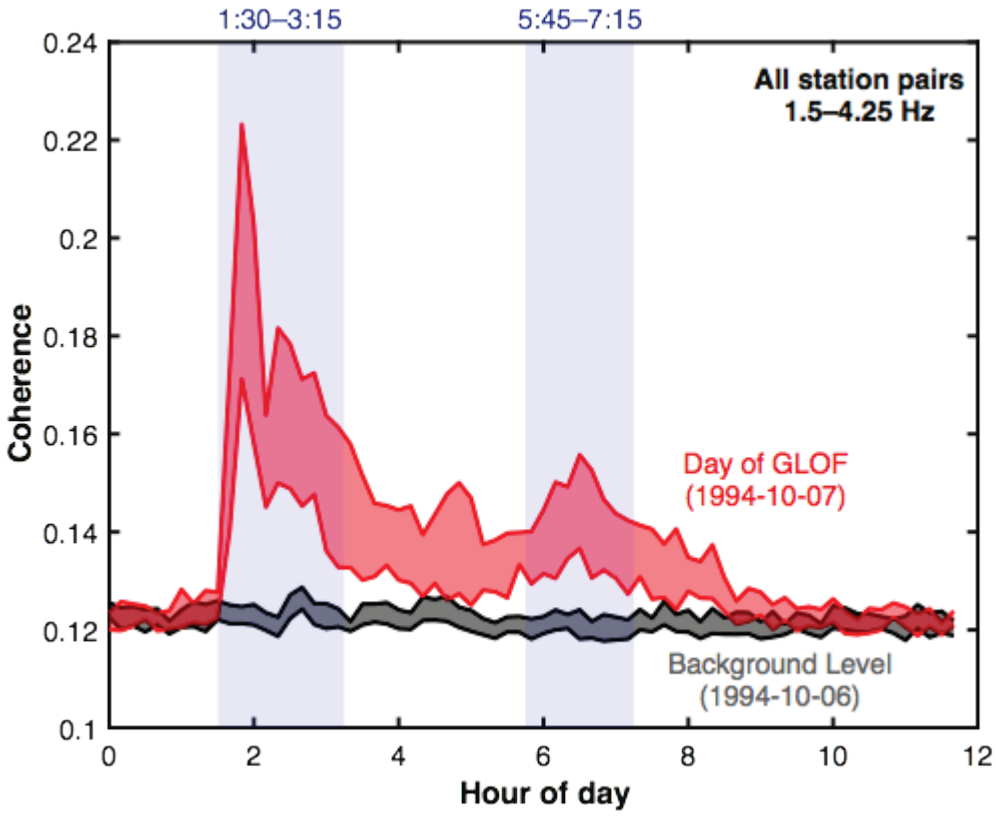


Figure S1.13. GLOF coherence relative to background level. 12-hour time series of signal coherence calculated for all station pairs and frequencies from 1.5–4.25 Hz as a function of time of day for the day containing the GLOF event (red) and the day prior to the GLOF event (black), which represents the background level. The upper and lower bounds of each shaded region represent the 95th and 75th percentile of coherence values across all lag times, respectively. The blue shaded regions mark the times of most significant GLOF signal relative to background levels.

Table S1.1. Selected station pairs and frequency ranges with clear CCF peaks used in Figure 1.2c

| $T_c$ = 2:30 am | | $T_c$ = 6:30 am | |
|---|---|---|---|
| **Station pair** | **Freq range (Hz)** | **Station pair** | **Freq range (Hz)** |
| BB18 - BB20 | 1.50 - 2.00 | BB18 - BB20 | 1.25 - 1.75 |
| BB20 - SP25 | 1.75 - 2.25 | BB18 - BB23 | 3.50 - 4.00 |
| BB20 - BB23 | 1.25 - 1.75 | BB23 - SP25 | 2.25 - 2.75 |
| BB20 - SP27 | 1.25 - 1.75 | BB23 - SP27 | 3.00 - 3.50 |
| BB23 - SP27 | 1.50 - 2.00 | SP25 - SP27 | 2.25 - 2.75 |
| SP25 - SP27 | 1.25 - 1.75 | BB18 - SP27 | 3.25 - 3.75 |
| BB18 - SP25 | 1.75 - 2.25 | BB23 - SP27 | 3.00 - 3.50 |

Table S1.2. Geographical and analytical data from the sampled moraine ridge below Thanza

| Sample | Lat (°N) | Lon (°E) | Elev (m a.s.l.) | Thickness (cm) | Topographic shielding | $^{10}Be$ (atoms $g^{-1}$)* | $^{10}Be/^{9}Be$ standard | Age (yr)† | Int (yr)‡ | Ext (yr)§ |
|---|---|---|---|---|---|---|---|---|---|---|
| LUNA-14-07 | 28.08207 | 90.20015 | 4163 | 1.94 | 0.975 | 176229 ± 3460 | 07KNSTD | 4700 | 90 | 370 |
| LUNA-14-04 | 28.08147 | 90.19990 | 4146 | 1.62 | 0.974 | 171016 ± 4063 | 07KNSTD | 4590 | 110 | 360 |
| LUNA-14-03 | 28.08141 | 90.19987 | 4152 | 1.75 | 0.975 | 163819 ± 3515 | 07KNSTD | 4380 | 90 | 340 |

* Shown are 1σ analytical AMS uncertainties.
† Calculated using the online exposure age calculator v3 (Balco et al., 2008) with default production rate and time-dependent Stone/Lal scaling scheme (Borchers et al., 2016; Lal, 1991)
‡ Internal analytical error
§ External error, including systematic uncertainties and scaling to the latitude and altitude of the study region.

# Chapter 2: Quantifying ice loss in the eastern Himalayas since 1974 using declassified spy satellite imagery

Note: a modified version of this chapter has been published in *The Cryosphere*: Maurer, J.M., Rupper, S., Schaefer, J.M., 2016. Quantifying ice loss in the eastern Himalayas since 1974 using declassified spy satellite imagery. The Cryosphere 10, 2203.

Himalayan glaciers are important natural resources and climate indicators for densely populated regions in Asia. Remote sensing methods are vital for evaluating glacier response to changing climate over the vast and rugged Himalayan region, yet many platforms capable of glacier mass balance quantification are somewhat temporally limited due to typical glacier response times. We here rely on declassified spy satellite imagery and ASTER data to quantify surface lowering, ice volume change, and geodetic mass balance during 1974–2006 for glaciers in the eastern Himalayas, centered on the Bhutan–China border. The wide range of glacier types allows for the first mass balance comparison between clean, debris, and lake-terminating (calving) glaciers in the region. Measured glaciers show significant ice loss, with an estimated mean annual geodetic mass balance of −0.13 ± 0.06 m w.e. $yr^{-1}$ (meters of water equivalent per year) for 10 clean-ice glaciers, −0.19 ± 0.11 m w.e. $yr^{-1}$ for 5 debris-covered glaciers, −0.28 ± 0.10 m w.e. $yr^{-1}$ for 6 calving glaciers, and −0.17 ± 0.05 m w.e. $yr^{-1}$ for all glaciers combined. Contrasting hypsometries along with melt pond, ice cliff, and englacial conduit mechanisms result in statistically similar mass balance values for both clean-ice and debris-covered glacier groups. Calving glaciers comprise 18% (66 $km^2$) of the glacierized area yet have contributed 30% (−0.7 $km^3$) to the total ice volume loss, highlighting the growing relevance of proglacial lake formation and associated calving for the future ice mass budget of the Himalayas as the number and size of glacial lakes increase.

## 2.1 Introduction

Glaciers in high-mountain Asia hold the largest store of ice outside the polar regions and contribute meltwater used by roughly 20% of the world's population for agriculture, energy production, and potable water (Immerzeel et al., 2010). Glacier changes must be quantified in order to evaluate impacts to hydrology and ecosystems, assess glacial lake outburst flood (GLOF) hazards, calculate recent contributions to sea level rise, and increase predictive capabilities regarding future change and resulting impacts.

The heterogeneity of Himalayan glaciers poses significant challenges in quantifying and modeling glacier changes. Debris cover in the ablation zone and calving in proglacial lakes are particularly noteworthy examples of complicating factors that may significantly affect the response of many glaciers. Bolch et al. (2012) estimate the proportion of debris-covered ice in the Himalayas is ~10%, and Scherler et al. (2011) estimate that 93% of glaciers in the Himalayas have >20% debris-covered areas. Debris-covered glaciers are difficult to model, since debris can either increase or suppress melt depending on debris thickness and extent, though debris-covered glaciers in the Himalayas are mostly assumed to be less responsive to ongoing warming (Scherler et al., 2011). Similarly, numerical models of glaciers terminating in moraine-dammed proglacial lakes are poorly constrained, and these glaciers can undergo enhanced ice loss through calving and thermal-undercutting processes independent of climate. Lake-terminating glaciers have particular societal relevance because the growing lakes can cause GLOFs and can impact glacier mass balance and hydrology.

Response of Himalayan glaciers to changing climate remains somewhat controversial, primarily due to this complexity of the glacier systems combined with scarcity of direct observation, and no unambiguous pattern has emerged (Berthier et al., 2007; Kääb et al., 2012).

Complex politics, rugged terrain, and the immense number of glaciers result in a severe lack of field data (Bolch et al., 2011; Rupper et al., 2012). The few available field records in the Himalayas are often biased towards small to medium-sized clean-ice glaciers due to logistical reasons and tend to be located in subregions where mass loss is greater than in the region as a whole (Gardner et al., 2013). Thus there is a critical need for spatially and temporally extensive glacier change data that capture the full spread of glacier complexities over timespans relevant to glacier response times. Here we focus on the eastern monsoonal Himalayas, centered on the Bhutan–China border. Few data on glacier changes are available and the region has a large diversity of glaciers with regard to elevation, size, debris cover, hypsometry, accumulation rates, and calving characteristics. Furthermore, glacier meltwater is an important hydrological resource in Bhutan, including for hydroelectric power generation (Beldring and Voksø, 2012). Recent hydrologic mixing model results using isotopic and geochemical chemistry have estimated glacier seasonal outflow contributions to the Chamkhar Chhu river in Bhutan ranging from ~76% at 4500 m to 31% at 3100 m elevation during September (post-monsoon) (Williams et al., 2015).

There are several clean glaciers flowing northward onto the Tibetan Plateau with high velocities, likely with large amounts of basal sliding (Kääb, 2005). On the southern flank, most large glaciers are debris covered, located in steep valleys, and show slow-to-nearly stagnant velocities, with many depressions and melt pond features. Additionally, several glaciers (including clean and debris covered) terminate in moraine-dammed lakes. The majority of clean-ice glaciers in the Bhutan-centered region have a high mass turnover, with most accumulation and ablation occurring during the summer months as a result of the Indian monsoon (Rupper et al., 2012). In regions with high accumulation, ablation is dominated by melt and thus particularly

sensitive to changes in temperature (Rupper and Roe, 2008). Robust melt models indicate these eastern Himalayan, temperature-sensitive glaciers are currently out of balance with present climatology. One estimate predicts a loss of almost 10% of the current glacierized area, with an associated drop in meltwater flux of as much as 30% even if climate were to remain at the present day mean values (Rupper et al., 2012). Kääb et al. (2012) computed a 2003–2008 specific mass balance of −0.26 ± 0.07 to −0.34 ± 0.08 m w.e. $yr^{-1}$ (depending on different density scenarios for snow and ice) for eastern Nepal and Bhutan using laser altimetry, while Gardelle et al. (Gardelle et al., 2013) estimated a 1999–2011 geodetic mass balance of −0.22 ± 0.12 m w.e. $yr^{-1}$ for Bhutan by differencing SPOT5 and SRTM DEMs (digital elevation models). Another recent study utilizing multi-temporal Landsat images to compute glacier area changes in Bhutan showed 23.3 ± 0.9% glacial area loss between 1980 and 2010, with loss mostly observed below 5600 m a.s.l., and greater area loss for clean glaciers (Bajracharya et al., 2014). The first decadal mass balance record of the Gangju La glacier in the Bhutan Himalaya was recently published, in which a mass balance of −1.12 to −2.04 m w.e. $yr^{-1}$ was estimated between 2003 and 2014 (Tshering and Fujita, 2015).

To build on these pioneering studies and further constrain glacier changes, we utilize a new pipeline (Maurer and Rupper, 2015) to extract DEMs from declassified Hexagon imagery (1974) and Advanced Spaceborne Thermal Emission and Reflection Radiometer (ASTER) scenes (2006), then use DEM differencing to measure ice volume change and geodetic mass balance between 1974 and 2006 in this temperature-sensitive, monsoon-influenced region. Our approach provides high spatial detail and longer temporal range compared to previous measurements, and it circumvents significant uncertainties regarding SRTM radar penetration in ice and snow (Gardelle et al., 2012).

## 2.2 Methods

Previous studies have demonstrated the value of declassified spy satellite imagery for glacier mass and volume change quantification in various regions of the Himalayas (Bhambri et al., 2013; Bolch et al., 2011; Holzer et al., 2015; Lamsal et al., 2011; Pellicciotti et al., 2015; Pieczonka and Bolch, 2015; Pieczonka et al., 2013; Racoviteanu et al., 2014; Ragettli et al., 2016; Raj et al., 2013). We rely here on a new workflow called HEXIMAP (Hexagon Imagery Automated Pipeline) which utilizes computer vision algorithms to extract DEMs with high efficiency and accuracy (Maurer and Rupper, 2015). Both Hexagon and ASTER DEMs are extracted using similar methods in order to minimize unwanted elevation bias caused by different image processing techniques. The resulting elevation change maps are used to compute average surface lowering of glaciers, changes in ice volume, and geodetic mass balance.

### 2.2.1 Hexagon

The Hexagon program consisted of a series of 20 photographic reconnaissance satellite systems developed and launched by the United States, operational from 1971 to 1986 during the Cold War era. Each satellite carried approximately 96.5 km of film, and thousands of photographs worldwide were acquired using the mapping camera system (ground resolution of 9 m, improved to 6 m in later missions). The Hexagon mapping camera system acquired multiple 3400 $km^2$ frames as the satellite proceeded along its orbital trajectory. After image acquisition, film-recovery capsules were ejected from the satellite and parachuted back to Earth over the Pacific Ocean, where they were retrieved midair via “air snatch” by C-130 Air Force planes. The images have overlap of approximately 55 to 70%, which allows for extraction of digital elevation models (Oder et al., 2012; Surazakov and Aizen, 2010).

Eight separate 5000×5000 pixel blocks are processed, which correspond to approximately 20×20 km regions with the Hexagon film scanned at 7 μm resolution (orange outlines in Figure 2.2), with blocks selected to maximize coverage of glaciers and avoid regions with cloud cover. The same HEXIMAP methodology, outlined in Maurer and Rupper (2015), is used to extract Hexagon DEMs. In summary, epipolar images are generated by computing homography transformations via automated point detectors and descriptors (Bay et al., 2006; Fusiello and Irsara, 2008). After epipolar resampling, image features line up horizontally and the disparity search is reduced to one horizontal dimension. Disparity maps are computed using the semi-global block matching algorithm (Hirschmüller, 2008), bundle adjustments are performed to minimize reprojection error, and stereo-matched points are triangulated in 3-D space using the direct linear method (Hartley and Zisserman, 2003). The 3-D point clouds are registered to the reference SRTM DEM using nonlinear optimization of pose parameters including rotation, translation, and a global scale factor. ICIMOD glacier outlines are utilized to exclude glacial terrain during optimization (after being manually edited to match the glacier extent in 1974). The glacier outlines are first converted to a raster binary mask to match the spatial resolution of the reference DEM. Next, dilation (a morphological operation which adds pixels to edge boundaries) is performed to slightly enlarge the glacier boundaries in the raster mask, which helps to eliminate unstable glacier pixels not contained by the glacier outlines, as well as eliminate possibly unstable moraines (see Figure S2.6 in the Supplement). Any elevation change pixels outside of 3 standard deviations are excluded during each iteration in the optimization routine, which effectively eliminates other unknown sources of error during optimization. The higher spatial-resolution Hexagon point clouds are then resampled to match ASTER data (~30 m

intervals) using linear interpolation. Data voids larger than 2 $km^2$ are not interpolated to avoid biasing glacier change results with unrealistic terrain (Figure S2.3 through Figure S2.5).

### 2.2.2 ASTER

The ASTER instrument was launched on board NASA's Terra spacecraft in December 1999 as part of a cooperative effort between NASA and Japan's Ministry of Economic Trade Industry (METI). In the visible and near-infrared (VNIR) spectral region (0.78–0.86 μm), ASTER has a nadir-view telescope as well as a backward-looking telescope to provide stereoscopic capability at 15 m ground resolution. Both use 4000 element charge-coupled detectors (CCDs), acquiring data via linear push broom scanning. Each ASTER scene covers approximately 60×60 km (Abrams, 2000). Although a global ASTER DEM (GDEM v2) is publicly available, anomalies and artifacts in the data limit its utility for glacier change quantification. Instead, two ASTER Level1A scenes (granule ID: ASTL1A 061204044623061207030 3 and ASTL1A 060203044541060206030 3) were downloaded from the GDS (ground data systems) ASTER/PALSAR Unified Search website, maintained by Japan Space Systems. DEMs were extracted from the scenes using similar methodology as previously described for the Hexagon imagery, with a few key differences. First, DN (digital number) pixel values from the VNIR images are converted to radiance and processed to remove residual striping artifacts. Second, since ASTER images are acquired by a linear pushbroom sensor they do not have a single fixed center of perspective (Kim, 2000). Consequently, epipolar images cannot be generated using a single homography transformation as was done with Hexagon images. Alternatively, sight vectors and satellite position matrices (supplied with ASTER ephemeris data) for each CCD row are used to project ASTER forward and backward-looking images to a common image plane, after which corresponding pixels in the stereo images are matched using the same stereo-

matching algorithm in HEXIMAP. Lastly, point clouds are triangulated by computing sight vector intersections in 3-D space rather than using the direct linear method. All other aspects regarding DEM extraction are identical to the Hexagon methodology, thus minimizing any unwanted potential elevation bias caused by different image processing techniques.

### 2.2.3 Geomorphic change

To compute glacier changes, the 1974 Hexagon DEMs are subtracted from the 2006 ASTER DEMs to create elevation change maps. Pixels located in areas with >30° slope are excluded from analysis due to lower accuracies during the DEM extraction process (Maurer and Rupper, 2015). Elevation changes over 100 m are likely due to stereo-matching errors from cloud cover or low radiometric contrast and are thus also excluded. To delineate glacier boundaries, polygons representing glacier outlines were downloaded from the ICIMOD mountain geoportal (http://geoportal.icimod.org/), which were found to have comparatively greater detail and accuracy for this region compared to the Randolph Glacier Inventory, based on overlay and visual inspection of Google Earth imagery. The polygons were then manually edited to reflect the spatial extent of glaciers in 1974 and 2006 based on visual interpretation of the Hexagon and ASTER imagery, along with examination of the elevation change maps. The 30° slope threshold also effectively excludes any steep parts (nunataks and rock cliffs) in accumulation regions which were erroneously delineated as glacier ice, and the glacier outlines are updated accordingly.

Relative vertical errors between the Hexagon and ASTER DEMs are expected due to different sensor characteristics such as viewing geometry, sun position, cloud cover, and atmospheric conditions. Further complicating this are non-ice geomorphic changes such as landslides, which can be triggered as glaciers recede and alter stress regimes along valley walls and moraine

ridges, exposing unstable slopes, and reorganizing large volumes of unconsolidated sediment (Richardson and Reynolds, 2000). Several collapsed moraines were observed in the region (Figure S2.6), and therefore we base our clean-ice and calving glacier outlines primarily on visible satellite imagery, with the thickness change maps as a secondary source. In contrast, we base our debris-covered glacier outlines primarily on the thickness change maps, as debris-covered glaciers are difficult to distinguish from surrounding terrain using visible imagery only. Future work could focus on utilization of SAR glacier tracking methods to further constrain the extent of debris-covered zones, including surface feature tracking, SAR interferometry, and coherence tracking (Atwood et al., 2010; Frey et al., 2012; Mattar et al., 1998; Schubert et al., 2013; Strozzi et al., 2002).

Glacier elevation models extracted using stereophotogrammetry often have errors and gaps over snow-covered accumulation zones due to low radiometric contrast and sensor oversaturation (Pellikka and Rees, 2009). Hexagon film strips are especially vulnerable to this problem, resulting in large regions of missing data and some apparently erratic thickness changes over glacier accumulation zones. To exclude these erroneous regions, we compute the neighborhood standard deviation of each image pixel (a measure of local image contrast, using a 5×5 window), along with the gradient and curvature of the thickness change map for each glacier. Pixels with neighborhood standard deviations less than 3, which also have either a thickness change gradient >45, or a curvature value >0.005$m^{-1}$ are excluded, and gaps in the thickness change maps smaller than 2 $km^2$ are interpolated (Figure S2.3 through Figure S2.5). This method allows for removal of erroneous pixels in low-contrast accumulation zones, while retaining pixels in debris-covered zones which often have greater local gradient and curvature values due to melt ponds and ice cliffs.

To close remaining data gaps in accumulation regions, various approaches can be found in the literature. Gardelle et al. (2013) replace missing thickness change data over glaciers by the regional mean of the corresponding elevation band for a given glacier type, based on the assumption that thickness changes should be similar at a given altitude across the region. Pieczonka and Bolch (2015) assume no change in the accumulation regions and replace missing data values with 0. Due to the spatially heterogeneous nature of glacier changes in Bhutan, and the limited number of contributing pixels at high elevation bands (Figure 2.4), the regional extrapolation method introduces significant bias, especially regarding the large region of missing data in the accumulation zone of glacier c. Thus, all regional glacier change values reported in the text are derived using the method which assumes zero change for missing data. To examine the effect on geodetic mass balance and facilitate a comparison between the two methods, we also include separate results derived using each assumption (replacing missing data with zero change vs. regional extrapolation) in Table S2.3 in the Supplement. For the extrapolation method, missing data for different glacier types are extrapolated using the corresponding thickness change profiles (either clean, debris, or calving).

A total of 21 glaciers are selected (Figure 2.2, outlined in white) based on size (glaciers larger than 3 $km^2$*)* and data coverage (glaciers with at least 25% glacier area covered by the DEMs). Unfortunately, incomplete coverage of remote sensing data, clouds, and poor radiometric contrast in some areas prevent accurate investigation of all glaciers. While this does limit direct comparison to previous studies which measure all glaciers in a region, these 21 largest glaciers give a good regional picture of thickness changes over the 3-decade timespan.
Debris-covered areas for each glacier are delineated using a Landsat TM4/TM5 DN band ratio image with a threshold of 2.0 (Paul, 2000). Non-calving glaciers with 20% or greater debris-

covered area are assigned the debris category (5 glaciers); non-calving glaciers with less than 20% are assigned the clean category (10 glaciers). The calving category (6 glaciers) includes both clean and debris types which terminate in lakes as determined by viewing the Hexagon and ASTER imagery.

For each glacier, the ice volume change, spatially averaged thickness change, and geodetic mass balance over the 32-year timespan are computed using the elevation change maps following Equations (2.1) – (2.3):

$$\Delta V = \sum_{i=1}^{n} D_i r^2, \quad (2.1)$$

$$\bar{h} = \frac{\Delta V}{A}, \quad (2.2)$$

$$\dot{b} = \bar{h}\rho, \quad (2.3)$$

where $\Delta V$ is ice volume change ($m^3$), $D_i$ is the elevation change (m) for pixel $i$ located within a glacier polygon, $n$ is the total number of pixels within a glacier polygon, $r$ is the resolution of the elevation change map (~30 m), $\bar{h}$ is the spatially averaged elevation change of the glacier, $A$ is the average of the 1974 and 2006 glacier areas ($m^2$), $\dot{b}$ is the geodetic (specific) mass balance, and $\rho$ is the estimated average density of glacier ice; here we use an intermediate value between firn and ice of 850 ± 60 kg $m^{-3}$ as recommended by Huss (2013). Geodetic mass balance values are converted to m w.e. (meters water equivalent) by dividing $\dot{b}$ by the density of water (1000 kg $m^{-3}$).

### 2.2.4 Relative accuracy between DEMs and glacier change uncertainties

Statistical significance of elevation changes is quantified by estimating the relative vertical accuracy between the Hexagon and ASTER DEMs. Table S2.1 shows the root-mean-square

error, mean, median, normalized median absolute deviation, standard deviation, 68.3% quantile, and 95% quantile of elevation changes between each approximately 20 by 20 km Hexagon DEM (orange outlines in Figure 2.2) and the ASTER DEM (blue outline in Figure 2.2) for assumed stable (ice-free) terrain. Plots of elevation change against elevation, slope, curvature, and ASTER along-track and cross-track were also examined for potential biases (Figure S2.1). We neglect any global corrections, as the vast majority of data lie in regions with close to zero bias, and pixels with high slope (>30°) are excluded as outlined in Sect. 2.3.

To assess uncertainties for glacier changes, the point elevation error ($E_{pt}$) and extrapolation error ($E_{ext}$) are used to calculate the total elevation error ($E_z$) for a given elevation band (Nuth et al., 2010):

$$E_z = \sqrt{\left(\frac{E_{pt}}{\sqrt{n_z}}\right)^2 + \left(\frac{E_{ext}}{\sqrt{n_z}}\right)^2} \quad (2.4)$$

The standard deviations of the relative elevation change over stable terrain are used for $E_{pt}$ (Table S2.1), while the standard deviations of glacial elevation change within each 100 m elevation band are used as approximations for $E_{ext}$. These $E_{ext}$ estimates are conservative because the elevation bands contain intrinsic natural variability, as not all glaciers have undergone the same elevation change at a given elevation (Gardelle et al., 2013). The $n_z$ value represents the number of independent pixel measurements. To account for spatial autocorrelation, we estimate $n_z$ as:

$$n_z = \frac{n_b * r^2}{\pi * d^2} \quad (2.5)$$

where $n_b$ is the number of pixels in a given glacier elevation band, $r$ is the pixel resolution (~30m), and $d$ is the distance of spatial autocorrelation (Nuth and Kääb, 2011; Nuth et al.,

2010). For glacier regions where data exist (i.e., covered by an elevation change map, thus no extrapolation is necessary), $E_{ext}$ is set to zero and the numerator in Eq. (2.5) is set to the area within the glacier covered by elevation change data. To estimate $d$, we perform a semivariogram analysis, which relates variance to sampling lag and gives a picture of the spatial dependence of each data point on its neighbor (Curran, 1988; Rolstad et al., 2009). For all eight regions, we find the range varies from approximately 300 to 450m and thus choose a conservative value of 500m for $d$. The volume change error for a given glacier is then estimated as:

$$E_{vol} = \sqrt{\sum_{1}^{z} (E_z * A_z)^2} \qquad (2.6)$$

where $A_z$ is the area of the glacier within a given elevation band $Z$. $E_{vol}$ is then combined with glacier area uncertainties of ±10% and an ice density uncertainty of ±60 kg m$^{-3}$ using standard quadratic (uncorrelated) error propagation. All final glacier change uncertainties are reported as ±1 SEM (standard error of the mean) unless noted otherwise.

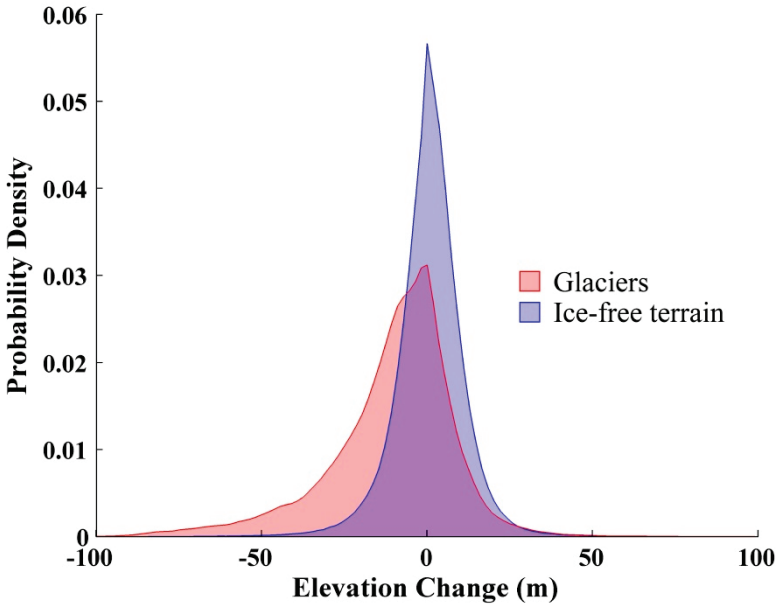

Figure 2.1. Probability density distributions for all pixels in the 2006 minus 1974 elevation change maps obtained via DEM differencing, separated into glacial ice terrain and surrounding ice-free terrain groups. The glacial terrain distribution has mean = −10.9 m, median = −7.3 m, and σ = 19.7 m. By comparison, the ice-free terrain distribution has mean = 0.7 m, median = 0.9 m, and σ = 10.9 m. Nonzero elevation changes in the ice-free terrain distribution are likely caused by a combination of actual changes such as landslides, along with intrinsic elevation error associated with stereophotogrammetric methods used to create the DEMs.

## 2.3 Results

Probability density plots of regional elevation change between the years 1974 and 2006 yield a negatively skewed distribution for glaciers with a mean of −11 m and a standard deviation of 20 m, reflecting the approximate span of ice surface lowering. The surrounding ice-free terrain shows a narrower distribution centered near zero, with a mean of 0.7 m and a standard deviation of 10 m (Figure 2.1). Nonzero elevation change values in the ice-free terrain distribution (blue region, Figure 2.1) are likely caused by a combination of actual changes such as landslides, errors caused by clouds, and other intrinsic errors associated with stereophotogrammetric methods used to create the DEMs.

All clean, debris, and calving glaciers investigated here for change during the 32-year timespan show predominate lowering and retreat of ice surfaces (Figure 2.2 and Figure 2.3). Individual glacier change statistics are also given in Table S2.2, including ice volume changes, spatially averaged thickness changes, and geodetic mass balances.

The relatively consistent negative mass balance trend includes both clean and debris-covered glaciers. Further insight into the ice-loss patterns can be obtained by examining the elevation change maps (Figure 2.3). Most clean glaciers are retreating and exhibit thinning near their toes. Conversely, the debris-covered glaciers exhibit irregular patterns of elevation loss in their ablation area. Several smaller debris-covered glaciers have varying amounts and distributions of debris and show different patterns of thinning. Some glaciers show the greatest thinning near their toes, others exhibit downwasting in midsection of the glacier, and still others display

scattered ice-loss features. Ice loss is greatly enhanced for several glacier toes terminating in moraine-dammed lakes.

The mean (area-weighted) geodetic mass balance for the selected glaciers (Figure 2.2, outlined in blue) is estimated to be −5.4 ± 1.6 m w.e. for the period 1974 to 2006. Averaged over the 32-year timespan, this yields an annual mass balance of −0.17 ± 0.05 m w.e. $yr^{-1}$. Clean glaciers comprise 61% (221 ± 11 $km^2$*)* of the total studied glacierized area (365 ± 12 $km^2$ for 21 glaciers) and have contributed 46% (1.09 ± 0.4 $km^3$*)* to the total ice volume loss with a mass balance of −0.13 ± 0.06 m w.e. $yr^{-1}$. The debris glaciers comprise 21% (78 ± 4 $km^2$*)* of the total glacierized area and have contributed 24% (−0.55 ± 0.4 $km^3$*)* to the total ice volume loss with a mass balance of −0.19 ± 0.11 m w.e. $yr^{-1}$. Calving glaciers comprise 18% (66 ± 3 $km^2$*)* of the total glacierized area and have contributed 30% (−0.70 ± 0.3 $km^3$*)* to the total ice volume loss with a mass balance of −0.28 ± 0.10 m w.e. $yr^{-1}$.

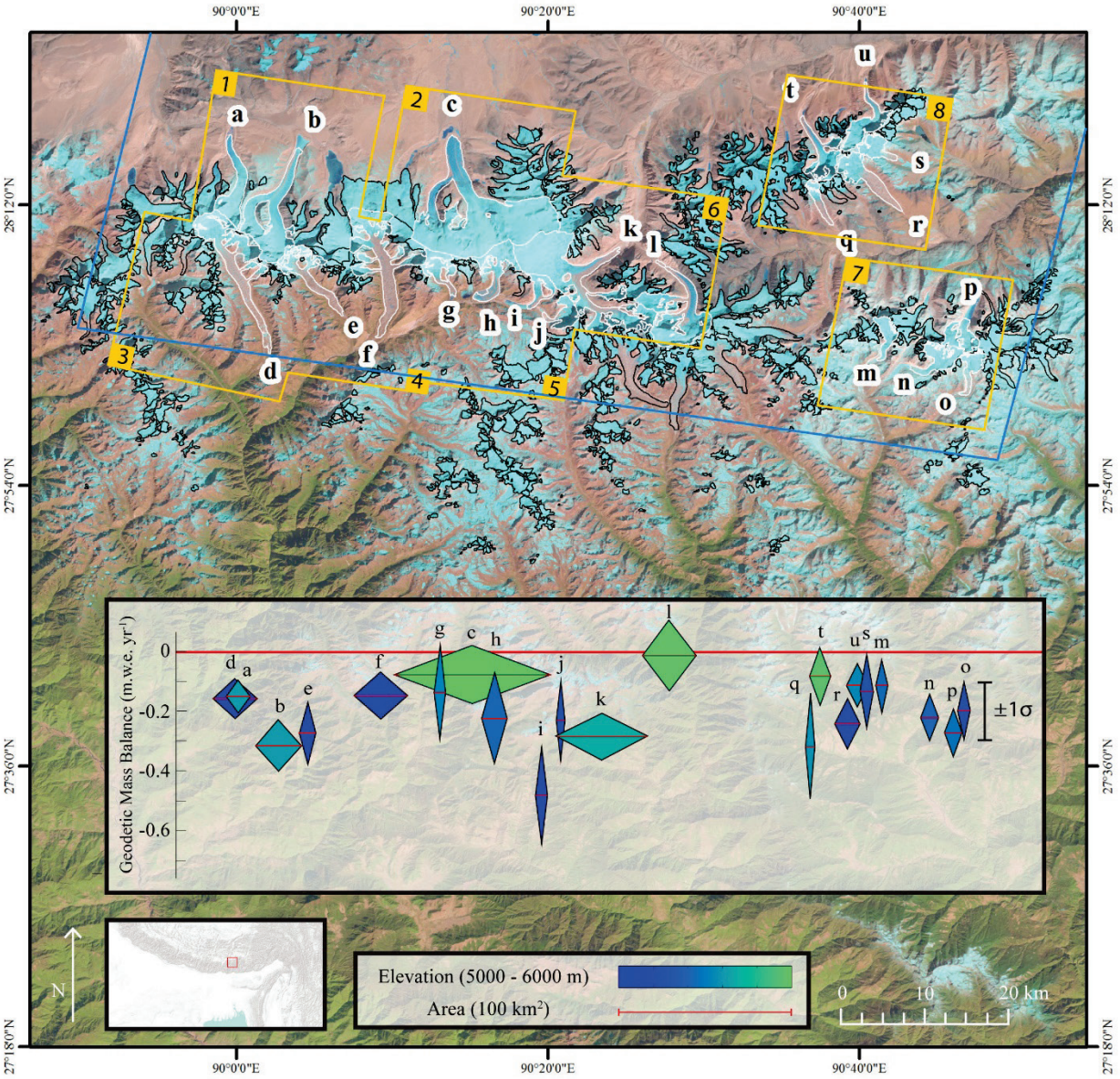


Figure 2.2. Landsat 8 image showing study region located in the eastern Himalayas and Tibetan Plateau. Black outlines identify all glaciers in the region, while white outlines denote glaciers used in this study, identified by letters a–u. Glacier outlines were downloaded from the ICIMOD mountain geoportal. Orange outlines indicated extent of extracted 1974 Hexagon DEMs; blue line indicates extent of the 2006 ASTER DEM. Inset: annual geodetic mass balances for selected glaciers during the 1974 to 2006 period (2006 ASTER DEM minus 1974 Hexagon DEMs), where each diamond represents a glacier. Central red lines are geodetic mass balances for each glacier in m w.e. $yr^{-1}$ (meters water equivalent per year). Diamond widths are proportional to total glacier area, heights indicate ±1 standard error (SEM) uncertainty, and colors specify mean glacier elevations. Thick red line indicates zero change.

## 2.4 Discussion Regional glacier change

The regional mass budget result of −0.17 ± 0.05 m w.e. $yr^{-1}$ from 1974 to 2006 is less negative than other estimates derived from remote sensing over shorter time periods. For example, Gardelle et al. (2013) reported a mass budget of −0.22 ± 0.12 m w.e. $yr^{-1}$ during 1999–2011 and recalculated the Kääb et al. (2012) results to obtain −0.52 ± 0.16 m w.e. $yr^{-1}$ during 2003–2008 for the Bhutan region. Additionally, our estimate is significantly less negative compared to the 1970–2007 mass budget of 0.32 ± 0.08 m w.e. $yr^{-1}$ in the neighboring Everest region estimated by Bolch et al. (2011). We hypothesize that the shorter, more recent timespans of the Kääb et al. (2012) and Gardelle et al. (2013) studies result in more negative mass budgets due to accelerating glacier retreat in Asia since the end of the 1970s (Zemp et al., 2009). Additional influencing factors include different spatial extents covered, radar penetration uncertainties involved with SRTM data (not an issue in this study), and different methods of dealing with data gaps in accumulation zones.

Table S2.3 gives results obtained using the two different gapfilling methods in accumulation zones. Both methods yield similar geodetic mass balance values when glacier c (which has a disproportionately large region of missing data at high elevation) is not extrapolated and purely by chance add up to exactly similar values for $\Delta V$ and $\dot{b}$ in the "all" category. When glacier c is extrapolated using the limited number of contributing pixels at high elevation, it introduces significant unrealistic bias which overshadows the measured ice thickness changes of other glaciers, making the regional mass balance values unrealistically positive. This illustrates that care must be taken when extrapolating from individual elevation bands from regional profiles to avoid extrapolating large regions from a few unreliable data points.

Using a degree-day melt model, Rupper et al. (2012) estimated an area-averaged, net mass balance of −1.4 ± 0.6 m w.e. $yr^{-1}$ (averaged over the time period 1980–2000) for the entire glacierized area (glaciers and perennial snowpack) of the Bhutanese watershed. Recently published in situ measurements of −1.12 to −2.04 m w.e. $yr^{-1}$ between 2003 and 2014 for the Gangju La glacier (located approximately 15 km southwest from the toe of glacier d in Figure 2.2) agree well with the melt model results (Tshering and Fujita, 2015). Compared to the remote sensing estimates, the modeled and in situ results are significantly more negative. Though difficult to compare regional changes to local ones, Cogley (2012) suggests that the discrepancy between in situ vs. remote sensing measurements may be explained by the smaller size and lower elevations of glaciers selected for fieldwork, along with unquantified local factors such as mass gain by snow avalanching. Regarding the melt model, it does not account for the insulating effects of debris cover but does account for the albedo effects of the debris, which would lead to a significant overestimation of modeled melt over debris-covered glaciers. For clean-ice glaciers and perennial snow, the modeled net mass balance is considerably less negative, −0.3 ± 0.2 m w.e. $yr^{-1}$. This latter value is more consistent with our geodetic mass balance of −0.17 ± 0.05 m w.e. $yr^{-1}$ presented here, yet still on the high end. Taken together, the remote sensing data support a more conservative model scenario of future glacierized area loss and meltwater flux change, highlight the benefit of informing modeling and in situ approaches with remote sensing, and exemplify the need for further understanding of these discrepancies.

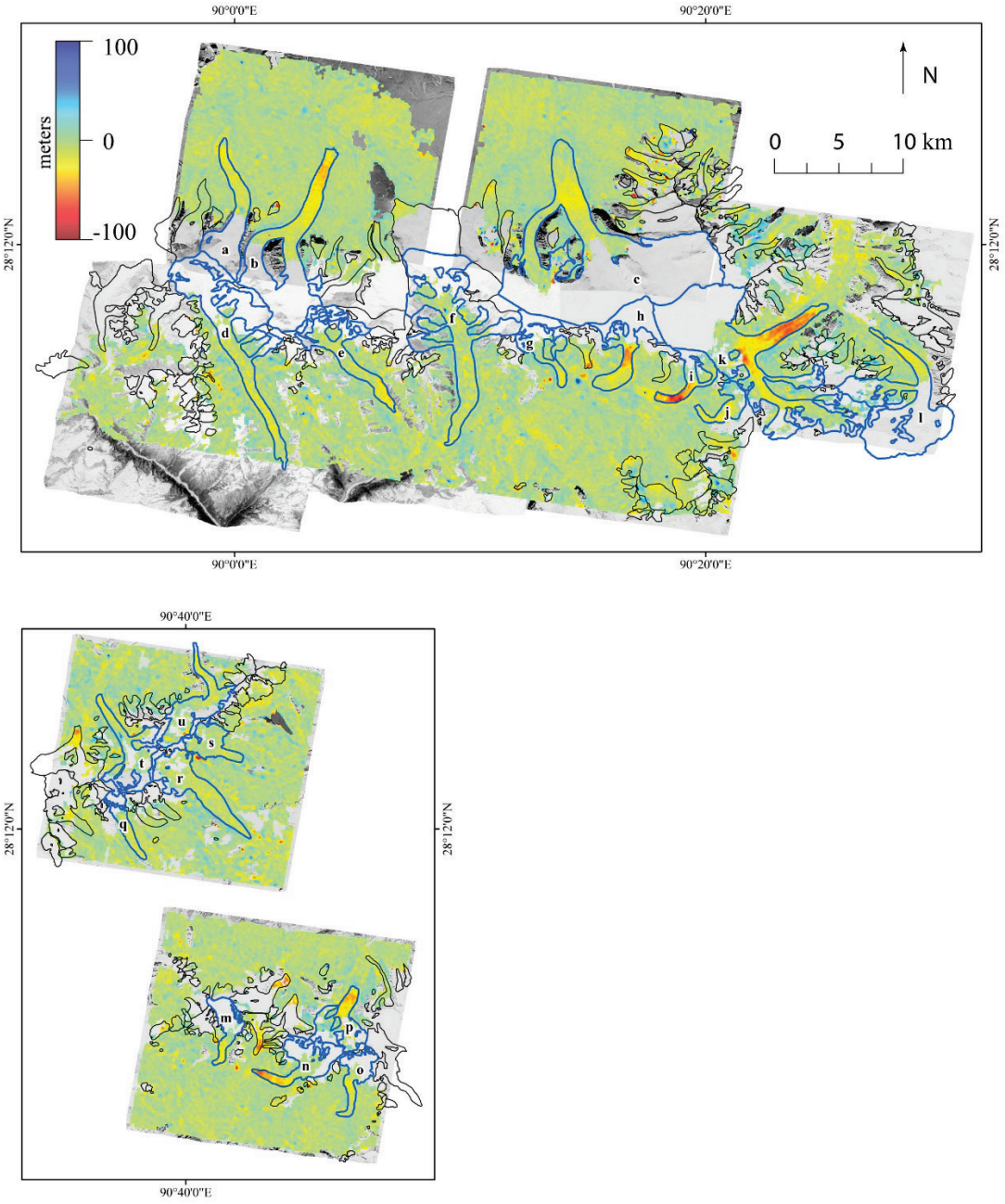


Figure 2.3. Elevation change maps for 2006 minus 1974. Blue outlines denote glaciers used in this study, identified by letters a–u. Note regions of missing data in glacier accumulation zones, where the stereo-matching algorithm failed due to poor radiometric contrast and oversaturation caused by snow cover. Glaciers a and b exhibit thinning near their toes, while glacier c is thinning at the transition point between a steep slope and nearly flat terrain. Three large debris-covered glaciers (d–f) show somewhat irregular patterns of thinning due to downwasting. Glaciers g–j (located in the Lunana region of Bhutan where a 1994 fatal GLOF event occurred) show significant thinning and retreating of glacier toes, which have contributed to the growth of unstable moraine-dammed proglacial lakes (glaciers g, h, and i are classified as calving glaciers in this study). Glacier k shows the greatest ice volume loss in the study region. Glaciers m–p are located in eastern Bhutan and also show significant downwasting and retreat. Glaciers q–u are the most northeastern, are mostly debris covered, and show a moderate rate of thinning.

### 2.4.2 Glacier dynamics

The elevation change maps presented in Figure 2.3 reveal a variety of decadal-scale glacier change patterns. Two north-flowing clean glaciers (a and b) appear to be retreating, losing ice near their toes as most simple glacier models predict. Another large north-flowing clean glacier has experienced thinning at the transition point between a steep slope and nearly flat terrain (glacier c). The downstream "piedmont" portion of the glacier spilling onto flat terrain has not thinned as much, suggesting it is dynamically decoupled from the thinning steeper glacier portion above. The thinning pattern may also be influenced by a decrease in mass flux of the smaller confluence glacier. This would result in thinning of the ice fall at the confluence, thus strengthening the disconnect between upper and lower reaches of the glacier. The observed decoupling of the "piedmont" tongue may indicate potential for the onset of proglacial lake formation, because decreasing flow velocities and increased mass losses can induce the formation and expansion of glacial lakes under favorable topographic conditions (Thakuri et al., 2015). Modeled bed overdeepenings in this region also suggest that gently sloping thick glacier tongues of these north-flowing glaciers (including glacier c) have high potential for lake formation and enlargement (Linsbauer et al., 2016). Other glaciers terminating in nearly flat valleys have already begun to form such lakes, which can become highly hazardous due to GLOF potential. In the Lunana region for example, the proglacial lake Lugge Tsho (located at the toe of glacier i in Figure 2.2 and Figure 2.3) burst on 6 October 1994, resulting in the deaths of 21 people (Watanabe and Rothacher, 1996).

Three large south-flowing glaciers (d, e, and f) are heavily debris covered. Modern satellite imagery viewed in Google Earth reveals melt ponds and associated ice cliffs on the surfaces of these glaciers, which can explain their irregular downwasting patterns. Recent studies have

shown a disproportionately large amount of melting occurs along exposed ice cliffs compared to debris-covered regions. Supraglacial melt ponds are formed as the ice cliffs retreat, and the ponds interact with englacial conduits to enhance melting (Immerzeel et al., 2014a; Reid and Brock, 2014; Sakai and Fujita, 2010). Ice cliff formation is still not well understood, but possible mechanisms include collapse of englacial voids (initially created by drainage of melt ponds), aspect-induced differences in solar radiation, and debris slope slumping (Benn et al., 2012). A recent grid-based model of supraglacial ice cliff backwasting on debris-covered glaciers has confirmed the importance of cliffs as contributors to total mass loss of debris-covered glaciers and shown that melt is highly variable in space, suggesting that simple models provide inaccurate estimates of total melt volumes (Buri et al., 2015). Miles et al. (2016) also showed that supraglacial ponds efficiently convey atmospheric energy to a glaciers interior, promoting the downwasting process.

Thorthormi glacier (glacier h) is a distinct example of a debris-covered calving glacier, with ice loss due to calving and thermal undercutting apparently far outweighing downwasting associated with ice cliffs and melt ponds. The largest thickness changes are occurring on the steep midsection portion of the glacier, which may indicate a dynamic thinning response to calving as ice is lost at the glacier toe. As ice is removed from the glacier and stored in the lake, areas once covered by ice are now replaced by water, resulting in small thickness changes observed near the glacier toe. This is consistent with observations of the rapid growth of the Thorthormi lake, which is a potential GLOF hazard (Fujita et al., 2008), and suggests that ice loss is slightly underestimated by DEM differencing methods for these calving glaciers.

Glacier k has an anomalously large ice volume loss (~0.5 $km^3$), accounting for approximately 20% of the total ice volume loss of the 21 analyzed glaciers. No stereomatching or

georeferencing problems are apparent, and Gardelle et al. (2013) show a similar large ice loss during a different timespan (1999–2011) using different elevation data (SRTM and SPOT5); thus our result is not likely due to image processing errors. It is currently unclear why this glacier has undergone such a comparatively large ice loss; however, glacier k has a large, wide accumulation area to the west (Figure 2.2). One possible explanation could be that glacier thinning has caused the ice divide between glaciers k and c to shift and change position over time, thus decreasing the accumulation area and reducing the supply of ice mass for glacier k, causing a drastic reduction in volume.

### 2.4.3 Glacier types comparison

Profiles of ice thickness change vs. elevation show distinct thinning patterns for each glacier type (Figure 2.4). The clean-ice thickness change profile appears slightly positive in the accumulation zones, and thinning generally becomes greater with decreasing elevation, reaching approximately −40m of thinning over the 32-year timespan at 5000 m elevation, then exhibiting less thinning near glacier toes. First, glacier k does not contribute to the lowest elevation bin, which results in smaller thickness change since glacier k is dominantly affecting the regional thinning profile (see Figure S2.2). While some of the lower thinning rates may be due to insulating effects of more comprehensive debris cover on glacier toes, we conclude that the primary factor is that the toes are thinner to begin with and thus have less ice to lose. Our 1974 glacier outlines include glacier toes which were already thin at that time, and we expect thinning from 1974 onwards to be smaller near the toes. The debris-covered thickness change profile starts near 0 m ice loss at 5700 m elevation, with thinning rates increasing steadily towards lower elevations, reaching around −20 m of thinning at 4200 m. The calving-glaciers thickness profile is somewhat erratic,

fluctuating between −10 and −50 m of ice loss from 6000 m down to 4400 m elevation, as several glaciers residing at different elevations have undergone significant ice loss due to calving.

Although elevation distributions of ice loss differ between glacier types, overall geodetic mass balance values for both debris-covered and clean glacier groups are similar in magnitude, with overlapping uncertainties (−0.13 ± 0.06 for clean ice and −0.19 ± 0.11 m w.e. $yr^{-1}$ for debris covered). This supports previous findings of similar regional averaged thinning rates between glacier types in the Himalayas over more recent ∼10-year time frames (Gardelle et al., 2013; Kääb et al., 2012). We hypothesize that the similar magnitudes of ice loss can largely be explained by contrasting glacier hypsometries. In this region, most clean-ice glaciers have large accumulation zones, while most debris-covered glaciers have small accumulation zones. Since the debris-covered glaciers have greater proportions of ice residing at lower elevations, any given increase in temperature melts and thins a larger portion of debris-covered glacier area compared to clean-ice glacier area. As Figure 2.4 illustrates, the magnitude of thinning for debris-covered glaciers is significantly less that for clean-ice glaciers, presumably due to insulating effects of the debris. However, integrating this smaller thinning across comparatively larger regions at lower elevations yields similar and even more negative mass balance values compared to the clean-ice glaciers. While these hypsometry effects are certainly not universal, further investigations are needed to determine their prevalence in other regions. Additionally, our measured geodetic thinning is influenced by both mass balance processes and ice dynamics (emergent velocities). Kääb et al. (2005) showed that the large north-flowing clean-ice glaciers in Bhutan have flow velocities up to 200 m $yr^{-1}$, while south-flowing debris-covered glaciers are nearly stagnant. Thus, ice advection down glacier is significantly greater for these clean-ice glaciers, making the

apparent mass balance less negative in the ablation zones of the clean-ice glaciers as compared to the debris-covered glaciers.

Recent studies have identified relationships between glacier slope, surface velocity, and thinning rates. For example in the Langtang Himal (Nepal), zones with low surface flow velocities and low slopes tend to be associated with dynamic decay of surface features, and local accelerations in thinning for these regions correlate with development of supraglacial ice cliffs and lakes (Pellicciotti et al., 2015; Ragettli et al., 2016). We find a similar relationship in Bhutan, especially regarding glaciers d, e, and f, which have large, flat, debris-covered ablation zones, near-stagnant flow velocities (Kääb, 2005), and supraglacial ponds. Melt ponds, ice cliff dynamics, and englacial conduits likely play a significant role in enhancing melt for these glaciers. Additionally, longwave radiative flux change for a given temperature change is greater in regions at warmer temperatures. This may further enhance melt for lower elevation debris-covered glaciers, given that longwave atmospheric radiation is the most important heat source for melting of snow and ice (Ohmura, 2001).

Some glaciers in the region are partially debris covered, with greater proportions of debris-covered area near glacier toes and lower proportions of debris-covered area moving up the glacier (glaciers h and o). The mid-glacier regions with less debris-covered area exhibit greater thinning; this may be a result of enhanced ice melt due to the albedo effect of supra-glacial debris cover that is thin enough to not provide considerable insulation effects and the fact that bare ice melts at a faster rate than debris-covered ice at the same elevation. Modeling studies in the Khumbu region indicate that debris-covered tongues will detach from their accumulation areas in the future, leading to greater future melt rates (Rowan et al., 2015; Shea et al., 2015).

Calving glaciers in the study area have more negative mass balances compared to both types of land-terminating glaciers (both clean and debris covered) and represent a disproportionately large amount of the total ice volume loss relative to their aerial extent. For these glaciers, large moraine-dammed lakes have formed as a result of expansion and merging of smaller supraglacial lakes, and glacial meltwater is effectively stored adjacent to glacier termini (Basnett et al., 2013). As changing climate increases glacier melt, the resulting lakes interact with remaining ice to further enhance melt through thermal undercutting processes independent of climate (Sakai et al., 2009; Thompson et al., 2012). This positive feedback mechanism has important implications for future hazard and water resource issues, especially for glaciers terminating in flat valleys with potential lake-forming topographies. Gardelle et al. (2011) estimated that in the eastern HKH (India, Nepal, and Bhutan) glacial lakes have grown continuously between 1990 and 2009 by 20 to 65%. Thus, these glacier-lake systems not only represent GLOF hazards but also will likely play a key role in the Himalayan ice mass budget during the coming decades.

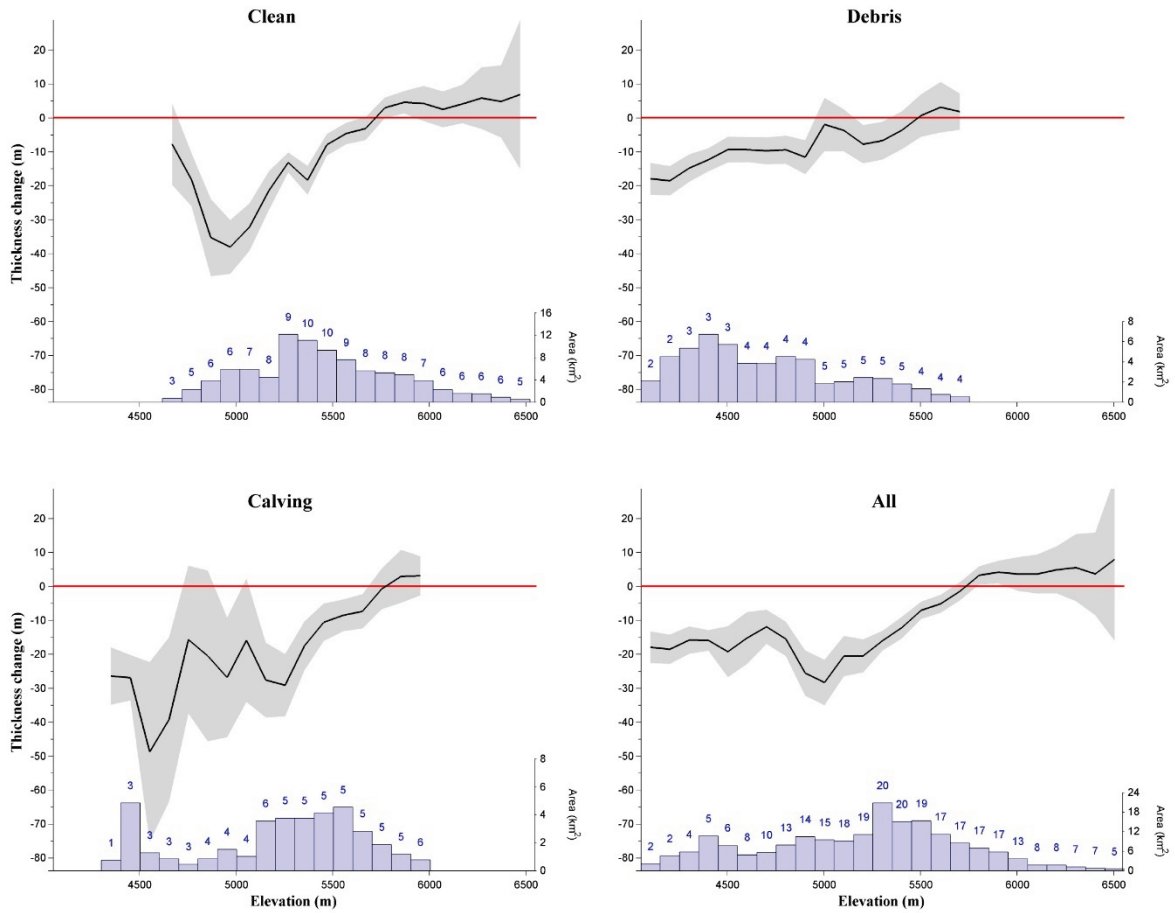


Figure 2.4. Ice thickness change profiles for clean ice, debris covered, calving, and all glaciers combined (rates of change can be obtained by dividing values on the vertical axis by 32 years). Thickness change pixels are separated into 100 m bands; black lines are the mean, and the grey shaded regions represent the standard error of the mean estimated as $\sigma_z/\sqrt{n_z}$ , where $\sigma_z$ is the standard deviation of elevation change for each band and $n_z$ is calculated using Eq. (2.5). The glacier area (km$^2$) contained in each band is indicated by the blue histogram bars, and the number of glaciers contributing to each elevation band is shown by the blue number above each bin. Note that the histogram bars do not include extrapolated data.

## 2.5 Conclusions

We applied a new DEM extraction pipeline toward Hexagon spy satellite imagery and ASTER data to compute glacier thickness changes over a multi-decadal timescale across a large glacierized area (~365 km$^2$) in the eastern Himalayas. The consistency of the DEM extraction method provided high geolocational accuracy and minimized elevation biases when differencing the DEMs. In addition, the long timespan (1974–2006) allowed for effective separation of glacier

change from noise inherent in the remote sensing methods. Results provide insight into the complex dynamics of glaciers in the monsoonal Himalayas and highlight similarities and differences in the decadal responses of clean, debris-covered, and calving glaciers. Though regional thinning and ice loss is apparent, individual glacier dynamics vary widely depending on elevation, hypsometry, extent and thickness of debris, and potential for calving in proglacial lakes. Both clean and debris-covered glaciers show similar negative geodetic mass balances, while lake-terminating glaciers have geodetic mass balances more negative than land-terminating glaciers. The more negative mass balances of lake-terminating glaciers suggest that calving and thermal undercutting are important mechanisms contributing to ice loss in the region and highlight the rapidly growing hazard potential of GLOFs in the monsoonal Himalayas. Overall, these results enhance understanding regarding potential glacier contribution to sea-level rise, impact on hydrological resources, and hazard potential for high mountain regions and downstream populations in Asia.

## 2.6 Acknowledgements

This work was funded by NSF grants 1256551 and 1304397 to S.R. and a Rocky Mountain NASA Space Grant Consortium (RMNSGC) fellowship to J.M.M. J.M.S. acknowledges support by the NSF grant EAR-1304351 and by the Lamont Climate Center. We thank the USGS, NASA, and Japan Space Systems for providing access to Hexagon and ASTER data and gratefully acknowledge B.Bickmore, J. Radebaugh, E. Berthier, J. M. Shea, T. Nuimura, and T. Pieczonka for their valuable feedback and constructive comments on the manuscript.

## 2.7 Supplementary

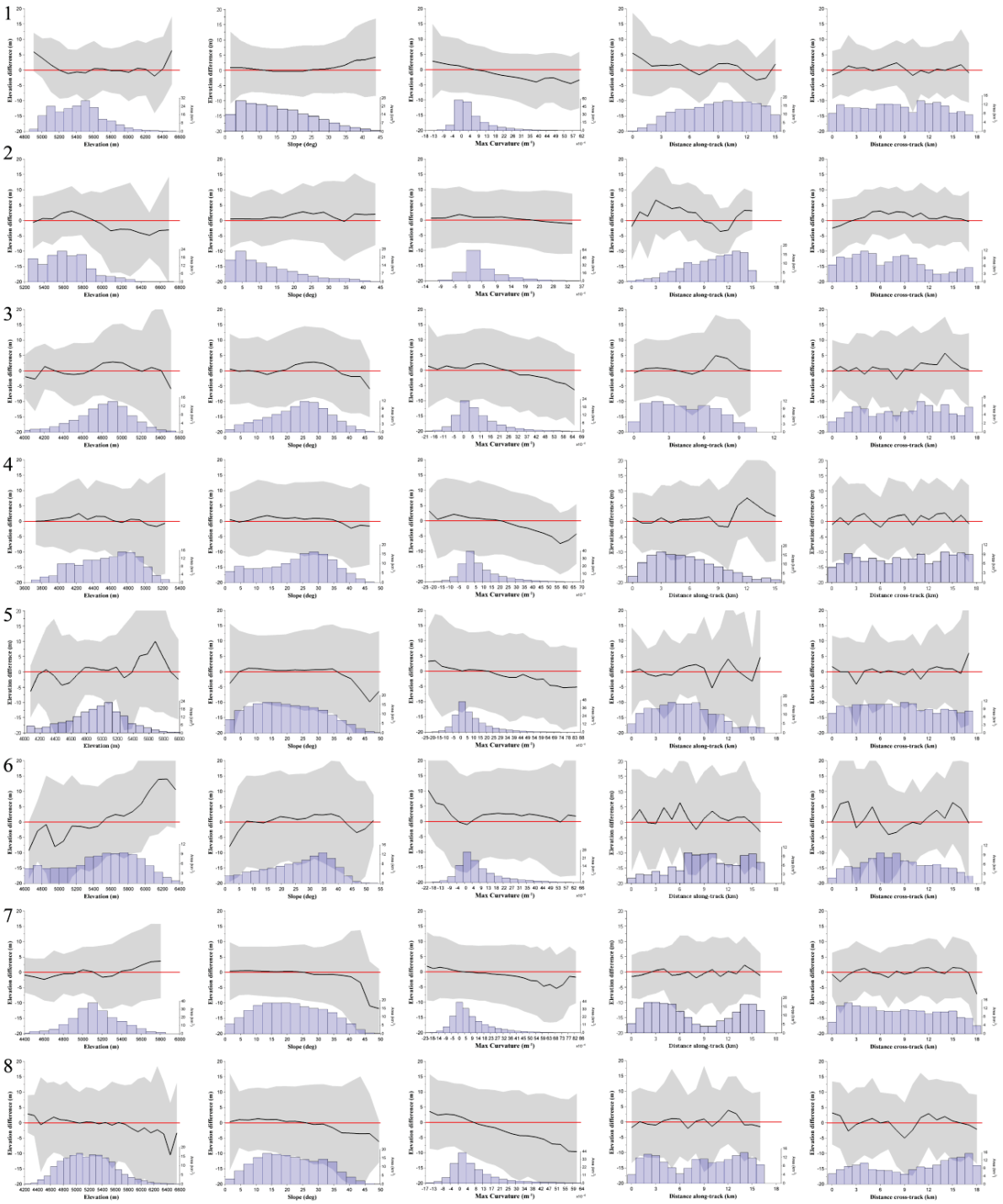

Figure S2.1. Plots of elevation change vs. elevation, slope, maximum curvature, and ASTER along-track and cross-track directions for assumed stable terrain in each of the 8 Hexagon DEM regions given in Table S2.1. Black curves and grey shaded regions indicate the mean and standard deviation of each bin, respectively. The area ($km^2$) contained in each bin is indicated by the blue histogram bars, calculated as the number of pixels per bin * pixel resolution$^2$.

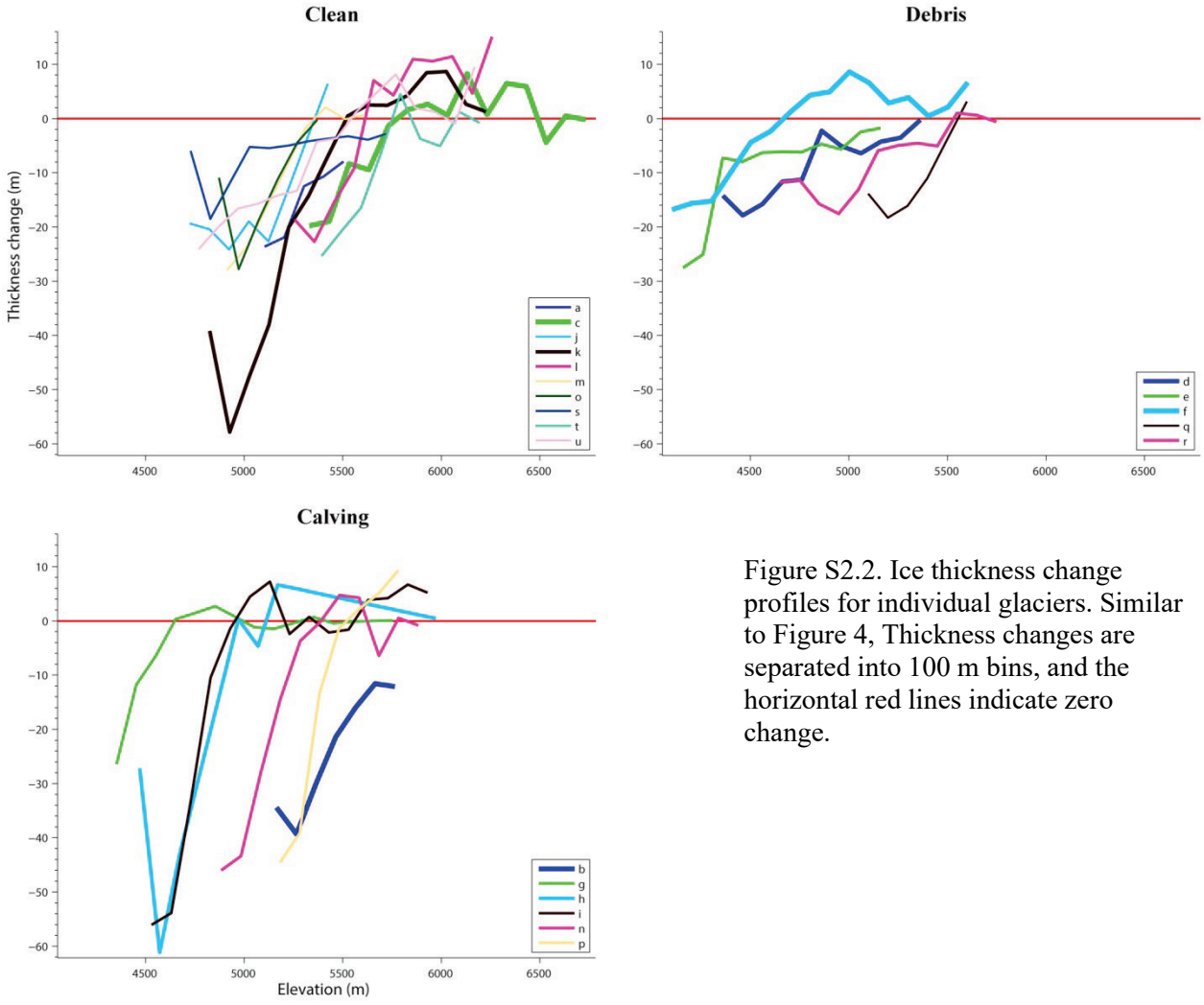


Figure S2.2. Ice thickness change profiles for individual glaciers. Similar to Figure 4, Thickness changes are separated into 100 m bins, and the horizontal red lines indicate zero change.

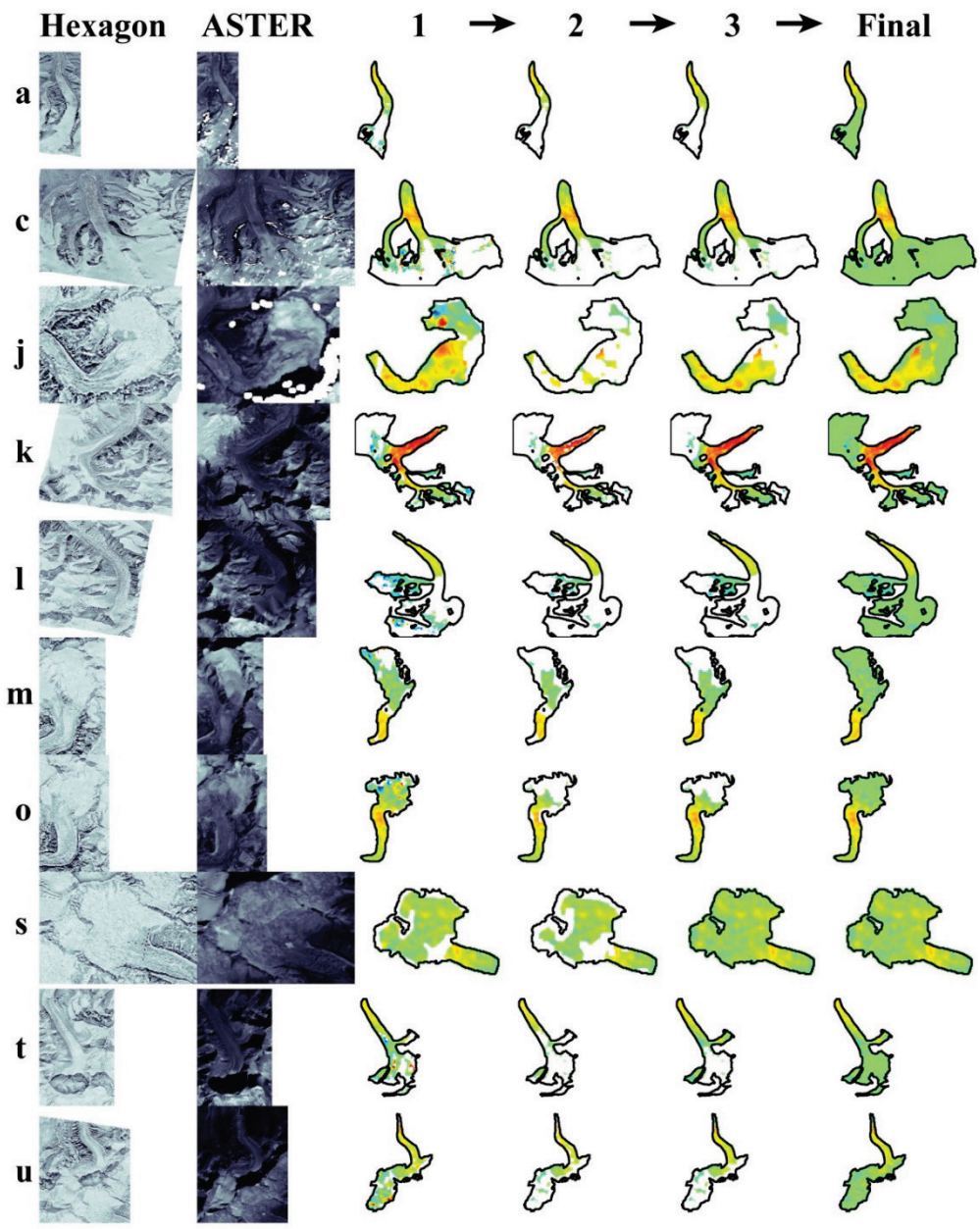


Figure S2.3. Hexagon and ASTER images, along with thickness change map processing stages for clean ice glaciers. Stage 1: raw elevation change maps; stage 2: after excluding erroneous pixels; stage 3: after interpolating gaps smaller than 2 $km^2$, and stage 4: after filling remaining accumulation zone gaps with zero elevation change.

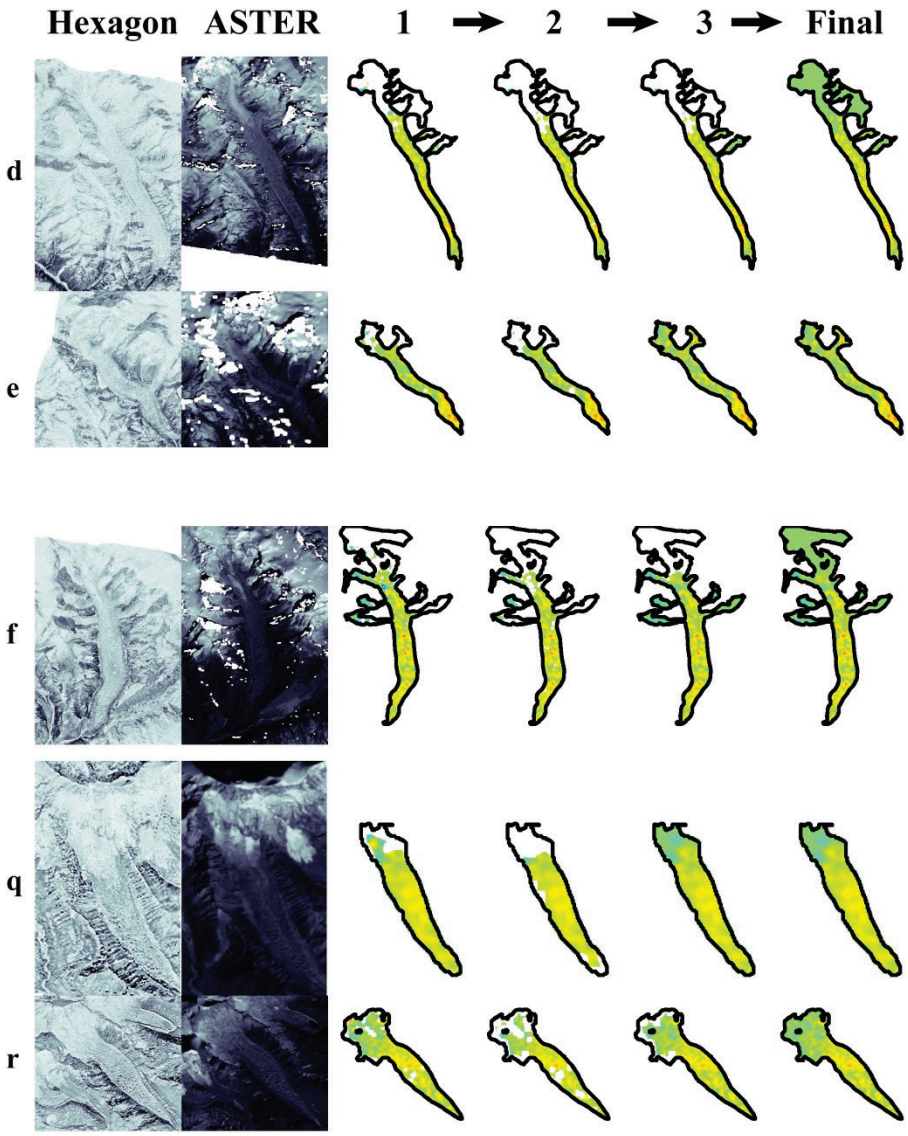


Figure S2.4. Same as Figure S2.3, but for debris-covered glaciers.

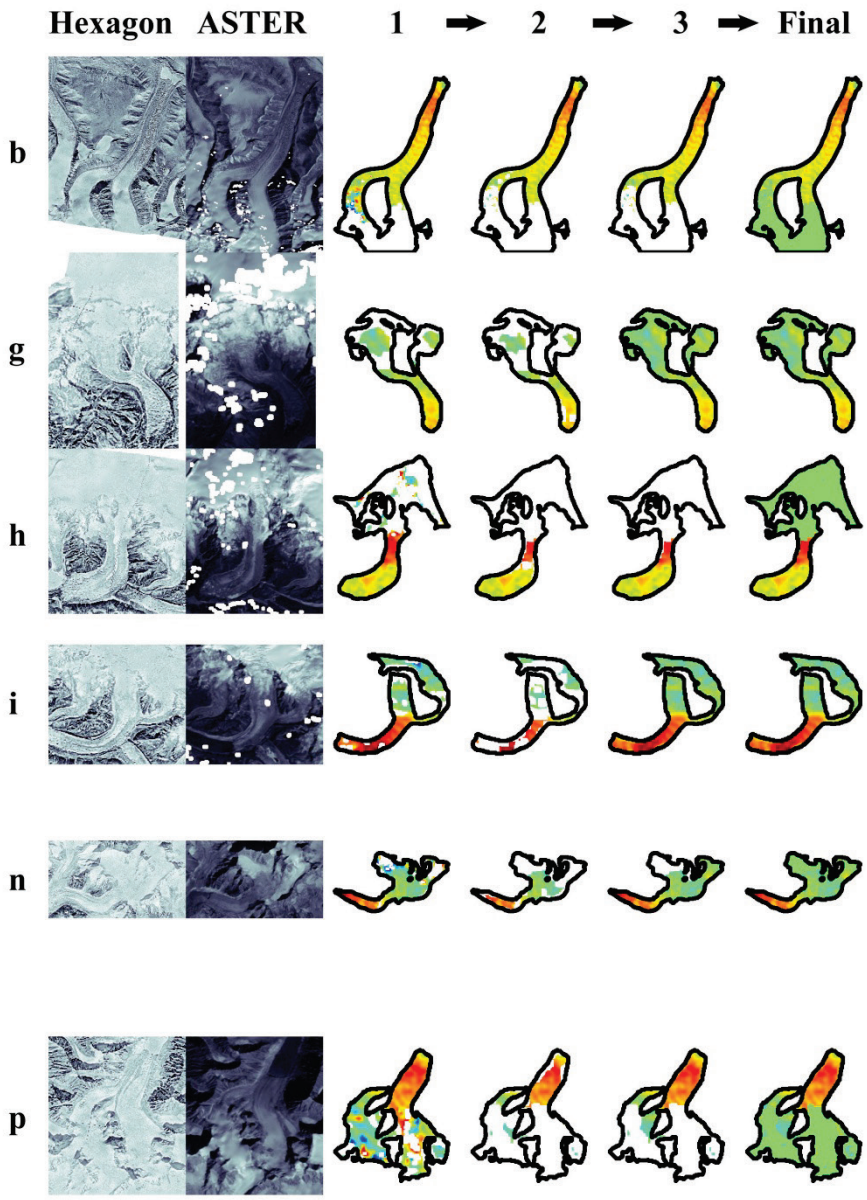


Figure S2.5. Same as Figure S2.3, but for calving glaciers.

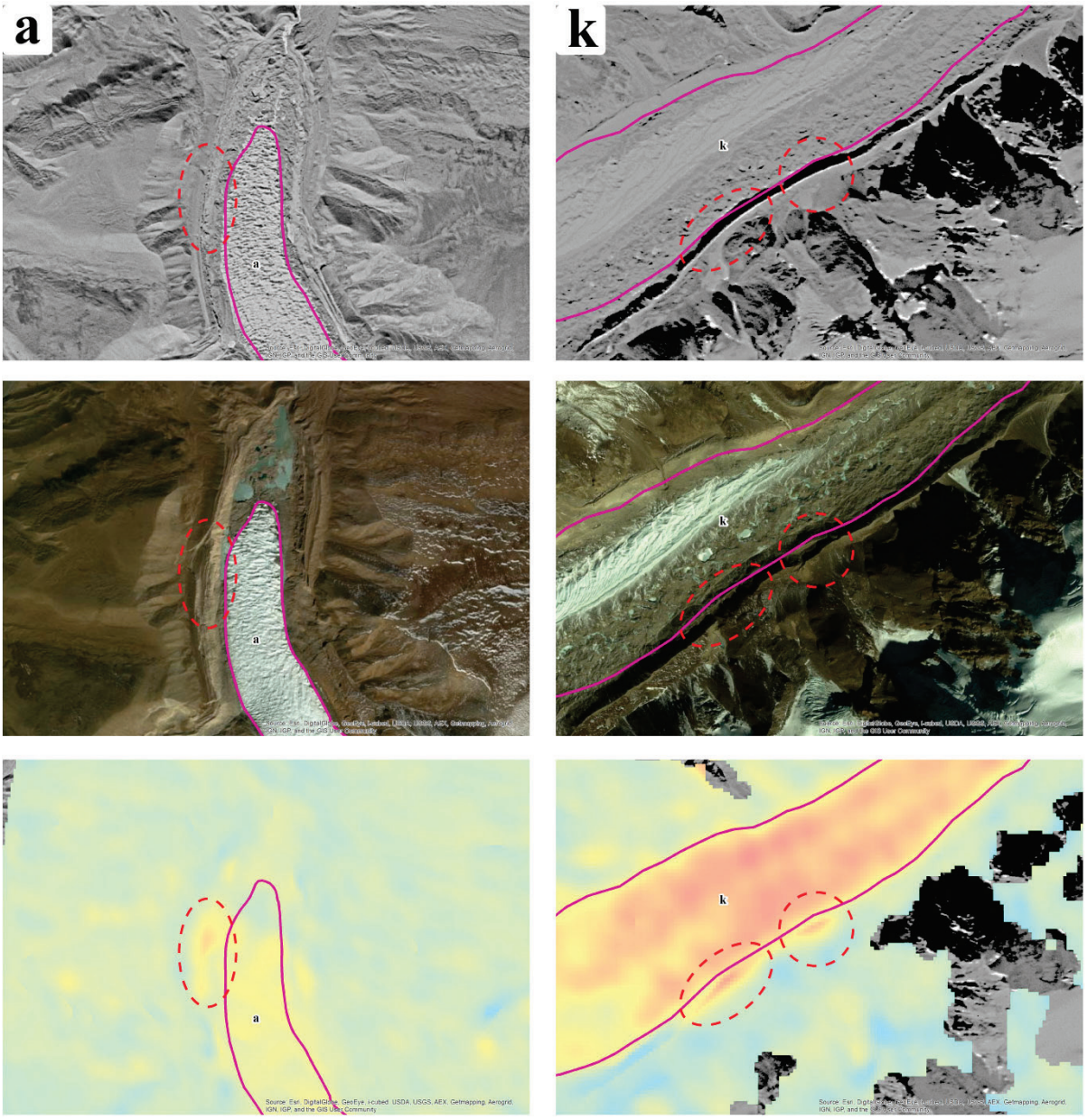


Figure S2.6. Two examples of unstable moraine ridges. Red dotted ellipses indicate sections which have collapsed near glaciers a and k.

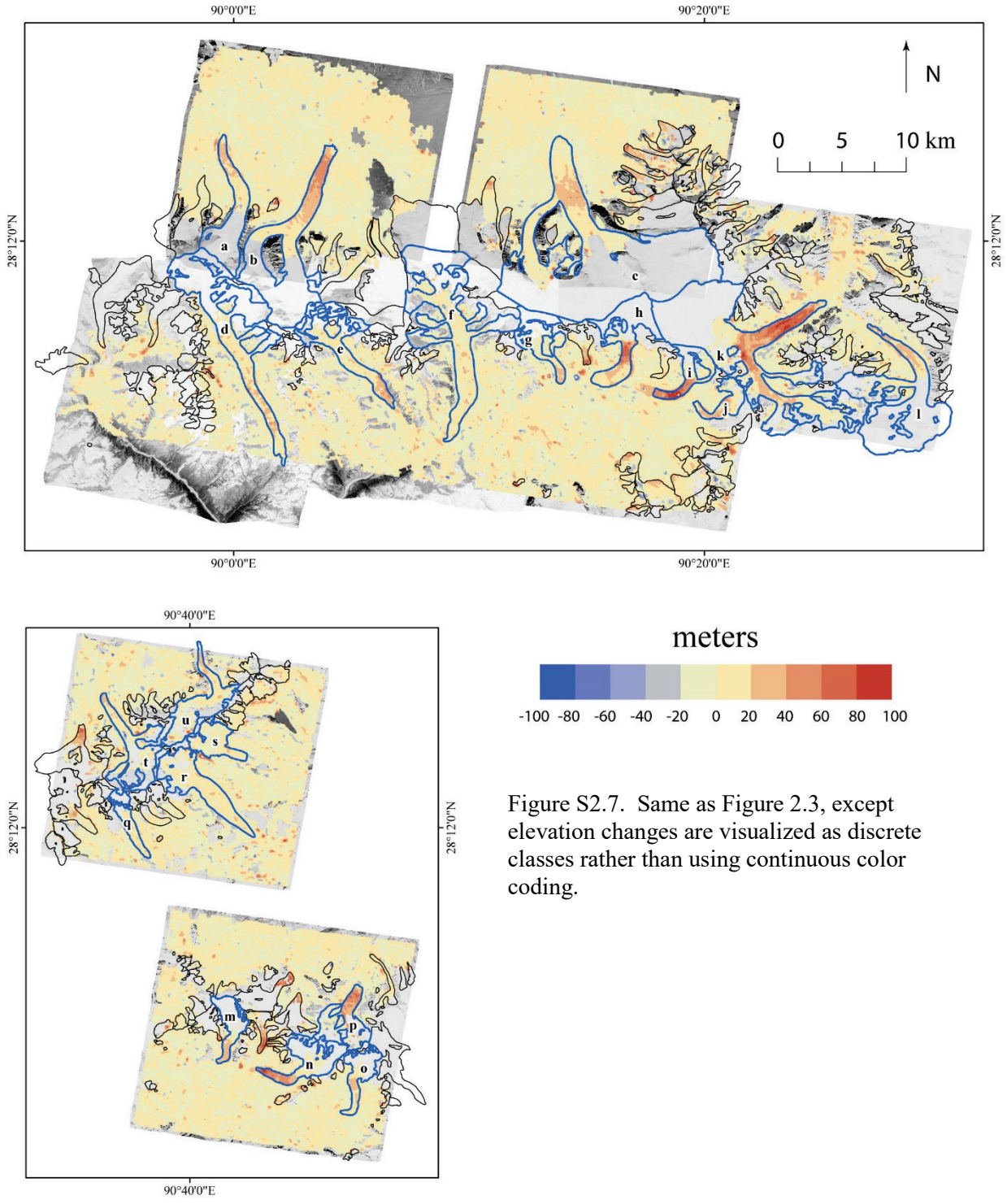


Figure S2.7. Same as Figure 2.3, except elevation changes are visualized as discrete classes rather than using continuous color coding.

Table S2.1. Vertical accuracy statistics[a] of Hexagon DEMs relative to the 2006 ASTER DEM (meters)

| ID | Lon | Lat[b] | $RMSE_z$ | Mean | Median | NMAD[c] | STD | 68.3%Q | 95%Q |
|---|---|---|---|---|---|---|---|---|---|
| **1** | 90.05 | 28.25 | 8.1 | 0.5 | 0.7 | 6.4 | 8.1 | 6.8 | 15.9 |
| **2** | 90.26 | 28.24 | 8.6 | 1.2 | 1.3 | 7.3 | 8.5 | 7.5 | 15.6 |
| **3** | 89.97 | 28.09 | 11.5 | 1.4 | 1.4 | 8.7 | 11.5 | 9.4 | 22.5 |
| **4** | 90.12 | 28.10 | 11.6 | 0.7 | 0.8 | 9.2 | 11.6 | 9.8 | 21.9 |
| **5** | 90.27 | 28.08 | 12.8 | 0.6 | 1.0 | 8.7 | 12.8 | 9.4 | 24.4 |
| **6** | 90.42 | 28.14 | 14.9 | 1.6 | 1.5 | 11.6 | 14.8 | 12.7 | 30.3 |
| **7** | 90.73 | 28.05 | 8.9 | 0.1 | 0.6 | 6.6 | 8.9 | 7.0 | 17.8 |
| **8** | 90.66 | 28.25 | 11.8 | 0.4 | 1.1 | 8.9 | 11.8 | 9.5 | 22.5 |

[a] Over assumed stable terrain (i.e. excluding glaciers). [b] Center of each Hexagon DEM region.
[c] Normalized median absolute deviation. [d] Hole interpolation max area ($km^2$).

Table S2.2. Glacier Change Statistics

| Glacier ID | a | b | c | d | e | f | g |
|---|---|---|---|---|---|---|---|
| Longitude (deg) | 89.99 | 90.04 | 90.25 | 89.99 | 90.07 | 90.15 | 90.21 |
| Latitude (deg) | 28.21 | 28.18 | 28.19 | 28.16 | 28.14 | 28.16 | 28.13 |
| Mean Elevation (m) | 5710 | 5712 | 6183 | 4940 | 4565 | 4853 | 5012 |
| 1974 Area ($km^2$) | 13.4 ± 1.3 | 25.0 ± 2.5 | 86.2 ± 8.6 | 23.5 ± 2.3 | 8.8 ± 0.9 | 30.1 ± 3.0 | 5.4 ± 0.5 |
| $\Delta V$ ($km^3$) | -0.08 ± 0.03 | -0.29 ± 0.07 | -0.26 ± 0.31 | -0.14 ± 0.06 | -0.09 ± 0.03 | -0.17 ± 0.09 | -0.03 ± 0.03 |
| $\Delta V_{extrap}$ ($km^3$) | -0.05 ± 0.03 | -0.27 ± 0.07 | 0.09 ± 0.31 | -0.20 ± 0.06 | -0.09 ± 0.03 | -0.18 ± 0.09 | -0.03 ± 0.03 |
| $\bar{h}$ (m) | -5.6 ± 2.2 | -12.0 ± 3.2 | -3.0 ± 3.6 | -6.1 ± 2.5 | -10.3 ± 4.0 | -5.5 ± 2.9 | -5.2 ± 5.9 |
| $\dot{b}$ (m.w.e.) | -0.15 ± 0.06 | -0.32 ± 0.09 | -0.08 ± 0.10 | -0.16 ± 0.07 | -0.27 ± 0.11 | -0.15 ± 0.08 | -0.14 ± 0.16 |
| Data coverage (%) | 39 | 48 | 28 | 49 | 100 | 68 | 100 |
| Debris coverage (%) | 1 | 6 | 3 | 41 | 37 | 44 | 16 |
| Calving (y/n) | n | y | n | n | n | n | y |

| h | i | j | k | l | m | n |
|---|---|---|---|---|---|---|
| 90.27 | 90.33 | 90.35 | 90.39 | 90.47 | 90.7 | 90.75 |
| 28.13 | 28.11 | 28.09 | 28.1 | 28.08 | 28.06 | 28.04 |
| 5486 | 5151 | 5154 | 5749 | 6133 | 5505 | 5450 |
| 13.8 ± 1.4 | 6.1 ± 0.6 | 5.0 ± 0.5 | 49.8 ± 5.0 | 29.7 ± 3.0 | 5.7 ± 0.6 | 9.2 ± 0.9 |
| -0.12 ± 0.08 | -0.10 ± 0.03 | -0.04 ± 0.02 | -0.52 ± 0.13 | -0.02 ± 0.13 | -0.02 ± 0.02 | -0.08 ± 0.03 |
| -0.16 ± 0.08 | -0.10 ± 0.03 | -0.08 ± 0.02 | -0.45 ± 0.13 | 0.07 ± 0.13 | -0.02 ± 0.02 | -0.09 ± 0.03 |
| -8.5 ± 5.7 | -18.3 ± 6.0 | -8.7 ± 4.8 | -10.7 ± 2.8 | -0.6 ± 4.3 | -4.4 ± 3.3 | -8.4 ± 3.1 |
| -0.23 ± 0.15 | -0.48 ± 0.16 | -0.23 ± 0.13 | -0.28 ± 0.08 | -0.02 ± 0.11 | -0.12 ± 0.09 | -0.22 ± 0.08 |
| 30 | 100 | 58 | 54 | 26 | 60 | 76 |
| 17 | 11 | 10 | 11 | 14 | 1 | 1 |
| y | y | n | n | n | n | y |

| o | p | q | r | s | t | u |
|---|---|---|---|---|---|---|
| 90.79 | 90.78 | 90.62 | 90.66 | 90.68 | 90.63 | 90.67 |
| 28.03 | 28.06 | 28.21 | 28.24 | 28.26 | 28.25 | 28.29 |
| 5216 | 5540 | 5342 | 5139 | 5304 | 6034 | 5602 |
| 5.7 ± 0.6 | 9.1 ± 0.9 | 3.1 ± 0.3 | 12.5 ± 1.3 | 6.5 ± 0.7 | 9.8 ± 1.0 | 10.2 ± 1.0 |
| -0.04 ± 0.02 | -0.09 ± 0.02 | -0.04 ± 0.02 | -0.11 ± 0.04 | -0.03 ± 0.03 | -0.03 ± 0.03 | -0.04 ± 0.03 |
| -0.07 ± 0.02 | -0.12 ± 0.02 | -0.04 ± 0.02 | -0.11 ± 0.04 | -0.03 ± 0.03 | -0.01 ± 0.03 | -0.05 ± 0.03 |
| -7.6 ± 3.4 | -10.1 ± 3.0 | -11.9 ± 6.4 | -9.1 ± 3.1 | -5.1 ± 4.4 | -3.2 ± 3.4 | -4.3 ± 2.9 |
| -0.20 ± 0.09 | -0.27 ± 0.08 | -0.32 ± 0.17 | -0.24 ± 0.09 | -0.13 ± 0.12 | -0.08 ± 0.09 | -0.11 ± 0.08 |
| 63 | 41 | 100 | 84 | 100 | 55 | 51 |
| 8 | 1 | 42 | 39 | 1 | 19 | 9 |
| n | y | n | n | n | n | n |

$\Delta V$ is ice volume change without extrapolation, $\Delta V_{extrap}$ is ice volume change after extrapolating missing data using regional data from individual elevation bands, $\bar{h}$ is the spatially-averaged elevation change of the glacier, and $\dot{b}$ is the geodetic mass balance for each glacier over the 32-year timespan.

Table S2.3 Results using different gapfilling methods

| | clean | debris | calving | all |
|---|---|---|---|---|
| **Area (km$^2$)** | 221 ± 11 | 78 ± 4 | 66 ± 3 | 365 ± 12 |
| **Area (%)** | 61 | 21 | 18 | |
| | **Assuming zero change for missing data** | | | |
| **ΔV (km$^3$)** | -1.09 ± 0.4 | -0.55 ± 0.4 | -0.70 ± 0.3 | -2.34 ± 0.6 |
| **ΔV (%)** | 46 | 24 | 30 | |
| **$\dot{b}$ (m.w.e. yr$^{-1}$)** | -0.13 ± 0.06 | -0.19 ± 0.11 | -0.28 ± 0.10 | -0.17 ± 0.05 |
| | **Extrapolating missing data using regional profiles** | | | |
| **ΔV (km$^3$)** | -0.60 ± 0.4 | -0.62 ± 0.4 | -0.77 ± 0.3 | -1.99 ± 0.6 |
| **ΔV (%)** | 30 | 31 | 39 | |
| **$\dot{b}$ (m.w.e. yr$^{-1}$)** | -0.07 ± 0.06 | -0.21 ± 0.11 | -0.31 ± 0.10 | -0.14 ± 0.05 |
| | **Assuming zero change for missing data in glacier c, extrapolating missing data for all other glaciers** | | | |
| **ΔV (km$^3$)** | -0.95 ± 0.4 | -0.62 ± 0.4 | -0.77 ± 0.3 | -2.34 ± 0.6 |
| **ΔV (%)** | 41 | 26 | 33 | |
| **$\dot{b}$ (m.w.e. yr$^{-1}$)** | -0.11 ± 0.06 | -0.21 ± 0.11 | -0.31 ± 0.10 | -0.17 ± 0.05 |

# Chapter 3: Acceleration of ice loss across the Himalayas over the past 40 years

Note: a modified version of this chapter has been published in *Science Advances*: Maurer, J., Schaefer, J., Rupper, S., Corley, A., 2019. Acceleration of ice loss across the Himalayas over the past 40 years. Science Advances 5, eaav7266. This publication also received widespread media coverage (https://scienceadvances.altmetric.com/details/62415511).

Himalayan glaciers supply meltwater to densely populated catchments in South Asia, and regional observations of glacier change over multiple decades are needed to understand climate drivers and assess resulting impacts on glacier-fed rivers. Here, we quantify changes in ice thickness during the intervals 1975–2000 and 2000–2016 across the Himalayas, using a set of digital elevation models derived from cold war–era spy satellite film and modern stereo satellite imagery. We observe consistent ice loss along the entire 2000-km transect for both intervals and find a doubling of the average loss rate during 2000–2016 [$-0.43 \pm 0.14$ m w.e. year$^{-1}$ (meters of water equivalent per year)] compared to 1975–2000 ($-0.22 \pm 0.13$ m w.e. year$^{-1}$). The similar magnitude and acceleration of ice loss across the Himalayas suggests a regionally coherent climate forcing, consistent with atmospheric warming and associated energy fluxes as the dominant drivers of glacier change.

## 3.1 Introduction

The Intergovernmental Panel on Climate Change 5th Assessment Report estimates that mass loss from glaciers contributed more to sea-level rise than the ice sheets during 1993–2010 (0.86 mm year$^{-1}$ versus 0.60 mm year$^{-1}$, respectively), yet uncertainties for the glacier contribution are three times greater (Church et al., 2013). Glaciers also contribute locally to water resources in

many regions and serve as hydrological buffers vital for ecology, agriculture, and hydropower, particularly in High Mountain Asia (HMA), which includes all mountain ranges surrounding the Tibetan Plateau (Azam et al., 2018; Lutz et al., 2014). Shrinking Himalayan glaciers pose challenges to societies and policy-makers regarding issues such as changing glacier melt contributions to seasonal runoff, especially in climatically drier western regions (Lutz et al., 2014), and increasing risk of outburst floods due to expansion of unstable proglacial lakes (Harrison et al., 2018). Yet, substantial gaps in knowledge persist regarding rates of ice loss, hydrological responses, and associated climate drivers in HMA (Azam et al., 2018).

Mountain glaciers are known to respond dynamically to a variety of drivers on different time scales, with faster response times than the large ice sheets (Oerlemans and Fortuin, 1992; Roe et al., 2017). In the Himalayas, in situ studies document significant interannual variability of mass balances (Vincent et al., 2013; Wagnon et al., 2013; Zemp et al., 2015) and relatively slower melt rates on debris-covered glacier tongues over interannual time scales (Pratap et al., 2015; Vincent et al., 2016). Yet, the overall effects of surface debris cover are uncertain, as many satellite observations suggest similar ice losses relative to clean-ice glaciers over similar or longer periods (Gardelle et al., 2013; Pellicciotti et al., 2015). Because of the complex monsoon climate in the Himalayas, dominant causes of recent glacier changes remain controversial, although atmospheric warming, the albedo effect due to deposition of anthropogenic black carbon (BC) on snow and ice, and precipitation changes have been suggested as important drivers (Gertler et al., 2016; Kraaijenbrink et al., 2017; Salerno et al., 2015).

Model projections of future Himalayan ice loss and resulting impacts require robust observations of glacier response to past and ongoing climate change. Recent satellite remote sensing studies have made substantial advances with improved spatial coverage and resolution to

quantify ice mass changes during 2000–2016 (Brun et al., 2017; Gardelle et al., 2013; Kääb et al., 2015), and former records extending back to the 1970s have been presented for several areas using declassified spy satellite imagery (Bolch et al., 2011; Maurer et al., 2016; Pellicciotti et al., 2015; Ragettli et al., 2016; Zhou et al., 2018). These long-term records are especially critical for extracting robust mass balance signals from the noise of interannual variability (Roe et al., 2017). Many studies also report the highly heterogeneous behavior of glaciers in localized regions, with some glaciers exhibiting faster rates of ice loss during the 21st century (Ragettli et al., 2016; Zhou et al., 2018). Independent analyses document simultaneously increasing atmospheric temperatures at high-elevation stations in HMA (Dimri et al., 2017; Kattel and Yao, 2013; Ren et al., 2017; Yang et al., 2011). To robustly quantify the regional sensitivity of these glaciers to climate change, a reliable Himalaya-wide record of ice loss extending back several decades is needed.

Here we provide an internally consistent dataset of glacier mass change across the Himalayan range over approximately the past 40 years. We use recent advances in digital elevation model (DEM) extraction methods from declassified KH-9 Hexagon film (Maurer and Rupper, 2015) and ASTER stereo imagery to quantify ice loss trends for 650 of the largest glaciers during 1975–2000 and 2000–2016. All aspects of the analysis presented here only use glaciers with data available during both time intervals unless specified otherwise. We investigate glaciers along a 2000-km transect from Spiti Lahaul to Bhutan (75°E to 93°E), which includes glaciers that accumulate snow primarily during winter (western Himalayas) and during the summer monsoon (eastern Himalayas), but excludes complications of surging glaciers in the Karakoram and Kunlun regions where many glaciers appear to be anomalously stable or advancing (Azam et al., 2018). Our compilation includes glaciers comprising approximately 34% of the total glacierized

area in the region, which represents roughly 55% of the total ice volume based on recent ice thickness estimates (Frey et al., 2014; Kraaijenbrink et al., 2017). This diverse dataset adequately captures the statistical distribution of large (>3 $km^2$) glaciers, thus providing the first spatially robust analysis of glacier change spanning four decades in the Himalayas. We extract DEMs from declassified KH-9 Hexagon images for the 650 glaciers, compile a corresponding set of modern ASTER DEMs, fit a robust linear regression through every 30-m pixel of the time series of elevations, sum the resulting elevation changes for each glacier, divide by the corresponding areas, and translate the volume changes to mass using a density conversion factor of 850 ± 60 kg $m^{-3}$ (see Materials and Methods).

## 3.2 Results

### 3.2.1 Glacier mass changes

Our results indicate that glaciers across the Himalayas experienced significant ice loss over the past 40 years, with the average rate of ice loss twice as rapid in the 21st century compared to the end of the 20th century (Figure 3.1). We calculate a regional average geodetic mass balance of −0.43 ± 0.14 m w.e. $year^{-1}$ (meters of water equivalent per year) during 2000–2016, compared to −0.22 ± 0.13 m w.e. $year^{-1}$ during 1975–2000 (−0.31 ± 0.13 m w.e. $year^{-1}$ for the full 1975–2016 interval) (see Materials and Methods). A 30-glacier moving average shows a quasi-consistent trend across the 2000-km longitudinal transect during both time intervals (Figure 3.1), and subregions have similar means and distributions of glacier mass balance. Some central catchments deviate somewhat from the Himalaya-wide mean during 2000–2016 (by approximately 0.1 to 0.2 m w.e. $year^{-1}$) in the Uttarakhand (~79.0° to 80.0°E), the Gandaki catchment (~83.5° to 84.5°E), and the Karnali catchment (~81° to 83°E), which has fewer larger glaciers and relatively incomplete data coverage. Similar to previous in situ and satellite-based

studies (Brun et al., 2017; Sherpa et al., 2017), we observe considerable variation among individual glacier mass balances, with area-weighted SDs of 0.1 and 0.2 m w.e. $year^{-1}$ during each respective interval for the 650 glaciers. This variability most likely reflects different glacier characteristics such as sizes of accumulation zones relative to ablation zones, topographic shading, and amounts of debris cover. Yet we find that in our survey (using a rough average of 60 glaciers per 7000-$km^2$ subregion), local variations tend to average out and mean values are similar across most catchments.

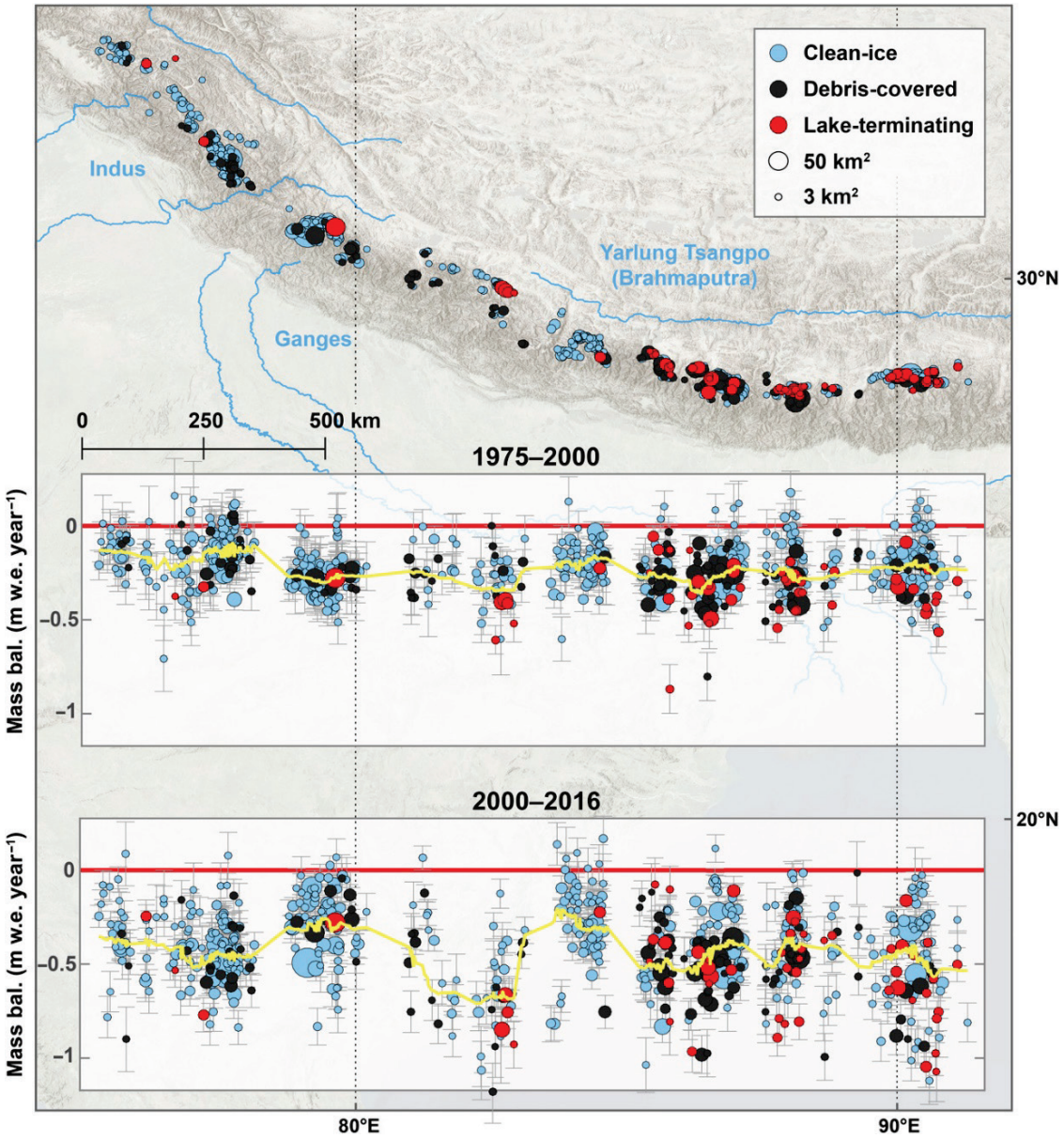


Figure 3.1. Map of glacier locations and geodetic mass balances for the 650 glaciers. Circle sizes are proportional to glacier areas, and colors delineate clean-ice, debris-covered, and lake-terminating categories. Insets indicate ice loss, quantified as geodetic mass balances (m w.e. year$^{-1}$) plotted for individual glaciers along a longitudinal transect during 1975–2000 and 2000–2016. Both inset plots are horizontally aligned with the map view. Gray error bars are 1σ uncertainty, and the yellow trend is the (area-weighted) moving-window mean, using a window size of 30 glaciers.

Contrasting distributions of glacier mass balances are evident when comparing between time intervals. The 1975–2000 distribution has a negative tail extending to −0.6 m w.e. year$^{-1}$, while the 2000–2016 distribution is more negative, extending to −1.1 m w.e. year$^{-1}$ (Figure 3.2A).

During the more recent interval, glaciers are losing ice twice as fast on average (Figure 3.2B), though this varies somewhat between subregions. For example, we find that the average rate of ice loss has increased by a factor of 3 in the Spiti Lahaul region, and by a factor of 1.4 in West Nepal. We also compile altitudinal distributions of ice thickness change for the glaciers and create a Himalaya-wide average thickness change profile versus elevation (Figure 3.2, C and D). These distributed thinning profiles are a function of both thinning by mass loss and of dynamic thinning due to ice flow. We find that the 2000–2016 thinning rate (m $year^{-1}$) profile is considerably steeper, which is likely caused by a combination of faster mass loss and widespread slowing of ice velocities during the 21st century (Azam et al., 2018; Dehecq et al., 2019).

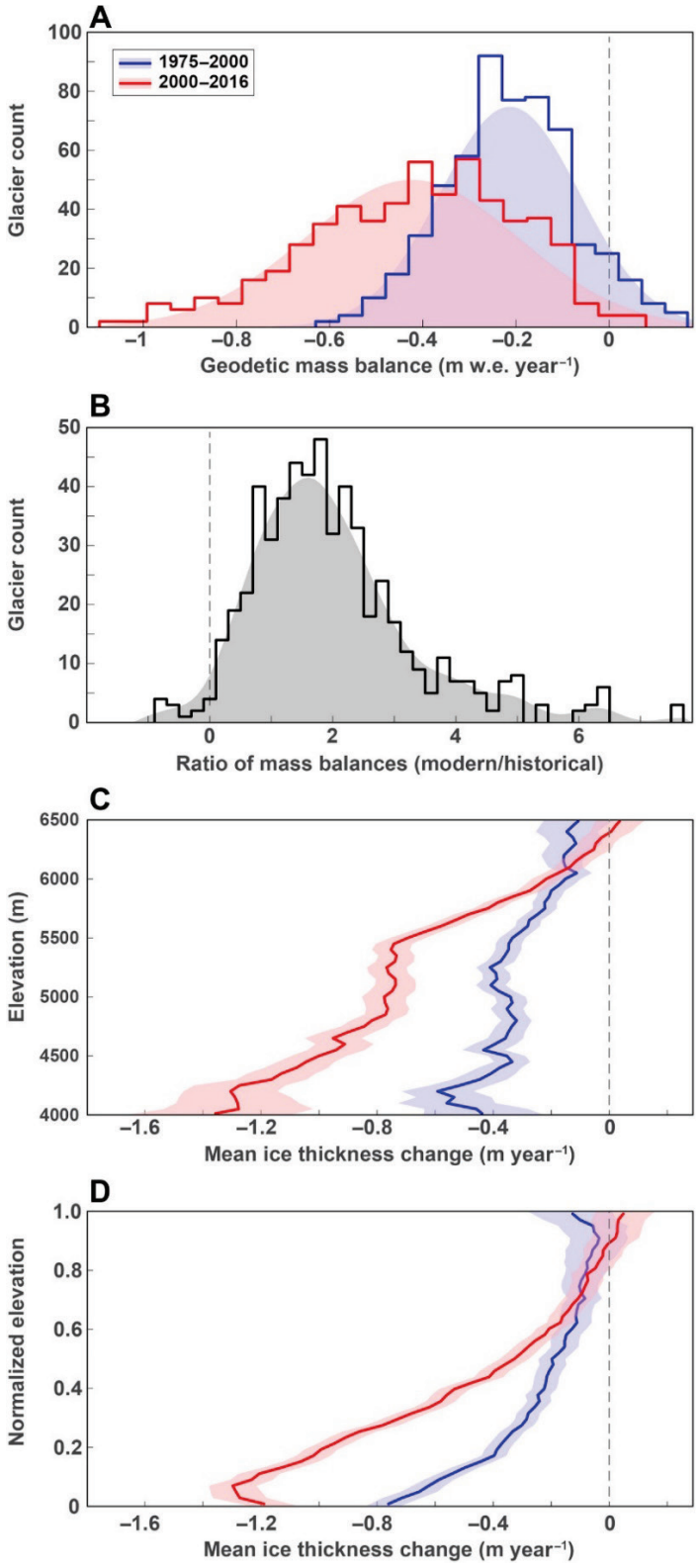


Figure 3.2. Comparison of ice losses between 1975–2000 and 2000–2016 for the 650 glaciers. (A) Histograms of individual glacier geodetic mass balances (m w.e. year$^{-1}$) during 1975–2000 (mean = −0.21, SD = 0.15) and 2000–2016 (mean = −0.41, SD = 0.24). Shaded regions behind the histograms are

fitted normal distributions. (B) Result of dividing the modern (2000–2016) mass balances by the historical (1975–2000) mass balances for each glacier, showing the resulting distribution of the mass balance change (ratio) between the two intervals (mean = 2.01, SD = 1.36). In this case, the shaded region is a fitted kernel distribution. (C) Altitudinal distributions of ice thickness change (m year$^{-1}$) separated into 50-m elevation bins during the two intervals. (D) Normalized altitudinal distributions of ice thickness change. Normalized elevations are defined as $(z - z_{2.5})/(z_{97.5} - z_{2.5})$, where $z$ is elevation and subscripts indicate elevation percentiles. This scales all glaciers by their elevation range (i.e., after scaling, glacier termini = 0 and headwalls = 1), allowing for more consistent comparison of ice thickness changes across glaciers with different elevation ranges. Note the abrupt inflection point in the 2000–2016 profile at ~0.1; this is likely due to retreating glacier termini. Shaded regions in the altitudinal distributions indicate the SEM estimated as $\sigma_z/\sqrt{n_z}$, where $\sigma_z$ is the SD of the thinning rate for each 50-m elevation bin and $n_z$ is the number of independent measurements when accounting for spatial autocorrelation (see Materials and Methods).

We multiply geodetic mass balances by the full glacierized area in the Himalayas between 75° and 93° longitude to estimate region-wide ice mass changes of −7.5 ± 2.3 Gt year$^{-1}$ during 2000–2016, compared to −3.9 ± 2.2 Gt year$^{-1}$ during 1975–2000 (−5.2 ± 2.2 Gt year$^{-1}$ during the full 1975–2016 interval). Recent models using Shuttle Radar Topography Mission (SRTM) elevation data for ice thickness inversion estimate the total glacial ice mass in our region of study to be approximately 700 Gt in the year 2000 (see Materials and Methods) (Frey et al., 2014; Kraaijenbrink et al., 2017). If this estimate is accurate, our observed annual mass losses suggest that of the total ice mass present in 1975, about 87% remained in 2000 and 72% remained in 2016.

### 3.2.2 Comparison of clean-ice, debris-covered, and lake-terminating glaciers

We study mass changes for different glacier types by separating glaciers into clean-ice (<33% area covered by debris), debris-covered (≥33% area covered by debris), and lake-terminating categories based on a Landsat band ratio threshold and manual delineation of proglacial lakes (see Materials and Methods). All three categories have undergone a similar acceleration of ice loss (Table 3.1), and debris-covered glaciers exhibit similar and often more negative geodetic mass balances compared to clean-ice glaciers over the past 40 years (Figure 3.3). Altitudinal distributions indicate slower thinning for lower-elevation regions of debris-covered glaciers

(glacier tongues where debris is most concentrated) relative to clean-ice glaciers, but comparatively faster thinning in mid- to upper elevations (Figure 3.4). Lake-terminating glaciers concentrated in the eastern Himalayas exhibit the most negative mass balances due to thermal undercutting and calving (Ren et al., 2017; Sakai et al., 2009), though they only comprise around 5 to 6% of the estimated total Himalaya-wide mass loss during both intervals.

Table 3.1. Himalaya-wide geodetic mass balances (m w.e. $yr^{-1}$)

| | 1975-2000 | 2000-2016 | 1975-2016 |
|---|---|---|---|
| **All glaciers** | -0.22 ± 0.13 | -0.43 ± 0.14 | -0.31 ± 0.13 |
| **Clean-ice** | -0.19 ± 0.07 | -0.38 ± 0.08 | -0.27 ± 0.07 |
| **Debris-covered** | -0.24 ± 0.06 | -0.44 ± 0.08 | -0.32 ± 0.06 |
| **Lake-terminating** | -0.33 ± 0.07 | -0.56 ± 0.08 | -0.40 ± 0.07 |

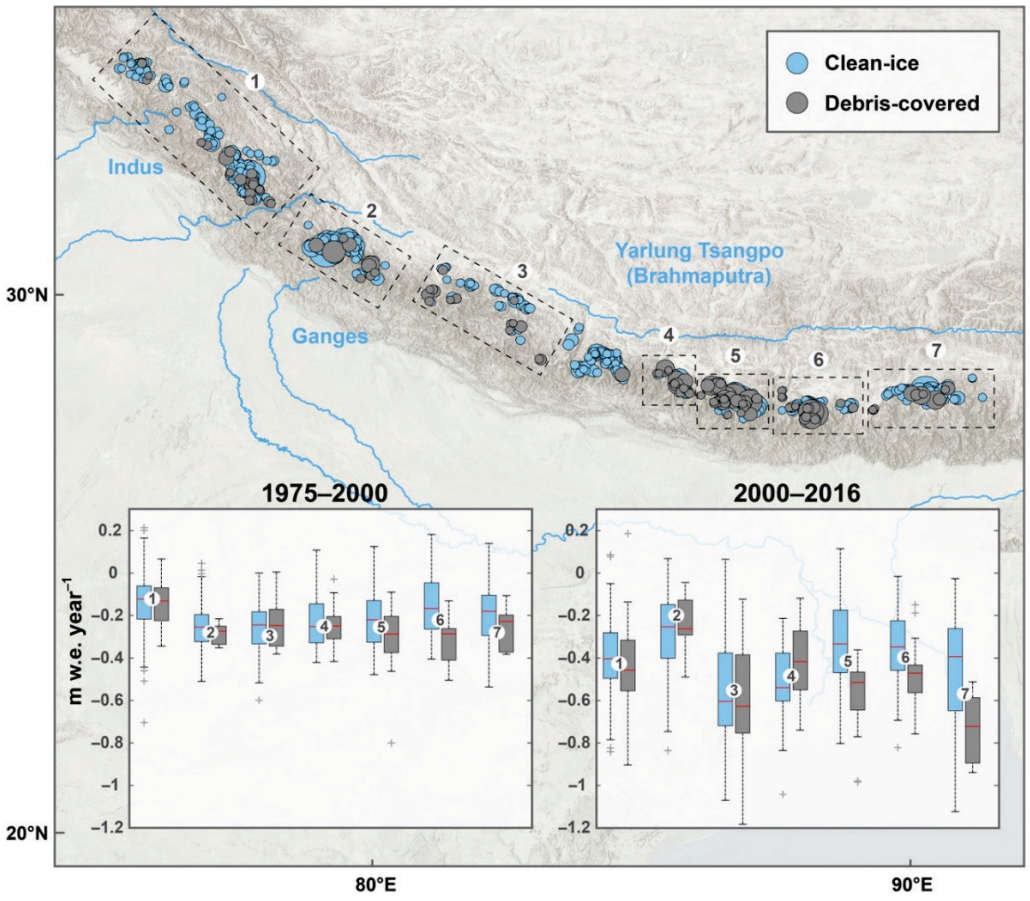


Figure 3.3. Comparison between clean-ice (<33% debris-covered area) and debris-covered (≥33% debris-covered area) glaciers for seven subregions. Circle sizes are proportional to glacier areas, colors delineate clean-ice versus debris-covered categories, and boxplots indicate geodetic mass balance (m w.e. year$^{-1}$). Box center marks (red lines) are medians; box bottom and top edges indicate the 25th and 75th percentiles, respectively; whiskers indicate $q_{75} + 1.5 \cdot (q_{75} - q_{25})$ and $q_{25} - 1.5 \cdot (q_{75} - q_{25})$, where subscripts indicate percentiles and "+" symbols are outliers.

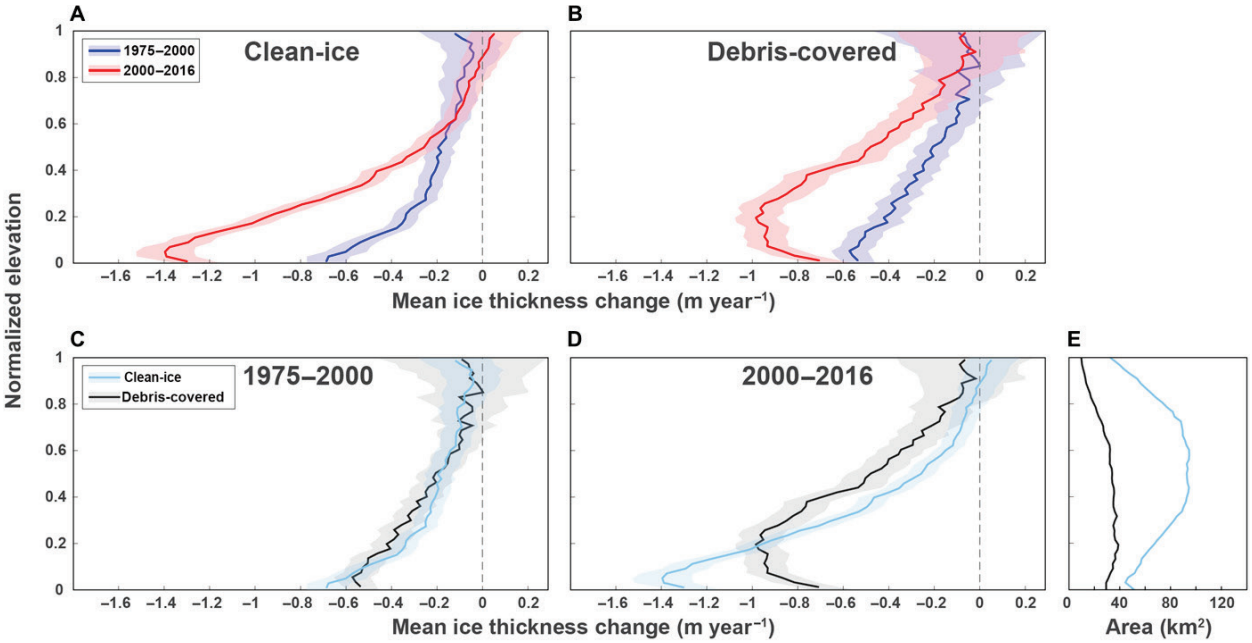


Figure 3.4. Altitudinal distributions of ice thickness change (m year$^{-1}$) for the 650 glaciers. Glaciers are separated by time interval (top) and category (<33% versus ≥33% debris-covered area) (bottom). (A) Altitudinal distributions of ice thickness change for clean-ice glaciers during 1975–2000 and 2000–2016. The y axes are normalized elevation as in Figure 3.2. (B) Same as (A), but for debris-covered glaciers. (C) Altitudinal distributions of ice thickness change during 1975–2000 for clean-ice and debris-covered glaciers. (D) Same as (C), but for 2000–2016. (E) Altitudinal distributions of glacierized area for both glacier categories. Elevational extent of debris cover varies widely between individual glaciers, but is mostly concentrated in lower ablation zones. The clean-ice category includes 478 glaciers and the debris-covered category includes 124 glaciers.

## 3.3 Approximation of required temperature change

As a first approximation of the consistency between observed glacier mass balances and available temperature records, we estimate the energy required to melt the observed ice losses and conservatively estimate the atmospheric temperature change that would supply this energy via longwave radiation to the glaciers, using a simple energy balance approach (see Materials and Methods). We propagate significant uncertainties associated with input from global climate reanalysis data, scaling of temperatures from coarse reanalysis grids to specific glacier elevations, and averaging of climate data over the glacierized region. Results suggest that the observed acceleration of ice loss can be explained by an average temperature ranging from 0.4° to 1.4°C warmer during 2000–2016, relative to the 1975–2000 average. This approximately

agrees with the magnitude of warming observed by meteorological stations located throughout HMA, which have recorded air temperatures around 1°C warmer on average during 2000–2016, relative to 1975–2000 (Figure 3.5). More comprehensive climate observations and models will be essential for further investigation, but these simple energy constraints suggest that the acceleration of mass loss in the Himalayas is consistent with warming temperatures recorded by meteorological stations in the region.

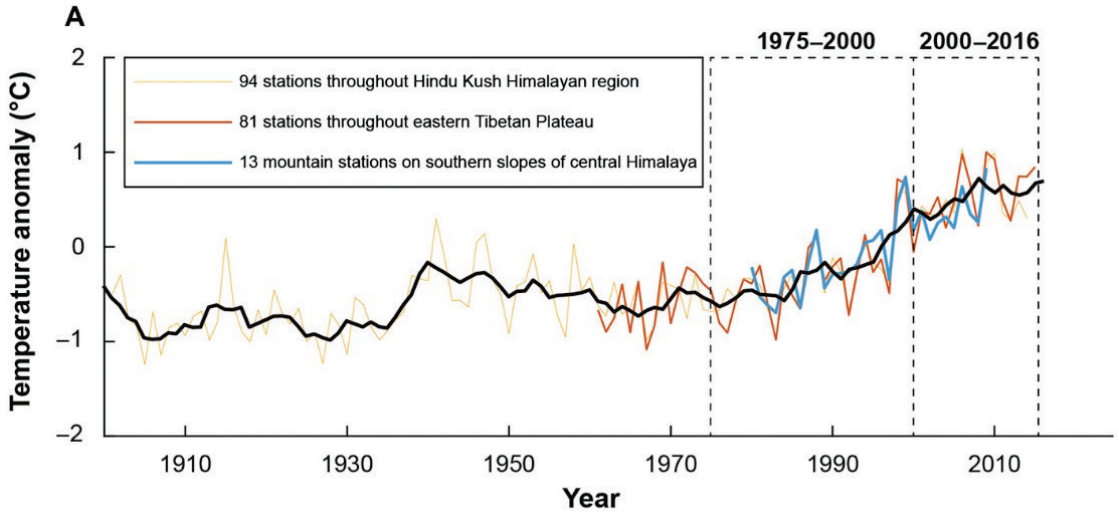


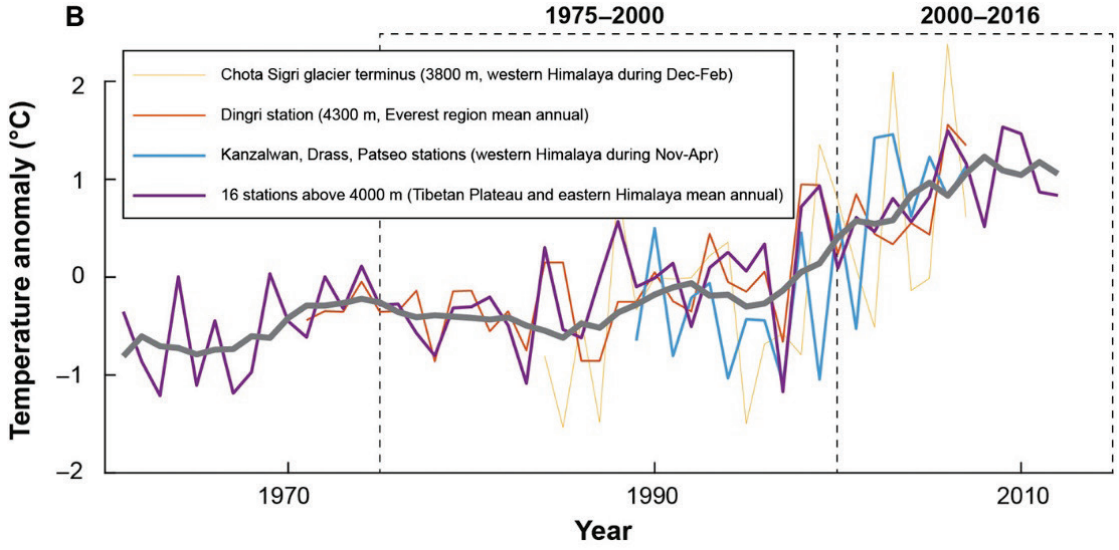


C

| High-elevation meteorological station(s) | Mean *T* of 2000–2016 interval relative to 1975–2000 mean (°C)* |
|---|---|
| Chota Sigri (Dec-Feb) | +0.9 |
| Dingri (annual) | +0.9 |
| Kanzalwan, Drass, Patseo (Nov-Apr) | +1.3 |
| 16 stations on Tibetan Plateau (annual) | +1.0 |

* Using available data within each interval

Figure 3.5. Compilation of previously published instrumental temperature records in HMA. (A) Regional temperature anomalies, relative to the 1980–2009 mean temperatures for each record. The yellow trend (Ren et al., 2017) from the quality-controlled and homogenized climate datasets LSAT-V1.1 and CGP1.0 recently developed by the China Meteorological Administration (CMA), using approximately 94 meteorological stations located throughout the Hindu Kush Himalayan region. The orange trend (Xu et al., 2017) is from a similar CMA dataset derived from 81 stations more concentrated on the eastern Tibetan Plateau. The blue trend (Kattel and Yao, 2013) is from three decades of temperature data from 13 mountain stations located on the southern slopes of the central Himalayas. The black trend is the 5-year

moving mean. (B) Temperature anomalies from high-elevation stations at the Chhota Shigri glacier terminus (Dimri et al., 2017); Dingri station in the Everest region (Yang et al., 2011); average from the Kanzalwan, Drass, and Patseo stations (Shekhar et al., 2010); and average of 16 stations above 4000 m elevation on the Tibetan Plateau and eastern Himalayas (Yan and Liu, 2014). Here, temperature anomalies are relative to the mean of each record. The gray trend line is the 5-year moving mean. (C) Difference in mean temperature (°C) between the two intervals, i.e., the mean of the 2000–2016 interval relative to the mean of the 1975–2000 interval.

## 3.4 Discussion

### 3.4.1 Implications for dominant drivers of glacier change in the Himalayas

The parsing of Himalayan glacier energy budgets is not a straightforward task owing to the scarcity of meteorological data, in combination with the complex climate and topography of the region (Azam et al., 2018). Furthermore, the Himalayas border hot spots of high anthropogenic BC emissions, which may affect glaciers by direct heating of the atmosphere and decreasing albedo of ice and snow after deposition (Gertler et al., 2016). While improved analyses combining observations and high-resolution atmospheric and glacier energy balance models will be required to quantify these effects, the pattern of ice loss we observe has important implications regarding dominant climate influences on Himalayan glacier mass balances. Our results suggest that any drivers of glacier change must explain the region-wide consistency, the doubling of the average rate of ice loss in the 21st century compared to 1975–2000, and the observation that clean-ice, debris-covered, and lake-terminating glaciers have all experienced a similar acceleration of mass loss.

Some studies have suggested a weakening of the summer monsoon and reduced precipitation as primary reasons for negative glacier mass balances, particularly in the Everest region (Salerno et al., 2015). While decreasing accumulation rates may account for a significant portion of the mass balance signal for some glaciers, an extreme Himalaya-wide decrease in precipitation would be required to explain the extensive ice losses we observe, especially given that monsoon-dominated glaciers with high accumulation rates are known to be much more sensitive to

temperature than accumulation changes (Oerlemans and Fortuin, 1992; Rupper and Roe, 2008). Regional studies of precipitation trends in the Himalayas do not suggest a widespread decrease in precipitation over the past four decades (Supplementary Materials). A uniform BC albedo forcing across the Himalayas is another possible explanation, although BC concentrations measured in snow and ice in the Himalayas have been found to be spatially heterogeneous (Gertler et al., 2016; Kaspari et al., 2014), and high-resolution atmospheric models also show large spatial variability of deposited BC originating from localized emissions in regions of complex terrain (Gertler et al., 2016; Qian et al., 2009). Future analyses focused on quantifying the spatial patterns of BC deposition will reveal further insights, yet given the rather homogeneous pattern of mass loss we observe across the 2000-km Himalayan transect, a strong, spatially heterogeneous mechanism seems improbable as a dominant driver of glacier ice loss in the region.

### 3.4.2 Debris-covered glaciers

Similar thinning rates of debris-covered (thermally insulated) glaciers relative to clean-ice glaciers have been observed by previous studies and have been not only ascribed to surface melt ponds and associated ice cliffs acting as localized hot spots to concentrate melting but also attributed to declining ice flux causing dynamic thinning and stagnation of debris-covered glacier tongues (Azam et al., 2018). While we cannot yet directly deconvolve relative contributions from these processes, we find that average thinning rates for debris-covered glaciers are slower than clean-ice glaciers at low elevations (glacier tongues where debris is most concentrated), which agrees with reduced melt rates from field studies. In turn, debris-covered glaciers tend to have comparatively faster thinning at mid-range elevations, where debris cover is sparser and also where the majority of total glacierized area resides (Figure 3.4). Models of debris-covered

glacier processes suggest that this pattern of thinning may cause a reduction in down-glacier surface gradient, which, in turn, reduces driving stress and ice flux and explains why debris-covered ablation zones become stagnant (Benn et al., 2012). We also find that clean-ice glaciers exhibit a much more pronounced steepening of the thinning profile over time, compared to debris-covered glaciers. It may be that both glacier types experience a uniform thinning phase followed by a changing terminus flux and retreat phase, but the clean-ice glaciers are in a later phase of response to recent climate change (Roe and Baker, 2014).

### 3.4.3 Comparison with previous studies in the Himalayas

To compare our results with previous remote sensing studies that derive mass changes from various sensors (including Hexagon, SRTM, SPOT5, ICESat, and ASTER), we restrict our results to the approximate geographical regions covered by each corresponding study (Bolch et al., 2011; Brun et al., 2017; Gardelle et al., 2013; Kääb et al., 2015; Maurer et al., 2016; Pellicciotti et al., 2015; Ragettli et al., 2016; Zhou et al., 2018) and then compute area-weighted average geodetic mass balances. In addition, we compare individual glacier mass balances for the Everest and Langtang Himal regions, where mass changes were previously estimated using declassified Corona and Hexagon imagery (Bolch et al., 2011; Pellicciotti et al., 2015; Ragettli et al., 2016). Despite factors such as variable spatial resolutions, distinct void-filling methods, heterogeneous spatial and temporal coverages, and different definitions of glacier boundaries, we find that our average mass balances generally agree with previous analyses and overlap within uncertainties (Table S3.1). However, because of the significant variability of individual glacier mass changes within subregions, our results also highlight the importance of sampling a large number of glaciers to obtain a robust average trend for any given area.

### 3.4.4 Comparison with benchmark mid-latitude glaciers and global average

To gain perspective on mass losses from these low-latitude glaciers in the monsoonal Himalayas, we compare our results with benchmark mid-latitude glaciers in the European Alps, as well as with a global average mass balance trend (Figure S3.1) (Zemp et al., 2017). The Alps contain the most detailed long-term glaciological and high-elevation meteorological records on Earth, and the climatic sensitivity and behavior of these European glaciers are well understood compared to glaciers in HMA. Air temperatures in the Alps show an abrupt warming trend beginning in the mid-1980s, and Alpine mass balance records display a concurrent acceleration of ice loss, with a continual strongly negative mass balance after that time. Himalayan weather station data indicate a more gradual warming trend, with the strongest warming beginning in the mid-1990s (Figure S3.1, A and B). We find that mass balance in the Himalayas is less negative compared to the Alps and the global average, despite close proximity to a known hot spot of increasing BC emissions with rapid growth and accompanying combustion of fossil fuels and biomass in South Asia (Bond et al., 2013). The concurrent acceleration of ice loss observed in both the Himalayas and Europe over the past 40 years coincides with a distinct warming trend beginning in the latter part of the 20th century, followed by the consistently warmest temperatures through the 21st century in both regions.

## 3.5 Conclusion

Our analysis robustly quantifies four decades of ice loss for 650 of the largest glaciers across a 2000-km transect in the Himalayas. We find similar mass loss rates across subregions and a doubling of the average rate of loss during 2000–2016 relative to the 1975–2000 interval. This is consistent with the available multi-decadal weather station records scattered throughout HMA, which indicate quasi-steady mean annual air temperatures through the 1960s to the 1980s with a

prominent warming trend beginning in the mid-1990s and continuing into the 21st century (23–26) (Dimri et al., 2017; Kattel and Yao, 2013; Ren et al., 2017; Yang et al., 2011). We suggest that degree-day and energy balance models focused on accurately quantifying glacier responses to air temperature changes (including energy fluxes and associated feedbacks) will provide the most robust estimates of glacier response to future climate scenarios in the Himalayas.

## 3.6 Materials and methods

### 3.6.1 Hexagon

U.S. intelligence agencies used KH-9 Hexagon military satellites for reconnaissance from 1973 to 1980. A telescopic camera system acquired thousands of photographs worldwide, after which film recovery capsules were ejected from the satellites and parachuted back to Earth over the Pacific Ocean. With a ground resolution ranging from 6 to 9 m, single scenes from the mapping camera cover an area of approximately 30,000 $km^2$ with overlap of 55 to 70%, allowing for stereo photogrammetric processing of large regions. Images were scanned by the U.S. Geological Survey (USGS) at a resolution of 7 μm and downloaded via the Earth Explorer user interface (earthexplorer.usgs.gov). Digital elevation models were extracted using the Hexagon Imagery Automated Pipeline methodology, which is coded in MATLAB and uses the OpenCV library for Oriented FAST and Rotated BRIEF (ORB) feature matching, uncalibrated stereo rectification, and semiglobal block matching algorithms (Maurer and Rupper, 2015). The majority of the KH-9 images here were acquired within a 3-year interval (1973–1976), and we processed a total of 42 images to provide sufficient spatial coverage (Figure S3.2).

### 3.6.2 ASTER

The ASTER instrument was launched as part of a cooperative effort between NASA and Japan's Ministry of Economy, Trade and Industry in 1999. Its nadir and backward-viewing telescopes

provide stereoscopic capability at 15-m ground resolution, and a single DEM covers approximately 3600 $km^2$. Approximately 26,000 ASTER DEMs were downloaded via the METI AIST Data Archive System (MADAS) satellite data retrieval system (gbank.gsj.jp/madas), a portal maintained by the Japanese National Institute of Advanced Industrial Science and Technology and the Geological Survey of Japan. To use all cloud-free pixels (including images with a high percentage of cloud cover), no cloud selection criteria were applied when downloading the images. We used the Data1.l3a.demzs geotiff product, which has a spatial resolution of 30 m. After downloading, the DEMs were subjected to a cleanup process: For a given scene, any saturated pixels (i.e., equal to 0 or 255) in the nadir band 3 (0.76 to 0.86 μm) image were masked in the DEM. Next, the SRTM dataset was used to remove any DEM values with an absolute elevation difference larger than 150 m (relative to SRTM), which effectively eliminated the majority of errors caused by clouds. While more sophisticated cloud masking procedures are possible, the ASTER shortwave infrared detectors failed in April 2008, making cloud detection after this time impossible using standard methods. We examined existing cloud masks derived using Moderate Resolution Imaging Spectroradiometer images as another option (tonolab.cis.ibaraki.ac.jp/ASTER/cloud/). However, these are not optimized for snow-covered regions and often misclassify glacier pixels as clouds. Instead, our large collection of multitemporal ASTER scenes, the SRTM difference threshold, and our robust linear trend fitting algorithm [see description of Random Sample Consensus (RANSAC) in the "Trend fitting of multitemporal DEM stacks" section] effectively excluded any remaining erroneous cloud elevations after the initial threshold. As a final step, all ASTER DEMs were coregistered to the SRTM using a standard elevation–aspect optimization procedure (Nuth and Kääb, 2011). We did not apply fifth-order polynomial correction procedures to the ASTER DEMs for satellite "jitter"

effects and curvature bias as done in some previous studies (Brun et al., 2017). We found that while these types of corrections may reduce the overall average elevation error in a scene, the polynomial fitting can be unwieldy and may introduce unwanted localized biases. By stacking many ASTER DEMs (with 20.5 being the average number of observations per pixel stack during the ASTER trend fitting, see Figure S3.3E) and using a robust fitting procedure, we found that biases do not correlate across overlapping scenes, and thus tend to cancel out one another. Furthermore, the elevation change results from this portion of our study overlap within uncertainties with Brun et al. (2017) (Supplementary Materials) who did perform polynomial corrections. This suggests that for a large-scale regional study using a high number of overlapping ASTER scenes, the satellite jitter and curvature bias corrections have a relatively minimal impact on the final results.

### 3.6.3 Glacier polygons

To delineate glaciers during all portions of the analysis, we used manually refined versions of the Randolph Glacier Inventory (RGI 5.0) (Arendt et al., 2015). Starting with the original RGI dataset, we edited the glacier polygons to reflect glacier areas during 1975, 2000, and 2016. For the 1975 edit, we used a combination of Hexagon imagery, the Global Land Survey (GLS) Landsat Multispectral Scanner mosaic (GLS1975), and glacier thickness change maps derived from differencing the Hexagon and modern ASTER DEMs, which are particularly useful for debris-covered glacier termini that often have spectral characteristics indistinguishable from surrounding terrain. Debris-covered areas for each glacier were delineated using a Landsat DN TM4/TM5 band ratio with a threshold of 2.0, and glaciers with ≥33% debris cover were assigned to the debris-covered category. For the 2000 edit, we used the GLS2000 Landsat Enhanced Thematic Mapper Plus mosaic, along with glacier thickness change maps derived from

differencing ASTER DEMs. For the 2016 edit, we used a custom mosaic of Landsat 8 imagery with acquisition dates spanning 2014–2016. The individually edited glacier polygons were used for all ice volume change and geodetic mass balance computations. The polygons were also used during alignment of the DEMs, where the shapefiles were converted to raster masks with a dilation (morphological operation) of 250 m on the binary rasters. This effectively excluded unstable terrain surrounding the glaciers during the DEM alignment process, such as steep avalanching slopes and unstable moraines.

### 3.6.4 Trend fitting of multitemporal DEM stacks

Glacier polygons were processed individually—all DEMs from a given time interval (1975–2000 or 2000–2016) that overlap a polygon were selected and resampled to the same 30-m resolution using linear interpolation. The overlapping DEMs were sampled with a 25% extension around each glacier to include nearby stable terrain for alignment and uncertainty analysis (Figure S3.4). After ensuring that there is no vertical bias, the aligned DEMs were sorted in temporal order as a three-dimensional matrix, and linear trends were fit to every pixel "stack" (i.e., along the third dimension of the matrix) using the RANSAC method. During each RANSAC iteration, a random set of two elevation pixels per stack were selected. A linear trend was fit to these two values, and then all remaining elevation pixels were compared to the trend. Any elevation pixels within 15 m of the trend line were marked as inliers. This process was repeated for 100 iterations, and the iteration with the greatest number of inliers was selected. A final linear fit was performed using all inliers from the best iteration, and this trend was used for each pixel stack's thickness change estimate. The thickness change maps were subjected to outlier removal using thresholds for maximum slope, maximum thickness change, minimum count per pixel stack, minimum timespan per pixel stack, maximum SD of inlier elevations per pixel stack, and maximum

gradient of the thickness change map (Figure S3.3). In addition, the thickness change pixels were separated into 50-m elevation bins, and pixels falling outside the 2 to 98% quantile range were excluded. Any bins with less than 100 pixels were removed and then interpolated using the two adjacent bins. Before computing ice volume change for the glaciers, the final thickness change maps were visually inspected, any remaining erroneous pixels (which occurred almost exclusively in low-contrast, snow-covered accumulation zones) were manually masked, and a 5 × 5 pixel median filter was applied. We did not attempt to perform seasonality corrections, as no seasonal snowfall records are available and because nearly all the Hexagon DEMs were acquired during winter, thus minimizing any seasonality offsets between regions. For the 1975–2000 interval, we used the Hexagon DEMs and sampled ASTER thickness change trends at the start of the year 2000. For regions with multiple overlapping Hexagon DEMs, we used the same RANSAC method. During the 1975–2000 interval, only two DEMs were available for most glaciers. In these cases, the RANSAC iterations were unnecessary, and we simply differenced the two available DEMs. We did not use SRTM for any thickness change estimates; thus, no correction for radar penetration was necessary.

### 3.6.5 Mass changes

To compute (mean annual) ice volume changes for individual glaciers, all thickness change pixels falling within a glacier polygon were transformed to an appropriate projected WGS84 UTM coordinate system (zones 43 to 46, depending on longitude of the glacier). Pixel values (m $year^{-1}$) were then multiplied by their corresponding areas (pixel width × pixel height) and summed together. The resulting ice volume change was then divided by the average glacier area to obtain a glacier thickness change. We used the average of the initial and final glacier areas for a given time interval and excluded slopes greater than 45° to remove any cliffs and nunataks.

Last, the glacier thickness change was multiplied by an average ice-firn density (Huss, 2013) of 850 kg $m^{-3}$ and then divided by the density of water (1000 kg $m^{-3}$) to compute glacier geodetic mass balance in m w.e. $year^{-1}$. Because of cloud cover, shadows, and low radiometric contrast, some glacier accumulation zones had gaps in the DEMs and resulting thickness change maps. This is particularly evident in the Hexagon DEMs for the Spiti Lahaul region owing to extensive cloud cover. To fill these gaps, we tested two different void-filling methods for comparison. In the first method, we defined a circular search area with a radius of 50 km around the center of a given glacier. All thickness change pixels from glaciers in this surrounding area were binned (into 50-m elevation bins, and following the same outlier-removal procedure given in the preceding section), and any missing data in the glacier were set to this "regional bin" mean value at the corresponding elevation. In the second method, we filled data gaps using an interpolation procedure, where voids in an individual glacier were linearly interpolated using bin values at upper and lower elevations relative to the missing data (those belonging to the same glacier), and assumed zero change at the highest elevation bin (headwall). Both methods yielded similar results (Table S3.1). In addition, no obvious trends were apparent when geodetic mass balance was plotted versus percent data coverage or glacier size (Figure S3.5). While smaller glaciers exhibited more scatter, the average mass balance was similar for all glacier sizes. These observations indicate that our representative sample of glaciers, while biased toward larger glaciers, adequately captures the statistical distribution of glacier mass balances in the Himalayas.

To calculate regional geodetic mass balances, we separated glaciers into four subregions (Spiti Lahaul, West Nepal, East Nepal, and Bhutan) as defined by Brun et al. (Brun et al., 2017). We then calculated the average mass balance for each of these four subregions, weighted by

individual glacier areas. Last, we calculated a final average mass balance for the Himalayas, weighted by the total glacierized area (from the RGI 5.0 database) in each of the four subregions, between 75° to 93° longitude. Because of the relatively homogeneous mass balance distribution, we found that this approach resulted in similar values (well within the uncertainties) compared to simply calculating the area-weighted average mass balance of the 650 measured glaciers. To obtain the total mass changes in Gt $year^{-1}$, we multiplied each subregion mass balance by its total glacierized area and then summed the results from all subregions to get Himalaya-wide totals of −3.9 Gt $year^{-1}$ for 1975–2000 and −7.5 Gt $year^{-1}$ for 2000–2016. To calculate contributions to sea-level rise, we used a global ocean surface area of $361.9 \times 10^6$ $km^2$ (Figure S3.4G).

To estimate the total ice mass present in our region of study, we used ice thickness estimates from Kraaijenbrink et al. (2017), who used the Glacier bed Topography version 2 model to invert for ice thickness (Frey et al., 2014) with input from the SRTM DEM (acquired in February of 2000). The ice thickness estimates from (Kraaijenbrink et al., 2017) did not include glaciers smaller than 0.4 $km^2$, and to estimate the additional mass contribution from these smallest glaciers (along with any other glaciers that are missing thickness estimates), we fit a second-order polynomial to the logarithm of glacier volumes versus the logarithm of glacier areas and evaluated this fit equation for any glaciers without volume data (Figure S3.6). We then converted glacier volume to mass using a density value of 850 kg $m^{-3}$. Over our region of study, the ice volumes from the thickness data amounted to 649 Gt, with an additional contribution of 35 Gt from the fitting procedure, for a total of 684 Gt.

### 3.6.6 Uncertainty assessment

We quantified statistical uncertainty for individual glaciers using an iterative random sampling approach. For a given glacier, the SD of elevation changes from the surrounding stable terrain ($\sigma_z$) was first calculated. For any missing thickness change pixels within the glacier polygon, we also included an extrapolation uncertainty $\sigma_e$. This accounts for additional error in regions with incomplete data, i.e., those glacier regions filled by extrapolating thickness changes from surrounding glaciers, or linear interpolation assuming zero change at the headwall, as described in the previous section. We found that in the Himalaya-wide altitudinal distributions, the maximum SD of thickness change in any 50-m elevation bin above 5000 m is 0.56 m year$^{-1}$. Nearly all regions with incomplete data coverage are above this elevation, resulting from poor radiometric contrast for snow-covered glacier accumulation zones. We thus conservatively set $\sigma_e$ equal to 0.6 m year$^{-1}$. We then combined both sources of error to get $\sigma_p$ for every individual thickness change pixel:

$$\sigma_p = \sqrt{\sigma_z^2 + \sigma_e^2} \tag{3.1}$$

To account for spatial autocorrelation, we started with a normally distributed random error field (with a mean of 0 and an SD of 1) the same size as the thickness change map and then filtered it using an *n*-by-*n* moving window average to add spatial correlation, where *n* is defined as the spatial correlation range divided by the spatial resolution of the thickness change map. We used 500 m for the spatial correlation range, which is a conservative value based on semivariogram analysis in mountainous regions from previous studies (Brun et al., 2017; Maurer et al., 2016; Rolstad et al., 2009). The resulting artificial error field $E_n$ (now with spatial correlation) is scaled by the $\sigma_p$ values and added to the thickness change map $\Delta H$ as follows, where ($x$, $y$) are pixel coordinates:

$$\Delta H_E(x,y) = \Delta H(x,y) + E_n(x,y) \cdot \frac{\sigma_p(x,y)}{\sigma_n} \quad (3.2)$$

If thickness change data exist at a given pixel location ($x$, $y$) on the glacier, $\sigma_n$ is the SD of the set of all $E_n$ values where data exist (i.e., where $\sigma_e$ is equal to zero). Conversely, if thickness change data do not exist at a given pixel location ($x$, $y$) on the glacier, $\sigma_n$ is the SD of the set of all $E_n$ values where data do not exist (i.e., where $\sigma_e$ is equal to 0.6 m year$^{-1}$). In this way, the second term of Eq. (3.2) assigns larger uncertainties to regions with incomplete data. Last, all glacier thickness change pixels in $\Delta H_E$ were summed together to compute a volume change with the introduced error. This procedure was repeated for 100 iterations, and the volume change uncertainty $\sigma_{\Delta V}$ was computed as the SD of the resulting distribution (Figure S3.4). For region-wide volume change estimates, we conservatively assumed total correlation between glaciers and computed region-wide uncertainty as follows, where $g$ is the total number of glaciers (~17,400)

$$\sigma_{\Delta V\ region} = \sum_{1}^{g} \sigma_{\Delta V} \quad (3.3)$$

For glaciers where thickness change data are not available, a measure of uncertainty is still required to factor into the final regional uncertainty estimate. For these glaciers, we estimated $\sigma_{\Delta V}$ as (Rolstad et al., 2009):

$$\sigma_{\Delta V} = \sqrt{\sigma_{z\ region}^2 \cdot \frac{A_{cor}}{5 \cdot A}} \quad (3.4)$$

$$A_{cor} = \pi \cdot L^2 \quad (3.5)$$

In this case, $\sigma_{z\ region}$ is the region-wide SD of elevation change over stable terrain (0.42 m year$^{-1}$) (Figure S3.7), $A_{cor}$ is the correlation area, $L$ is the correlation range (500 m), and $A$ is the glacier

area. Last, all $\sigma_{\Delta V}$ and $\sigma_{\Delta V\, regjon}$ estimates were combined with an area uncertainty (Paul et al., 2013) of 10% and a density uncertainty (Huss, 2013) of 60 kg $m^{-3}$ using standard uncorrelated error propagation.

### 3.6.7 Sensitivity of region-wide glacier mass change estimates

We further tested the sensitivity of our region-wide estimates to potential biases, including (i) the exclusion of small glaciers, (ii) incomplete data coverage for many glacier accumulation zones during 1975–2000, and (iii) void-filling technique. First, we note that our geodetic mass balance analysis only includes glaciers larger than 3 $km^2$. This is because mass balance uncertainties increase with decreasing glacier size, and we find that uncertainties often exceed the magnitude of mass changes for glaciers smaller than ~3 $km^2$. To test whether the neglected small glaciers appreciably affect the result, we also computed mass balances using all available glaciers (i.e., all glaciers with ≥33% data coverage, including those smaller than 3 $km^2$). We find that including the full set of smaller glaciers changes the region-wide geodetic mass balance estimates by a maximum of 0.04 m w.e. $year^{-1}$ (Figure S3.4G). Next, we note that the Hexagon DEMs in particular have poor data coverage over glacier accumulation zones (Figure S3.8 and Figure S3.9). However, the vast majority of thinning occurs in glacier ablation zones, and the amount of thinning decreases with elevation in a quasi-linear fashion, especially in mid- to upper regions of the glaciers where data gaps are most common. Thus, we hypothesize that we can extrapolate and interpolate with reasonable confidence over accumulation areas. To test the robustness of this assumption, we used the 2000–2016 glacier change data. The ASTER data over this interval have superior radiometric contrast and adequately capture elevation change trends for most accumulation zones. We first set all 2000–2016 thickness change pixels to be empty where the 1975–2000 data are missing to simulate the same data gaps over accumulation zones as in the

1975–2000 data. We then performed the same geodetic mass balance calculations and found that the region-wide geodetic mass balance only changes by 0.01 m w.e. $year^{-1}$ (Figure S3.4G, comparing test 3 to test 1). Last, we performed two separate void-filling methods for all tests (see the "Mass changes" section for descriptions of void-filling methods) and observed a maximum change in geodetic mass balance of 0.04 m w.e. $year^{-1}$. Overall, the relatively small impact of each test suggests that our results are robust to the exclusion of small glaciers, incomplete data coverage over glacier accumulation zones, and void-filling technique.

## 3.7 Acknowledgements

We thank C. Small and S. Hemming for valuable discussions on the research and manuscript, and B. Raup for helping archive the data at NSIDC (National Snow and Ice Data Center). J.M.M. was funded by a NASA Earth and Space Science Fellowship (NNX16AO59H). J.M.S. was funded by NSF/EAR-1304351, the G. Unger Vetlesen Foundation, and the Center for Climate and Life, Columbia University. S.R. was funded by NASA 15-HMA15-0030. Glacier thickness change data from this study are archived at the NSIDC (https://doi.org/10.5067/GGGSQ06ZR0R8).

## 3.8 Supplementary Materials

### 3.8.1 Approximation of required temperature change

We calculate the energy required to melt the observed mass losses during 1975-2000 and 2000-2016, and approximate the atmospheric temperature change needed to supply this extra energy via longwave (LW) radiation to the glaciers using a simple energy balance approach. We assume that precipitation has remained constant, surface albedo feedbacks are small, and that energy supplied via increasing LW radiation is the dominant component in the energy balance (Ohmura,

2001) (i.e. shortwave solar radiation remains steady through time, and turbulent and latent heat fluxes are small compared to the radiative balance terms) (Rupper and Roe, 2008).

We start with our observed Himalayas-wide geodetic mass balances ($G$) in m w.e. $yr^{-1}$ during 1975-2000 and 2000-2016, and multiply by the density of water ($\rho_w$) and the corresponding period of mass change ($t_{mass}$) to calculate the total mass loss per unit area ($M$) during each interval (25 or 16 years, respectively):

$$M = G\rho_w t_{mass} \tag{3.6}$$

We then divide by the latent heat of fusion ($L_f$), and the estimated total time that melt occurs over the period of mass change ($t_{melt}$) to calculate the imbalance of energy per unit time ($\Delta R$), which we assume is supplied via changes in LW radiation (W $m^{-2}$):

$$\Delta R = \frac{M}{L_f t_{melt}} \tag{3.7}$$

Next we define the temperature change per unit change in LW radiation, which comes from the derivative of the Stefan-Boltzmann law:

$$\lambda = \frac{\Delta T}{\Delta R} = \frac{1}{4\sigma\varepsilon T_a^3} \tag{3.8}$$

where σ is the Stefan-Boltzmann constant, $\varepsilon$ is the emissivity of the atmosphere, and $T_a$ is the atmospheric temperature at the time the perturbation to the system is applied (i.e. the temperature of the reference state). We also take surface albedo feedbacks into consideration, as these feedbacks are a significant source of increasing ice loss via melting for a given change in temperature on alpine glaciers. We use a value of 50% to calculate the feedback factor ($c_1\lambda$), which is proportional to the fraction of a system output fed back into the input (Roe, 2009).

Including the feedback factor, we estimate temperature change per unit change in LW radiation as:

$$\Delta T = \frac{\lambda \cdot \Delta R}{1 - c_1 \lambda} \tag{3.9}$$

Note that in Equation (3.9) above, $\lambda$ is the reference-system sensitivity parameter defined in Equation (3.8), and remains unchanged by inclusion of the feedback (Roe, 2009).

The climate variables ($t_{melt}$, $\varepsilon$, and $T_a$) are derived from the ERA-Interim product (Dee et al., 2011). ERA-Interim is a global atmospheric reanalysis from 1979 to present, which uses a data assimilation system to forecast a full range of climate variables. We calculate the reference temperature ($T_a$) over the average period of melt (May 1-August 31 of each year) during 1979-1985 (overlapping with the start of the satellite observation period) at the average elevation of the assumed area of melt (e.g. the lowest half of the glacierized area). Temperature lapse rates ($\Gamma$) are calculated at each grid point within ERA-Interim corresponding to a glacier, by fitting linear trends to atmospheric temperatures at each pressure level from the surface up to the 200 hPa geopotential height. $\Gamma$ is calculated for the climatology of each month, and the mean lapse rate over the period of melt is then used. The average duration of melt ($t_{melt}$) is calculated at the average elevation of the melt area using average daily temperatures. Emissivity of the atmosphere ($\varepsilon$) was derived from the temperature and downwelling longwave radiation at the surface, averaged over the glacierized area and the period of melt. The average area of melt was assumed to range between the full glacierized area to one quarter of the glacierized area. These areas likely represent extreme end-members of possible areas of melt. However, as the assumed area of melt increases, the average number of days over which melt occurs decreases accordingly. We note that there are significant uncertainties associated with input data from

ERA-Interim, scaling of temperatures from coarse reanalysis grids to specific glacier elevations, and the averaging of climate data over the glacierized region. As practical quantification of these uncertainties, we use the standard deviations of all inputs across the glacierized region to estimate of the range in possible input values.

### 3.8.2 Temperature trends

We first summarize several studies which compile temperature records across large regions in HMA and South Asia (Figure 3.5A), and also highlight meteorological data from key high elevation weather stations in the Himalayas (Figure 3.5B), including two temperature records from individual stations located in close proximity to benchmark glaciers in the western Himalaya (Chhota Shigri glacier) and in the Everest region (Dingri station). The longest analysis from Ren et al. (2017) is based on the quality-controlled and homogenized climate datasets LSAT-V1.1 and CGP1.0 recently developed by the China Meteorological Administration (CMA), using approximately 94 meteorological stations located throughout the Hindu Kush Himalayan region. The study finds a significant increasing trend in mean air temperature of 0.104 °C/decade during 1901-2014. Xu et al. (2017) present results derived from a similar CMA dataset (81 stations), but more focused in the eastern Tibetan Plateau. They calculate an area-weighted warming rate of 0.35 °C/decade during 1961-2015, with winter temperatures having the highest rates of warming, followed by autumn, spring, and summer (0.44, 0.38, 0.30, and 0.30 °C/decade, respectively). Kattel et al. (2013) utilize three decades of temperature data from 13 mountain stations located on the southern slopes of the central Himalayas to determine that the thermal regime likely shifted in the mid-1990's, and observe a dramatic increase in mean annual average and maximum temperatures after 1997. Dimri et al. (2017) analyze trends in winter temperature (Dec-Feb) during 1985-2007 at three glacierized regions in the western

Himalayas; for a station near the Chhota Shigri glacier terminus (within our region of study), they calculate a positive trend of 0.6 °C/decade. Yang et al. (2011) present air temperature records in the Everest region, including a multi-decade record from Dingri meteorological station, and calculate an increase of 0.62 °C/decade in mean annual temperature during 1959-2007, with a moderate warming trend in the mid-1980's and an accelerated warming trend after 1998. Another study by Shekhar et al. (2010) includes an analysis of temperature data from three stations in the western Himalayas (Kanzalwan, Drass, and Patseo stations). They calculate increases of 1.1 °C and 0.5 °C/decade in maximum and minimum annual temperatures, respectively, during Nov-Apr of 1988-2007. Yan and Liu (2014) analyzed temperatures during 1961-2012 from 16 weather stations above 4000 m in the Tibetan Plateau and eastern Himalaya, and found the annual mean temperature increased by 0.24 °C/decade during 1961-2000, and 0.5 °C/decade during 2001-2012. A common pattern appears when these temperature records are plotted together (Figure 3.5). Quasi-steady mean annual air temperatures are evident during the 1960-80's, with a clear warming trend beginning in the mid -1990's and continuing into the 2000's. This is true for both the regional HMA temperature compilations and high elevation station data located near Himalayan glaciers. In turn, our observations of more rapid ice loss across the Himalayas during 2000-2016 (relative to the 1975-2000 interval) correlate with the consistently warmer air temperatures during the 21$^{st}$ century.

### 3.8.3 Precipitation trends

Summer precipitation largely exceeds winter precipitation in the Himalayas, due to moisture advected northward from the Indian Ocean by the summer monsoon in late June through September (Palazzi et al., 2013). As a result of the monsoon, most Himalayan glaciers accumulate the majority of their snow during summer months (Ageta and Higuchi, 1984). In situ

and satellite precipitation rate estimates face major challenges over the Himalayan range, due to the topographic complexity of the region, sparsity of high elevation weather stations, coarse resolution of gridded datasets, and difficulties in detecting the snow component of precipitation from satellite assessments. Large precipitation gradients over short horizontal distances are common due to the extreme topography, and overall spatial heterogeneity of precipitation in the region is high (Immerzeel et al., 2014b). Palazzi et al. (2013) analyzed mountain precipitation trends using several satellite, reanalysis, and gridded rain gauge datasets, and found averaged precipitation data over the Himalayas resulted in slightly negative summer daily precipitation trends for two of the longest observational datasets, specifically -0.01 mm $yr^{-1}$ (APHRODITE) and -0.02 mm $yr^{-1}$ (GPCC) over a 60 year interval; though the authors note difficulties with coarse resolution of the datasets, and inhomogeneities in the spatial and altitudinal distribution of the measuring sites. On the other hand, Shrestha et al. (2000) analyzed precipitation records from 78 stations distributed across Nepal during 1959-1994, and found significant variability on annual and decadal timescales, yet no distinct long-term trends in precipitation. Spectral analysis of some speleothem $\delta^{18}O$ and instrumental records indicate nonstationary 30-60 year periodicities in monsoon strength (Bhutiyani et al., 2010; Sinha et al., 2015), a weakening of El Niño–Southern Oscillation (ENSO) teleconnections since the 1960's (Krishnamurthy and Goswami, 2000), and a slight decreasing trend in monsoon precipitation over India during the last 50 years, possibly due to anthropogenic aerosol loading (Bollasina et al., 2011). However, an extreme decrease in precipitation across the entire Himalayan range would be needed to explain the magnitude, acceleration, and spatial consistency of glacier changes we observe. Rupper et al. (2012) estimate that Bhutanese glaciers would require a precipitation decrease on the order of 500 mm to raise the ELA (equilibrium line altitude) by the same amount as would

occur from a 1 °C increase in air temperature, although the mass balance value of -1.4 m w.e. $yr^{-1}$ from that study appears to be too negative compared to recent remote sensing estimates. In general, energy and mass balance models indicate monsoon-dominated glaciers with high accumulation rates are much more sensitive to temperature than accumulation changes (Naito et al., 2001; Oerlemans and Fortuin, 1992; Rupper and Roe, 2008; Shea and Immerzeel, 2016), and a large widespread decrease in precipitation has not been observed across the Himalayas during the last four decades.

### 3.8.4 Detailed comparison with prior studies in the Himalayas

We compare our results with mass balances reported by previous remote sensing studies in the Himalayas, in order to evaluate similarities and differences between them. Many factors may contribute to the variation of results between studies, including different spatial resolutions of imagery, DEM alignment techniques, interpolation methods, definitions of glacier boundaries, spatial and temporal coverage, and ice/firn density assumptions. Yet we find that in general, estimates overlap within uncertainties. In the eastern Himalayas, Maurer et al. (2015) calculated $-0.17 \pm 0.05$ m w.e. $yr^{-1}$ during 1974-2006, which was a conservative estimate because data gaps were filled assuming zero elevation change for regions of no data. Using additional Hexagon imagery and the improved methodology in this study, we now estimate a geodetic mass balance of $-0.21 \pm 0.08$ m w.e. $yr^{-1}$ for this same region during 1975-2000. Zhou et al. (2018) recently used declassified Hexagon imagery and SRTM data to estimate mass balances in various regions of HMA during 1975-2000. Their work encompasses several areas which our survey does not include, for example parts of the Karakoram, Kunlun Shan, and the Tibetan Plateau. In the Himalayas, our presented analysis provides a comparatively greater extent of measured glaciers (total area of 6100 $km^2$, compared to 2271 $km^2$), which is more representative of the region as a

whole. We find that restricting our results to more limited regions covered by Zhou et al. yields similar values, with the greatest differences in the Spiti Lahaul and West Nepal regions but still overlapping within uncertainties (Table S3.1A). In Spiti Lahaul, we estimate an average mass balance less negative than reported by Vijay and Braun (2016) during 2000-2012, and more negative than reported by Mukherjee et al. (2017) during 1971-1999 and 2000-2013 (Table S3.1D).

We also compare our 1975-2000 glacier change data to previous landmark studies at the individual glacier level in both the Everest (Bolch et al., 2011) and the Langtang Himal (Pellicciotti et al., 2015; Ragettli et al., 2016) regions. In the Everest region, Bolch et al. (2011) used declassified Corona imagery and ASTER to estimate mass changes during 1970-2007 and 2002-2007. After adjusting our mass changes for the 1970-2007 timespan (see footnote in Table S3.1) we find relatively good agreement during this interval, with most glacier mass change estimates overlapping within uncertainties. On the other hand, our average value of -0.48 ± 0.03 m w.e. $yr^{-1}$ (here ± is the standard error of the weighted mean of six glaciers) during 2000-2016 is significantly different from the Bolch et al. estimate of -0.73 ± 0.24 m w.e. $yr^{-1}$ during 2002-2007. However this may be explained by the larger error bars resulting from their shorter timespan (2002-2007), and more recent studies are in agreement with our value for the Khumbu region (Gardelle et al., 2013; Nuimura et al., 2012). In the Langtang Himal, we compare our results for three separate glaciers with two prior analyses (Pellicciotti et al., 2015; Ragettli et al., 2016) (Table S3.1F). While estimates vary significantly for individual glaciers, area-weighted mean values are similar across all three studies (-0.28 ± 0.12 m w.e. $yr^{-1}$ during 1974-1999, -0.24 ± 0.06 m w.e. $yr^{-1}$ during 1974-2006, and -0.25 ± 0.04 m w.e. $yr^{-1}$ during 1975-2000). For the more recent interval, the weighted mean from the Ragettli et al. (2016) data during 2006-2015 is

-0.45 ± 0.09 m w.e. $yr^{-1}$, which is comparable to our estimate of -0.58 ± 0.04 m w.e. $yr^{-1}$ during 2000-2016.

For the 2000-2016 interval we compare our results to prior remote sensing estimates over the Spiti Lahaul, West Nepal, East Nepal, and Bhutan regions (Table S3.1C). These combined regions approximately match our study area, and include mass balances of -0.35 ± 0.08 m w.e. $yr^{-1}$ from SRTM/SPOT5 during 1999-2011 (Gardelle et al., 2013), -0.42 ± 0.12 m w.e. $yr^{-1}$ from ICESat during 2003-2008 (Kääb et al., 2015), and -0.36 ± 0.07 m w.e. $yr^{-1}$ from ASTER during 2000-2016 (Brun et al., 2017). Our Himalayas-wide estimate of -0.43 ± 0.14 m w.e. $yr^{-1}$ during 2000-2016 is consistent with these prior estimates. Compared to the values reported by Brun et al. (2017), our ASTER processing methodology yields more negative mass balances, but still overlapping within uncertainties. However, we multiply our mass balances by the smaller total glacierized area from our manually refined RGI inventory, while Brun et al. use the larger GAMDAM glacier inventory. Thus, both estimates arrive at similar region-wide ice mass changes of -7.5 ± 2.3 Gt $yr^{-1}$ and -7.1 ± 1.4 Gt $yr^{-1}$ using the same ASTER data.

Based on our manually edited glacier polygons for 1975 and 2016 (Materials and Methods), we find that the total area of the 650 largest glaciers decreased by approximately 5% over the 40-year interval (0.13% per year). As expected this area change rate is smaller than reported by previous studies (Bajracharya et al., 2014; Bolch et al., 2012; Ojha et al., 2016; Racoviteanu et al., 2014). This may be explained by the omission of small glaciers in our dataset which tend to have the largest % changes in area (Ojha et al., 2016; Racoviteanu et al., 2014), and also because our manually edited polygons focus on capturing frontal variations of the large glaciers, rather than other factors such as decreasing snow cover. This supports the use of geodetic mass balance as the metric of ice loss for our purposes, rather than glacier area or length changes.

### 3.8.5 Supplementary Figures and Tables

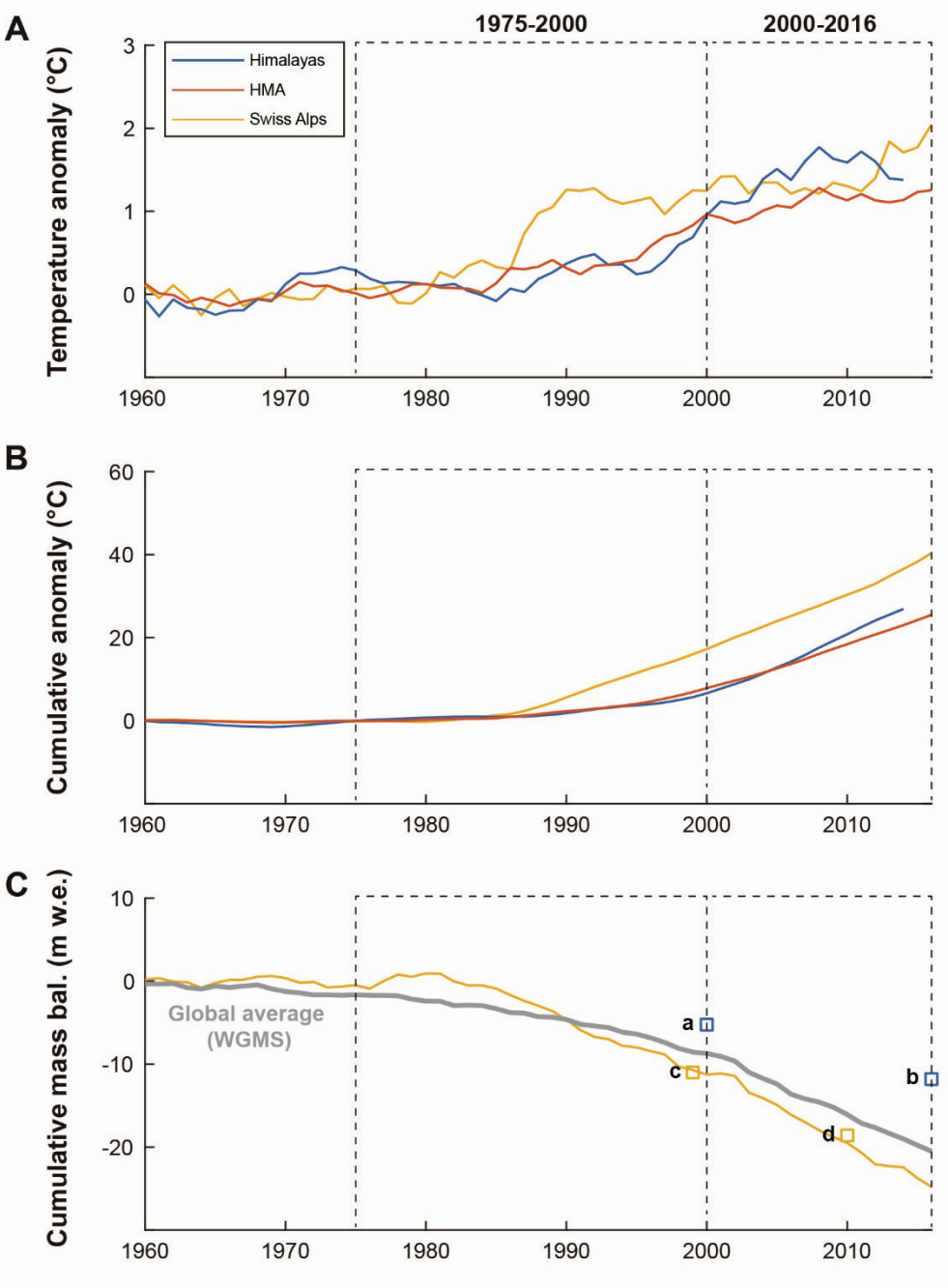


D

| Average mass balances (m w.e. yr$^{-1}$) | | |
|---|---|---|
| | 1975-2000 | 2000-2016 |
| Himalayas | -0.22 | -0.43 |
| Swiss Alps | -0.43 | -0.84 |
| Global average | -0.28 | -0.74 |

Figure S3.1. Comparison of Himalayan temperature trends and regional mass balance with benchmark mid-latitude glaciers and a global average trend. (A) Five-year moving means of air temperature anomalies in the Himalayas and HMA (from Figure 3.5) and the Swiss Alps above 1000 m elevation (Begert and Frei, 2018) relative to the 1960-1975 mean. (B) Cumulative sum of air temperature anomalies in A. (C) Cumulative mass balances. Thick grey line is the WGMS global average from 30 reference glaciers with long-term glaciological measurements (Zemp et al., 2017). Yellow line is the WGMS area-weighted average of glaciers located in the Alps. Corresponding yellow square symbols (c,d) are geodetic estimates from the Alps, assuming cumulative mass balances of zero in 1980 and 1985, respectively (Fischer et al., 2015; Paul and Haeberli, 2008), and blue square symbols (a,b) are geodetic estimates from this study, assuming a cumulative mass balance of zero in 1975. (D) Average mass balances (m w.e. $yr^{-1}$) for each region during 1975-2000 and 2000-2016.

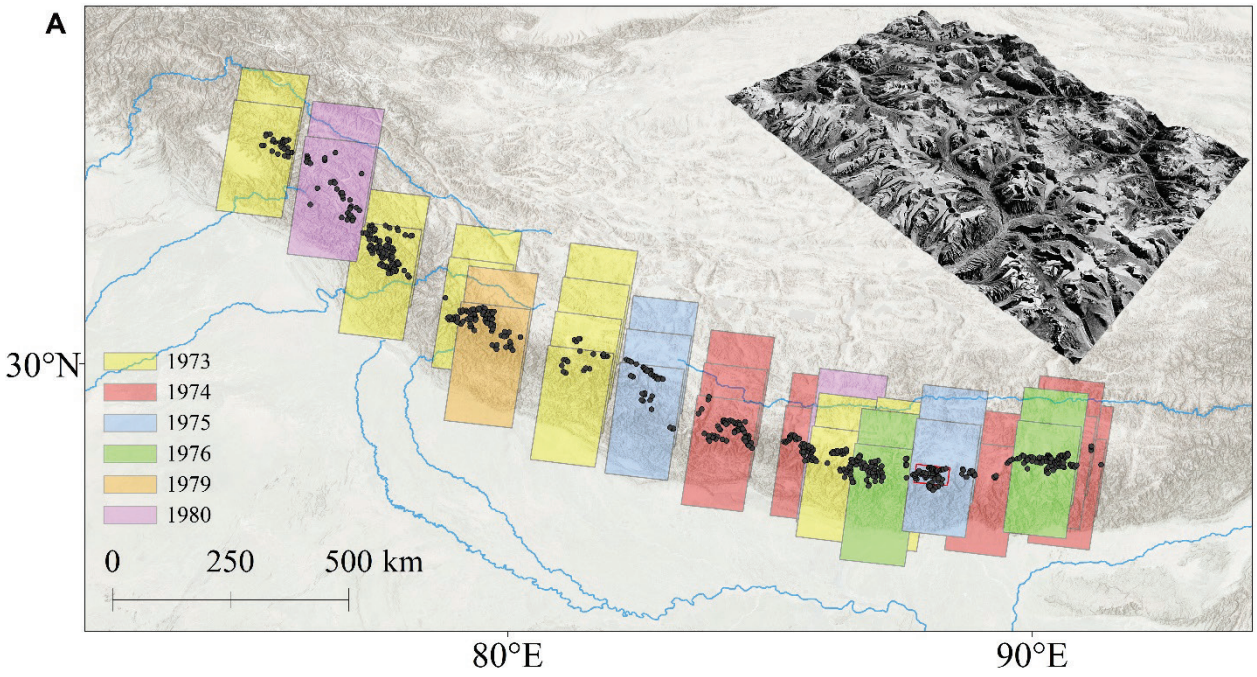


B

| | 1975-2000 | | 2000-2016* | | 1975-2016 | |
|---|---|---|---|---|---|---|
| | Area ($km^2$) | Count | Area ($km^2$) | Count | Area ($km^2$) | Count |
| Glaciers > 3 $km^2$ with >33% coverage | 6.1E+03 | 650 | 9.5E+03 | 1038 | 6.1E+03 | 650 |
| Thickness change data coverage | 3.8E+03 | -- | 7.3E+03 | -- | 3.7E+03 | -- |
| All Glaciers > 3 $km^2$ | 1.0E+04 | 1098 | 9.9E+03 | 1098 | 1.0E+04 | 1098 |
| All Glaciers | 1.8E+04 | 17373 | 1.7E+04 | 17373 | 1.8E+04 | 17373 |

* While this interval has better spatial coverage, we only use data common to all intervals (i.e. 650 glaciers) during the analysis

Figure S3.2. Coverage of glacierized area in the Himalayas. (A) Footprints of KH-9 Hexagon images used in this study. Box colors indicate acquisition dates, and black dots are locations of glaciers used in this study. The small red box shows location of the inset, which is an oblique view of a Hexagon image acquired in 1975 on the Nepal-Sikkim border. (B) Coverage of glacierized area in the Himalayas during each respective interval. For the 1975-2000 interval the average individual glacier data coverage is 63% (min = 34%, max = 95%), and for 2000-2016 the average is 82% (min = 36%, max = 96%) for the 650 glaciers common to both intervals.

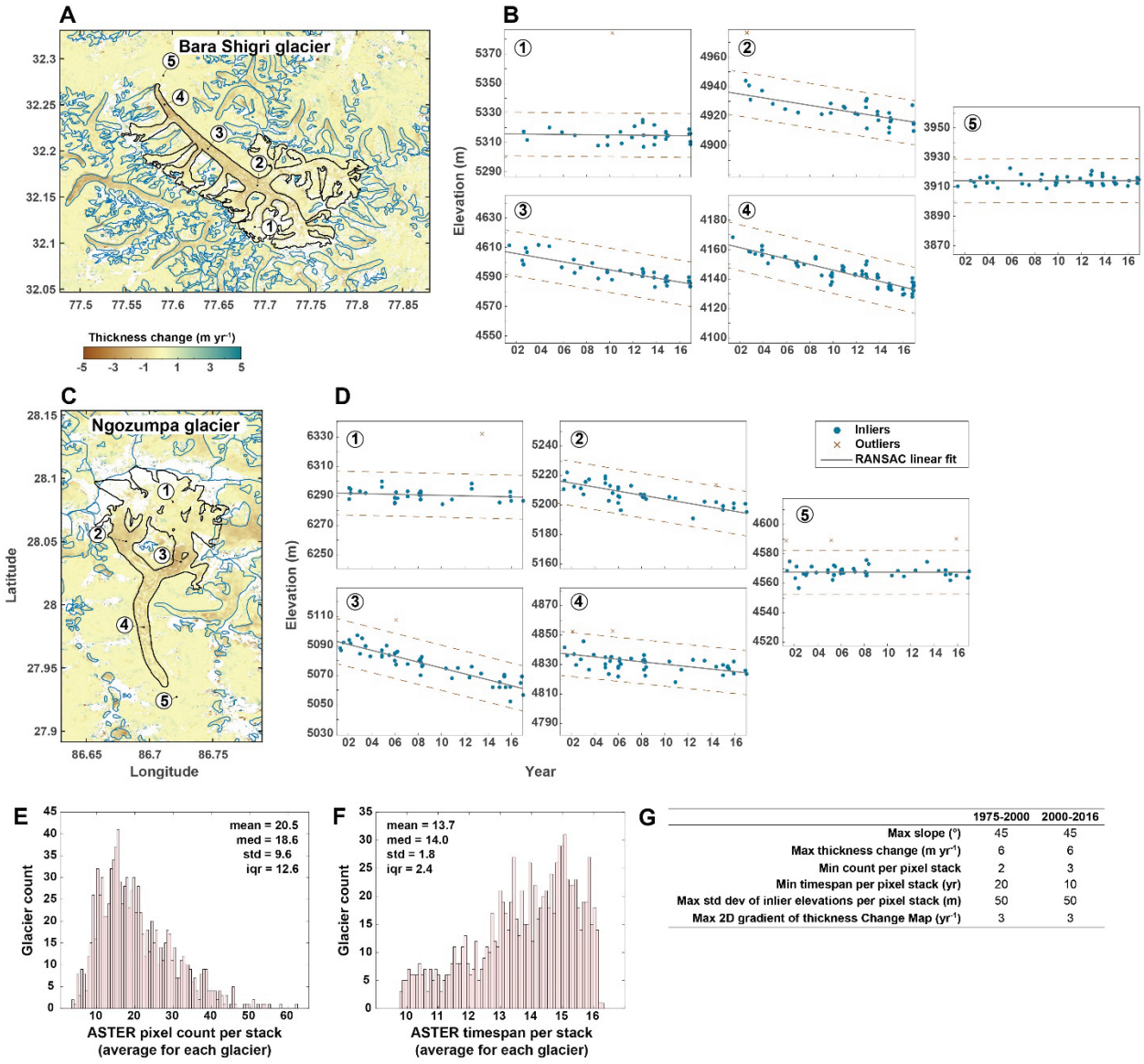


G

| | 1975-2000 | 2000-2016 |
|---|---|---|
| Max slope (°) | 45 | 45 |
| Max thickness change (m yr⁻¹) | 6 | 6 |
| Min count per pixel stack | 2 | 3 |
| Min timespan per pixel stack (yr) | 20 | 10 |
| Max std dev of inlier elevations per pixel stack (m) | 50 | 50 |
| Max 2D gradient of thickness Change Map (yr⁻¹) | 3 | 3 |

Figure S3.3. Trend fit examples for two large glaciers using ASTER DEMs during 2000-2016, histograms of ASTER pixel counts and timespans per stack (glacier averages), and outlier thresholds. (A) Thickness change map (m $yr^{-1}$) for the Bara Shigri glacier (western Himalaya). Labels 1-5 correspond to plots on the right. (B) Corresponding RANSAC linear fits for individual pixels. Blue dots represent inlier elevations, dotted red lines represent the ±15 m outlier threshold, and red 'x' symbols are outliers detected and excluded by the RANSAC algorithm. (C, D) same, except for the Ngozumpa glacier (eastern Himalaya). (E) This gives a sense of the number of ASTER DEMs used per glacier during the RANSAC trend fitting procedure for all glaciers in our region of study. Computed by counting the number of elevation pixels in each pixel stack (after RANSAC exclusion), then taking the average over all pixel stacks for a given glacier. The average number of ASTER elevation pixels used (per glacier) is 20.5. (F) Similar to E, but gives a sense of the timespan of ASTER data for each glacier. (G) Outlier thresholds for computing trends.

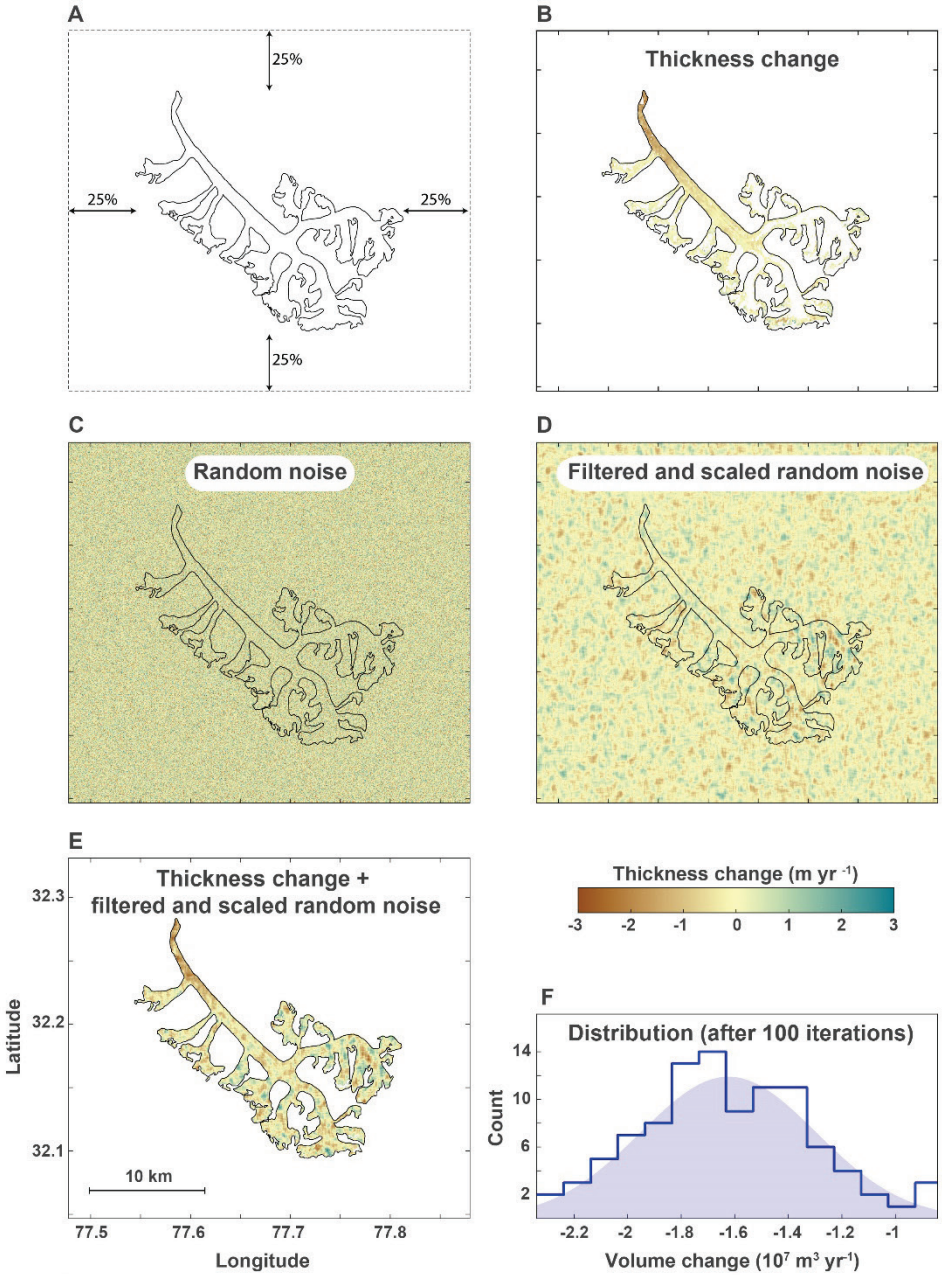


G

| Interval | Test | Void-filling method | Mean thickness change (m yr$^{-1}$) | Geodetic mass balance (m.w.e. yr$^{-1}$) | Mass change (Gt yr$^{-1}$) | Sea level rise (mm yr$^{-1}$) |
|---|---|---|---|---|---|---|
| 1975-2000 | 1 | a | -0.26 | -0.22 | -3.8 | 0.009 |
| | | b | -0.27 | -0.23 | -4.1 | 0.010 |
| 1975-2000 | 2 | a | -0.23 | -0.20 | -3.5 | 0.008 |
| | | b | -0.26 | -0.22 | -3.8 | 0.009 |
| 2000-2016 | 1 | a | -0.48 | -0.41 | -7.2 | 0.017 |
| | | b | -0.50 | -0.43 | -7.4 | 0.017 |
| 2000-2016 | 2 | a | -0.44 | -0.37 | -6.6 | 0.016 |
| | | b | -0.47 | -0.40 | -7.0 | 0.016 |
| 2000-2016 | 3 | a | -0.47 | -0.40 | -7.1 | 0.017 |
| | | b | -0.51 | -0.44 | -7.6 | 0.018 |
| 1975-2016 | 1 | a | -0.34 | -0.29 | -5.1 | 0.012 |
| | | b | -0.36 | -0.30 | -5.3 | 0.013 |

**Tests:** 1 - glaciers larger than 3 km$^2$, 2 - all available glaciers, 3 - only using 2000-2016 pixels where 1975-2000 pixels also exist

**Void filling methods:** a - interpolation, b - extrapolation from surrounding glaciers (Methods)

Figure S3.4. Illustration of uncertainty estimation procedure for a single iteration/glacier, and Himalaya-wide sensitivity tests. (A) All raster DEMs are allowed a 25% extended border around each glacier, in order to provide sufficient stable terrain for uncertainty analysis. The 25% refers to the width and height of the glacier bounding box. The Bara Shigri glacier during 1975-2000 is used as an example. (B) Ice thickness change map in m $yr^{-1}$, note missing data in high elevation accumulation zones. (C) Random error field with a mean of zero and standard deviation of one. (D) Random error field after filtering and scaling [see second term in Equation (3.2)] using an autocorrelation range of 500 m. This random error field now has spatial autocorrelation, with greater amplitude of noise over incomplete data regions (see panel b). (E) Ice thickness change map + filtered and scaled random noise field. This is $\Delta H_E$ in Equation (3.2). (F) Resulting distribution of volume change estimates for the glacier after 100 iterations, using a different random error field each time. The standard deviation of this distribution is used for the glacier's 1-sigma uncertainty estimate $\sigma_{\Delta V}$. (G) Sensitivity tests for Himalaya-wide estimates to potential biases, including the exclusion of small glaciers, incomplete data coverage for many glacier accumulation zones during 1975-2000, and void-filling technique (Materials and Methods).

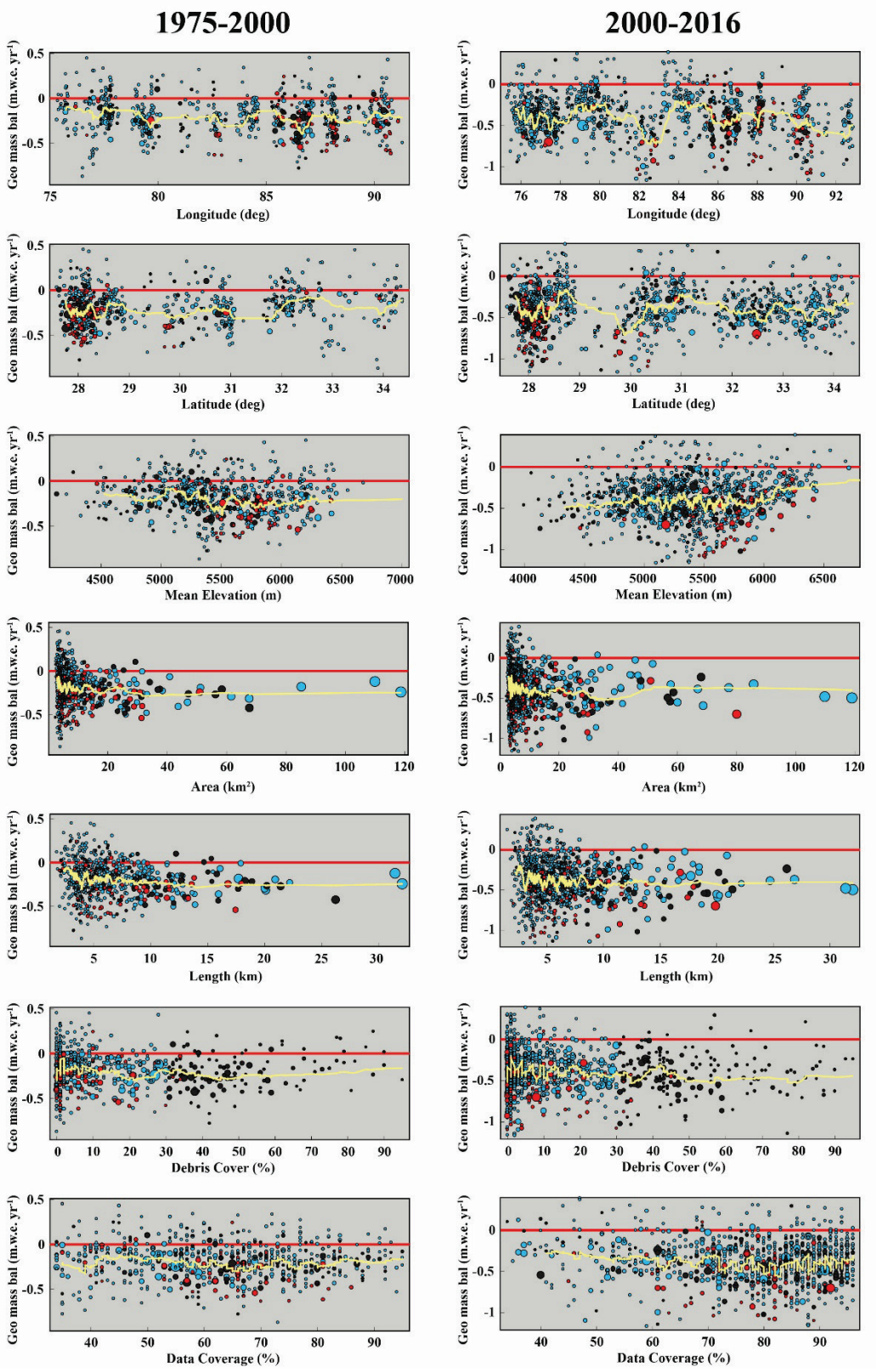


Figure S3.5. Geodetic mass balances during 1975-2000 and 2000-2016 plotted against various parameters. Circle sizes are proportional to glacier areas, and colors delineate clean-ice (blue), debris-

covered (black), and lake-terminating (red) categories. Yellow trends are the (area-weighted) moving-window mean, using a window size of 30 glaciers. Note that in this figure only, we include all glaciers available during the 2000-2016 interval, instead of only including glaciers with data available during both intervals as in most other portions of the study.

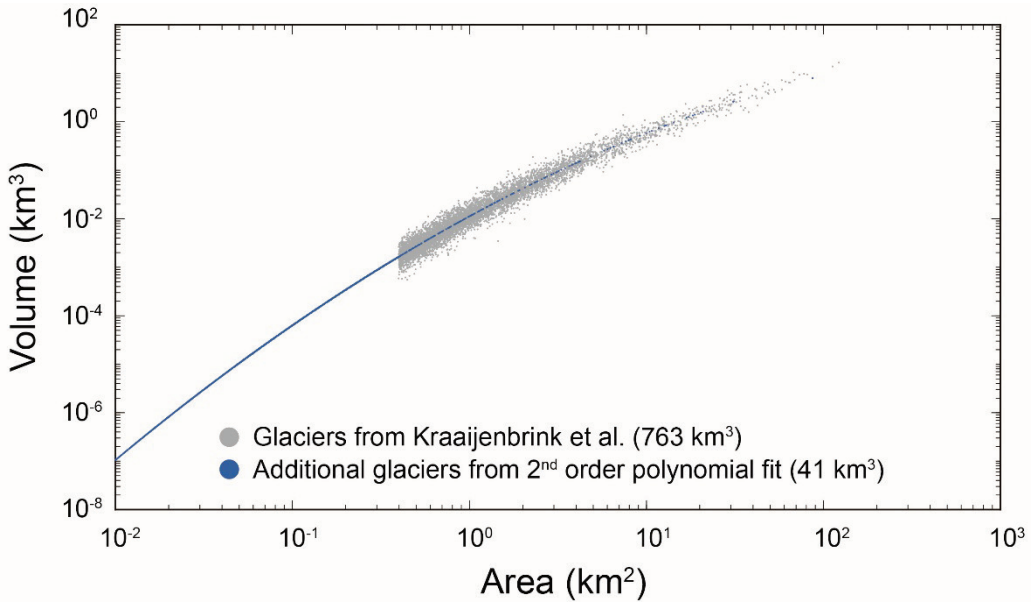


Figure S3.6. Log-log plot of glacier volumes versus areas, used to estimate the total ice mass present in our region of study. Grey points are glaciers from Kraaijenbrink et al. which amount to a total of 763 $km^3$ (15), and blue points are glaciers which were missing ice thickness estimates, thus ice volumes were estimated using a 2nd order polynomial fit, contributing an additional 41 $km^3$.

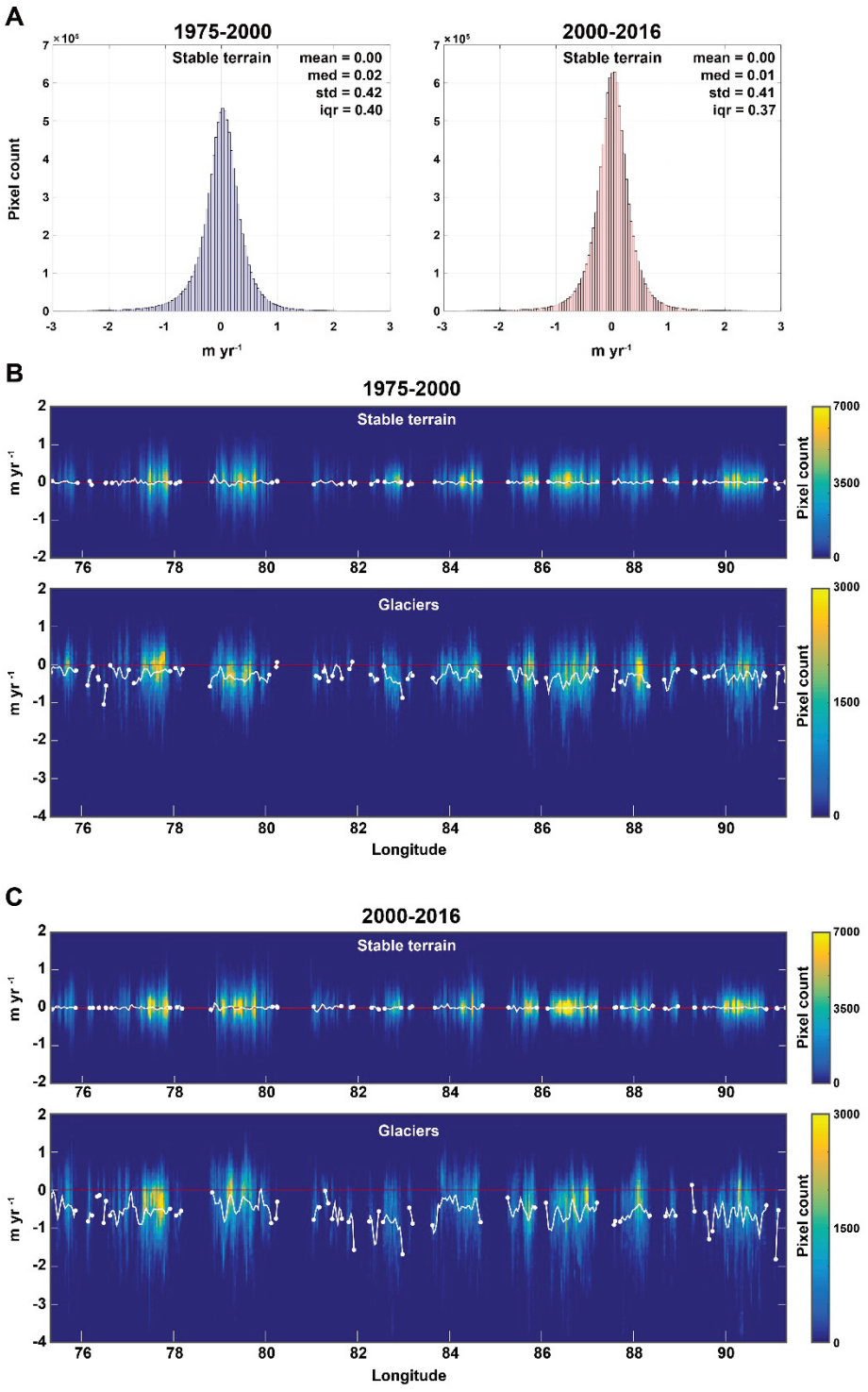


Figure S3.7. Analysis of elevation change for non-glacier pixels (stable terrain) during both intervals. (A) Elevation change histograms. The mean, median, standard deviation, and inter-quartile range of distributions are also given. (B) Density plots of elevation change along the longitudinal transect during 1975-2016, separated into non-glacier (stable terrain) and glacier pixels. Colors indicate pixel counts at the given longitude and the y-axis represents elevation change (m $yr^{-1}$). White lines are the mean trend fit using a smoothing spline. (C) Same, but for the 2000-2016 interval.

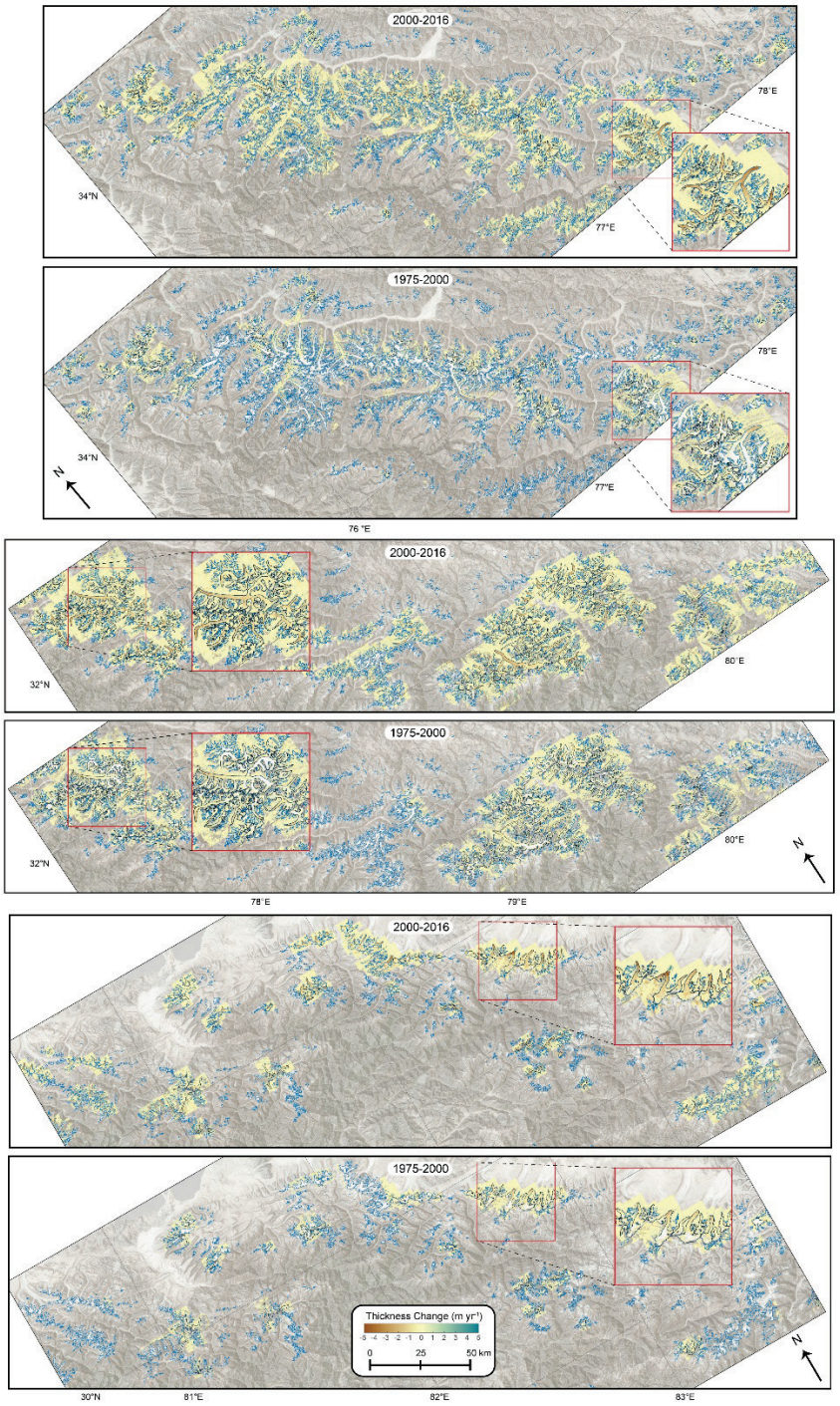


Figure S3.8. Thickness change maps used in the analysis. Thickness changes (m $yr^{-1}$) are shown for three regions of the Himalayas for both 1975-2000 and 2000-2016 intervals. Glaciers used in the analysis are outlined in black, all other glaciers are outlined in blue. Note that the 2000-2016 data coverage is generally more comprehensive, and 1975-2000 data is particularly sparse in the Spiti Lahaul region (top panels).

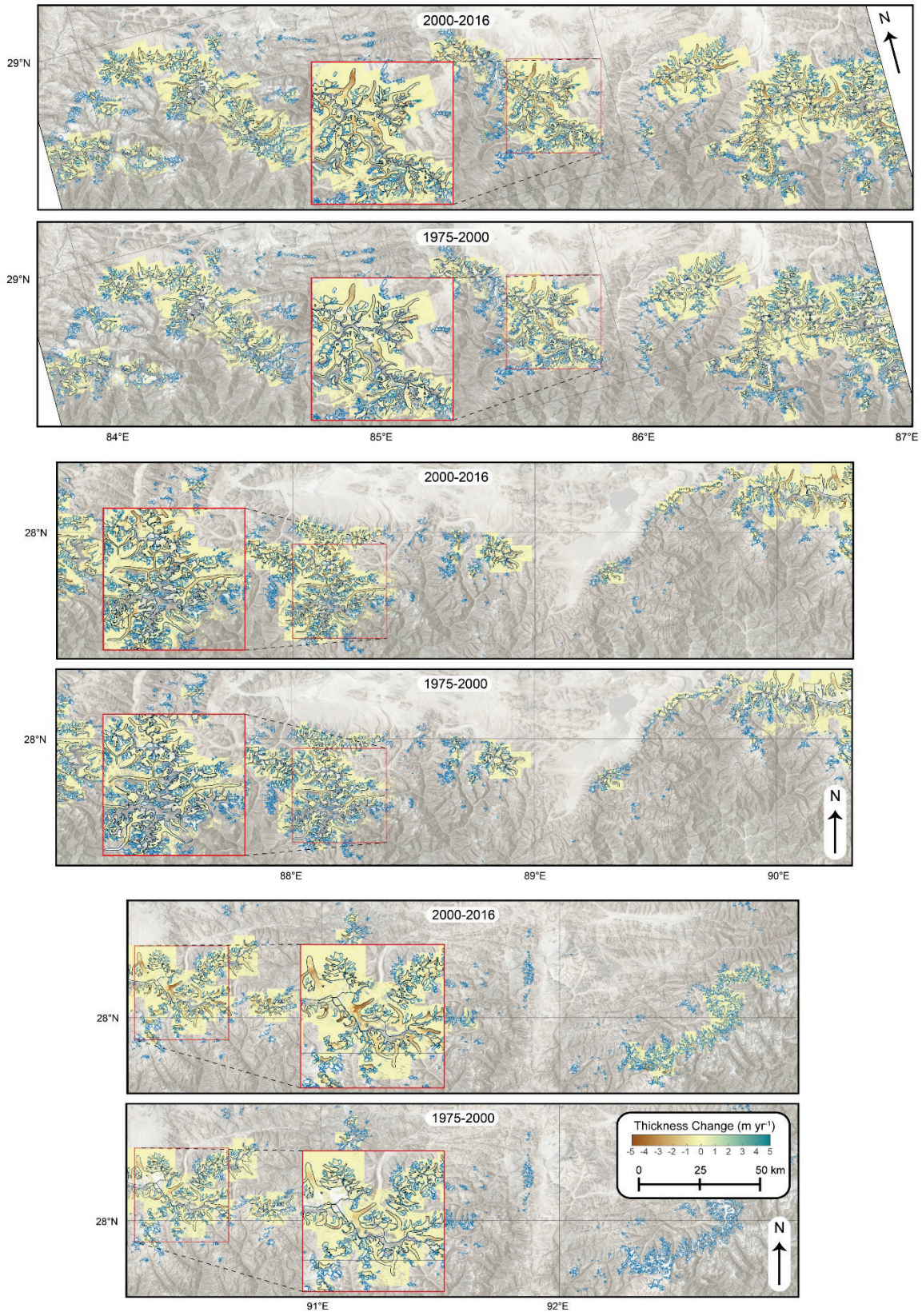


Figure S3.9. Thickness change maps for the three remaining Himalayan regions.

Table S3.1. Geodetic mass balance comparisons with prior studies. For each comparison, we restrict our data to roughly the same general regions defined by each corresponding study. (A-D) Comparisons of regional averages. (E, F) Comparisons of individual glaciers in the Everest and Langtang Himal regions, respectively. Means (weighted by glacierized areas) are given in the last row of each table.

**A**

| | Zhou et al. (2018) | this study | |
|---|---|---|---|
| | 1975-2000 | 1975-2000 | 2000-2016 |
| **Spiti Lahaul** | -0.04 ± 0.10 | -0.13 ± 0.11 | -0.48 ± 0.11 |
| **West Nepal** | -0.23 ± 0.18 | -0.35 ± 0.12 | -0.70 ± 0.15 |
| **Central Nepal** | -0.28 ± 0.11 | -0.25 ± 0.10 | -0.46 ± 0.12 |
| **Sikkim** | -0.30 ± 0.12 | -0.27 ± 0.12 | -0.42 ± 0.12 |
| **weighted mean*** | -0.20 ± 0.06 | -0.22 ± 0.06 | -0.48 ± 0.06 |

**B**

| | Maurer et al. (2016) | this study | | |
|---|---|---|---|---|
| | 1974-2006 | 1975-2000 | 1974-2006† | 2000-2016 |
| **Bhutan** | -0.17 ± 0.05 | -0.21 ± 0.08 | -0.26 ± 0.08 | -0.48 ± 0.10 |

**C**

| | Gardelle et al. (2013) | Kääb et al. (2015) | Brun et al. (2017) | this study | |
|---|---|---|---|---|---|
| | 2000-2010 | 2003-2008 | 2000-2016 | 1975-2000 | 2000-2016 |
| **Spiti Lahaul** | -0.45 ± 0.14 | -0.42 ± 0.26 | -0.37 ± 0.09 | -0.15 ± 0.14 | -0.45 ± 0.15 |
| **West Nepal** | -0.32 ± 0.14 | -0.37 ± 0.15 | -0.34 ± 0.09 | -0.28 ± 0.13 | -0.38 ± 0.14 |
| **East Nepal** | -0.26 ± 0.14 | -0.31 ± 0.14 | -0.33 ± 0.20 | -0.22 ± 0.12 | -0.41 ± 0.12 |
| **Bhutan** | -0.22 ± 0.14 | -0.76 ± 0.20 | -0.42 ± 0.20 | -0.25 ± 0.12 | -0.51 ± 0.15 |
| **weighted mean*** | -0.35 ± 0.08 | -0.42 ± 0.12 | -0.36 ± 0.07 | -0.21 ± 0.07 | -0.43 ± 0.08 |

**D**

| | Vijay and Braun (2016) | Mukherjee et al. (2018) | | this study | |
|---|---|---|---|---|---|
| | 2000-2012 | 1971-1999 | 2000-2013 | 1975-2000 | 2000-2016 |
| **Spiti Lahaul** | -0.55 ± 0.37 | -0.07 ± 0.10 | -0.30 ± 0.10 | -0.14 ± 0.07 | -0.46 ± 0.08 |

**E**

| | Bolch et al. (2011) | | this study | | |
|---|---|---|---|---|---|
| | 1970-2007 | 2002-2007 | 1975-2000 | 1970-2007† | 2000-2016 |
| **Everest** | | | | | |
| Lhotse | -0.26 ± 0.08 | -1.10 ± 0.52 | -0.09 ± 0.08 | -0.20 ± 0.08 | -0.67 ± 0.09 |
| Nuptse | -0.25 ± 0.08 | -0.40 ± 0.53 | -0.12 ± 0.06 | -0.17 ± 0.07 | -0.38 ± 0.08 |
| Changri Shar/Nup | -0.28 ± 0.08 | -0.29 ± 0.52 | -0.18 ± 0.06 | -0.24 ± 0.06 | -0.48 ± 0.07 |
| Khumbu | -0.27 ± 0.08 | -0.45 ± 0.52 | -0.29 ± 0.05 | -0.31 ± 0.05 | -0.39 ± 0.06 |
| Amadablam | -0.29 ± 0.08 | -0.56 ± 0.52 | -0.32 ± 0.09 | -0.35 ± 0.09 | -0.49 ± 0.10 |
| Imja/Lhotse Shar | -0.50 ± 0.09 | -1.45 ± 0.52 | -0.39 ± 0.08 | -0.42 ± 0.08 | -0.53 ± 0.08 |
| **weighted mean*** | -0.32 ± 0.04 | -0.73 ± 0.24 | -0.26 ± 0.03 | -0.30 ± 0.03 | -0.48 ± 0.03 |

**F**

| | Pellicciotti et al. (2015) | Ragettli et al. (2016) | | this study | | |
|---|---|---|---|---|---|---|
| | 1974-1999 | 1974-2006 | 2006-2015 | 1975-2000 | 1974-2006† | 2000-2016 |
| **Langtang Himal** | | | | | | |
| Langshisha | -0.79 ± 0.18 | -0.10 ± 0.08 | -0.38 ± 0.18 | -0.25 ± 0.06 | -0.34 ± 0.06 | -0.74 ± 0.09 |
| Langtang | -0.10 ± 0.18 | -0.24 ± 0.08 | -0.47 ± 0.13 | -0.25 ± 0.05 | -0.30 ± 0.05 | -0.55 ± 0.06 |
| Shalbachum | -0.40 ± 0.18 | -0.36 ± 0.09 | -0.45 ± 0.18 | -0.25 ± 0.06 | -0.30 ± 0.06 | -0.52 ± 0.07 |
| **weighted mean*** | -0.28 ± 0.12 | -0.24 ± 0.06 | -0.45 ± 0.09 | -0.25 ± 0.04 | -0.31 ± 0.04 | -0.58 ± 0.04 |

* Weighted by glacierized areas. Here the ± uncertainties are standard errors of the weighted means.

† Average of the two intervals (1975-2000 and 2000-2016), weighted by the amount of temporal overlap with the desired interval for comparison.

# Chapter 4: Glacier retreat through the Younger Dryas in the European Alps and climatic implications

The Late Glacial (LG) period (15-11 ka) was a dramatic interval of natural climate variability. Moraine chronologies around the globe preserve a record of glacier advances and stabilizations superimposed on a general pattern of recession, yet precise magnitude, timing, and climate drivers remain somewhat controversial. Here we present a high-precision $^{10}$Be chronology and geomorphic map from a sequence of well-preserved LG moraines in the Nendaz valley of the western European Alps, with the goal to shed light on the timing and magnitude of glacier responses in this region. Moraine boulders from the lower valley yield ages ranging from 13.3 ka to 12.7 ka corresponding to the early Younger Dryas, while boulders from the middle valley yield ages ranging from 12.1 to 11.4 ka corresponding to the late Younger Dryas. In an adjacent higher elevation tributary valley, boulders from an independent early Holocene terminal moraine and associated recessional moraine date to approximately 11.0 ka and 10.6 ka, respectively. These results bracket a coherent glacier recession through the Younger Dryas stadial similar to glacier records from the southern hemisphere and a new chronology from Arctic Norway, and provide insight into the relative influences of global radiative forcing versus abrupt AMOC-induced climate events on summer temperatures and mid-latitude mountain glaciers.

## 4.1 Introduction

The study of glacial geomorphology in the European Alps has provided valuable insights into patterns of Quaternary glaciation in the Northern Hemisphere (Braumann et al., in review; Ivy-Ochs, 2015; Krüger, 2013; Penck and Brückner, 1909; Protin et al., 2019; Schimmelpfennig et al., 2012). Modern advances toward high sensitivity $^{10}$Be surface exposure dating (SED) are progressing many traditional views about the timing, magnitude, and spatial patterns of glacier

responses to climate change in the past, and are providing a new framework for detailed investigation of paleoclimate drivers of glacier change. Particularly from the Last Glacial Maximum (LGM) (23-18 ka) to the current Holocene interglacial (the past 11.6 ky) these studies are opening new windows for viewing glacier configurations during a dramatic interval of natural climate variability.

Paleoclimate records show the transition from peak cold of the LGM to the ongoing warm Holocene was interrupted by an interval of cooling known the Late Glacial (LG) period (15–11 ka). In the Southern Hemisphere for example, the Antarctic Cold Reversal (ACR) (14.5–13 ka) triggered advances of southern mid-latitude glaciers (García et al., 2012; Putnam et al., 2010; Sagredo et al., 2018). Prominent cold intervals also occurred in Northern Hemisphere during the LGM to Holocene transition, such as the Oldest Dryas (18.0–14.7 ka), Older Dryas (14.1 ka) and Younger Dryas (YD) (12.9 –11.6 ka) during which $\delta^{18}O$ (water isotope) records from Greenland ice cores (North Greenland Ice Core Project members, 2004; Rasmussen et al., 2014) and other paleoclimate proxies (Heiri et al., 2014; Moreno et al., 2014) show excursions to cooler conditions. These abrupt cooling events have been linked to the slowdown of the Atlantic Meridional Overturning Circulation (AMOC) (McManus et al., 2004), superimposed on a general warming trend with increasing atmospheric greenhouse gas (GHG) concentrations (Clark et al., 2012; Shakun et al., 2012). Characterized by enhanced seasonality, numerous lines of evidence now suggest the colder temperatures during AMOC reduction primarily occurred during winter (Buizert et al., 2014; Buizert et al., 2018; Denton et al., 2005; Kelly et al., 2008) with summers remaining relatively warm (Schenk et al., 2018). As glaciers undergo the majority of melt during summer months, the relative influences of AMOC versus global GHG forcings on glacier mass balances during the LG are somewhat unclear. Significant uncertainties remain

regarding the precise timing of LG glacier fluctuations in the northern hemisphere, particularly in relation to these AMOC-triggered cooling events. Several recent studies are not entirely in tune with the view that glacier advances in the northern hemisphere were a direct response to YD cooling. Results from Greenland, the Scottish Isles, and Alaska suggest that glaciers attained their largest LG extent prior to or in the very early YD, with subsequent retreat through the YD (Bromley et al., 2018; Levy et al., 2016; Young et al., 2019). Following this line of reasoning, it's possible that glaciers in these regions were more strongly influenced by global radiative forcing rather than the winter-biased AMOC signal as previously thought.

In the European Alps, moraines have been traditionally grouped into a number of different stages based on their physical characteristics, morphostratigraphic positions, and estimated ELA depressions (Ivy-Ochs, 2015). Modern SED studies have shown that most moraine ages tend to cluster around two of these stages, locally known as the Gschnitz and the Egesen (Reitner et al., 2016). Moraines associated with the Gschnitz stage have been dated to approximately 17–16 ka, concomitant with Greenland Stadial 2 and Heinrich Event 1 within the Oldest Dryas (Boxleitner et al., 2019; Ivy-Ochs et al., 2006). Moraines associated with the Egesen stage have usually been attributed to the Younger Dryas (Boxleitner et al., 2019; Federici et al., 2008; Ivy-Ochs et al., 1996; Kelly et al., 2004; Protin et al., 2019), and the textbook paradigm that large moraines complexes across the Alps were formed as a result of YD cooling has become a mainstream view. Yet given the modern understand of AMOC seasonality and recent findings of glacier moraines dated to pre or early-YD in other locations, a detailed look at LG moraines and retreat patterns in the Alps may offer a deeper insight into this problem. Here we present a high-precision $^{10}$Be chronology and geomorphic map from a sequence of LG moraines in the western Alps, with the goal to shed light on the timing and magnitude of glacier responses in this region.

We focus on a moraine complex located in the Tortin area of the Nendaz valley, Valais region, in the western Swiss Alps. This well-resolved sequence preserves fine structure of LG and early Holocene glacier fluctuations, and provides an experiment that offers new insights into glacier-climate coupling. In turn, we compile previously published SED ages in the Alps to place the Nendaz valley results within a broader geographical context, and analyze characteristics of these Alpine glacier chronologies relative to cold pulses observed in other paleoclimate proxies.

## 4.2 Setting and methods

### 4.2.1 Study area

Our study area is located in a typical Alpine valley in the Pennine Alps, in the municipality of Nendaz, Valais, Switzerland. The Nendaz valley has a S-N orientation (perpendicular to the main mountain chain) descending into the Rhône Valley. The LG moraine complex is situated below the peaks of Mont Gelé (3023 m), Mont Fort (3328 m), Bec des Etagnes (3231 m) and Rosablanche (3335 m), and the area is a popular tourist destination for hiking in summer and skiing in winter. These mountain peaks are surrounded by several cirque glaciers including the Tortin, Mont Fort, Petit Mont Fort, Etagnes, and Grand Désert. Our target moraines are located in the middle-upper section of the Nendaz valley, near Tortin and Siviez. The region lies in a climatic transition zone with competing influence from the Mediterranean, Continental, Atlantic, and Polar climatological regimes (Beniston, 2005; Sturman and Wanner, 2001). In winter the Alps are influenced by the Icelandic Low and related westerly airflows, interrupted by anticyclonic blocking due to the influence of the Azores High and cold Siberian High. In summer the Azores High extends northeastward and interacts with continental low pressure systems over the region (Sturman and Wanner, 2001). Over decadal timescales, the climate in the Alps is influence by the North Atlantic Oscillation (NAO), which is a large-scale alternation of

atmospheric pressure fields between the Icelandic Low and the Azores High. The latitudinal temperature and pressure gradients associated with the NAO strongly influence storm track positions, precipitation, and temperature patterns in the Alps, particularly during winter months (Beniston, 2005). Generally a positive phase of the NAO results in anomalously low precipitation and higher than average temperatures from late fall to early spring (Casty et al., 2005), while a negative phase of the NAO results in inundation by cold continental air masses from the north and frigid winters in the Alps (Sturman and Wanner, 2001). Tectonically, this region is composed of the Pennenic (Siviez-Mischabel and Mont Fort) nappes, which are large thrust sheets with recumbent folds formed during continental collision between the Adriatic and Eurasian plates in Cenozoic times (Scheiber et al., 2013). Greenish grey to dark green schists comprise the morainic material (including sampled boulders) in the Nendaz valley, with the Métailler formation being the most likely provenance (Sartori et al., 2006). These foliated rocks have a greenschist metamorphic overprint (Scheiber et al., 2013), and are primarily composed of chlorite, amphiboles, albite, and muscovite, with veins and nodules of milky-white quartz common (Sartori et al., 2006).

### 4.2.2 Field and laboratory methods

Moraines were targeted using satellite imagery, aerial photos, and a high-resolution DEM provided by SwissTopo (Wiederkehr and Möri, 2013). Field mapping and sample collection were completed in June and August of 2016. We mapped the moraines based on morphostratigraphic positions, morphological character, continual extent of topographic relief, and cross-cutting relations. Large, well-embedded boulders in moraine ridge crests were sampled using a hammer and chisel on the boulder tops (Figure 4.1). Sampled boulder surfaces showed no evidence of recent post-depositional disturbance or surface erosion such as fresh-looking

surface breaks or lack of lichen cover, and precise boulder locations were measured using a handheld Trimble DGPS unit. Aerial imagery of the field area was aquired using a DJI Phantom quadcopter drone (Figure 4.2). Geochemical processing was performed at the Cosmogenic Nuclide Laboratory at LDEO following well-established standard protocols given in Schaefer et al. (2009), and AMS $^{10}Be/^{9}Be$ measurements were completed at the Purdue Rare Isotope Measurement (PRIME) Laboratory. Samples were measured relative to the 07KNSTD standard ($^{10}Be/^{9}Be = 2.85e{-}12$) (Nishiizumi et al., 2007). and corrected for $^{10}Be$ using procedural blanks, which represent an average change of 0.5% in the $^{10}Be$ concentrations. Analytical 1σ uncertainties ranged between 2 to 8% with an average of 3.9% (Table 4.1). Topographic shielding factors for cosmogenic rays were calculated using the open source code from TopoToolbox (Schwanghart and Kuhn, 2010). Exposure ages were calculated using the online exposure age calculator version 3, formerly known as the CRONUS-Earth online exposure age calculator (Balco et al., 2008) (http://hess.ess.washington.edu/). We used the production rate of Claude et al. (2014) from the independently dated Chironico landslide (southern Swiss Alps) and time-dependent Stone/Lal scaling scheme (Lm) (Borchers et al., 2016; Lal, 1991). For reference, we include ages based on the "St" scaling scheme (Lal, 1991) and compare with the default production ratio in the online exposure age calculator (Table 4.2). To place our results in a broader geographical context, we also compile a set of published LG and early Holocene $^{10}Be$ glacier chronologies in the Alps with all ages recalculated using the same parameters in the exposure age calculator, with a specified SED threshold of 15 to 9 ka comprising 352 samples from 35 studies.


Figure 4.1. Representative boulders from areas sampled in the Nendaz valley field area.

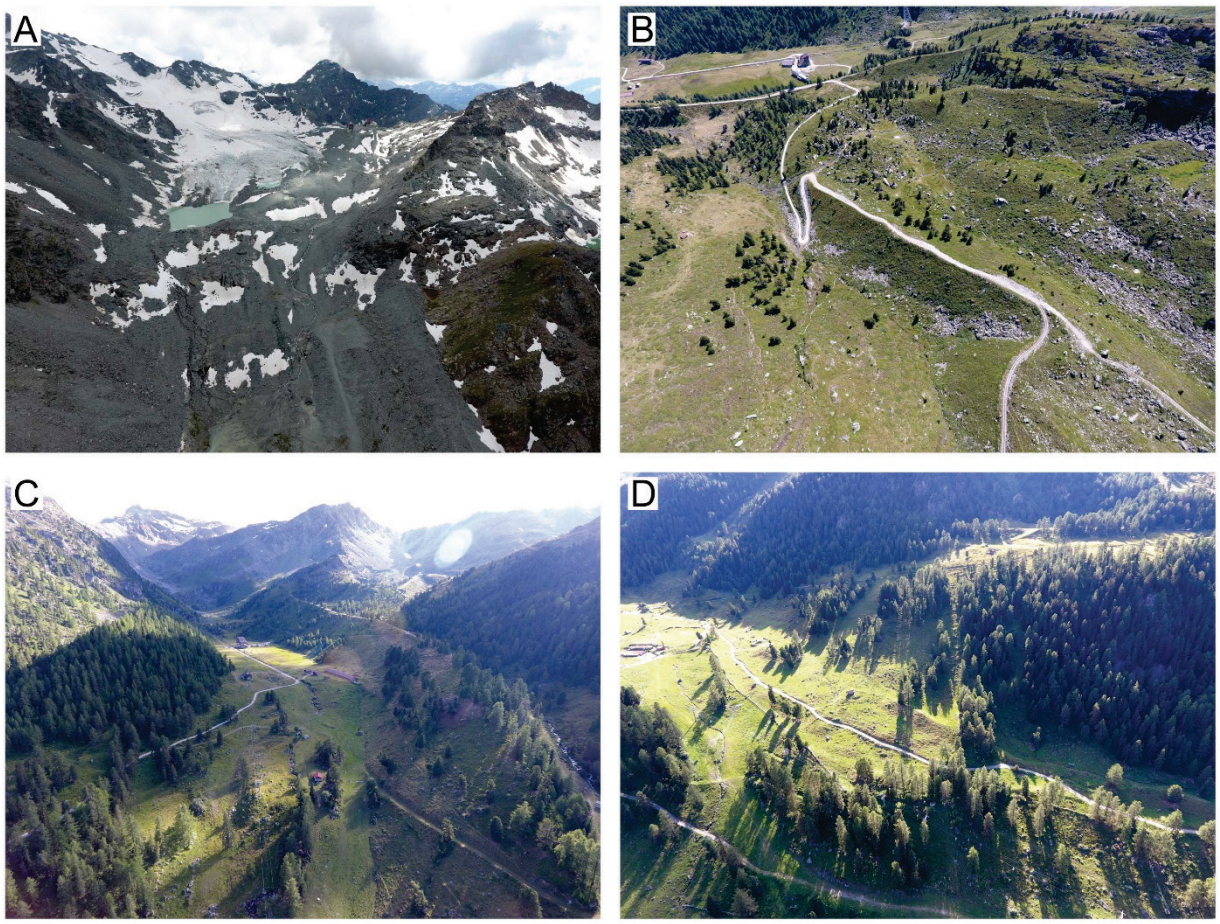


Figure 4.2. Aerial images of the field area acquired using a quadcopter drone. Panel A is looking upvalley toward the Tortin glacier. See Figure 4.3 for locations of panels B through D on map.

Table 4.1 Nendaz valley $^{10}$Be sample information.

| Sample ID | Latitude (DD) | Longitude (DD) | Elevation (m) | Elevation Flag | Thickness (cm) | Density (g cm$^{-3}$) | Shielding factor | Erosion | $^{10}$Be atoms* | $^{10}$Be uncertainty | $^{10}$Be standard | $^{10}$Be blank correction | Qtz weight (g) | Carrier added (g) | $^{10}$Be/$^{9}$Be | $^{10}$Be/$^{9}$Be uncertainty |
|---|---|---|---|---|---|---|---|---|---|---|---|---|---|---|---|---|
| MTF-16-15 | 46.11259 | 7.29113 | 2310.4 | std | 2.75 | 2.7 | 0.969 | 0 | 259083 | 6327 | 07KNSTD | 4970 | 10.5130 | 0.2022 | 1.956E-13 | 4.776E-15 |
| MTF-16-54 | 46.13299 | 7.31343 | 1818.2 | std | 2.76 | 2.7 | 0.959 | 0 | 207812 | 5687 | 07KNSTD | 4970 | 10.2577 | 0.2031 | 1.525E-13 | 4.173E-15 |
| MTF-16-55 | 46.13270 | 7.31344 | 1818.9 | std | 2.16 | 2.7 | 0.958 | 0 | 215383 | 6066 | 07KNSTD | 4970 | 10.1724 | 0.2034 | 1.565E-13 | 4.407E-15 |
| MTF-16-68 | 46.11954 | 7.30508 | 2080.3 | std | 1.47 | 2.7 | 0.966 | 0 | 232152 | 6519 | 07KNSTD | 4970 | 10.1026 | 0.2026 | 1.681E-13 | 4.722E-15 |
| MTF-16-72 | 46.12539 | 7.31008 | 1900.9 | std | 0.87 | 2.7 | 0.961 | 0 | 199575 | 6742 | 07KNSTD | 4970 | 10.0558 | 0.2037 | 1.432E-13 | 4.836E-15 |
| MTF-16-73 | 46.12271 | 7.30979 | 1944.5 | std | 2.48 | 2.7 | 0.969 | 0 | 207115 | 7042 | 07KNSTD | 4970 | 10.4164 | 0.2050 | 1.529E-13 | 5.198E-15 |
| MTF-16-77 | 46.11290 | 7.29802 | 2236.1 | std | 0.96 | 2.7 | 0.970 | 0 | 244115 | 6995 | 07KNSTD | 4970 | 10.0562 | 0.2037 | 1.750E-13 | 5.015E-15 |
| MTF-16-05 | 46.10897 | 7.28853 | 2386.4 | std | 1.75 | 2.7 | 0.953 | 0 | 267386 | 6194 | 07KNSTD | 1956 | 10.0436 | 0.2041 | 1.914E-13 | 4.434E-15 |
| MTF-16-10 | 46.10916 | 7.29009 | 2366.7 | std | 3.75 | 2.7 | 0.963 | 0 | 251382 | 5452 | 07KNSTD | 1956 | 10.1157 | 0.2045 | 1.809E-13 | 3.923E-15 |
| MTF-16-16 | 46.11940 | 7.30572 | 2058.1 | std | 2.11 | 2.7 | 0.951 | 0 | 233729 | 5751 | 07KNSTD | 1956 | 10.4578 | 0.2047 | 1.737E-13 | 4.274E-15 |
| MTF-16-33 | 46.11206 | 7.30038 | 2180.5 | std | 2.59 | 2.7 | 0.953 | 0 | 250443 | 6357 | 07KNSTD | 1956 | 8.8478 | 0.2042 | 1.579E-13 | 4.007E-15 |
| MTF-16-36 | 46.11311 | 7.29814 | 2232.8 | std | 1.34 | 2.7 | 0.968 | 0 | 248742 | 6132 | 07KNSTD | 1956 | 10.5630 | 0.2035 | 1.878E-13 | 4.631E-15 |
| MTF-16-53 | 46.11151 | 7.29055 | 2314.8 | std | 2.22 | 2.7 | 0.961 | 0 | 288105 | 7072 | 07KNSTD | 1956 | 10.1390 | 0.2035 | 2.088E-13 | 5.126E-15 |
| MTF-16-11 | 46.11049 | 7.28919 | 2337.1 | std | 3.22 | 2.7 | 0.959 | 0 | 229683 | 10404 | 07KNSTD | 13984 | 10.0799 | 0.1972 | 1.714E-13 | 7.762E-15 |
| MTF-16-35 | 46.11311 | 7.29792 | 2236.0 | std | 2.07 | 2.7 | 0.974 | 0 | 230521 | 14630 | 07KNSTD | 13984 | 10.18 | 0.2033 | 1.685E-13 | 1.069E-14 |
| MTF-16-37 | 46.11272 | 7.29817 | 2237.8 | std | 2.65 | 2.7 | 0.961 | 0 | 252336 | 9950 | 07KNSTD | 13984 | 10.0667 | 0.2009 | 1.844E-13 | 7.273E-15 |
| MTF-16-39 | 46.11153 | 7.29737 | 2253.0 | std | 3.48 | 2.7 | 0.971 | 0 | 251165 | 11182 | 07KNSTD | 13984 | 10.8029 | 0.2016 | 1.963E-13 | 8.738E-15 |
| MTF-16-49 | 46.10799 | 7.28980 | 2374.6 | std | 1.42 | 2.7 | 0.951 | 0 | 245758 | 12949 | 07KNSTD | 13984 | 10.1201 | 0.2004 | 1.811E-13 | 9.540E-15 |
| MTF-16-50 | 46.10813 | 7.29002 | 2371.8 | std | 1.49 | 2.7 | 0.951 | 0 | 425079 | 24277 | 07KNSTD | 13984 | 4.1757 | 0.1817 | 1.428E-13 | 8.158E-15 |
| MTF-16-51 | 46.10843 | 7.28992 | 2367.8 | std | 2.97 | 2.7 | 0.954 | 0 | 248235 | 11037 | 07KNSTD | 13984 | 10.052 | 0.2018 | 1.804E-13 | 8.021E-15 |
| MTF-16-56 | 46.13193 | 7.31372 | 1819.4 | std | 0.64 | 2.7 | 0.961 | 0 | 223398 | 13775 | 07KNSTD | 13984 | 4.8145 | 0.202 | 7.825E-14 | 4.825E-15 |
| MTF-16-58 | 46.13144 | 7.31429 | 1809.8 | std | 1.58 | 2.7 | 0.959 | 0 | 192025 | 15067 | 07KNSTD | 13984 | 3.5316 | 0.1825 | 5.502E-14 | 4.317E-15 |
| MTF-16-75 | 46.13233 | 7.31335 | 1821.2 | std | 2.28 | 2.7 | 0.959 | 0 | 210689 | 10514 | 07KNSTD | 13984 | 7.2096 | 0.2016 | 1.103E-13 | 5.505E-15 |

* Blank-corrected

## 4.3 Results

### 4.3.1 Geomorphic map

We first present a geomorphic map of the region to highlight key aspects of the glacial geomorphology (Figure 4.3). The Nendaz valley includes steep cliffs of exposed bedrock of the Col-de-Chassoure and Métailler formations, while valley floors are composed largely of undifferentiated glacial till and alluvial deposits. Higher sections along valley walls include remnants of LGM retreat such as kame terraces and associated ice contact margins. The target moraines are approximately 3 to 5 km downvalley from the existing Tortin glacier, where the eastern and western arms of the upper Nendaz valley converge. The most prominent moraines are a set of large, steep lateral ridges in Tortin, trending N-S parallel with the valley. The targeted left lateral moraine is around 1.75 km in length, with the crest extending from 1900 to 2200 meters in elevation, and a vertical relief from the valley floor as high as 100 meters in its upper sections. Interior to the main lateral moraine ridges are two minor recessional lateral moraines. Located 0.5 to 1.5 km down-valley from the primary lateral ridges we find a series of older and less-prominent moraine ridges which have a more subdued appearance, typically with less than 10 meters of topographic relief. They appear to be lateral based on their orientation, although some individual ridges are aligned SW-NE and may represent a transition to terminal moraines. Boulders comprising these moraines have heavier lichen cover and appear more weathered compared to those from higher elevation landforms in the valley. To the west of the primary lateral ridges is smaller tributary valley where we mapped another moraine complex situated at 2200 to 2400 meters in elevation. This set contains a blocky terminal moraine with continuous transition to a left lateral moraine. Another smaller recessional moraine is located 700 m inboard, and between these two moraines is hummocky terrain which may be due to past rock

glacier activity. To the northeast of this area along the valley wall are several additional rock glaciers. We note that the moraines in this higher elevation tributary valley are part of the same glacier complex, but were deposited independently from the older and larger Tortin moraines below.

### 4.3.2 $^{10}$Be surface exposure ages from the Nendaz valley

A total of 23 $^{10}$Be surface exposure ages were obtained in this study (Figure 4.3, Table 4.1, Table 4.2) providing a chronology spanning from approximately the earliest YD into the early Holocene. In general the SED ages are in chronostratigraphic order within analytical uncertainties. In the lower part of the valley, four ages from the outermost moraine remnants range from 13.3 ka to 12.7 ka (mean=12.9 ka). In the middle portion of the valley (Tortin) an additional six sampled boulders yield relatively younger ages, ranging from 12.1 ka to 11.4 ka (mean=11.7 ka). These mid-valley samples included boulders from the large primary left lateral ridge. In the smaller tributary valley to the west of the primary lateral ridge, five large boulders sampled from the blocky terminal moraine yield ages ranging from 11.5 ka to 10.4 ka (mean=11.0 ka). Inboard of the blocky terminal moraine, boulders from the recessional moraine yielded the youngest ages ranging from 11.0 ka to 10.3 ka (mean=10.6 ka). An additional three boulders were sampled adjacent to a steep hillslope (also within the tributary valley) dating to 12.3 ka, 11.2 ka, and 10.0 ka, respectively. The older 12.3 ka age is apparently inboard of the younger 11.2 ka age, although these three boulders may have undergone disturbance by adjacent rock glacier activity (Figure 4.3).

Table 4.2. Nendaz valley $^{10}$Be ages based on two commonly used scaling protocols, with 1σ analytical uncertainties.

| Sample ID | St age (ka) | 1σ uncertainty (ka) | Lm age (ka) | 1σ uncertainty (ka) |
|---|---|---|---|---|
| MTF-16-15 | 10.97 | 0.27 | 11.15 | 0.27 |
| MTF-16-54 | 12.59 | 0.35 | 12.64 | 0.35 |
| MTF-16-55 | 12.98 | 0.37 | 13.00 | 0.37 |
| MTF-16-68 | 11.45 | 0.32 | 11.60 | 0.33 |
| MTF-16-72 | 11.19 | 0.38 | 11.35 | 0.39 |
| MTF-16-73 | 11.31 | 0.39 | 11.47 | 0.39 |
| MTF-16-77 | 10.71 | 0.31 | 10.90 | 0.31 |
| MTF-16-05 | 10.85 | 0.25 | 11.03 | 0.26 |
| MTF-16-10 | 10.40 | 0.23 | 10.62 | 0.23 |
| MTF-16-16 | 11.95 | 0.30 | 12.06 | 0.30 |
| MTF-16-33 | 11.79 | 0.30 | 11.91 | 0.30 |
| MTF-16-36 | 11.00 | 0.27 | 11.18 | 0.28 |
| MTF-16-53 | 12.22 | 0.30 | 12.31 | 0.30 |
| MTF-16-11 | 9.70 | 0.44 | 9.95 | 0.45 |
| MTF-16-35 | 10.17 | 0.65 | 10.39 | 0.66 |
| MTF-16-37 | 11.32 | 0.45 | 11.49 | 0.45 |
| MTF-16-39 | 11.11 | 0.50 | 11.29 | 0.50 |
| MTF-16-49 | 10.05 | 0.53 | 10.28 | 0.54 |
| MTF-16-50 | 17.45 | 1.00 | 17.26 | 0.99 |
| MTF-16-51 | 10.29 | 0.46 | 10.51 | 0.47 |
| MTF-16-56 | 13.26 | 0.82 | 13.26 | 0.82 |
| MTF-16-58 | 11.59 | 0.91 | 11.72 | 0.92 |
| MTF-16-75 | 12.68 | 0.64 | 12.72 | 0.64 |

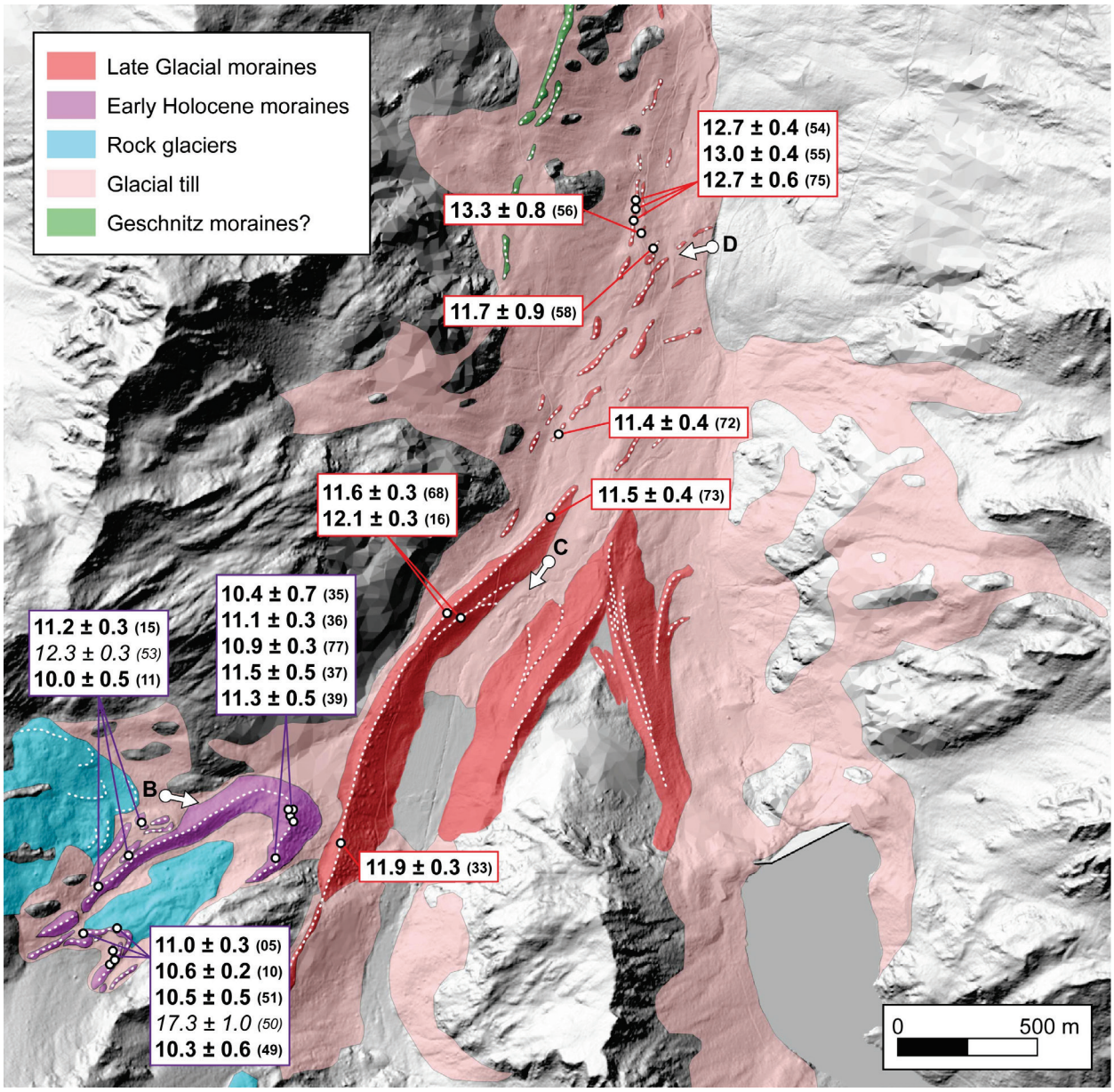


Figure 4.3. Geomorphic map of the Nendaz valley study area and $^{10}$Be ages. Ages in italics are those we consider to be influenced by inheritance. Mapped features are based on field investigations, analysis of satellite and aerial imagery, and DEM topographic relief. Approximate boundaries of glacial till from Swiss geological maps (Swisstopo, 2012). White arrow symbols (labeled B through D) indicate location and camera direction of the aerial images in Figure 4.2.

### 4.3.3 Alps-wide compilation of published $^{10}$Be surface exposure ages

We now compare our $^{10}$Be ages with those from previous studies in the Alps. A histogram plot of the Alps-wide compilation shows samples ages spread throughout the LG and early Holocene, roughly centered on the YD-early Holocene transition (mean = 11.9 ka, median = 11.7 ka, std =

1.3 kyrs) (Figure 4.4). Out of the 352 samples, 84 yield ages older than the onset of the YD (12.9 ka), 105 samples yield ages falling within the YD, and 163 samples yield ages falling after the termination of the YD (11.6 ka). Of the 105 samples within the YD, 48 samples fall within the first half of the stadial, and 57 samples fall within the second half of the stadial.

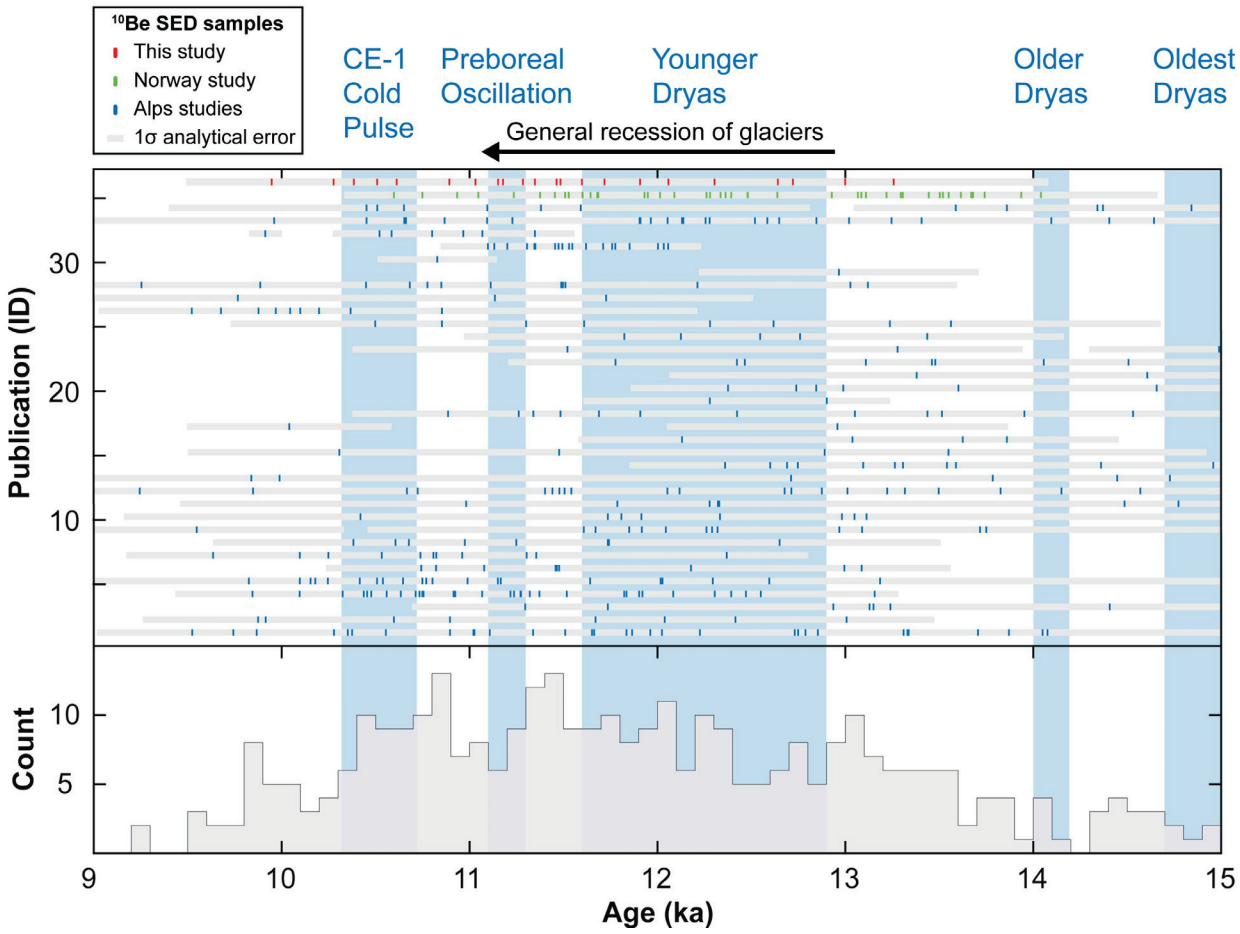


Figure 4.4. Compilation of published LG and early Holocene $^{10}$Be SED samples in the Alps, arranged by publication date from earliest (bottom) to latest (top). Horizontal grey bars represent 1σ analytical error. CE-1 cold pulse from Hass et al. (1998). Also included is a recent glacier chronology from Norway (Wittmeier et al., in press). We note that the primary signal in the Alps is one of glacier recession, with younger moraines generally inboard and/or upvalley of older moraines.

## 4.4 Discussion

### 4.4.1 Summary of glacier chronology in the Nendaz valley

The presented geomorphic map and moraine chronology from Nendaz valley provide a comprehensive view of the glacier system response during the LG and early Holocene. The 13.3–12.7 ka moraines in the lower part of the valley are evidence of the larger glacier configuration during this earlier time, near the beginning of the YD. In the middle valley, the 12.1–11.4 ka ages of the primary lateral ridges suggest that the glacier was actively building these moraines toward the end of the YD. Their topographic prominence may be due to various factors such as a plentiful supply of rock debris, a long duration of stable glacier extent during formation, or multiple intervals of building (composite moraine). This robust chronology with early and late YD moraine positions within a single valley suggest that the glacier underwent significant retreat through the YD stadial, and that climatic conditions during the early YD were more favorable for glacier growth compared to the late YD. In the side valley to the west of the primary lateral ridges, terminal moraine boulder ages ranging from 11.5–10.4 ka indicate that this moraine was formed during the early Holocene, and the 11.0–10.3 ka innermost recessional moraine suggests another brief period of stabilization. Previous studies finding similar early Holocene ages in the Alps have hypothesized an association with the Preboreal Oscillation and the CE-1 cold pulse (Boxleitner et al., 2019; Braumann et al., in review; Haas et al., 1998; Ivy-Ochs, 2015).

### 4.4.2 Contrasting views of glacier responses leading into the Younger Dryas

Contrasting views exist in the literature regarding glacier behavior during the interval immediately preceding the YD (Balco, 2020), during which the Bølling-Allerød (BA) interstadial and the Antarctic Cold Reversal (ACR) occurred in the northern and southern

hemispheres, respectively. Published $^{10}$Be ages falling within this interval are occasionally attributed to SED error, and some studies suggest that the Alps were largely ice-free during this time (Ivy-Ochs, 2015). On the other hand, pollen, chironomid, $\delta^{18}O$, and other paleoecological records (Lotter et al., 1992; Lotter et al., 2012) suggest that the Alps experienced two brief cold pulses during the BA (the Older Dryas and Intra-Allerød stadials), during which Egesen-like glacier configurations may have been reached. For example, Ohlendorf (1998) hypothesized that glacier dimensions comparable to the YD may have existed during the Older Dryas (known locally as the Aegelsee oscillation) based on an analysis of annually laminated sediments from alpine glacier lakes in southeastern Switzerland. Some evidence also exists for an intermediate glacier stage between the Gshnitz and the Egesen known as the "Daun", which may correspond to the Older Dryas cold pulse (van Husen, 2000). Moraines from this stage are often described as having subdued morphology, a clear solifluction overprint, and are poor in boulders (Ivy-Ochs, 2015; Ivy-Ochs et al., 2008). Such moraines are conspicuously difficult to exposure date, and recent studies have suggested that evidence for the Daun is too scant to establish it as an independent stage (Boxleitner et al., 2019; Reitner et al., 2016).

### 4.4.3 Evidence for glacier advances before the onset of the Younger Dryas

In addition to the previously-noted paleoclimate records in the Alps, other northern hemisphere glacier and ice sheet chronologies give credibility to pre-YD advances. SED ages from moraine boulders and varve sequences from glacial lakes in the White Mountains of New Hampshire indicate that the Laurentide ice sheet readvanced during the Older Dryas (Bromley et al., 2015; Thompson et al., 2017). In western Canada, results from Menounos et al. (2017) suggest early BA warmth caused significant mass loss of the ice sheet, followed by readvances during both the BA and YD. Briner et al. (2014) showed that classical Lysefjorden moraines deposited by the

Scandinavian ice sheet (which were earlier thought to be entirely of YD age) can be attributed to at least two advances of distinctly different ages, with the first advance (outermost moraines) of Older Dryas age, and later advance (innermost moraines) deposited near the end of the YD. The timing of sea level fluctuations in western Norway also imply that ice sheet expansion commenced during the Allerød rather than the YD as initially thought (Lohne et al., 2007). In Greenland, SED ages indicate that an outlet glacier of the ice sheet and an independent ice cap receded together during the YD (Levy et al., 2016). Young (2019) constrained the age of a LG terminal moraine in southern Alaska, and showed that a glacier culmination occurred in the early-to-mid YD followed by recession through the remainder of the YD. In Norway, radiocarbon data suggest that most glaciers reached their maximum LG extent during the Allerød and earliest YD, followed by net retreat (Andersen et al., 1995). In the Scottish Highlands, a $^{14}C$ chronology indicates that the last pulse of glaciation peaked during the earliest part of the YD, with subsequent deglaciation through the ensuing stadial (Bromley et al., 2018). Bromely et al. (2018) also discuss the improbability of accumulation, peak, and deglacation all within the few centuries of the YD, with the most likely explanation being a glacier advance largely predating the YD. This argument applies to our Nendaz valley results as well – the 13.3 to 12.7 ka moraine ages suggest that a preceding glacier buildup must have occurred before the onset of the YD. Most recently, a new glacier chronology from Norway shows that a glacier maxima was reached prior to the YD, followed by considerable retreat through the first part of the YD, brief restabilization in the mid-YD, and slower oscillatory retreat through the latter part of the YD (Wittmeier et al., in press).

### 4.4.4 Implications for Late Glacial climate drivers

Our results from the Nendaz valley support the occurrence of a LG glacier advance largely predating the YD with subsequent retreat through the YD, which has broad implications for interhemispheric climate, seasonality, and drivers of glacier change. Emerging glacier chronologies around the globe support the hypothesis that glaciers more closely followed summer temperatures extracted by Buizert et al. (2018) from Greenland ice core records and transient climate model simulations, rather than annually-averaged temperature proxies thought to be influenced by extreme winter cooling during AMOC slowdowns. Largely similar moraine chronologies in both hemispheres strengthen the hypothesis of interhemispherically synchronous summer temperatures during the LG, which highlights a correlation with $CO_2$ records and mirrors modern observations of near-global acceleration of ice loss due to increasing anthropogenic GHG emissions (Zemp et al., 2015). Additional research is needed to further test this hypothesis, including synoptic global analysis of published exposure ages (Balco, 2020), targeting and sampling of relevant moraines for future analysis, correlation of glacier chronologies with other paleoclimate proxies, and integration with climate models.

## 4.5 Conclusion

Geomorphic analysis and SED ages from glacier moraines in the Nendaz valley provide a coherent glacier chronology spanning from the early YD to the early Holocene. Results show extended glaciers already existed in the earliest YD, followed by an overall pattern of glacier retreat through the YD in the main valley. This is similar to moraine records from the southern hemisphere and agrees with an emerging pattern in the northern hemisphere, including a new record from Norway (Wittmeier et al., in press). We hypothesize that the observed wide spread of compiled $^{10}$Be ages reaching into the BA interval may not be solely a result of SED error.

Especially when viewed in a global context (Balco, 2020) Egesen-like moraines with pre-YD ages in the Alps need not be directly attributed to YD cooling. Alpine glaciers may have attained Egesen-like configurations significantly before the onset of the YD, with subsequent retreat through the YD punctuated by brief periods of stability and moraine building. This implies a glacier buildup occurred during the BA interstadial, which broadly agrees with recent summer temperature reconstructions during the most recent deglaciation (Buizert et al., 2018), and is in line with the concept of global radiative GHG forcing as a significant energy balance component for alpine glaciers during the LG.

# Chapter 5 Dynamic modeling of regional glacier change and spatiotemporal variability

## 5.1 Introduction

Accurate quantification of glacier responses to climate change is important for current and future water supply, sea level rise, ecosystems, hydropower, and natural hazards across vulnerable mountain regions (Carrivick and Tweed, 2016; Kaser et al., 2010; Kraaijenbrink et al., 2017; Marzeion et al., 2012; Zemp et al., 2015). Robust understanding requires study of glacier change over different timescales – this includes long term baseline glacier fluctuations due to natural climate variability, as well as the more recent superimposed signal of anthropogenic climate change (Marzeion et al., 2014; Roe et al., 2017). Modern scientific advances have made the study of glacier change across different timescales possible with techniques such as satellite imagery analysis, surface exposure dating (SED), and numerical modeling. Yet contrasting viewpoints exist in the literature regarding glacier observations spanning relatively short-term modern (decades) versus long-term paleo (centuries or millennia) timescales. Annual to multi-decadal studies of glacier change often highlight complex spatial patterns of ice loss and significant glacier-to-glacier variability (Brun et al., 2017; Foresta et al., 2018; Menounos et al., 2019; Paul and Haeberli, 2008; Scherler et al., 2011; Zheng et al., 2018), while centennial to millennial studies suggest largely synchronous glacier changes across regions and hemispheres in response to long-term natural climate variability (Bromley et al., 2018; García et al., 2012; Putnam et al., 2010; Schaefer et al., 2006; Young et al., 2019).

This apparent contrast elicits a question: for a typical population of mountain glaciers, what statistical spread of ice thickness change might we expect under a spatially uniform climate forcing, and how does it change through time as the glaciers approach a new equilibrium? The

final section of this dissertation addresses this issue in light of new findings. We first summarize relevant key points from preceding chapters with a specific focus on spatiotemporal variability, and outline differences between short-term glaciological observations versus long-term geomorphological and cosmogenic studies of glacier change. In turn, we use a numerical model to help bridge the time gap, by simulating the spatial variability of glacier mass balance across a region as a function of the observational timespan.

### 5.1.1 Societal relevance of glacier processes over various timescales

Mountain glacier processes operate over a wide range of timescales, from catastrophic releases of water which occur in a matter of minutes to the shaping of mountain topography over millions of years. With rapidly growing downstream populations and expanding hydropower-dependent economies in mountain regions such as the Himalayas, shorter-timescale glacier events are intensely studied as they present direct threats to the safety and welfare of local inhabitants. Such events in recent years include the sudden collapse of a glacier in Tibet (Kääb et al., 2018), surging glaciers in the Karakoram (Quincey et al., 2011), and glacial lake outburst floods (GLOFs) which are a significant hazard in many regions (Carrivick and Tweed, 2016). As triggers for these events are chaotic and unpredictable, efficient early warning systems are crucial for maximizing warning time and minimizing loss. Efforts to improve early warning systems are ongoing; Chapter 1 for example demonstrated how a real-time seismic monitoring system could potentially detect events such as GLOFs from many kilometers away, and would enhance the efficiency and reliability of existing automatic water level sensor systems.

Over multi-decadal timescales, the primary societal concern regarding glacier change is depleted water supply for downstream inhabitants in the near future (Kaser et al., 2010). This is particularly true for arid regions in South Asia such as the Indus watershed, where a significant

portion of seasonal meltwater is supplied by glacier melt from the Himalayan and Karakoram ranges (Azam et al., 2018; Kraaijenbrink et al., 2017). As a result, many recent studies have focused on quantifying glacier change across the larger High Mountain Asia region (Brun et al., 2017; Kääb et al., 2015; Maurer et al., 2019; Zhou et al., 2018). Toward this end, Chapters 2 and 3 utilized declassified spy satellite imagery to investigate glacier responses to climate change in the Himalayas over the past 40 years. The large sample size and multi-decade timespan of these analyses provided a unique perspective on the spatiotemporal variability of glacier change between sub-regions and individual glaciers over two distinct timespans, from 1975 to 2000 and from 2000 to 2016. Overall a similar average magnitude and acceleration of ice loss was observed across the 2000 km transect, yet significant glacier to glacier variability was also evident within subregions. Glaciers during the more recent interval were subject to more intense climate forcing and lost ice at a rate approximately twice the 1975-2000 rate, and the standard deviation (SD) of individual glacier mass balances increased from 0.15 m w.e. $year^{-1}$ during 1975-2000 to 0.24 m w.e. $year^{-1}$ during 2000-2016. The increase in SD suggests some correlation between 1) characteristics of the later interval (shorter timespan measured, stronger climate forcing, and greater rate of ice loss) and 2) a greater spatial variability of ice loss. This important detail will be the subject of further analysis and compared with model output in this study.

Observations of glacier change over centennial to millennial timescales are vital for quantifying past glacier responses to natural climate variability. The inverse is also true, in that moraine chronologies provide valuable insight into regional and global climate patterns. By linking glacier responses to long-term climate change in this way, a baseline is established which provides context for the superimposed anthropogenic forcing in modern times. For example, Chapter 4 investigated a glacier complex in the western Alps during the Late Glacial (LG) (11-

15 ka), an important interval of natural climate variability. While previous studies attributed LG glacier advances to Younger Dryas (YD) cooling in the European Alps (Boxleitner et al., 2019; Federici et al., 2008; Ivy-Ochs et al., 1996; Kelly et al., 2004; Protin et al., 2019), recent publications suggest that glacier culminations occurred in Greenland, the Scottish Isles, and Alaska prior to, or in the very early YD (Bromley et al., 2018; Levy et al., 2016; Young et al., 2019). Chapter 4 gave further credibility to this idea, via SED evidence suggesting substantial glacier retreat through the YD in the Nendaz valley in the European Alps, combined with a compilation of published $^{10}$Be data across the region showing a considerable percentage of pre-YD ages. This emerging picture resembles the global $CO_2$ curve and existing glacier record in the southern hemisphere, where evidence from midlatitude glaciers in New Zealand and Patagonia suggests a synchronous advance occurred during the Antarctic Cold Reversal (García et al., 2012; Kaplan et al., 2010; Kaplan et al., 2013; Putnam et al., 2010; Sagredo et al., 2018). Taken together, these interhemispheric glacier records strengthen the hypothesis that the YD stadial was primarily a North Atlantic winter phenomenon, and that glaciers (sensitive to summer temperatures) in both hemispheres may have experienced near-synchronous retreat through the LG period.

### 5.1.2 Different viewpoints of glacier change

These aforementioned studies highlight an apparent difference between observations over decadal versus centennial to millennial durations. In recent decades, field-based glaciologists have intensely monitored glacier mass balances over annual to multi-decadal timespans using methods such as ablation stakes, snow pits, photogrammetry, and automatic weather stations. Through the satellite era, remote sensing experts have also quantified glacier area changes and geodetic mass balances using satellite and airborne sensors. Both field-based and satellite-based

studies oftentimes show highly variable mass changes from glacier to glacier, even those adjacent to one another within the same climate setting. Conversely, mountain glacier studies spanning longer timescales tend to highlight overall homogeneity of glacier response. These are usually based on moraine morphostratigraphy and SED with some constraints provided by numerical simulations. Results from basic inverse models often indicate similar ELA depressions for moraines across many valleys, and precision SED of moraine boulders yield mostly consistent ages. Modern high-resolution satellite imagery (such as in Google Earth) also clearly show a near-worldwide occurrence of prominent Little Ice Age (LIA) moraines, suggesting a globally similar spatiotemporal glacier response during the past few centuries. Together with emerging evidence of similar glacier fluctuations in both hemispheres during the LG and established near-synchronous interhemispheric termination of the Last Glacial Maximum (LGM) in mid-latitudes, the long-term picture shows a largely near-synchronous pattern of glacier change through time. This apparent contrast between short-term complexity versus long-term simplicity highlights a key conceptual disparity and provides a focal point for further analysis. Here we address this question by modeling glacier dynamics in the Ötztal Alps, a typical mid-latitude alpine region with consistent instrumental temperature records and detailed glacier change observations extending back to the 1850's. This is accomplished by using the shallow ice approximation (SIA) equations to model ice thickness distributions across the region through time, with a subsequent analysis of spatial heterogeneity of change over different observational timespans. We emphasize that our goal here is not to precisely reproduce the historical record of glacier change in this specific region, but rather to use a basic modeling framework in typical alpine terrain to highlight and demonstrate key characteristics of glacier response. In so doing we

aim to clarify how glacier dynamics dictate spatial variability of glacier change over multi-decadal timescales, and help strengthen the connection between geomorphology and glaciology.

## 5.2 Methods

To model glacier dynamics we implement the shallow ice approximation (SIA) (Fowler and Larson, 1978; Hutter, 1981; Hutter, 1983) which treats ice as a viscous and incompressible non-Newtonian fluid (Cuffey and Paterson, 2010), and is based on the assumption that longitudinal stresses are negligible relative to vertical shear stresses:

$$\frac{\partial h}{\partial t} + \nabla \cdot \boldsymbol{q} = \dot{b} \tag{5.1}$$

$$\boldsymbol{q} = -D\nabla s \tag{5.2}$$

$$D = \Gamma h^{n+2} |\nabla s|^{n-1} + \Gamma_s h^n |\nabla s|^{n-1} \tag{5.3}$$

$$\Gamma = \frac{2A(\rho g)^n}{n+2} \tag{5.4}$$

$$\Gamma_s = A_s(\rho g)^n \tag{5.5}$$

where $h$ is ice thickness, $t$ is time, $\nabla$ is the 2D gradient operator, $\boldsymbol{q}$ is horizontal ice flux, $\dot{b}$ is surface mass balance rate, $D$ is the diffusivity (i.e. diffusion coefficient in a parabolic partial differential equation), $s$ is the ice surface elevation, $n$ is Glen's flow law exponent, $A$ is Glen's flow law coefficient, $\rho$ is ice density, $g$ is the gravitational constant, and $A_s$ is a sliding law coefficient. The primary advantage of the SIA over higher-order models (such as a full Stokes formulation) is simplicity of implementation and computational efficiency. The use of a more complex models of glacier physics is also not justified in this case, as it would require unavailable parameters such as ice temperatures and glacier bed conditions. Lower order

solutions such as the SIA has been shown to reasonably approximate ice thickness distributions of mountain glaciers (Leysinger Vieli and Gudmundsson, 2004), and comparisons of model hierarchies suggest higher order stresses do not play a large role in capturing basic glacier responses to warming (Christian et al., 2018). As the goal of this study is to demonstrate basic glacier dynamics over a representative range of glacier sizes and hypsometries across a region, the use of the SIA is an ideal compromise which allows for reasonably accurate simulation at the required spatiotemporal resolution while meeting practical computational limitations. To avoid spurious violations of mass conservation in this region of complex terrain, we modify diffusivities using the flux-limiting scheme from Jarosch et al. (2013), and solve Equation (5.1) using a semi-implicit time-stepping scheme (Hindmarsh, 2001) with a constant time step of one month and a horizontal grid resolution of 180 meters. All model parameter values are given in Table 5.1, and numerical benchmark tests confirm that the model is performing as expected (Figure 5.1) (Bueler et al., 2005; Jarosch et al., 2013). For bedrock elevation input, we use the ALOS 30 m global DEM (Tadono et al., 2014) in a projected coordinate system (WGS 84 / UTM 32N) resampled to the 180 m resolution model grid, and subtract existing glacier ice surfaces from the DEM using spatial ice thickness distributions from the third Austrian Glacier Inventory (Helfricht et al., 2019). For the surface mass balance rate ($\dot{b}$) we define:

$$\dot{b} = \min\left(\beta(s - s_{ELA}), \dot{b}_{max}\right) \tag{5.6}$$

where $\beta$ is the balance rate gradient, $s_{ELA}$ is the equilibrium line altitude (ELA), and $\dot{b}_{max}$ is a maximum ice accumulation rate.

Table 5.1 SIA model parameters

| Parameter | Symbol | Value | Units |
|---|---|---|---|
| Glen's flow law exponent | $n$ | 3 | |
| Glen's flow law coefficient | $A$ | 1E-24 | $Pa^{-3}s^{-1}$ |
| Ice density | $\rho$ | 910 | $kg\ m^{-3}$ |
| Gravitational constant | $g$ | 9.81 | $m\ s^{-2}$ |
| Sliding law coefficient | $A_s$ | 1E-19 | $Pa^{-3}m^{2}s^{-1}$ |
| Balance rate gradient | $\beta$ | 2.1E-10 | $s^{-1}$ |
| Max ice accumulation rate | $\dot{b}_{max}$ | 6.3E-08 | $m\ s^{-1}$ |

We use the SIA model to simulate glacier response in the Ötztal region in two distinct scenarios. In model run 1 (R1) we demonstrate a simple instantaneous climate forcing, while in model run 2 (R2) we use instrumental temperature data as input. To establish initial conditions in both runs, the glacier model is first allowed to reach a near-equilibrium state with a specified ELA. In R1, we subsequently apply an instantaneous ELA change of +100 m and run the model forward for an additional 200 years. In R2, a simple linear relationship between an 1850-2018 instrumental air temperature record and the regional ELA is used. We use the HISTALP mean monthly homogenized series from the Obergurgl-Vent station located at approximately 11.03°E, 46.87°N (1930 m elevation) within the study area (Auer et al., 2007). We note that the Ötztal Alps were chosen as an ideal region for this study with typical variation in glacier size and hypsometry, exceptional historical records of air temperature and glacier area changes, and accurate estimates of modern glacier ice thickness. An example of the SIA output illustrates the simulated ice thickness distributions across the region over a 100-year timespan (Figure 5.2).

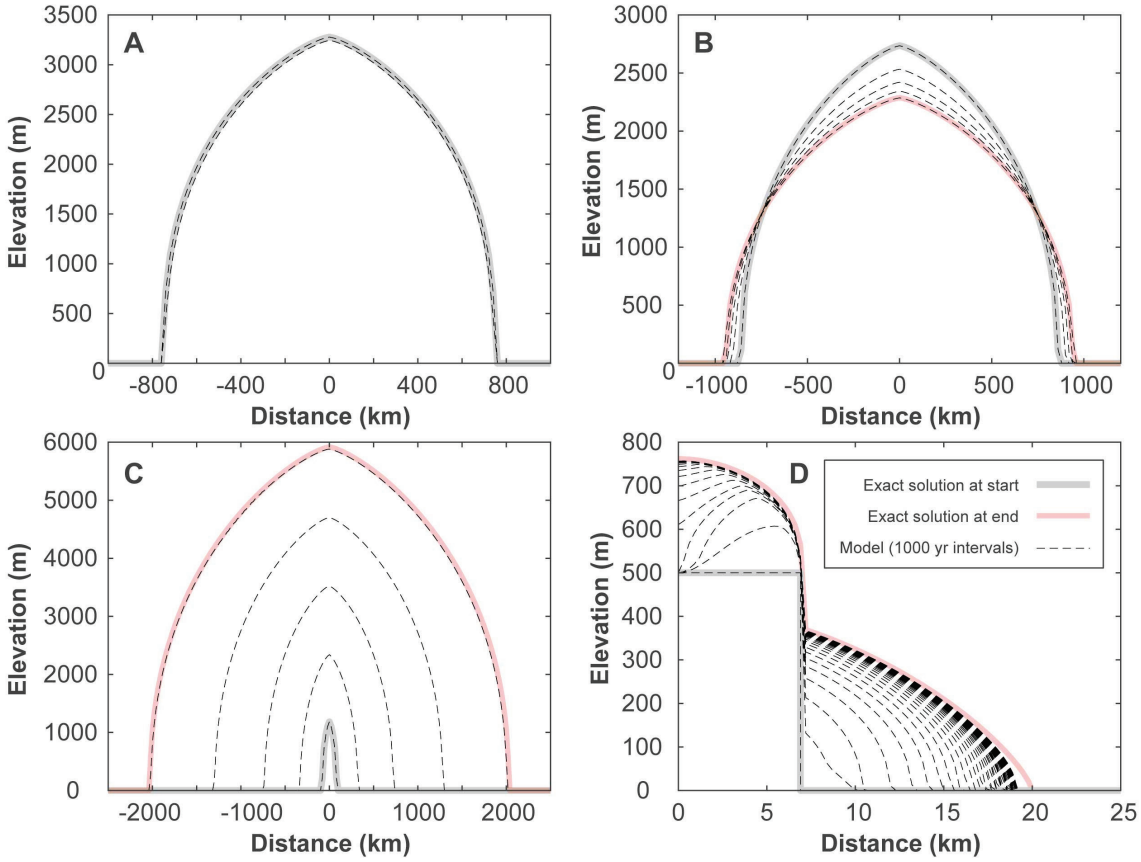


Figure 5.1. Numerical benchmark tests confirming the glacier model is performing as expected (Bueler et al., 2005; Jarosch et al., 2013). Thick grey and red lines are exact (analytical) solutions for the isothermal shallow ice sheet equation at the beginning and end of model runs, respectively. The thin dashed lines are from the SIA model output used in this study (at 1000-year intervals). A through C are tests on flat horizontal beds (Bueler et al., 2005), while D is on a bedrock step designed to test mass conservation of flux-limiting schemes (Jarosch et al., 2013).

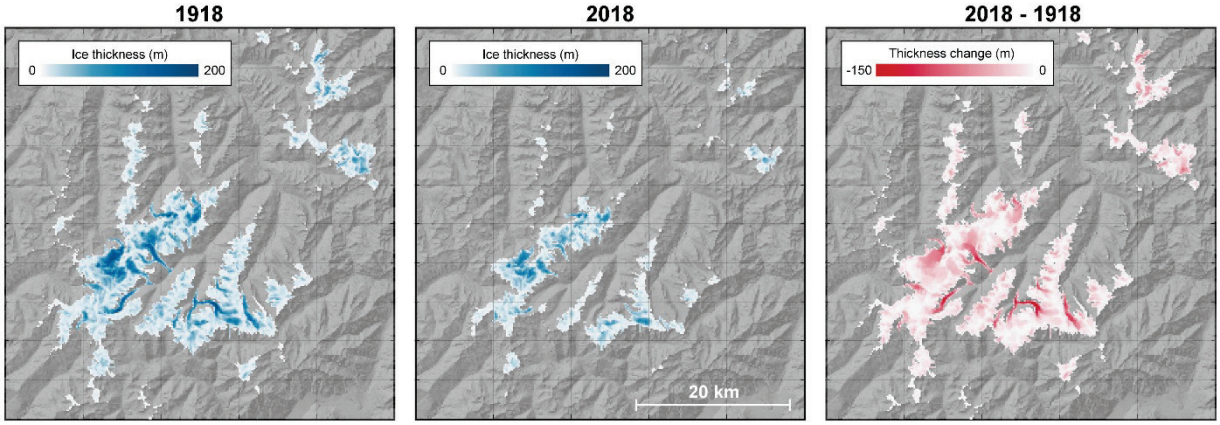


Figure 5.2. Modeled ice thickness (m) and ice thickness change (m) over a 100-year timespan in the Ötztal Alps region.

## 5.3 Results

We first present results from the model driven by a step-function with an instantaneous 100 m increase in ELA, and show the time-dependent response of the glaciers as they approach a new equilibrium (Figure 5.3). Both the volume and area curves exhibit the greatest rates of change initially, with rates lessening through time as the curves asymptote to new steady-state values. We also quantify the spatial variability of mean annual ice thickness change (m $yr^{-1}$) as a function of the observational timespan. This is accomplished by computing the difference in ice surface elevations between two given instances in time, performed for timespans ranging from 1 to 200 years (each beginning at year zero, see Figure 5.3A inset). We subsequently calculate the regional mean, median, and interquartile range (IQR) of ice thickness change for each timespan. Plotting these statistics versus the length of the timespan (Figure 5.3B) illustrates 1) the mean annual ice thickness change is more negative for shorter, earlier timespans (near the beginning of the response) and becomes less negative when computed over longer timespans, 2) the spatial variability of the change (measured by the IQR) is greater for shorter, earlier timespans (near the beginning of the response) and becomes smaller when computed over longer timespans. We also plot ice thickness change histograms for specific timespans of 5, 10, 20, 50, and 100 years (Figure 5.3C) to further illustrate characteristics of the respective distributions. We note the 5-year distribution has the widest spread and strongest negative skew, while the 100-year distribution has the smallest spread and weakest negative skew. Lastly, we plot ice thickness change versus elevation separated in to 100 m elevation bins (Figure 5.3D). The 5-year profile is the steepest with the greatest thinning rates at lower elevations, and the profile steepness decreases with longer timespans.

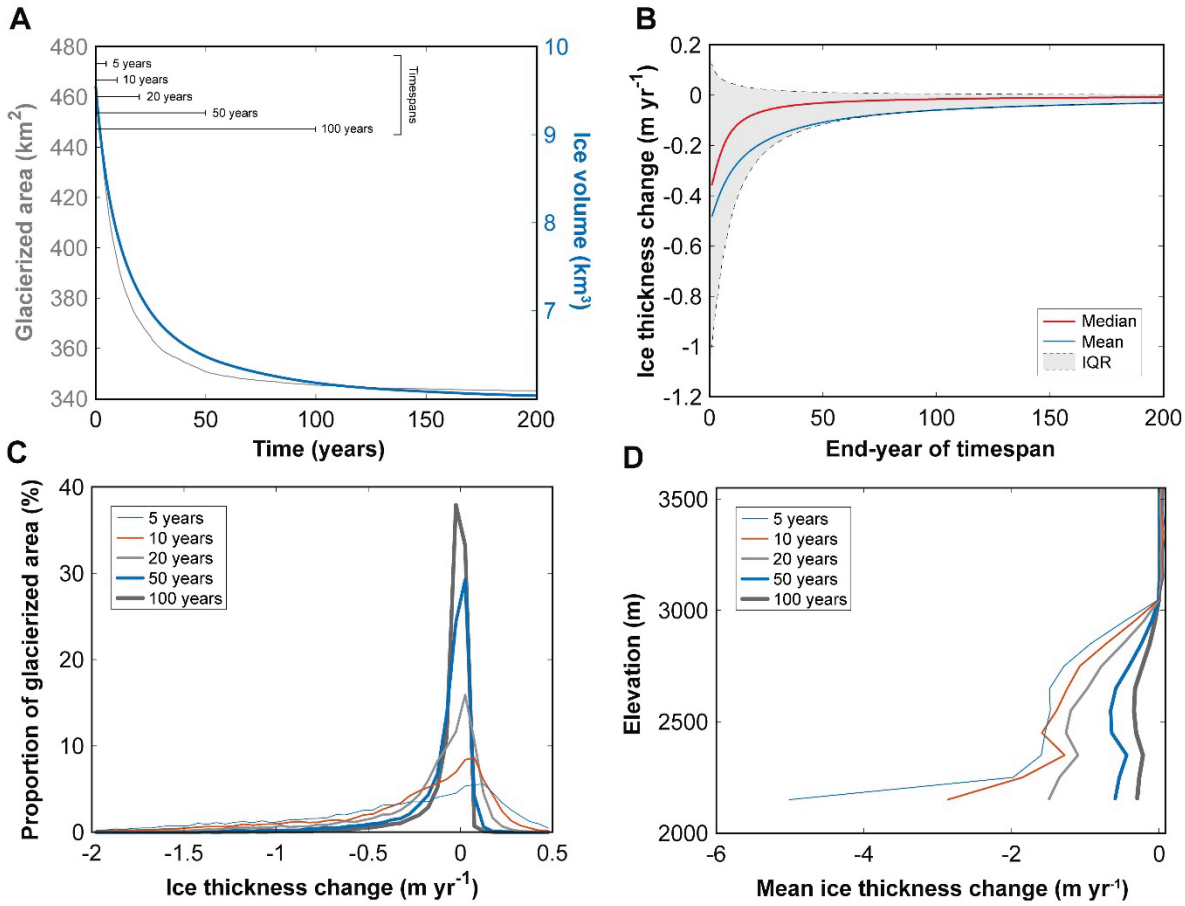


Figure 5.3. Glacier model response, driven by a step-function with an instantaneous 100 m increase in ELA at time = 0. A) Glacierized area and volume through time. B) Distributions of ice thickness change (m $yr^{-1}$) versus observational timespans, ranging from 1 to 200 years in length (each year beginning at zero). The red line is the median, blue line is the mean, and the grey area (IQR) is bounded by the first and third quartiles of ice thickness change. C) Distributions of ice thickness change corresponding to five distinct timespans of 5, 10, 20, 50, and 100 years. D) Mean ice thickness change (m $yr^{-1}$) versus elevation for the same timespans as in C.

We next discuss results from the second model run, driven by the HISTALP 1851-2018 instrumental temperature record. In contrast to the previous example of an instantaneous step-change, this climate forcing here is time-dependent. The glaciers are always moving towards equilibrium with the instantaneous climate state; however, the state is constantly changing, and the glaciers are essentially acting as a low-pass filter (Roe, 2011). The overall increase in air temperatures over the 167 year interval results in a generally decreasing ice volume trend, with some decades experiencing greater rates of change than others (Figure 5.4A). During the 20$^{th}$

century for example, the most rapid ice losses are evident during the late 1940's to early 1950's and from the 1980's to present day, while more stable conditions prevailed during the 1960's to 1970's. Similar to the previous model run, we compute the regional mean, median, and IQR of ice thickness change (m $yr^{-1}$) and plot the statistics versus the length of the respective timespan (Figure 5.4B). However, in this case the timespans are measured from the year 2018, extending backward in time rather than forward (see Figure 5.4A inset). This is to allow comparison with observational mass balance records, the vast majority of which have been obtained during the latter half of the $20^{th}$ and into the $21^{st}$ centuries. Figure 5.4B illustrates 1) the mean annual ice thickness change is most negative during the shorter, more recent timespans (in this case on the right side of Figure 5.4B) and becomes less negative when the start-year of the timespan is moved backward in time, 2) the spatial variability of the change (shown by the IQR) is greatest during the shorter, more recent timespans and becomes smaller when the start-year of the timespan is moved backward in time. Ice thickness change histograms and elevation profiles also show a similar pattern (Figure 5.4C and Figure 5.4D) with the shorter, more recent timespans exhibiting stronger negative skews and steeper "thickness change versus elevation" profiles, respectively.

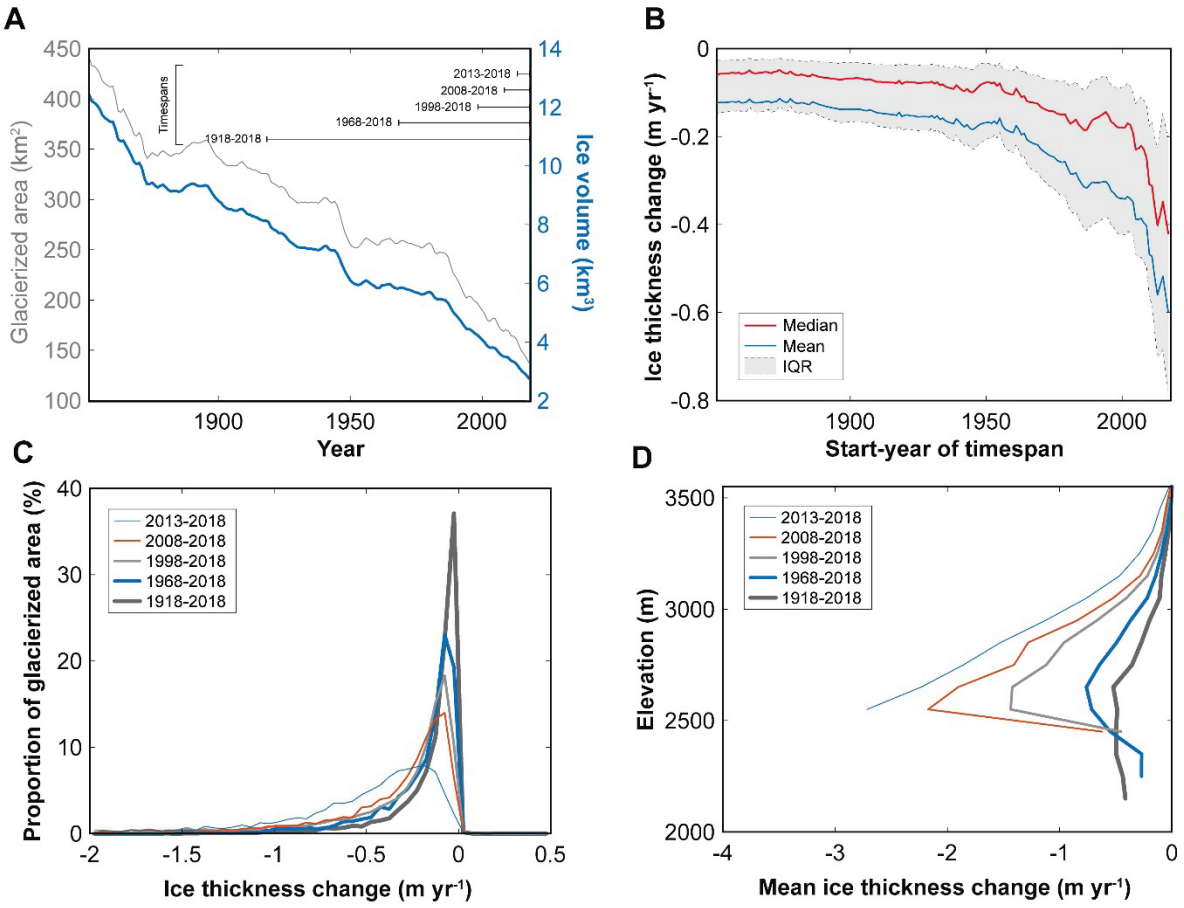


Figure 5.4. Glacier model response, driven by the HISTALP 1851-2018 instrumental temperature record. Panels are the same as described in Figure 5.3, except here the timespans are measured from the year 2018, extending backward in time rather than forward.

## 5.4 Discussion

### 5.4.1 Glacier dynamics

Changes in ice thickness at any given point on a land-terminating mountain glacier surface are controlled primarily by: 1) the surface mass balance, and 2) internal ice flux from higher to lower elevations due to gravity-induced pressure gradients, including ice deformation and sliding. Glacier surface mass balance is correlated with elevation due to the atmospheric lapse rate, with warmest temperatures, greatest ablation, and most negative specific mass balances generally occurring at the glacier terminus. In response to a climate forcing such as atmospheric warming,

a glacier will lose relatively more ice at lower elevations; in turn, this effectively increases the gradient of the glacier surface, and the steepened gradient drives ice flux, i.e. over time mass loss at lower elevations will be compensated by ice flowing down from higher elevations. However, surface mass balance and ice flow occur at different rates – ablation occurs in lockstep with the atmospheric warming, while the subsequent dynamic adjustment of the glacier takes much longer, on the order of decades. Roe (2011) described this concept from a spectral analysis viewpoint, noting that a dynamic flowline glacier length model yields relatively higher autocorrelations for lags shorter than ~15 years, compared to a simple linear model. This concept is often referred to as glacier "disequilibrium", i.e. the difference between transient and equilibrium glacier states (Christian et al., 2018). Because it takes time for mass to travel to the glacier terminus following a climate perturbation, less internal ice flux will have occurred if the observational timespan is shorter. This results in a steeper "ice thickness change versus elevation" profile because the glacier had less time to dynamically adjust to a new equilibrium. Figure 5.3D illustrates this effect, with steeper profiles for short timespans versus more gradual profiles for longer ones. It follows that ice thickness change distributions in a given region will also have stronger negative skews and wider IQRs over shorter observational timespans – because the distributions include the strongly negative mass losses at lower elevations which have not yet been compensated by internal ice flux.

### 5.4.2 Relationship between glacier disequilibrium and spatial variability of ice thickness change

Glacier dynamics dictate that for a given climate forcing over annual to multi-decade durations, shorter observational timespans (particularly those focused on periods during which glaciers are further from equilibrium, and are hence undergoing the most rapid change) will tend to exhibit

greater spatial variability (wider IQR) of mean annual ice thickness changes. Conversely, longer timespan measurements will tend to have less spatial variability (smaller IQR) due to the characteristic asymptotic approach toward an equilibrium state (i.e. both the mean and IQR of annual thickness change gradually decrease with time as steady-state is approached). This is shown in both model runs: 1) after an instantaneous climate perturbation, when the widest IQRs were observed for the shortest and earliest timespans during which the glaciers were furthest from steady-state and 2) in the HISTALP run, where the widest IQRs were observed for the shortest and most recent timespans, again during which glaciers are strongly out of equilibrium (Figure 5.5). For timespans which extend further back to include decades with more stability (such as during the mid-1950's to 1970's), the degree of spatial variability is lessened. This highlights a positive correlation between glacier disequilibrium and spatial variability of annual ice thickness changes, which should be taken into account in regional glacier mass balance studies, particularly when analyzing and discussing spatial patterns of ice loss.

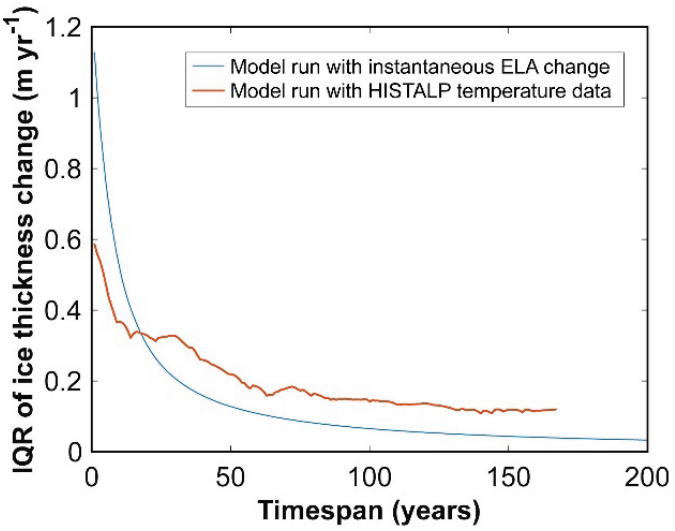


Figure 5.5. IQR of ice thickness change (m $yr^{-1}$) versus observational timespan for both an instantaneous climate perturbation (measured forward from year zero) and the HISTALP temperature forcing (measured backward from year 2018). Note each model run exhibits widest IQRs for shorter timespans, during which glaciers are also furthest from equilibrium.

### 5.4.3 Relevance for modern observations of glacier change

Modern observations of glacier change often utilize satellite-derived elevation models to estimate ice thickness changes over time across mountain regions, and most of these studies focus on glacier changes during the 21st century. Such studies often highlight complex spatial patterns of ice loss and highly variable mass balances between glaciers. In the Himalayas for example, ongoing research is investigating how spatially varying factors such as precipitation, surface debris cover, topographic shading, and anthropogenic black carbon emissions may influence patterns of glacier change (Gertler et al., 2016; Olson and Rupper, 2019; Salerno et al., 2015; Scherler et al., 2011). Results presented here highlight the importance of including effects of internal glacier dynamics in addition to these other factors. During the past four decades in the Himalayas for example (Chapter 3), the average rate of ice loss increased, the steepness of the "thickness change versus elevation" profile increased, and spatial variability of ice loss increased. All these observations are consistent with what would be expected dynamically under a uniform climate forcing, and support the idea of glacier dynamics contributing to "scatter" in regional geodetic mass balance studies over annual to multi-decadal timescales.

### 5.4.4 Broader outlook and proposed avenues for future research

The positive correlation between glacier disequilibrium and spatial variability of ice thickness change is a simple yet useful concept for understanding patterns of glacier change, and is capable of explaining some degree of scatter in regional mass balance compilations, particularly over annual to multi-decadal timescales during the 21st century. Recent global mass balance compilations suggest that global glacier decline in the early 21st century is historically unprecedented (Zemp et al., 2015), near-global retreat of glaciers during the last century is statistically robust evidence of climate change (Roe et al., 2017), and modern glaciers around the

globe are currently in a state of strong disequilibrium (Christian et al., 2018). As a result, the apparent contrast between short-term heterogeneity of satellite and field observations versus the long-term homogeneity of geomorphic and cosmogenic studies is predictable and an expected outcome of glacier dynamics. Multi-decadal regional observations from the Himalayas (Chapter 3) are consistent with this hypothesis, and future compilations of glacier change in other regions will provide a more robust global test.

Over the coming decades, the degree of glacier disequilibrium will largely depend on future emissions and resultant warming, and accurate quantification of glacier dynamics will be critical for understanding and predicting regional mass balance trends. The approach outlined here (with some modifications) could be used to further explore related topics in glaciology and paleoclimate, such as dynamics of clean-ice versus debris-covered glaciers, projections of glacier change and hydrological impacts in vulnerable regions, and variability of ELA-based paleoclimate reconstructions from individual glaciers situated in different topographic and climatic settings.

# References


Abrams, M., 2000. The Advanced Spaceborne Thermal Emission and Reflection Radiometer (ASTER): data products for the high spatial resolution imager on NASA's Terra platform. Int.J.Remote Sens. 21, 847.

Ageta, Y., Higuchi, K., 1984. Estimation of mass balance components of a summer-accumulation type glacier in the Nepal Himalaya. Geografiska Annaler.Series A.Physical Geography, 249.

Andersen, B.G., Mangerud, J., Sørensen, R., Reite, A., Sveian, H., Thoresen, M., Bergström, B., 1995. Younger Dryas ice-marginal deposits in Norway. Quaternary International 28, 147-169.

Arendt, A., Bliss, A., Bolch, T., Cogley, J.G., Gardner, A.S., Hagen, J.O., Hock, R., Huss, M., Kaser, G., Kienholz, C., 2015. Randolph Glacier Inventory–A Dataset of Global Glacier Outlines: Version 5.0. Global Land Ice Measurements from Space, Boulder Colorado, USA.

Atwood, D.K., Meyer, F., Arendt, A., 2010. Using L-band SAR coherence to delineate glacier extent. Canadian Journal of Remote Sensing 36, S186.

Auer, I., Böhm, R., Jurkovic, A., Lipa, W., Orlik, A., Potzmann, R., Schöner, W., Ungersböck, M., Matulla, C., Briffa, K., 2007. HISTALP—historical instrumental climatological surface time series of the Greater Alpine Region. International Journal of Climatology: A Journal of the Royal Meteorological Society 27, 17-46.

Azam, M.F., Wagnon, P., Berthier, E., Vincent, C., Fujita, K., Kargel, J.S., 2018. Review of the status and mass changes of Himalayan-Karakoram glaciers. Journal of Glaciology 64, 61-74.

Badoux, A., Graf, C., Rhyner, J., Kuntner, R., McArdell, B.W., 2009. A debris-flow alarm system for the Alpine Illgraben catchment: design and performance. Natural hazards 49, 517-539.

Bajracharya, S.R., Maharjan, S.B., Shrestha, F., 2014. The status and decadal change of glaciers in Bhutan from the 1980s to 2010 based on satellite data. Annals of Glaciology 55, 159.

Balco, G., 2011. Contributions and unrealized potential contributions of cosmogenic-nuclide exposure dating to glacier chronology, 1990–2010. Quaternary Science Reviews 30, 3-27.

Balco, G., 2020. Glacier Change and Paleoclimate Applications of Cosmogenic-Nuclide Exposure Dating. Annu.Rev.Earth Planet.Sci. 48.

Balco, G., Stone, J.O., Lifton, N.A., Dunai, T.J., 2008. A complete and easily accessible means of calculating surface exposure ages or erosion rates from 10Be and 26Al measurements. Quaternary geochronology 3, 174-195.

Basnett, S., Kulkarni, A.V., Bolch, T., 2013. The influence of debris cover and glacial lakes on the recession of glaciers in Sikkim Himalaya, India. Journal of Glaciology 59, 1035.

Bay, H., Tuytelaars, T., Van Gool, L., 2006. Surf: Speeded up robust features, Computer vision–ECCV 2006. Springer, p. 404.

Begert, M., Frei, C., 2018. Long-term area-mean temperature series for Switzerland—Combining homogenized station data and high resolution grid data. International Journal of Climatology 38, 2792-2807.

Beldring, S., Voksø, A., 2012. Climate Change Impact on Flow Regimes of Rivers in Bhutan and Possible Consequences for Hydropower Development. Hydro Nepal: Journal of Water, Energy and Environment 11, 67.

Beniston, M., 2005. Mountain climates and climatic change: an overview of processes focusing on the European Alps. Pure and Applied Geophysics 162, 1587-1606.

Benn, D.I., Bolch, T., Hands, K., Gulley, J., Luckman, A., Nicholson, L.I., Quincey, D., Thompson, S., Toumi, R., Wiseman, S., 2012. Response of debris-covered glaciers in the Mount Everest region to recent warming, and implications for outburst flood hazards. Earth-Sci.Rev. 114, 156.

Bensen, G., Ritzwoller, M., Barmin, M., Levshin, A., Lin, F., Moschetti, M., Shapiro, N., Yang, Y., 2007. Processing seismic ambient noise data to obtain reliable broad-band surface wave dispersion measurements. Geophysical Journal International 169, 1239-1260.

Berger, J., Davis, P., Ekström, G., 2004. Ambient earth noise: a survey of the global seismographic network. Journal of Geophysical Research: Solid Earth 109.

Berthier, E., Arnaud, Y., Kumar, R., Ahmad, S., Wagnon, P., Chevallier, P., 2007. Remote sensing estimates of glacier mass balances in the Himachal Pradesh (Western Himalaya, India). Remote Sens.Environ. 108, 327.

Beyreuther, M., Barsch, R., Krischer, L., Megies, T., Behr, Y., Wassermann, J., 2010. ObsPy: A Python toolbox for seismology. Seismological Research Letters 81, 530-533.

Bhambri, R., Bolch, T., Kawishwar, P., Dobhal, D.P., Srivastava, D., Pratap, B., 2013. Heterogeneity in glacier response in the upper Shyok valley, northeast Karakoram. The Cryosphere 7, 1385.

Bhutiyani, M.R., Kale, V.S., Pawar, N.J., 2010. Climate change and the precipitation variations in the northwestern Himalaya: 1866–2006. International Journal of Climatology 30, 535.

Bolch, T., Kulkarni, A., Kaab, A., Huggel, C., Paul, F., Cogley, J.G., Frey, H., Kargel, J.S., Fujita, K., Scheel, M., Bajracharya, S., Stoffel, M., 2012. The state and fate of Himalayan glaciers. Science 336, 310.

Bolch, T., Pieczonka, T., Benn, D.I., 2011. Multi-decadal mass loss of glaciers in the Everest area (Nepal Himalaya) derived from stereo imagery. The Cryosphere 5, 349.

Bolch, T., Pieczonka, T., Mukherjee, K., Shea, J., 2017. Brief communication: Glaciers in the Hunza catchment (Karakoram) have been nearly in balance since the 1970s. The Cryosphere 11, 531.

Bollasina, M.A., Ming, Y., Ramaswamy, V., 2011. Anthropogenic aerosols and the weakening of the South Asian summer monsoon. Science 334, 502.

Bond, T.C., Doherty, S.J., Fahey, D., Forster, P., Berntsen, T., DeAngelo, B., Flanner, M., Ghan, S., Kärcher, B., Koch, D., 2013. Bounding the role of black carbon in the climate system: A scientific assessment. Journal of Geophysical Research: Atmospheres 118, 5380-5552.

Borchers, B., Marrero, S., Balco, G., Caffee, M., Goehring, B., Lifton, N., Nishiizumi, K., Phillips, F., Schaefer, J., Stone, J., 2016. Geological calibration of spallation production rates in the CRONUS-Earth project. Quaternary Geochronology 31, 188-198.

Boxleitner, M., Ivy-Ochs, S., Egli, M., Brandova, D., Christl, M., Maisch, M., 2019. Lateglacial and Early Holocene glacier stages-New dating evidence from the Meiental in central Switzerland. Geomorphology 340, 15-31.

Braumann, S.M., Schaefer, J., Neuhuber, S., Reitner, J., Luethgens, C., Fiebig, M., in review. Holocene glacier change in the Silvretta Massif (Austrian Alps) constrained by a new 10Be chronology, historical records and instrumental data. Quaternary Science Reviews.

Briner, J.P., Svendsen, J.I., Mangerud, J., Lohne, Ø.S., Young, N.E., 2014. A 10Be chronology of south-western Scandinavian Ice Sheet history during the Lateglacial period. Journal of Quaternary Science 29, 370-380.

Bromley, G., Putnam, A., Borns Jr, H., Lowell, T., Sandford, T., Barrell, D., 2018. Interstadial Rise and Younger Dryas Demise of Scotland's Last Ice Fields. Paleoceanography and Paleoclimatology 33, 412-429.

Bromley, G.R., Hall, B.L., Thompson, W.B., Kaplan, M.R., Garcia, J.L., Schaefer, J.M., 2015. Late glacial fluctuations of the Laurentide ice sheet in the White Mountains of Maine and New Hampshire, USA. Quatern.Res. 83, 522-530.

Brun, F., Berthier, E., Wagnon, P., Kaab, A., Treichler, D., 2017. A spatially resolved estimate of High Mountain Asia glacier mass balances from 2000 to 2016. Nature Geoscience 10, 668.

Brunner, G.W., 2010. HEC-RAS river analysis system: hydraulic reference manual. US Army Corps of Engineers, Institute for Water Resources, Hydrologic Engineering Center.

Brzak, K., Gu, Y.J., Ökeler, A., Steckler, M., Lerner-Lam, A., 2009. Migration imaging and forward modeling of microseismic noise sources near southern Italy. Geochem.Geophys.Geosyst. 10.

Bueler, E., Lingle, C.S., Kallen-Brown, J.A., Covey, D.N., Bowman, L.N., 2005. Exact solutions and verification of numerical models for isothermal ice sheets. Journal of Glaciology 51, 291-306.

Buizert, C., Gkinis, V., Severinghaus, J.P., He, F., Lecavalier, B.S., Kindler, P., Leuenberger, M., Carlson, A.E., Vinther, B., Masson-Delmotte, V., 2014. Greenland temperature response to climate forcing during the last deglaciation. Science 345, 1177-1180.

Buizert, C., Keisling, B., Box, J., He, F., Carlson, A., Sinclair, G., DeConto, R., 2018. Greenland-Wide Seasonal Temperatures During the Last Deglaciation. Geophysical Research Letters 45, 1905-1914.

Buri, P., Pellicciotti, F., Steiner, J.F., Miles, E.S., Immerzeel, W.W., 2015. A grid-based model of backwasting of supraglacial ice cliffs on debris-covered glaciers. Annals of Glaciology.

Burtin, A., Bollinger, L., Vergne, J., Cattin, R., Nábělek, J., 2008. Spectral analysis of seismic noise induced by rivers: A new tool to monitor spatiotemporal changes in stream hydrodynamics. Journal of Geophysical Research: Solid Earth 113.

Burtin, A., Hovius, N., Turowski, J.M., 2016. Seismic monitoring of torrential and fluvial processes. Earth Surface Dynamics 4.

Burtin, A., Vergne, J., Rivera, L., Dubernet, P., 2010. Location of river-induced seismic signal from noise correlation functions. Geophysical Journal International 182, 1161-1173.

Carrivick, J.L., Tweed, F.S., 2016. A global assessment of the societal impacts of glacier outburst floods. Global Planet.Change 144, 1-16.

Casty, C., Wanner, H., Luterbacher, J., Esper, J., Böhm, R., 2005. Temperature and precipitation variability in the European Alps since 1500. International Journal of Climatology: A Journal of the Royal Meteorological Society 25, 1855-1880.

Chao, W.-A., Wu, Y.-M., Zhao, L., Tsai, V.C., Chen, C.-H., 2015. Seismologically determined bedload flux during the typhoon season. Sci.Rep. 5, 8261.

Christian, J.E., Koutnik, M., Roe, G., 2018. Committed retreat: controls on glacier disequilibrium in a warming climate. Journal of Glaciology 64, 675-688.

Church, J.A., Clark, P.U., Cazenave, A., Gregory, J.M., Jevrejeva, S., Levermann, A., Merrifield, M.A., Milne, G.A., Nerem, R.S., Nunn, P.D., 2013. Climate change 2013: the physical science basis. Contribution of Working Group I to the Fifth Assessment Report of the Intergovernmental Panel on Climate Change. Sea level change, 1137.

Clark, P.U., Shakun, J.D., Baker, P.A., Bartlein, P.J., Brewer, S., Brook, E., Carlson, A.E., Cheng, H., Kaufman, D.S., Liu, Z., 2012. Global climate evolution during the last deglaciation. Proceedings of the National Academy of Sciences 109, E1134-E1142.

Claude, A., Ivy-Ochs, S., Kober, F., Antognini, M., Salcher, B., Kubik, P.W., 2014. The Chironico landslide (Valle Leventina, southern Swiss Alps): age and evolution. Swiss Journal of Geosciences 107, 273.

Cogley, J.G., 2012. Climate science: Himalayan glaciers in the balance. Nature 488, 468.

Cook, K.L., Andermann, C., Gimbert, F., Adhikari, B.R., Hovius, N., 2018. Glacial lake outburst floods as drivers of fluvial erosion in the Himalaya. Science 362, 53-57.

Cuffey, K.M., Paterson, W.S.B., 2010. The physics of glaciers. Academic Press.

Curran, P.J., 1988. The semivariogram in remote sensing: an introduction. Remote Sens.Environ. 24, 493.

Dee, D.P., Uppala, S.M., Simmons, A.J., Berrisford, P., Poli, P., Kobayashi, S., Andrae, U., Balmaseda, M.A., Balsamo, G., Bauer, P., 2011. The ERA-Interim reanalysis: Configuration and performance of the data assimilation system. Q.J.R.Meteorol.Soc. 137, 553.

Dehecq, A., Gourmelen, N., Gardner, A.S., Brun, F., Goldberg, D., Nienow, P.W., Berthier, E., Vincent, C., Wagnon, P., Trouvé, E., 2019. Twenty-first century glacier slowdown driven by mass loss in High Mountain Asia. Nature Geoscience 12, 22-27.

Denton, G.H., Alley, R.B., Comer, G.C., Broecker, W.S., 2005. The role of seasonality in abrupt climate change. Quaternary Science Reviews 24, 1159-1182.

Dimri, A.P., Immerzeel, W.W., Salzmann, N., Thayyen, R.J., 2017. Comparison of climatic trends and variability among glacierized environments in the Western Himalayas. Theoretical and Applied Climatology, 1.

Federici, P.R., Granger, D.E., Pappalardo, M., Ribolini, A., Spagnolo, M., Cyr, A.J., 2008. Exposure age dating and Equilibrium Line Altitude reconstruction of an Egesen moraine in the Maritime Alps, Italy. Boreas 37, 245-253.

Fischer, M., Huss, M., Hoelzle, M., 2015. Surface elevation and mass changes of all Swiss glaciers 1980–2010. The Cryosphere 9, 525.

Foresta, L., Gourmelen, N., Weissgerber, F., Nienow, P., Williams, J.J., Shepherd, A., Drinkwater, M.R., Plummer, S., 2018. Heterogeneous and rapid ice loss over the Patagonian Ice Fields revealed by CryoSat-2 swath radar altimetry. Remote Sens.Environ. 211, 441-455.

Fowler, A., Larson, D., 1978. On the flow of polythermal glaciers-I. Model and preliminary analysis. Proceedings of the Royal Society of London. A. Mathematical and Physical Sciences 363, 217-242.

Frey, H., Machguth, H., Huss, M., Huggel, C., Bajracharya, S., Bolch, T., Kulkarni, A., Linsbauer, A., Salzmann, N., Stoffel, M., 2014. Estimating the volume of glaciers in the Himalayan–Karakoram region using different methods. The Cryosphere 8, 2313.

Frey, H., Paul, F., Strozzi, T., 2012. Compilation of a glacier inventory for the western Himalayas from satellite data: methods, challenges, and results. Remote Sens.Environ. 124, 832.

Fujita, K., Suzuki, R., Nuimura, T., Sakai, A., 2008. Performance of ASTER and SRTM DEMs, and their potential for assessing glacial lakes in the Lunana region, Bhutan Himalaya. Journal of Glaciology 54, 220.

Fusiello, A., Irsara, L., 2008. Quasi-euclidean uncalibrated epipolar rectification, Pattern Recognition, 2008. ICPR 2008. 19th International Conference on. IEEE, p. 1.

García, J.L., Kaplan, M.R., Hall, B.L., Schaefer, J.M., Vega, R.M., Schwartz, R., Finkel, R., 2012. Glacier expansion in southern Patagonia throughout the Antarctic cold reversal. Geology 40, 859-862.

Gardelle, J., Arnaud, Y., Berthier, E., 2011. Contrasted evolution of glacial lakes along the Hindu Kush Himalaya mountain range between 1990 and 2009. Global Planet.Change 75, 47.

Gardelle, J., Berthier, E., Arnaud, Y., 2012. Impact of resolution and radar penetration on glacier elevation changes computed from DEM differencing. Journal of Glaciology 58, 419.

Gardelle, J., Berthier, E., Arnaud, Y., Kääb, A., 2013. Region-wide glacier mass balances over the Pamir-Karakoram-Himalaya during 1999-2011 (vol 7, pg 1263, 2013). The Cryosphere 7, 1885.

Gardner, A.S., Moholdt, G., Cogley, J.G., Wouters, B., Arendt, A.A., Wahr, J., Berthier, E., Hock, R., Pfeffer, W.T., Kaser, G., Ligtenberg, S.R., Bolch, T., Sharp, M.J., Hagen, J.O., van den Broeke, M.R., Paul, F., 2013. A reconciled estimate of glacier contributions to sea level rise: 2003 to 2009. Science 340, 852.

Gertler, C.G., Puppala, S.P., Panday, A., Stumm, D., Shea, J., 2016. Black carbon and the Himalayan cryosphere: A review. Atmos.Environ. 125, 404.

Gimbert, F., Tsai, V.C., Lamb, M.P., 2014. A physical model for seismic noise generation by turbulent flow in rivers. Journal of Geophysical Research: Earth Surface 119, 2209-2238.

González-Vida, J.M., Macías, J., Castro, M.J., Sánchez-Linares, C., Asunción, M.d.l., Ortega-Acosta, S., Arcas, D., 2019. The Lituya Bay landslide-generated mega-tsunami–

numerical simulation and sensitivity analysis. Natural Hazards and Earth System Sciences 19, 369-388.

Goodling, P.J., Lekic, V., Prestegaard, K., 2018. Seismic signature of turbulence during the 2017 Oroville Dam spillway erosion crisis. Earth Surface Dynamics 6.

Gorelick, N., Hancher, M., Dixon, M., Ilyushchenko, S., Thau, D., Moore, R., 2017. Google Earth Engine: Planetary-scale geospatial analysis for everyone. Remote Sens.Environ. 202, 18-27.

Haas, J.N., Richoz, I., Tinner, W., Wick, L., 1998. Synchronous Holocene climatic oscillations recorded on the Swiss Plateau and at timberline in the Alps. The holocene 8, 301-309.

Harrison, S., Kargel, J.S., Huggel, C., Reynolds, J., Shugar, D.H., Betts, R.A., Emmer, A., Glasser, N., Haritashya, U.K., Klimeš, J., Reinhardt, L., Schaub, Y., Wiltshire, A., Regmi, D., Vilímek, V., 2018. Climate change and the global pattern of moraine-dammed glacial lake outburst floods. The Cryosphere 12, 1195-1209.

Hartley, R., Zisserman, A., 2003. Multiple view geometry in computer vision. Cambridge university press.

Heiri, O., Koinig, K.A., Spötl, C., Barrett, S., Brauer, A., Drescher-Schneider, R., Gaar, D., Ivy-Ochs, S., Kerschner, H., Luetscher, M., 2014. Palaeoclimate records 60–8 ka in the Austrian and Swiss Alps and their forelands. Quaternary Science Reviews 106, 186-205.

Helfricht, K., Huss, M., Fischer, A., Otto, J.-C., 2019. Spatial ice thickness distribution and glacier bed elevation for glaciers of the third Austrian Glacier Inventory (GI3), Supplement to: Helfricht, K et al. (2019): Calibrated Ice Thickness Estimate for All Glaciers in Austria. Frontiers in Earth Science, 7, https://doi.org/10.3389/feart.2019.00068. PANGAEA.

Hindmarsh, R.C., 2001. Notes on basic glaciological computational methods and algorithms, Continuum Mechanics and Applications in Geophysics and the Environment. Springer, pp. 222-249.

Hirschmüller, H., 2008. Stereo processing by semiglobal matching and mutual information. Pattern Analysis and Machine Intelligence, IEEE Transactions on 30, 328.

Holzer, N., Vijay, S., Yao, T., Xu, B., Buchroithner, M., Bolch, T., 2015. Four decades of glacier variations at Muztagh Ata (eastern Pamir): a multi-sensor study including Hexagon KH-9 and Pléiades data. The Cryosphere 9, 2071.

Huss, M., 2013. Density assumptions for converting geodetic glacier volume change to mass change. The Cryosphere 7, 877.

Hutter, K., 1981. The effect of longitudinal strain on the shear stress of an ice sheet: in defence of using stretched coordinates. Journal of Glaciology 27, 39-56.

Hutter, K., 1983. Theoretical Glaciology: Material Science of Ice and the Mechanics of Glaciers and Ice Sheets. Springer.

Hydrology-Division, 2013. GLOF Early Warning System in the Punakha Wangdue Valley. Department of Hydro-met Services, Ministry of Economic Affair, Thimphu, Bhutan.

Immerzeel, W.W., Kraaijenbrink, P.D.A., Shea, J.M., Shrestha, A.B., Pellicciotti, F., Bierkens, M.F.P., De Jong, S.M., 2014a. High-resolution monitoring of Himalayan glacier dynamics using unmanned aerial vehicles. Remote Sens.Environ. 150, 93.

Immerzeel, W.W., Petersen, L., Ragettli, S., Pellicciotti, F., 2014b. The importance of observed gradients of air temperature and precipitation for modeling runoff from a glacierized watershed in the Nepalese Himalayas. Water Resour.Res. 50, 2212.

Immerzeel, W.W., van Beek, L.P., Bierkens, M.F., 2010. Climate change will affect the Asian water towers. Science 328, 1382.

Ivy-Ochs, S., 2015. Glacier variations in the European Alps at the end of the last glaciation. Cuadernos de investigación geográfica/Geographical Research Letters, 295-315.

Ivy-Ochs, S., Schlüchter, C., Kubik, P.W., Synal, H.-A., Beer, J., Kerschner, H., 1996. The exposure age of an Egesen moraine at Julier Pass, Switzerland measured with the cosmogenic radionuclides Be-10, Al-26 and Cl-36. Eclogae Geologicae Helvetiae 89, 1049-1063.

Ivy-Ochs, S., Kerschner, H., Kubik, P.W., Schlüchter, C., 2006. Glacier response in the European Alps to Heinrich Event 1 cooling: the Gschnitz stadial. Journal of Quaternary science 21, 115-130.

Ivy-Ochs, S., Kerschner, H., Reuther, A., Preusser, F., Heine, K., Maisch, M., Kubik, P.W., Schlüchter, C., 2008. Chronology of the last glacial cycle in the European Alps. Journal of Quaternary Science: Published for the Quaternary Research Association 23, 559-573.

Iwata, S., 2002. Glacier lakes and their outburst flood assessment in the Bhutan Himalaya. Global Environ. Res. 6, 3-17.

Jarosch, A., Schoof, C., Anslow, F., 2013. Restoring mass conservation to shallow ice flow models over complex terrain. Cryosphere 7.

JICA, 2001. Feasibility study on the development of Punatsangchhu hydropower project in the Kingdom of Bhutan final report. Japan International Cooperation Agency.

Joshi, R., Satyal, P., Setzer, W., 2016. Himalayan aromatic medicinal plants: a review of their ethnopharmacology, volatile phytochemistry, and biological activities. Medicines 3, 6.

Kääb, A., 2005. Combination of SRTM3 and repeat ASTER data for deriving alpine glacier flow velocities in the Bhutan Himalaya. Remote Sens.Environ. 94, 463.

Kääb, A., Berthier, E., Nuth, C., Gardelle, J., Arnaud, Y., 2012. Contrasting patterns of early twenty-first-century glacier mass change in the Himalayas. Nature 488, 495.

Kääb, A., Leinss, S., Gilbert, A., Bühler, Y., Gascoin, S., Evans, S.G., Bartelt, P., Berthier, E., Brun, F., Chao, W.-A., 2018. Massive collapse of two glaciers in western Tibet in 2016 after surge-like instability. Nature Geoscience 11, 114-120.

Kääb, A., Treichler, D., Nuth, C., Berthier, E., 2015. Brief Communication: Contending estimates of 2003–2008 glacier mass balance over the Pamir–Karakoram–Himalaya. The Cryosphere 9, 557.

Kaplan, M.R., Schaefer, J.M., Denton, G.H., Barrell, D.J., Chinn, T.J., Putnam, A.E., Andersen, B.G., Finkel, R.C., Schwartz, R., Doughty, A.M., 2010. Glacier retreat in New Zealand during the Younger Dryas stadial. Nature 467, 194-197.

Kaplan, M.R., Schaefer, J.M., Denton, G.H., Doughty, A.M., Barrell, D.J.A., Chinn, T.J.H., Putnam, A.E., Andersen, B.G., Mackintosh, A., Finkel, R.C., 2013. The anatomy of long-term warming since 15 ka in New Zealand based on net glacier snowline rise. Geology 41, 887.

Kaser, G., Grosshauser, M., Marzeion, B., 2010. Contribution potential of glaciers to water availability in different climate regimes. Proc.Natl.Acad.Sci.U.S.A. 107, 20223.

Kaspari, S., Painter, T.H., Gysel, M., Skiles, S.M., Schwikowski, M., 2014. Seasonal and elevational variations of black carbon and dust in snow and ice in the Solu-Khumbu, Nepal and estimated radiative forcings. Atmospheric chemistry and physics 14, 8089.

Kattel, D.B., Yao, T., 2013. Recent temperature trends at mountain stations on the southern slope of the central Himalayas. Journal of Earth System Science 122, 215.

Kelly, M.A., Kubik, P.W., Von Blanckenburg, F., SchlÜchter, C., 2004. Surface exposure dating of the Great Aletsch Glacier Egesen moraine system, western Swiss Alps, using the cosmogenic nuclide 10Be. Journal of Quaternary Science: Published for the Quaternary Research Association 19, 431-441.

Kelly, M.A., Lowell, T.V., Hall, B.L., Schaefer, J.M., Finkel, R.C., Goehring, B.M., Alley, R.B., Denton, G.H., 2008. A 10Be chronology of lateglacial and Holocene mountain glaciation in the Scoresby Sund region, east Greenland: implications for seasonality during lateglacial time. Quaternary Science Reviews 27, 2273-2282.

Kim, T., 2000. A study on the epipolarity of linear pushbroom images. Photogramm.Eng.Remote Sensing 66, 961.

Koike, T., Takenaka, S., 2012. Scenario analysis on risks of glacial lake outburst floods on the Mangde Chhu River, Bhutan. Global Environmental Research 16, 41-49.

Kos, A., Amann, F., Strozzi, T., Delaloye, R., Ruette, J., Springman, S., 2016. Contemporary glacier retreat triggers a rapid landslide response, Great Aletsch Glacier, Switzerland. Geophysical Research Letters 43.

Kraaijenbrink, P.D.A., Bierkens, M.F.P., Lutz, A.F., Immerzeel, W.W., 2017. Impact of a global temperature rise of 1.5 degrees Celsius on Asia's glaciers. Nature 549, 257.

Krishnamurthy, V., Goswami, B.N., 2000. Indian monsoon–ENSO relationship on interdecadal timescale. J.Clim. 13, 579.

Krüger, T., 2013. Discovering the Ice Ages: international reception and consequences for a historical understanding of climate. Brill.

Kuensel, 2019. Heat wave and delayed monsoon caused Thorthormi to breach. Kuensel Corporation Ltd. .

Lai, V.H., Tsai, V.C., Lamb, M.P., Ulizio, T.P., Beer, A.R., 2018. The seismic signature of debris flows: Flow mechanics and early warning at Montecito, California. Geophysical Research Letters 45, 5528-5535.

Lal, D., 1991. Cosmic ray labeling of erosion surfaces: in situ nuclide production rates and erosion models. Earth and Planetary Science Letters 104, 424-439.

Lamsal, D., Sawagaki, T., Watanabe, T., 2011. Digital terrain modelling using Corona and ALOS PRISM data to investigate the distal part of Imja Glacier, Khumbu Himal, Nepal. Journal of Mountain Science 8, 390.

Levy, L.B., Kelly, M.A., Lowell, T.V., Hall, B.L., Howley, J.A., Smith, C.A., 2016. Coeval fluctuations of the Greenland ice sheet and a local glacier, central East Greenland, during late glacial and early Holocene time. Geophysical Research Letters 43, 1623-1631.

Leysinger Vieli, G.M., Gudmundsson, G.H., 2004. On estimating length fluctuations of glaciers caused by changes in climatic forcing. Journal of Geophysical Research: Earth Surface 109.

Linsbauer, A., Frey, H., Haeberli, W., Machguth, H., Azam, M.F., Allen, S., 2016. Modelling glacier-bed overdeepenings and possible future lakes for the glaciers in the Himalaya–Karakoram region. Annals of Glaciology 57, 119.

Lohne, Ø.S., Bondevik, S., Mangerud, J., Svendsen, J.I., 2007. Sea-level fluctuations imply that the Younger Dryas ice-sheet expansion in western Norway commenced during the Allerød. Quaternary Science Reviews 26, 2128-2151.

Lotter, A.F., Eicher, U., Birks, H.J.B., Siegenthaler, U., 1992. Late-glacial climatic oscillations as recorded in Swiss lake sediments. Journal of Quaternary Science 7, 187 - null.

Lotter, A.F., Heiri, O., Brooks, S., van Leeuwen, J.F., Eicher, U., Ammann, B., 2012. Rapid summer temperature changes during Termination 1a: high-resolution multi-proxy climate reconstructions from Gerzensee (Switzerland). Quaternary Science Reviews 36, 103-113.

Lutz, A.F., Immerzeel, W.W., Shrestha, A.B., Bierkens, M.F.P., 2014. Consistent increase in High Asia's runoff due to increasing glacier melt and precipitation. Nature Climate Change 4, 587.

Marzeion, B., Cogley, J.G., Richter, K., Parkes, D., 2014. Glaciers. Attribution of global glacier mass loss to anthropogenic and natural causes. Science 345, 919.

Marzeion, B., Jarosch, A.H., Hofer, M., 2012. Past and future sea-level change from the surface mass balance of glaciers. The Cryosphere 6, 1295.

Mattar, K.E., Vachon, P.W., Geudtner, D., Gray, A.L., Cumming, I.G., Brugman, M., 1998. Validation of alpine glacier velocity measurements using ERS tandem-mission SAR data. IEEE Trans.Geosci.Remote Sens. 36, 974.

Maurer, J., Rupper, S., 2015. Tapping into the Hexagon spy imagery database: A new automated pipeline for geomorphic change detection. ISPRS Journal of Photogrammetry and Remote Sensing 108, 113.

Maurer, J., Schaefer, J., Rupper, S., Corley, A., 2019. Acceleration of ice loss across the Himalayas over the past 40 years. Science Advances 5, eaav7266.

Maurer, J.M., Rupper, S.B., Schaefer, J.M., 2016. Quantifying ice loss in the eastern Himalayas since 1974 using declassified spy satellite imagery. The Cryosphere 10, 2203.

McManus, J.F., Francois, R., Gherardi, J.-M., Keigwin, L.D., Brown-Leger, S., 2004. Collapse and rapid resumption of Atlantic meridional circulation linked to deglacial climate changes. Nature 428, 834-837.

Menounos, B., Goehring, B.M., Osborn, G., Margold, M., Ward, B., Bond, J., Clarke, G.K., Clague, J.J., Lakeman, T., Koch, J., 2017. Cordilleran Ice Sheet mass loss preceded climate reversals near the Pleistocene Termination. Science 358, 781-784.

Menounos, B., Hugonnet, R., Shean, D., Gardner, A., Howat, I., Berthier, E., Pelto, B., Tennant, C., Shea, J., Noh, M.-J., Brun, F., Dehecq, A., 2019. Heterogeneous Changes in Western North American Glaciers Linked to Decadal Variability in Zonal Wind Strength. Geophysical Research Letters 46, 200-209.

Meyer, M., Wiesmayr, G., Brauner, M., Häusler, H., Wangda, D., 2006. Active tectonics in Eastern Lunana (NW Bhutan): Implications for the seismic and glacial hazard potential of the Bhutan Himalaya. Tectonics 25.

Meyer, M.C., Hofmann, C.-C., Gemmell, A.M., Haslinger, E., Häusler, H., Wangda, D., 2009. Holocene glacier fluctuations and migration of Neolithic yak pastoralists into the high valleys of northwest Bhutan. Quaternary Science Reviews 28, 1217-1237.

Miles, E.S., Pellicciotti, F., Willis, I.C., Steiner, J.F., Buri, P., Arnold, N.S., 2016. Refined energy-balance modelling of a supraglacial pond, Langtang Khola, Nepal. Annals of Glaciology 57, 29.

Moreno, A., Svensson, A., Brooks, S.J., Connor, S., Engels, S., Fletcher, W., Genty, D., Heiri, O., Labuhn, I., Perşoiu, A., 2014. A compilation of Western European terrestrial records 60–8 ka BP: towards an understanding of latitudinal climatic gradients. Quaternary Science Reviews 106, 167-185.

Moussa, R., Bocquillon, C., 1996. Algorithms for solving the diffusive wave flood routing equation. Hydrol.Process. 10, 105-123.

Naito, N., Ageta, Y., Nakawo, M., Edwin, D.W., Charles, F.R., Howard, C., 2001. Response sensitivities of a summer-accumulation type glacier to climate changes indicated with a glacier fluctuation model. Bulletin of glaciological research 18, 1-8.

Nelson, K.D., Zhao, W., Brown, L., Kuo, J., Che, J., Liu, X., Klemperer, S., Makovsky, Y., Meissner, R., Mechie, J., 1996. Partially molten middle crust beneath southern Tibet: synthesis of project INDEPTH results. Science 274, 1684-1688.

Nishiizumi, K., Imamura, M., Caffee, M.W., Southon, J.R., Finkel, R.C., McAninch, J., 2007. Absolute calibration of 10Be AMS standards. Nuclear Instruments and Methods in Physics Research Section B: Beam Interactions with Materials and Atoms 258, 403-413.

North Greenland Ice Core Project members, 2004. High resolution record of Northern Hemisphere climate extending into the last interglacial period. Nature 431, 147-151.

Nuimura, T., Fujita, K., Yamaguchi, S., Sharma, R.R., 2012. Elevation changes of glaciers revealed by multitemporal digital elevation models calibrated by GPS survey in the Khumbu region, Nepal Himalaya, 1992-2008. Journal of Glaciology 58, 648-656.

Nuth, C., Kääb, A., 2011. Co-registration and bias corrections of satellite elevation data sets for quantifying glacier thickness change. The Cryosphere 5, 271.

Nuth, C., Moholdt, G., Kohler, J., Hagen, J.O., Kääb, A., 2010. Svalbard glacier elevation changes and contribution to sea level rise. Journal of Geophysical Research: Earth Surface 115.

Oder, F.C.E., Fitzpatrick, J.C., Worthman, P.E., 2012. The HEXAGON Story. Center for the Study of National Reconnaissance.

Oerlemans, J., Fortuin, J., 1992. Sensitivity of glaciers and small ice caps to greenhouse warming. Science 258, 115-117.

Ohlendorf, C., 1998. High Alpine lake sediments as chronicles for regional glacier and climate history in the Upper Engadine, southeastern Switzerland. ETH Zurich.

Ohmura, A., 2001. Physical basis for the temperature-based melt-index method. J.Appl.Meteorol. 40, 753.

Ojha, S., Fujita, K., Asahi, K., Sakai, A., Lamsal, D., Nuimura, T., Nagai, H., 2016. Glacier area shrinkage in eastern Nepal Himalaya since 1992 using high-resolution inventories from aerial photographs and ALOS satellite images. Journal of Glaciology 62, 512.

Olson, M., Rupper, S., 2019. Impacts of topographic shading on direct solar radiation for valley glaciers in complex topography. Cryosphere 13.

Osti, R., Egashira, S., Adikari, Y., 2013. Prediction and assessment of multiple glacial lake outburst floods scenario in Pho Chu River basin, Bhutan. Hydrol.Process. 27, 262.

Palazzi, E., Hardenberg, J., Provenzale, A., 2013. Precipitation in the Hindu-Kush Karakoram Himalaya: Observations and future scenarios. Journal of Geophysical Research: Atmospheres 118, 85.

Paul, F., 2000. Evaluation of different methods for glacier mapping using Landsat TM, Proceedings, EARSeL-SIG Workshop.

Paul, F., Barrand, N.E., Baumann, S., Berthier, E., Bolch, T., Casey, K., Frey, H., Joshi, S.P., Konovalov, V., Le Bris, R., 2013. On the accuracy of glacier outlines derived from remote-sensing data. Annals of Glaciology 54, 171.

Paul, F., Haeberli, W., 2008. Spatial variability of glacier elevation changes in the Swiss Alps obtained from two digital elevation models. Geophysical Research Letters 35.

Pellicciotti, F., Stephan, C., Miles, E., Herreid, S., Immerzeel, W.W., Bolch, T., 2015. Mass-balance changes of the debris-covered glaciers in the Langtang Himal, Nepal, from 1974 to 1999. Journal of Glaciology 61, 373.

Pellikka, P., Rees, W.G., 2009. Remote sensing of glaciers: techniques for topographic, spatial and thematic mapping of glaciers. CRC Press.

Penck, A., Brückner, E., 1909. Die alpen im Eiszeitalter. CH Tauchnitz.

Pieczonka, T., Bolch, T., 2015. Region-wide glacier mass budgets and area changes for the Central Tien Shan between~ 1975 and 1999 using Hexagon KH-9 imagery. Global Planet.Change 128, 1.

Pieczonka, T., Bolch, T., Junfeng, W., Shiyin, L., 2013. Heterogeneous mass loss of glaciers in the Aksu-Tarim Catchment (Central Tien Shan) revealed by 1976 KH-9 Hexagon and 2009 SPOT-5 stereo imagery. Remote Sens.Environ. 130, 233.

Pratap, B., Dobhal, D.P., Mehta, M., Bhambri, R., 2015. Influence of debris cover and altitude on glacier surface melting: a case study on Dokriani Glacier, central Himalaya, India. Annals of Glaciology 56, 9.

Protin, M., Schimmelpfennig, I., Mugnier, J.-L., Ravanel, L., Le Roy, M., Deline, P., Favier, V., Buoncristiani, J.-F., Aumaître, G., Bourlès, D.L., 2019. Climatic reconstruction for the Younger Dryas/Early Holocene transition and the Little Ice Age based on paleo-extents of Argentière glacier (French Alps). Quaternary Science Reviews 221, 105863.

Putnam, A.E., Denton, G.H., Schaefer, J.M., Barrell, D.J., Andersen, B.G., Finkel, R.C., Schwartz, R., Doughty, A.M., Kaplan, M.R., Schlüchter, C., 2010. Glacier advance in southern middle-latitudes during the Antarctic Cold Reversal. Nature Geoscience 3, 700-704.

Qian, Y., Gustafson, W.I., Leung, L.R., Ghan, S.J., 2009. Effects of soot-induced snow albedo change on snowpack and hydrological cycle in western United States based on Weather Research and Forecasting chemistry and regional climate simulations. Journal of Geophysical Research: Atmospheres 114.

Quincey, D., Braun, M., Glasser, N.F., Bishop, M., Hewitt, K., Luckman, A., 2011. Karakoram glacier surge dynamics. Geophysical Research Letters 38.

Racoviteanu, A., Arnaud, Y., Williams, M.W., Manley, W.F., 2014. Spatial patterns in glacier characteristics and area changes from 1962 to 2006 in the Kanchenjunga–Sikkim area, eastern Himalaya. The Cryosphere 9, 505.

Ragettli, S., Bolch, T., Pellicciotti, F., 2016. Heterogeneous glacier thinning patterns over the last 40 years in Langtang Himal. The Cryosphere 10, 2075-2097.

Raj, K.B.G., Remya, S.N., Kumar, K.V., 2013. Remote sensing-based hazard assessment of glacial lakes in Sikkim Himalaya. Current Science(Bangalore) 104, 359.

Rasmussen, S.O., Bigler, M., Blockley, S.P., Blunier, T., Buchardt, S.L., Clausen, H.B., Cvijanovic, I., Dahl-Jensen, D., Johnsen, S.J., Fischer, H., 2014. A stratigraphic framework for abrupt climatic changes during the Last Glacial period based on three synchronized Greenland ice-core records: refining and extending the INTIMATE event stratigraphy. Quaternary Science Reviews 106, 14-28.

Reid, T.D., Brock, B.W., 2014. Assessing ice-cliff backwasting and its contribution to total ablation of debris-covered Miage glacier, Mont Blanc massif, Italy. Journal of Glaciology 60, 3.

Reitner, J.r.M., Ivy-Ochs, S., Drescher-Schneider, R., Hajdas, I., Linner, M., 2016. Reconsidering the current stratigraphy of the Alpine Lateglacial: Implications of the sedimentary and morphological record of the Lienz area (Tyrol/Austria). E & G Quaternary Science Journal 65, 113-144.

Ren, Y.-Y., Ren, G.-Y., Sun, X.-B., Shrestha, A.B., You, Q.-L., Zhan, Y.-J., Rajbhandari, R., Zhang, P.-F., Wen, K.-M., 2017. Observed changes in surface air temperature and precipitation in the Hindu Kush Himalayan region over the last 100-plus years. Advances in Climate Change Research 8, 148.

Richardson, S.D., Reynolds, J.M., 2000. An overview of glacial hazards in the Himalayas. Quaternary International 65, 31.

Roe, G., 2009. Feedbacks, timescales, and seeing red. Annu.Rev.Earth Planet.Sci. 37, 93.

Roe, G.H., 2011. What do glaciers tell us about climate variability and climate change? Journal of Glaciology 57, 567-578.

Roe, G.H., Baker, M.B., 2014. Glacier response to climate perturbations: an accurate linear geometric model. Journal of Glaciology 60, 670.

Roe, G.H., Baker, M.B., Herla, F., 2017. Centennial glacier retreat as categorical evidence of regional climate change. Nature Geoscience 10, 95.

Rolstad, C., Haug, T., Denby, B., 2009. Spatially integrated geodetic glacier mass balance and its uncertainty based on geostatistical analysis: application to the western Svartisen ice cap, Norway. Journal of Glaciology 55, 666.

Rounce, D., Watson, C., McKinney, D., 2017. Identification of hazard and risk for glacial lakes in the Nepal Himalaya using satellite imagery from 2000–2015. Remote Sensing 9, 654.

Rowan, A.V., Egholm, D.L., Quincey, D.J., Glasser, N.F., 2015. Modelling the feedbacks between mass balance, ice flow and debris transport to predict the response to climate change of debris-covered glaciers in the Himalaya. Earth and Planetary Science Letters 430, 427.

Rupper, S., Roe, G., 2008. Glacier changes and regional climate: a mass and energy balance approach. J.Clim. 21, 5384.

Rupper, S., Schaefer, J.M., Burgener, L.K., Koenig, L.S., Tsering, K., Cook, E.R., 2012. Sensitivity and response of Bhutanese glaciers to atmospheric warming. Geophysical Research Letters 39.

Sagredo, E.A., Kaplan, M.R., Araya, P.S., Lowell, T.V., Aravena, J.C., Moreno, P.I., Kelly, M.A., Schaefer, J.M., 2018. Trans-pacific glacial response to the Antarctic Cold Reversal in the southern mid-latitudes. Quaternary Science Reviews 188, 160-166.

Sakai, A., Fujita, K., 2010. Formation conditions of supraglacial lakes on debris-covered glaciers in the Himalaya. Journal of Glaciology, 177.

Sakai, A., Nishimura, K., Kadota, T., Takeuchi, N., 2009. Onset of calving at supraglacial lakes on debris-covered glaciers of the Nepal Himalaya. Journal of Glaciology 55, 909.

Salerno, F., Guyennon, N., Thakuri, S., Viviano, G., Romano, E., Vuillermoz, E., Cristofanelli, P., Stocchi, P., Agrillo, G., Ma, Y., 2015. Weak precipitation, warm winters and springs impact glaciers of south slopes of Mt. Everest (central Himalaya) in the last 2 decades (1994–2013). The Cryosphere 9, 1229-1247.

Sandvol, E., Ni, J., Kind, R., Zhao, W., 1997. Seismic anisotropy beneath the southern Himalayas-Tibet collision zone. Journal of Geophysical Research: Solid Earth 102, 17813-17823.

Sartori, M., Gouffon, Y., Marthaler, M., 2006. Harmonisation et définition des unités lithostratigraphiques briançonnaises dans les nappes penniques du Valais. Eclogae Geologicae Helvetiae 99, 363-407.

Schaefer, J.M., Denton, G.H., Barrell, D.J., Ivy-Ochs, S., Kubik, P.W., Andersen, B.G., Phillips, F.M., Lowell, T.V., Schluchter, C., 2006. Near-synchronous interhemispheric termination of the last glacial maximum in mid-latitudes. Science 312, 1510.

Schaefer, J.M., Denton, G.H., Kaplan, M., Putnam, A., Finkel, R.C., Barrell, D.J., Andersen, B.G., Schwartz, R., Mackintosh, A., Chinn, T., 2009. High-frequency Holocene glacier fluctuations in New Zealand differ from the northern signature. science 324, 622-625.

Scheiber, T., Adrian Pfiffner, O., Schreurs, G., 2013. Upper crustal deformation in continent-continent collision: A case study from the Bernard nappe complex (Valais, Switzerland). Tectonics 32, 1320-1342.

Schenk, F., Väliranta, M., Muschitiello, F., Tarasov, L., Heikkilä, M., Björck, S., Brandefelt, J., Johansson, A.V., Näslund, J.-O., Wohlfarth, B., 2018. Warm summers during the Younger Dryas cold reversal. Nature communications 9, 1-13.

Scherler, D., Bookhagen, B., Strecker, M.R., 2011. Spatially variable response of Himalayan glaciers to climate change affected by debris cover. Nature geoscience 4, 156.

Schimmelpfennig, I., Schaefer, J.M., Akçar, N., Ivy-Ochs, S., Finkel, R.C., Schlüchter, C., 2012. Holocene glacier culminations in the Western Alps and their hemispheric relevance. Geology 40, 891.

Schmandt, B., Aster, R.C., Scherler, D., Tsai, V.C., Karlstrom, K., 2013. Multiple fluvial processes detected by riverside seismic and infrasound monitoring of a controlled flood in the Grand Canyon. Geophysical Research Letters 40, 4858-4863.

Schubert, A., Faes, A., Kääb, A., Meier, E., 2013. Glacier surface velocity estimation using repeat TerraSAR-X images: Wavelet-vs. correlation-based image matching. ISPRS journal of photogrammetry and remote sensing 82, 49.

Schwanghart, W., Kuhn, N.J., 2010. TopoToolbox: A set of Matlab functions for topographic analysis. Environmental Modelling & Software 25, 770-781.

Schwanghart, W., Scherler, D., 2014. TopoToolbox 2–MATLAB-based software for topographic analysis and modeling in Earth surface sciences. Earth Surface Dynamics 2, 1-7.

Schwanghart, W., Worni, R., Huggel, C., Stoffel, M., Korup, O., 2016. Uncertainty in the Himalayan energy–water nexus: Estimating regional exposure to glacial lake outburst floods. Environmental Research Letters 11, 074005.

Shakun, J.D., Clark, P.U., He, F., Marcott, S.A., Mix, A.C., Liu, Z., Otto-Bliesner, B., Schmittner, A., Bard, E., 2012. Global warming preceded by increasing carbon dioxide concentrations during the last deglaciation. Nature 484, 49-54.

Shea, J.M., Immerzeel, W.W., 2016. An assessment of basin-scale glaciological and hydrological sensitivities in the Hindu Kush–Himalaya. Annals of Glaciology 57, 308-318.

Shea, J.M., Immerzeel, W.W., Wagnon, P., Vincent, C., Bajracharya, S., 2015. Modelling glacier change in the Everest region, Nepal Himalaya. The Cryosphere 9, 1105.

Shekhar, M.S., Chand, H., Kumar, S., Srinivasan, K., Ganju, A., 2010. Climate-change studies in the western Himalaya. Annals of Glaciology 51, 105.

Sherpa, S.F., Wagnon, P., Brun, F., Berthier, E., Vincent, C., Lejeune, Y., Arnaud, Y., Kayastha, R.B., Sinisalo, A., 2017. Contrasted surface mass balances of debris-free glaciers observed between the southern and the inner parts of the Everest region (2007–15). Journal of Glaciology, 1.

Shrestha, A.B., Wake, C.P., Dibb, J.E., Mayewski, P.A., 2000. Precipitation fluctuations in the Nepal Himalaya and its vicinity and relationship with some large scale climatological parameters. International Journal of Climatology 20, 317.

Sinha, A., Kathayat, G., Cheng, H., Breitenbach, S.F.M., Berkelhammer, M., Mudelsee, M., Biswas, J., Edwards, R.L., 2015. Trends and oscillations in the Indian summer monsoon rainfall over the last two millennia. Nature communications 6.

Strozzi, T., Luckman, A., Murray, T., Wegmuller, U., Werner, C.L., 2002. Glacier motion estimation using SAR offset-tracking procedures. IEEE Trans.Geosci.Remote Sens. 40, 2384.

Sturman, A., Wanner, H., 2001. A comparative review of the weather and climate of the Southern Alps of New Zealand and the European Alps. Mountain Research and Development, 359-369.

Surazakov, A., Aizen, V., 2010. Positional accuracy evaluation of declassified Hexagon KH-9 mapping camera imagery. Photogrammetric Engineering & Remote Sensing 76, 603.

Suzuki, R., Fujita, K., Ageta, Y., 2007. Spatial distribution of thermal properties on debris-covered glaciers in the Himalayas derived from ASTER data. Bulletin of Glaciological Research 24, 13.

Swisstopo, 2012. Geological Vector Datasets GeoCover, in: Topography, F.O.o. (Ed.), Wabern, Switzerland.

Tadono, T., Ishida, H., Oda, F., Naito, S., Minakawa, K., Iwamoto, H., 2014. Precise global DEM generation by ALOS PRISM. ISPRS Annals of the Photogrammetry, Remote Sensing and Spatial Information Sciences 2, 71.

Thakuri, S., Salerno, F., Bolch, T., Guyennon, N., Tartari, G., 2015. Factors controlling the accelerated expansion of Imja Lake, Mount Everest region, Nepal. Annals of Glaciology.

Thompson, S.S., Benn, D.I., Dennis, K., Luckman, A., 2012. A rapidly growing moraine-dammed glacial lake on Ngozumpa Glacier, Nepal. Geomorphology 145, 1.

Thompson, W.B., Dorion, C.C., Ridge, J.C., Balco, G., Fowler, B.K., Svendsen, K.M., 2017. Deglaciation and late-glacial climate change in the White Mountains, New Hampshire, USA. Quatern.Res. 87, 96-120.

Tsai, V.C., Minchew, B., Lamb, M.P., Ampuero, J.P., 2012. A physical model for seismic noise generation from sediment transport in rivers. Geophysical Research Letters 39.

Tshering, P., Fujita, K., 2015. First in situ record of decadal glacier mass balance (2003–2014) from the Bhutan Himalaya. Annals of Glaciology.

Uddin, S.N., Taplin, R., Yu, X., 2007. Energy, environment and development in Bhutan. Renewable and Sustainable Energy Reviews 11, 2083-2103.

van Husen, D., 2000. Geological processes during the Quaternary. Mitteilungen der Österreichischen Geologischen Gesellschaft 92, 135-156.

Veh, G., Korup, O., von Specht, S., Roessner, S., Walz, A., 2019. Unchanged frequency of moraine-dammed glacial lake outburst floods in the Himalaya. Nature Climate Change, 1.

Vijay, S., Braun, M., 2016. Elevation change rates of glaciers in the Lahaul-Spiti (Western Himalaya, India) during 2000–2012 and 2012–2013. Remote Sensing 8, 1038.

Vincent, C., Ramanathan, A., Wagnon, P., Dobhal, D.P., Linda, A., Berthier, E., Sharma, P., Arnaud, Y., Azam, M.F., Gardelle, J., 2013. Balanced conditions or slight mass gain of glaciers in the Lahaul and Spiti region (northern India, Himalaya) during the nineties preceded recent mass loss. The Cryosphere 7, 569.

Vincent, C., Wagnon, P., Shea, J.M., Immerzeel, W.W., Kraaijenbrink, P., Shrestha, D., Soruco, A., Arnaud, Y., Brun, F., Berthier, E., Sherpa, S.F., 2016. Reduced melt on debris-covered glaciers: investigations from Changri Nup Glacier, Nepal. The Cryosphere 10, 1845-1858.

Wagnon, P., Vincent, C., Arnaud, Y., Berthier, E., Vuillermoz, E., Gruber, S., Ménégoz, M., Gilbert, A., Dumont, M., Shea, J.M., 2013. Seasonal and annual mass balances of Mera and Pokalde glaciers (Nepal Himalaya) since 2007. The Cryosphere 7, 1769.

Wahl, T.L., 2004. Uncertainty of predictions of embankment dam breach parameters. Journal of hydraulic engineering 130, 389-397.

Wangdi, N., Kusters, K., 2012. The costs of adaptation in Punakha, Bhutan: Loss and damage associated with changing monsoon patterns. London: Climate Development Knowledge Network.

Watanabe, T., Rothacher, D., 1996. The 1994 Lugge Tsho Glacial Lake Outburst Flood, Bhutan Himalaya. Mountain Research and Development 16, 77-81.

Watson, C.S., Carrivick, J., Quincey, D., 2015. An improved method to represent DEM uncertainty in glacial lake outburst flood propagation using stochastic simulations. Journal of Hydrology 529, 1373-1389.

Webb, S.C., 1998. Broadband seismology and noise under the ocean. Reviews of Geophysics 36, 105-142.

Westoby, M.J., Glasser, N.F., Brasington, J., Hambrey, M.J., Quincey, D.J., Reynolds, J.M., 2014. Modelling outburst floods from moraine-dammed glacial lakes. Earth-Sci.Rev. 134, 137-159.

Wiederkehr, M., Möri, A., 2013. swissALTI3D–a new tool for geological mapping. Swiss Bulletin for Applied Geology 18, 61-69.

Williams, M.W., Wilson, A., Tshering, D., Thapa, P., Kayastha, R.B., 2015. Using geochemical and isotopic chemistry to evaluate glacier melt contributions to the Chamkar Chhu (river), Bhutan. Annals of Glaciology.

Wittmeier, H.E., Schaefer, J.M., Bakke, J., Rupper, S., Paasche, Ø., Schwartz, R., Finkel, R.C., in press. Late Glacial mountain glacier culmination in Arctic Norway prior to the Younger Dryas.

Xu, Y., Knudby, A., Ho, H.C., Shen, Y., Liu, Y., 2017. Warming over the Tibetan Plateau in the last 55 years based on area-weighted average temperature. Regional Environmental Change 17, 2339.

Yamada, T.N., N.; Kohshima, S.; Fushimi, H.; Nakazawa, F.; Segawa, T.; Uetake, J.; Suzuki, R.; Sato, N.; Chhetri, I.K.; Gyenden, L.; Yabuki, H.; Chikita, K.A., 2004. Outline of 2002-research activities on glaciers and glacier lakes in Lunana region, Bhutan Himalayas. Bull. Glaciol. Res. 21, 79-90.

Yan, L., Liu, X., 2014. Has climatic warming over the Tibetan Plateau paused or continued in recent years. J Earth Ocean Atmos Sci 1, 13.

Yang, X., Zhang, T., Qin, D., Kang, S., Qin, X., 2011. Characteristics and changes in air temperature and glacier's response on the north slope of Mt. Qomolangma (Mt. Everest). Arct.Antarct.Alp.Res. 43, 147.

Young, N.E., Briner, J.P., Schaefer, J., Zimmerman, S., Finkel, R.C., 2019. Early Younger Dryas glacier culmination in southern Alaska: Implications for North Atlantic climate change during the last deglaciation. Geology 47, 550-554.

Yuan, X., Ni, J., Kind, R., Mechie, J., Sandvol, E., 1997. Lithospheric and upper mantle structure of southern Tibet from a seismological passive source experiment. Journal of Geophysical Research: Solid Earth 102, 27491-27500.

Zemp, M., Frey, H., Gärtner-Roer, I., Nussbaumer, S.U., Hoelzle, M., Paul, F., Haeberli, W., Denzinger, F., Ahlstrøm, A.P., Anderson, B., 2015. Historically unprecedented global glacier decline in the early 21st century. Journal of Glaciology 61, 745.

Zemp, M., Hoelzle, M., Haeberli, W., 2009. Six decades of glacier mass-balance observations: a review of the worldwide monitoring network. Annals of Glaciology 50, 101.

Zemp, M., Nussbaumer, S., Gärtner-Roer, I., Huber, J., Machguth, H., Paul, F., Hoelzle, M., 2017. Glacier Mass Balance Bulletin No. 2 (2014-2015), in: WGMS (Ed.), Zurich, Switzerland, p. 244.

Zheng, W., Pritchard, M.E., Willis, M.J., Tepes, P., Gourmelen, N., Benham, T.J., Dowdeswell, J.A., 2018. Accelerating glacier mass loss on Franz Josef Land, Russian Arctic. Remote Sens.Environ. 211, 357-375.

Zhou, Y., Li, Z., Li, J., Zhao, R., Ding, X., 2018. Glacier mass balance in the Qinghai–Tibet Plateau and its surroundings from the mid-1970s to 2000 based on Hexagon KH-9 and SRTM DEMs. Remote Sens.Environ. 210, 96.